Alkane Activation on Pt(111): Thermal Kinetics, Thermodynamics, and the Role of Van der Waals Interactions

Thomas Jackson Eldridge
Salem, Virginia

B.S., University of Mary Washington, 2013

A Dissertation presented to the Graduate Faculty
of the University of Virginia in Candidacy for the Degree of
Doctor of Philosophy

Department of Chemistry

University of Virginia
December, 2018

_____

_____

_____

_____

_____

Acknowledgements

I would like to thank Dr. Ian Harrison for giving me the opportunity to join his research group and study kinetics and surface chemistry. He put a lot of time and effort into guiding me through my project, and I have learned an extensive amount along the way. I would like to thank all the members of the Harrison research group who have helped me out throughout my project. I'd like to recognize Dr. Jason Navin and Yifeng Song, who taught me so much of the technical aspects of laboratory work and were always willing to help regardless of the difficulty of the problem or question, even after graduating from the group. Without them, I would not have accomplished as much as I have. I want to recognize Hongying Dong and Grayson Johnson, who were present for most of my time in the Harrison lab and helped me countless times.

I want to thank my family for encouraging me throughout my studies and giving me the education and foundation for reaching this point in my life. Without their unending support, I would not have come nearly this far. My friends also helped me tremendously through my time in graduate school. Most notably, I'd like to thank Matthew Cline, Ellen Speers, Dr. Christopher Shingledecker, and Anna Shingledecker, and Dr. Charles McAnany for their friendship. Without them, I would not have made it through the hardest moments of graduate school. They also broadened my field of knowledge in different fields of chemistry, and helped me develop programming and computational skills which have assisted me numerous times.

I would like to thank Sara Plante, Dr. Raymond Scott and Dr. Leanna Giancarlo for starting me down the path of chemistry research and honing my interest in catalysis, kinetics, and surface science.

Abstract

Transition metal catalysts are used in a wide variety of industrial processes, including steam reforming of methane, which is the main source of synthesis gas used for producing ammonia, large hydrocarbons, and olefins. Dissociative chemisorption by initial C-H bond cleavage is considered to be the rate limiting step in steam reforming. At the high surface temperatures used in industrial reactors (ca. 800 K) molecular desorption is highly competitive to dissociative chemisorption. Alkanes can be molecularly physisorbed to the surface through van der Waals interactions at low surface temperatures (T_s < 300 K), but rapidly desorb at high temperatures. It is critical to understand both the kinetics of molecular desorption and dissociative chemisorption, as well as how they relate to each other, in order to better model industrial catalysts and catalytic processes. This study reports on the thermal rate constants for molecular desorption and dissociative chemisorption, and the role van der Waals interactions play in stabilizing the dissociative chemisorption for alkanes ranging from methane to n-nonane.

The molecular desorption rate constants were determined by analysis of temperature programmed desorption (TPD) spectra, to extract pre-exponential factors (ν_d) and desorption energies (E_D). The pre-exponential factors and desorption energies are reported for the branched alkanes of isobutane, neopentane, and 2,2,3,3-tetramethylbutane (TMB). The latter two molecules were found to have weaker desorption energies than their n-alkane isomer counterparts due to their branched geometry and different van der Waals attraction to the surface that falls off as $1/z^3$.

The rate constants for dissociative chemisorption of alkanes from methane to n-nonane were calculated from a fit of alkane thermal dissociative sticking coefficients (DSC) to a precursor-mediated thermal trapping (PMTT) model, which assumes gas molecules undergo full

energy exchange with the surface and thermalize to the surface temperature prior to undergoing either desorption or reaction, with thermal rate constants. Even for molecules which are known to have poor gas-surface energy exchange (e.g. methane), the PMTT model was able to adequately model thermal equilibrium DSCs, to yield reaction activation energies ($E_{a,r}$) and pre-exponential factors (ν_r). For the majority of alkanes, $\nu_d > \nu_r$ with both values increasing with increasing alkane size. TMB was found to have special reactivity at temperatures above 560 K, where it underwent trapping-mediated C-C bond pyrolysis with a $\nu_{r,C-C}$ and $E_{a,C\text{-}C}$ significantly larger than that of ν_d and E_D.

Additional studies were done into the formation of graphene on Pt(111), a material which has been a topic of great interest in the recent decade because of its unique electrical properties as a semi-conductor, by TMB chemical vapor deposition. Although larger alkanes were shown by this study to be more reactive on Pt(111) than smaller alkanes, TMB formed smaller coverages (1.35 ML) of graphene than ethylene (2.57 ML). This was determined to be due to many scattered graphene islands, between which were regions inaccessible to the large TMB molecules, which require an ensemble of binding sites to adsorb and react.

The transition state and products of dissociative chemisorption were found to be stabilized by van der Waals interactions, which the E_D of the reagent gas molecules well approximates. $E_{a,r}$ decreased proportional to the increase in E_D as molecular size increased, yielding an Evans-Polanyi correlation with a slope $dE_{a,r}/dE_D = -0.50 \pm 0.04$. In general, larger alkanes were found to be more reactive on surfaces than smaller alkanes. Because van der Waals interactions cause dissociative chemisorption to become more exothermic, it was possible to predict heats of reaction and Pt-C bond energies for a wide range of alkanes, from ethane to n-nonane, using data from methane and isobutane Pt(111) single crystal calorimetry experiments.

The Evans-Polanyi correlation was reproduced between the apparent activation energies and heats of reaction yielding a slope $dE_{a,r}/dE_D = -0.46 \pm 0.09$. This study demonstrates a method of predicting heats of reaction and activation energies for surface reactions using data from a small set of very difficult single crystal calorimetry experiments.

Table of Contents

Section 1 – Introduction

Section **Page**

1.1 Purpose

Transition metal catalysts have been used to facilitate and significantly lower the energy requirements of the cleavage of bonds which have large bond dissociation energies. Nitrogen, which is vital to all forms of life, is present in high quantities in air as $N_{2(g)}$. However, the bond dissociation energy of $N_{2(g)}$ (944.87 ± 0.05 kJ/mol) is so massive that it is effectively inert without the aid of a catalyst.[1] An iron metal catalyst can activate $N_{2(g)}$, in the presence of hydrogen gas, $H_{2(g)}$, at high temperature and pressure, via the Haber-Bosch process, to form ammonia, a nitrogen containing molecule which is useful as a synthesis reagent. Approximately 120 Mt of ammonia are formed annually using the Haber-Bosch process, consuming 29 GJ of energy per ton of synthesized ammonia.[2] However, the energy consumption of the Haber-Bosch process does not fully encompass the full amount of energy used to synthesize ammonia, because $H_{2(g)}$ is not naturally present in high quantities in the air and must be synthesized from other hydrogen containing molecules. The most common method of forming hydrogen is steam reforming of natural gas (20 Mt/year) and consumes 12.6 GJ for every ton of hydrogen produced. Steam reforming is favored over electrolysis of water for hydrogen synthesis, because even an electrolysis system with 100% energy-to-hydrogen conversion would require a minimum of 119 GJ per ton of hydrogen produced.[3] In addition to hydrogen and ammonia, steam reforming of natural gas is used to form synthesis gas ($H_{2(g)}$ + $CO_{(g)}$, 300 Mt/year, 13.6 GJ/t), which is used to produce large hydrocarbons such as synthetic fuels and olefins, via the Fischer-Tropsch process (15 Mt/year, 67 GJ/t), and methanol (30 Mt/year, 28 GJ/t).[2] All of these industrial processes, which make use of short contact time reactors, depend in some part on the interactions of small alkanes with transition metal surfaces, most significantly the dissociative chemisorption reaction where a C-H bond cleaves at the surface and metal-alkyl and metal-H

bonds form, and consume a significant amount of the world's total energy (> 2%). There are also industrial processes which offer opportunities to introduce catalysis. The dehydrogenation of small alkanes to form unsaturated hydrocarbons, such as ethylene (100 Mt/year, 15 GJ/t) and propylene (55 Mt, 15 GJ/t), involves high temperature and pressure gas-phase pyrolysis.[2] A study by Schmidt showed that partial oxidation of alkanes ($C_nH_{2n+2} + 1/2\,O_2 \rightarrow C_nH_{2n} + H_2O$) is possible for short contact time reactors using rhodium supported alumina foam,[4] and could offer chemical engineers insight for future industrial reactors. For this reason, the dissociative chemisorption of small alkanes on transition metal surfaces has been a topic of great economic importance. An improved understanding of the kinetics of small hydrocarbon molecular adsorption, by either physisorption (van der Waals interactions) or chemisorption (covalent bonding), and subsequent reactivity on transition metal surfaces is desired to support scientific design of more energy efficient catalysts and reactors.

Significant study has been done on alkane dissociative chemisorption by initial C-H bond cleavage, the rate limiting step in steam reforming, on transition metal surfaces.[5] Relatively little research has addressed the gas-surface energy exchange or stabilizing factors, such as van der Waals interactions between the gas molecules and the surface. Effusive molecular beam experiments, unique to this lab, permit both thermal equilibrium and non-equilibrium (e.g. with unequal gas and surface temperatures, $T_g \neq T_s$), studies of molecules of any size, with well-defined characterization of all degrees of freedom. This versatile range of study is not generally possible for supersonic beams due to supersonic expansion, in which the rotational temperature is cooled to the beam translational temperature and the vibrational temperatures are ambiguous, which will be discussed in more detail in a later section. The impact of van der Waals interactions as a stabilizing force for dissociative chemisorption of alkanes has not been previous

investigated. In the studies reported here in, an alkane impinging on a surface is assumed to be accelerated by van der Waals interactions, exchange energy with the surface atoms, and then either react with the surface atoms or molecularly desorb from the surface. For the purpose of studying alkane reactivity and energy exchange, the dissociative sticking coefficients (DSC) of alkanes from methane to pentane were measured, both under thermal equilibrium, where the gas and surface temperature are equal, and in thermal imbalance, where the gas and surface temperatures differ. Thermal programmed desorption (TPD) was used to characterize the kinetics of intact molecular desorption. The measured dissociative sticking coefficients in conjunction with the measured molecular desorption rate constants could be used to fix dissociative chemisorption rate constants from the transient physisorbed precursor complex. Kinetic schemes which account for competitive molecular desorption vary in complexity. In the absence of thermal equilibrium between the molecule and surface, the precursor-mediated microcanonical trapping (PMMT) model, which disregards energy exchange, or the master-equation precursor-mediated microcanonical trapping (ME-PMMT) model, which permits realistic energy exchange between the molecule and surface oscillators, provide the most accurate rate constants for alkane dissociative chemisorption when compared to experimental values.[6-8] This study intends to demonstrate that the simplest kinetic scheme, the precursor-mediated thermal trapping model (PMTT), which assumes full energy exchange between the molecule and surface and relaxation to the physisorption potential energy minima at T_s, yields sufficiently accurate rate constants for gas molecules which are in thermal equilibrium with the surface, both prior and after interaction with the surface. The rate constants and activation energies derived from the PMTT model are then compared to demonstrate the importance of van der Waals interactions via Evans-Polanyi correlations, which relate the activation energies for dissociative chemisorption to desorption

energies and van der Waals stabilized heats of reactions. The crux of the analysis reported in this study hinges on the impinging molecules being in thermal equilibrium with the surface, either prior and after encountering the surface ($T_g = T_s$, pseudo-equilibrium) or as a result of energy exchange with and thermalization to the surface. Only experiments with effusive molecular beams, which only this lab has incorporated, permit the characterization of gas-surface energy transfer of molecules of any size under well-defined conditions.

1.2 Heterogeneous Catalysis

Catalysts are an important aspect of chemical synthesis, as they are able to reduce the energy requirements for a reaction without being directly consumed by the reaction. Homogeneous catalysts exist in the same phase state as the reactants, but have a few problems that limit their use in industry. If the products are also homogenous, it is difficult to separate the products, reactants, and catalysts. Without this separation, secondary reactions may occur between the initial products and the reagents which reduces the percent yield of the desired products. While homogenous catalysts are left unchanged by the desired reaction, secondary reactions may denature the catalysts over time and limit the catalyst turnover number, an important factor for their practical use. On the other hand, heterogenous catalysts, which exist in a different phase state relative to the reactants and products, avoid some of these limitations. Rather, heterogenous catalysts allow for the synthesis of large molecules from simple reactants with relatively easy product separation and high catalyst reusability.[9] While the reactive sites on heterogeneous catalysts can be poisoned by contaminants, limiting the turnover number, it is possible to clean contaminants off surfaces using reactive gases, such as oxidizers for carbon species. Although, the type of reactive gases which can be used without damaging the surface

depends on the transition metal, where noble metals are more forgiving than more reactive metals like iron. On the other hand, homogenous catalysts which have expired typically cannot be easily recovered. Expired homogeneous catalysts have to be remade through synthesis reactions, which at best directly uses the expired catalysts within a few steps. At worst the expired catalysts cannot be simply converted back into their useful state and it is more economical to synthesize new catalysts instead of recovering old ones. In general, transition metal heterogeneous catalysts are simpler to use and maintain that homogeneous catalysts. For these reasons, industrial processes make wide use of heterogenous catalysis.

One of the earliest and most important industrial processes which make use of heterogenous transition metal catalysts is the activation of nitrogen into ammonia via the Haber-Bosch process. Nitrogen and hydrogen gases dissociate on a potassium doped iron catalyst and recombine to form ammonia.[10-11]

$$N_{2(g)} + 3H_{2(g)} \xrightarrow{Fe} 2NH_{3(g)} \qquad \Delta_r H^0_{298K} = -92 \text{ kJ/mol}$$

The necessity of hydrogen gas as a reactant is the major energy cost in the hydrogenation of nitrogen. Hydrogen is produced from endothermic steam reforming of methane on a nickel catalyst, which requires a significant amount of energy.

$$CH_{4(g)} + H_2O_{(g)} \xrightarrow{Ni} CO_{(g)} + 3H_{2(g)} \qquad \Delta_r H^0_{298K} = 206 \text{ kJ/mol}$$

Synthesis gas, also known as syngas, is the product of the steam reforming reaction and is used in a wide variety of processes separate from the Haber-Bosch process. Carbon monoxide from syngas can be combined with water in the water-gas shift reaction in order to form additional hydrogen.

$$CO_{(g)} + H_2O_{(g)} \xrightarrow{Ni} CO_{2(g)} + H_{2(g)} \qquad \Delta_r H^0_{298K} = -41 \text{ kJ/mol}$$

A significant proportion of hydrogen used in industrial hydrogenation reactions is obtained from syngas. Large alkanes can be synthesized from syngas on cobalt or iron catalysts as precursors to polymers and olefins by means of the Fischer-Tropsch reaction.

$$(2n+1)H_{2(g)} + nCO_{(g)} \xrightarrow{Fe} C_nH_{(2n+2)(g)} + nH_2O_{(g)}$$

Methanol is formed most commonly from synthesis gas using a copper-zinc oxide catalyst with aluminum oxide or chromium(III) oxide ($Cu/ZnO/Al_2O_3$, $Cu/ZnO/Cr_2O_3$).[12]

$$CO_{(g)} + 2H_{2(g)} \xrightarrow{Cu/ZnO} CH_3OH_{(g)} \quad \Delta_r H^0_{298K,5MPa} = -90.7 \text{ kJ/mol}$$

Saturated hydrocarbons can be formed by hydrogenation reactions with unsaturated hydrocarbons on platinum catalysts. Using the platinum catalysts, alkanes can be converted into olefins through dehydrogenation by decreasing the partial pressure of hydrogen.

$$C_mH_{n(g)} + H_{2(g)} \xrightleftharpoons{Pt} C_mH_{(n+2)(g)}$$

An additional use of hydrogen from steam reforming and water-gas shift reactions is in hydrogen fuel cells, which have no carbon dioxide emissions.

1.3 Platinum Catalysts

Platinum is a noble metal which is resistant to oxidation and is closely related to ruthenium, rhodium, palladium, osmium, and iridium, which are all platinum-group noble metals often used as catalysts. As a transition metal catalyst, platinum plays a major role in the synthesis of high-octane gasoline from naphtha,[13] a flammable oil which consists of a variety of hydrocarbons and is dry distilled from petroleum, as well as the synthesis of several other chemicals.[14-15] Along with rhodium, platinum is the main catalyst in the catalytic converters found in the exhaust system of combustion engines like those found in automobiles.[16-17] Platinum is also known to be an efficient catalyst in both hydrogenation and dehydrogenation

reactions, where the reaction pathway is tuned by the partial pressure of hydrogen in the reactor.[15] Direct methanol fuel cells (DMFCs) are a safer alternative to hydrogen fuel cells and use platinum electrodes on both the anode and cathode.[18-20]

1.4 Alkanes

Alkanes are saturated hydrocarbons with a wide range of sizes, dependent on carbon chain length, with a chemical formula of $C_nH_{(2n+2)}$. Natural sources of alkanes are primarily natural gas and crude oil. Natural gas consists of mostly small alkanes, with 85% methane, 3-8% ethane, 1-2% propane, and < 2% butane, propane, and hexane.[21] Crude oil contains mostly unsaturated hydrocarbons, including benzene analog cyclic-aromatics, with only 30% saturated alkanes.[22] Relatively large alkanes are obtained through distillation of crude oil, but can also be obtained from thermal cracking and hydrogenation of the unsaturated hydrocarbons. Synthetic sources of alkanes, as previously mentioned, include the Fischer-Tropsch reaction, which converts carbon monoxide and hydrogen gases into small chain alkanes. In addition to being a valuable fuel source, alkanes can be dehydrogenated into olefins for the use in alkylation, hydration, and halogenation reactions.

1.5 Dissociative Chemisorption

The initial dissociative chemisorption of a gas phase molecule on transition metal catalysts results in the cleavage of a bond with the fragments forming covalent bonds with surface atoms. A gas-surface collision complex is formed, composed of the molecule and a few immediately adjacent surface atoms, in the vicinity of the physisorption well, and can be treated as a trapped precursor species which can go on to react or desorb. A potential energy surface

diagram for alkane dissociative chemisorption by initial C-H bond cleavage is shown in Figure 1.1 below. There tends to be two limiting reactive scenarios. In the case of small molecules with relatively stiff vibrational modes, an impinging molecule which does not have enough energy to react on the initial collision rapidly desorbs from the surface with negligible gas-surface energy exchange. At energies sufficient to access the transition state region it is assumed that the precursor complex state distribution is microcanonically randomized and that ultrafast desorption lifetimes at reactive energies limits any further gas-surface energy transfer to the surrounding surface. This defines the PMMT model in which RRKM rate constants are employed. A dynamically biased version, d-PMMT, is available to address deviations from statistical behavior. The reaction which occurs with the initial collision is direct dissociative chemisorption. The second limit apples primarily to larger molecules which have softer vibrational modes that can echange energy efficiently with the surface. When surch molecules strike the surface, they promptly exchange energy and thermalize into the physisorption potential energy well, from where they can go on to react or desorb with thermal Arrhenius rate constants. This limit defines the PMTT model. The reaction where the molecule initiates from the physisorption potential energy minima is indirect dissociative chemisorption. Molecules which thermalize fully to the surface temperature may or may not be in thermal equilibrium with the surface atoms on the initial collision, but are in thermal equilibrium after falling into the physisorption potential energy minima. The Master Equation (ME)-PMMT model is an intermediate which explicitly builds in energy transfer between the collisional precursor complex and the surrounding surface atoms.

Molecular desorption and dissociative chemisorption are competitive reactions. In the case where more energy is required to react than desorb, the reaction is an activated process. The

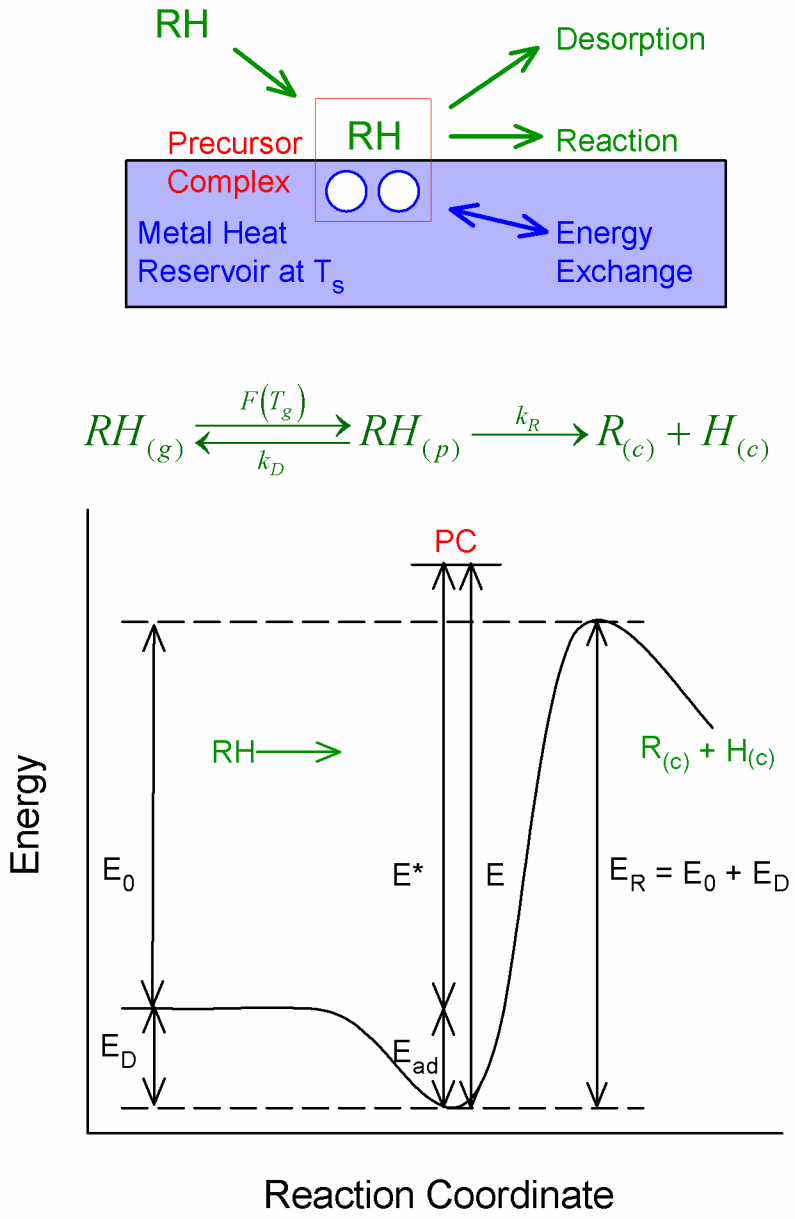

Figure 1.1: A two dimensional potential energy surface for an activated process with respect to the reaction coordinate of alkane dissociative chemisorption by initial C-H bond cleavage, which includes the gas-surface precursor complex at an average energy, E, with respect to the physisorption potential energy minima.

gas-surface complex resulting from an activated process is short lived due to the more facile desorption pathway. Because molecules need more energy to react than desorb, an increase in either the energy of the impinging gas molecule or the surface atoms results in an increase in the reaction probability. An unactivated process occurs when the energy required to desorb is greater than the energy required for dissociative chemisorption. In such cases, an impinging molecule is more likely to be trapped in the physisorbed state and react with the surface than to desorb. With an unactivated process, an increase in the surface temperature leads to a decrease in the reaction probability because significantly more molecules can overcome the less favorable and larger activation energy of desorption when compared to the reaction energy from the perspective of the physisorption well minima.

The probability that a molecule will react via dissociative chemisorption per gas-surface collision is referred to as the dissociative sticking coefficient (DSC). For alkanes, the rate of carbon deposition, $d\theta_C/dt$, is given by

$$\frac{d\theta_C}{dt} = S\left(T_g, T_s\right) F\left(T_g\right) \qquad \text{Equation 1.1}$$

where $S(T_g,T_s)$ is the molecular DSC, n_C is the number of C atoms per molecule, $F(T_g)$ is the flux of impinging gas molecules at T_g, and θ_C is the carbon coverage in monolayers (ML). The flux of molecules onto the surface from a random ambient gas is generally,[23]

$$F = \frac{d^2N}{dAdt} = \frac{dP}{dt} = \frac{1}{4}\langle v \rangle \rho \qquad \text{Equation 1.2}$$

where N is the number of molecules, A is the area of gas-surface collisions, t is time, P is the pressure, $\langle v \rangle$ is the average velocity of the molecules, and ρ is the number density of gas molecules. The total gas exposure, ε, is the time integral of the flux, dN/dA. The DSC is equal to the total chemisorbed coverage divided by the exposure. Measuring the DSC of a molecule at a

different gas and surface temperatures can give insight into non-equilibrium kinetics of dissociative chemisorption which is coupled to gas-surface energy exchange rates. The precursor-mediated microcanonical trapping (PMMT) model, which does not account for gas-surface energy exchange, yields kinetic rate constants which fit well to experimental data for non-equilibrium, direct dissociative chemisorption, where negligible energy transfer occurs in the precursor complex prior to reaction or desorption. In the non-equilibrium case where gas molecules exchange a non-negligible amount of energy with the surface, but do not fully thermalize to the surface temperature, the master-equation precursor-mediated microcanonical trapping (ME-PMMT) model, which accounts for realistic energy exchange in the precursor complex, best fits experimental data. When impinging molecules are in thermal equilibrium with the surface atoms or when energy exchange within the precursor complex is sufficient to thermalize the majority of gas molecules to the surface temperature, the precursor-mediated thermal trapping (PMTT) model, which uses thermal kinetic rate equations where $T = T_s = T_g$, fits experimental data as well as the more complex ME-PMMT model. Traditional thermal Arrhenius activation energies and pre-exponential factors can be calculated from DSC data when the gas and surface are in thermal equilibrium, and match well with activation energies yielded from the PMTT model.

In addition to studying gas-surface energy exchange, angular DSC experiments can be made to determine the reactivity of a molecule relative to its approach angle, ϑ, away from the surface normal.[8] Considering the 1D approximation by van Willgen, which assumes only translational energy, E_t, normal to the surface, E_n, is effective in overcoming the barrier for direct dissociative chemisorption, where impinging molecules react on initial collision or desorb, the DSC, $S(E_n)$, scales by

$$E_n = E_t \cos^2 \vartheta \qquad \text{Equation 1.3}$$

where ϑ is the angle away from the direction of the surface at normal.[24] While van Willgen's approximation ultimately fails quantitatively, overestimating experimental DSC, due to the multidimensional nature of dissociative sticking, it demonstrates the qualitative relationship between the sharpness of DSC angular variation and the availability of normal translational energy. Molecules which have few vibrational modes, do not exchange energy with the surface well, and favor direct dissociative chemisorption, such as methane, are known to have sharp angular dependences for the DSC (e.g. CH_4/Pt(111), $S(\vartheta,T) = S_0\cos^{12.8}\vartheta$).[8] Methane and ethane react in a dynamically biased fashion, such that rotational and surface-parallel translational degrees of freedom are spectators, and vibrational energy has a mean efficacy of $\eta_v = 0.40$ relative to normal translation with respect to overcoming the barrier for dissociative chemisorption. If these dynamical biases held for all alkanes, the angular dependence on the DSC would be expected to decrease with the number of vibrational modes (3N – 6). The angular dependence on the DSC ($S(\vartheta,T) = S_0\cos^n\vartheta$) was observed to decrease from methane (n = 12.8) to ethane (n = 5.6) to propane (n = 1.10) on Pt(111), however propane was not found to deviate significantly from statistical behavior, with only surface-parallel translational energy assumed to be a spectator for dissociative chemisorption.[8] The rapid decrease in dynamical biases and angular dependence on the DSC with increasing alkane size has a few implications. As the number of vibrational modes in a molecule increases, vibrational energy eventually provides sufficient energy to overcome the barrier for dissociative chemisorption without substantial assistance from normal translation energy or the surface phonons. Increased number of vibrational modes which are not degenerate typically leads to smaller energy steps between modes, which facilitates gas-surface energy exchange, because of the limited vibrational

frequencies of the crystal lattice phonons (i.e. platinum Debye frequency, $\hat{\nu}_D$ = 184 cm^{-1}),[25] and promotes indirect dissociative chemisorption. The combination of normal translational energy becoming less important for overcoming the barrier for direct dissociative chemisorption and the increasing favorability of indirect dissociative chemisorption with each increase in carbon chain length suggests angular variations of DSCs will be negligible for alkanes larger than propane.

1.5.1 By Initial C-H Bond Cleavage

The dissociative chemisorption of small alkanes is known to be an activated process. In the case of methane, the initial C-H bond dissociation, where a carbon-hydrogen bond is cleaved at a metal surface in a concerted process to yield hydrogen and methyl fragments covalently bound to the surface, is widely considered to be the rate-limiting step in steam reforming.[26-27] Wei and Iglesia demonstrated this by experiments with methane on supported metal nanocatalysts, which also indicated that methane reforming was a structure sensitive process.[28-29] Other surface science studies have found that methane on flat transition metal surfaces has thermal sticking coefficients which are several orders of magnitude higher than those found on nanocatalysts.[30-32]A wide range of experiments support C-H cleavage as the initial step for alkane dissociative chemisorption on several transition metal surfaces,[23, 33-41] even though C-C bonds have far weaker bond dissociation energies (e.g. methyl C-H 440 kJ/mol, methyl-methyl C-C 377 kJ/mol).[1] While C-C bond cleavage happens readily as a secondary reaction on hot surfaces after dissociative chemisorption by initial C-H bond cleavage, little evidence points to C-C dissociation as the initial step. This is due to C-C bonds having an internal position in each molecule, shielded from the surface by the C-H bonds which have more facile geometric access to the surface. Initial C-C bond dissociative chemisorption is more sterically hindered and

limited in viable orientations when compared to initial C-H bond dissociative chemisorption, which predicts both a higher transition state barrier and lower kinetic rate pre-exponential for C-C cleavage. This is due to the process through which the surface catalyzes the dissociative chemisorption reaction. In order for surface atoms to reduce the energy requirements for the initial C-H bond dissociation of methane from 439.3 to 58.1 kJ/mol, the d-orbital electrons must transfer into the empty π^* anti-bonding orbitals of the C-H bond and weaken the bond. As the C-H bond weakens, there is a concerted formation of metal-H and metal-alkyl covalent bonds. Because radical species are not produced as intermediates though this dissociative chemisorption reaction mechanism, as they are in gas-phase bond dissociation, it is reasonable for activation energies for dissociative chemisorption to be significantly lower than the full gas-phase bond dissociation energy.

1.5.2 By Initial C-C Bond Cleavage

Despite the poor sterics involved, Weinberg demonstrated that C-C bond cleavage can be an alternate pathway to the initial C-H bond dissociative chemisorption and is favorable for certain larger alkanes at high temperatures on Ir(111),[42-44] Ir(110),[45-46] and Ru(0001)[43, 47-48] surfaces. In the case of the iridium studies, alkanes larger than ethane underwent initial C-C bond dissociative chemisorption at surface temperatures greater than 500 K. The activation barriers for the C-C dissociative chemisorption were far below the gas-phase bond dissociation energy, showing that catalysis effectively lowers the required energy to break C-C bonds, despite poor sterics. Neopentane on Ir(111) was proposed to have a significantly lower barrier for C-C dissociation relative to propane and butane due to the relatively weak tertiary-butyl C-C bond (t-butyl-methyl C-C 364 kJ/mol, methyl-methyl 377 kJ/mol).[1, 44] In the case of cyclo-alkanes,

initial C-C dissociative chemisorption was favored over initial C-H cleavage on Ir(111)[43] at surface temperatures greater than 500 K. On Ru(0001)[43, 47], cyclo-alkanes smaller than c-hexane were found to favor initial C-C dissociative chemisorption at all temperatures, whereas c-alkanes equal to or larger than c-hexane favored initial C-H dissociation at all temperatures. Weinberg reported two temperature dependent reaction mechanisms for alkanes on Ir(111).[44] Propane, isobutane, n-butane, and neopentane all favored initial C-H dissociative chemisorption at surface temperatures less than 600 K and initial C-C dissociative chemisorption at surface temperatures greater than 600 K.[44] Weinberg used thermal rate equations to model the kinetics and estimated the reaction activation energies and pre-exponential factors for each alkane. In the cases where initial C-C dissociative chemisorption only occurred at high temperatures, the reaction energies and pre-exponential factors were found to be higher than the initial C-H dissociative chemisorption. However, Weinberg's papers did not suggest a reaction mechanism for dissociative chemisorption by initial C-C bond cleavage, which could justify having a larger pre-exponential factor and a less entropically constrained transition state than dissociative chemisorption by initial C-H scission.

1.6 Alkane Dissociative Chemisorption Studies

1.6.1 Thermal Bulb

Activated dissociative chemisorption kinetics are difficult to characterize for gas molecules which desorb at temperatures lower than those at which they appreciably react using traditional ultra-high vacuum techniques.[49] Yates and Goodman developed intermediate "thermal bulb" techniques in order to measure the kinetics of molecules with extremely low sticking coefficients.[50] Thermal bulb experiments are the simplest method for measuring thermal

equilibrium DSCs, where the gas molecules are exposed to the crystal surface as an ambient gas. When the chamber and surface temperatures are not equal, the pressure within the chamber must be at least 3 Torr for gas molecules striking the surface to fully thermalize to the surface temperature over the distance of roughly a mean free collision path length above the surface.[51-52] The high gas-surface collision flux due to the relatively high pressure employed restricts the range of molecules that can be studied to those with low DSC ($<10^{-8}$), in order to avoid impractically short dosing periods. This is a massive limitation, because most molecules have DSC too high to be measured using thermal bulb techniques. One method of resolving this limitation involved using chambers with high pumping speeds in order to obtain reliable data from short dosing periods. The reagent gas was introduced into the chamber while the crystal was cold. Once the desired pressure was obtained, the crystal would be rapidly heated to the desired temperature. After the dosing period, the chamber would be rapidly evacuated. Some the earliest experiments using these techniques were performed by Winters for methane on tungsten.[53-54] Brass and Yates followed with methane experiments on rhodium.[55-56] Further methane experiments were performed on platinum[35] and nickel[50, 57]. An alternate method, which eliminated the necessity of either massive pumping speeds or impractically short dosing periods, used a high pressure of inert gases, such as argon or nitrogen, to dilute the reagent gas, which was found to yield better results than shorter dosing times.[51] Because reaching thermal equilibrium between the gas and the surface is difficult and unreliable even at high pressures, a few methods were developed to pre-heat the gas molecules prior to exposure to the crystal surface. Brass used a heated water bath in a separated section of the chamber to increase the gas temperature before the dosing period.[58] Chorkendorff used a thermal finger near the face of the crystal to heat gas molecules directly before they collided with the surface and measured thermal

equilibrium DSCs with pressures below 3 mbar.[30, 59] Despite this innovative technique, the largest DSC measured was 2 x 10^{-7}.

Non-equilibrium DSC measurements [i.e. $S\left(T_g = T_{chamber}, \text{variable } T_s\right)$], due to the lack of the necessity for the gas molecules to thermalize to the surface temperature, were done at lower pressures (~10^{-4} Torr). Methane and deuterated methane were studied on Ir(111)[60] as well as Pt(110)[51], along with ethane and d-ethane, under such conditions. In the case of each ambient gas dosing experiment, both thermal equilibrium and non-equilibrium, the studied alkanes were found to undergo dissociative chemisorption as an activated process, with the DSC increasing with an increase in either gas or surface temperature.

1.6.2 Supersonic Molecular Beams

A major weaknesses of the thermal bulb experiment is the inability to investigate the dynamical behavior of the dissociative chemisorption of small molecules. A few thermal bulb experiments attemped laser pumping of vibrational modes, but due to the low number of excited molecules, no measureable changes in DSC were found.[55-56] In order to better characterize the dynamics of reactions on surfaces, supersonic molecular beams replaced thermal bulb techniques and are currently a favored method for the measurement of DSCs.

Supersonic molecular beams are created when a high pressure of gas is supersonically expanded through a small aperture of a nozzle into high vacuum. A series of differentially pumped regions and skimmers with small orifices results in a highly collimated beam entering the main UHV chamber. The supersonic expansion yields molecules with an average translational energy equal to 5/2 $k_B T_{nozzle}$, along the axis of the beam. Due to the massive pressure difference between the vacuum chamber and the backing pressure, where the gas is in

viscous flow, the beam undergoes supersonic expansion. Collisional cooling of the translational motion along the beam direction occurs during the supersonic expansion. The beam translation temperature, T_b, measured from the internal perspective of the beam, is typically about 20 K, such that there is a relatively narrow distribution of translational energies within the beam. Because collision-based rotational to translational energy conversion is facile, rotations are also cooled to T_b, often about 20 K. Vibrational states remain mostly unaffected by supersonic expansion for small molecules like methane, because there is poor collisional energy transfer between translational and vibrational energy.[61] Larger molecules, which have more closely spaced vibrational states, experience more collisional vibrational energy cooling, which is poorly understood and so the vibrational energy content of larger molecule supersonic molecular beams is unpredictable and rarely, if ever, characterized.[62] Hence, DSC measurements for supersonic beams with molecules larger than methane cannot be theoretically modeled with any confidence, because the beam energy distributions are not well-defined.

The range of translational energy in a well collimated supersonic molecular beam is extremely narrow. By changing the backing pressure, nozzle temperature, or the mass of a "seeding" gas, the translational energy can be specifically tuned. However, because changing the nozzle temperature also affects the rotational and vibrational modes the gas molecules, it is typically favored to adjust the translational energy using inert carrier gases of different masses. Despite the ability to change the nozzle temperature, backing pressure, and carrier gas, supersonic expansion and collisional cooling of degrees of freedom limits the characterization of non-equilibrium DSCs. The relative efficacy of vibrational energy (η_{vib}) to normal translational energy to promote reactivity has been possible to study using laser-pumped supersonic beams, but the efficacy of rotational energy cannot be simply evaluated using these techniques.

The King and Wells[63] method is the most widely used supersonic beam technique for measuring DSCs. A flag of an inert material is placed between the crystal surface and the supersonic beam and the ambient pressure is measured as a function of time. When the beam enters the UHV chamber, there is a significant spike in pressure which is given sufficient time to equilibrate. The flag is then lifted to expose the crystal surface to the molecular beam. A drop in pressure occurs due to the uptake of molecules on the crystal surface. The DSC is then the resultant pressure drop from the equilibrated high pressure to the chamber pressure after the flag has been lifted. This technique can only be used to measure relatively high DSCs ($>10^{-2}$), because most pressure gauges have at best a 1% noise limit at any given pressure.

The impact of translational energy on light alkane DSCs have been widely studied on platinum,[37, 64-71] nickel,[38-39, 69-79] and iridium.[40, 45-46, 80-81] In each experiment, the alkanes were determined to be translationally activated. The exception to this was on Ir(110) at low translational energies, where alkanes underwent an unactivated chemisorption. Alkane DSCs on Pt(111) were found to scale based on the translation energy normal to the surface, $S(E) = S(E_n)$. The normal translational energy is defined as $E_n = E_t \cos^2\vartheta$, where E_n is the translational energy normal to the surface, E_t is the total translational energy, and ϑ is the molecular angle of incidence with respect to the surface normal.

Supersonic molecular beams have been critical for measuring non-equilibrium dissociative sticking coefficients as functions of translational energy, internal energy, and surface temperature.[64, 72, 82-84] By laser-pumping the molecular beam, rovibrational eigenstate-resolved dissociative sticking coefficients for methane been measured.[67, 74-75] From these studies, methane was found to react dynamically, having a vibrational efficacy of $\eta_{vib} = 0.44$ with respect to normal translational energy,[70] while the value of η_{vib} appropriate to statistical transition state

theories is $\eta_{vib} = 1$. Most vibrational mode pumping experiments have been done on methane. This is because larger molecules with more vibrational modes experience spectral dilution of oscillator strengths, diminishing of the thermal population in individual modes, and intra-vibrational redistribution (IVR), all of which combine to make it increasingly difficult to pump a large fraction of the beam population into a single excited vibrational structural mode as molecular size increases. Small molecules with rigid vibrational modes like methane, which has a rovibrational density of fewer than 10 states per cm^{-1}, do not experience significant IVR and there is no mixing between structural vibrational modes.[85]

1.6.3 Effusive Molecular Beams

In the study of gas-surface reactivity, an alternative to supersonic molecular beams are effusive molecular beams. The backing pressure of gas molecules in an effusive beam doser is sufficiently low that the gas remains in molecular flow. No supersonic expansion occurs, and so no degrees of freedom undergo collisional cooling. This allows each degree of freedom to be thermalized to the nozzle temperature, $T_{nozzle} = T_g = T_{vib} = T_{rot} = T_{trans}$, leading to full knowledge of the energy distributions of the internal modes within an effusive beam.[86] This is essential when studying and modeling the gas-surface reactivity of large molecules. By contrast, both rotational and erratic vibrational cooling can occur during supersonic expansions, which makes supersonic beams unsuitable for quantitative reactivity studies for molecules larger than methane. When the aperture of an effusive beam doser is thin enough, the directed flow of gas molecules leaves as a cosine angular flux. This allows for the study of angle-resolved DSCs, while maintaining internal thermalized degrees of freedom, without changing the angle of the crystal with respect to the beam (i.e. distance across the surface maps onto angle). While effusive

molecular beams avoid collisional cooling of modes, it is not possible to change the energy of one internal mode and observe a change in DSC. For example, translational energy cannot be tuned by a carrier gas in an effusive beam doser, as the pressure is so low that the mean free path of gas molecules is wide enough that most collisions occur with the walls of the doser; energy exchange between the reagent gas and a carrier gas is insignificant. An increase in the nozzle temperature increases the energy of all modes and is not selective for individual nodes. In a similar manner to thermal bulb experiments, due to broad internal and translational energy distributions, laser-pumping of internal rovibrational modes is not practical with effusive beams as it is with supersonic beams. While the mode selectivity of effusive molecular beam dosers is poor compared to supersonic dosers, the ability to always know the energy distribution of the incident molecules from effusive molecular beams makes them preferable over supersonic beams for theoretical analysis of gas-surface reactivity for larger molecules.

The use of effusive molecular beams for measuring DSCs [e.g. $S\left(T_g, T_s, \vartheta\right)$] has been limited to this lab. Methane,[8, 23, 41, 86-88] ethane,[8, 23, 41, 89] propane,[8, 23, 41] and ethylene[23, 90] have all been studied on Pt(111) using an effusive molecular beam doser. The alkanes were found to react through an activated process where the DSCs increased with either an increase in surface or gas temperature. The apparent activation energies for initial dissociative chemisorption for these small alkanes decreased significantly with each increase in carbon chain length. Ethylene had a strange temperature dependent DSC relative to the alkanes, but primarily showed unactivated behavior with an initial decrease in DSC with an increase in surface temperature, until 1000K when the DSC began to increase. The angular-resolved DSCs of methane, ethane, and propane were measured,[8] confirming that the DSCs scale with translational energy normal to the surface. Methane and ethane were found to have dynamical biases such that rotations and surface-parallel

translations were spectator degrees of freedom for overcoming the barrier for dissociative chemisorption. Vibrational energy was shown to have a relative efficacy for promoting reaction of η_{vib} = 0.40 with respect to normal translation for both molecules. The angle resolved thermal DSCs at 700 K varied as $S(\vartheta,T) = S_0\cos^n\vartheta$ where n = 12.8, 5.6, and 1.10 for methane, ethane, and propane, respectively. Because the number of vibrational modes double from methane (9 modes) to ethane (18 modes), leading to a significant increase in the fraction of vibrational energy relative to normal translation, the angular dependence on the DSC for ethane was found to decrease drastically compared to methane. For each additional carbon added to the chain, an alkane gains 9 more vibrational modes, further increasing the total energy fraction of vibrational energy. It was also determined that the dynamic bias reducing the relative efficacy of vibrational energy relative to normal translation, could not be discerned for propane, and that propane did not deviate significantly from statistical behavior. The sheer number of vibrational modes in alkanes larger than propane, assuming a statistical vibrational efficacy of η_{vib} = 1 with respect to normal translation, make the total energy fraction due to normal translation negligible when compared to the total vibrational energy. It can then be predicted that angle resolved thermal DSCs for n-butane and larger alkanes would vary little over the range of incident angles. The thermal DSC relevant to industrial catalysis is available as the cosine weighted average of $S(\vartheta,T)$ measurements over the angular flux distribution of an ambient gas hitting a surface under thermal equilibrium,

$$S(T) = \int S(\vartheta,T)\frac{\cos\vartheta}{\pi}d\Omega \qquad \text{Equation 1.4}$$

These kinds of results would be impossible to determine using non-equilibrium and vibrationally ambiguous supersonic beams, especially because an increase in vibrational modes also leads to an increase in the erratic vibrational cooling of the supersonic expansion for molecules larger

than methane. Though, arguably in the limit of very large molecules, with sufficiently dense vibrational modes for vibrational-translational energy transfer to be efficient, vibrational cooling could be complete so $T_b = T_{rot} = T_{vib} = T_{trans}$. No experimental data currently exists to define this size threshold.

1.6.4 Density Functional Theory

The initial dissociative chemisorption of alkanes on Pt(111) surfaces is widely considered to occur at C-H bonds.[34, 37, 44, 91] Because the variation among C-H bond dissociation energies is negligible among alkanes of different chain lengths,[1] it might be predicted that the activation energies for dissociative chemisorption are roughly the same as well. Density functional theory (DFT) is a computational technique which allows for the prediction of bond and reaction energies for multi-atom systems in reasonable computational timeframes. However, the large number of DFT functionals, which offer some degree of choice between accuracy and computational time, result in wide variety of results for the same initial conditions of the reactants. This is definitely the case for methane dissociation on Pt(111) which has been studied extensively using different DFT functionals.[8, 92-96] Kroes calculated the transition state energy for methane dissociation on Pt(111) using eight separate density functionals, PBE, RPBE, and modified variants of the two, including van der Waals corrections, and found values which ranged from 61.6 to 101 kJ/mol with a standard deviation of 15.8 kJ/mol.[92] Because there is significant deviation in results depending on the basis sets or functional chosen as well as the initial and final state parameters, DFT trends for different alkanes cannot be directly compared unless the DFT parameters are consistent. King studied methane[97] and ethane[98] on Pt(110) using the same DFT functionals and predicted identical energy barriers of 0.40 eV for initial C-H bond

dissociative chemisorption. Our lab used the PBE functional for a DFT study of methane, ethane, and propane dissociation on Pt(111) and calculated zero-point energy corrected activation energies of 77.2, 75.3, and 75.3 kJ/mol, respectively.[8] However, experimental data from our effusive molecular beam studies show that activation energies decrease significantly with each increase in carbon chain length,[41] indicating there is some stabilization factor which common DFT functionals do not consider. Among published values, Kroes reported the closest transition state barrier to experimental values for methane dissociative chemisorption on Pt(111) using the optPBD-vdW functional, which predicted a barrier energy of 61.6 kJ/mol[92] and has a percent error of 4.51% relative to the 58.9 kJ/mol experimental value, as determined by effusive molecular beam studies.[8]

1.7 Alkane Desorption Studies

Temperature programmed desorption (TPD) is a technique used to estimate the binding energy between a gas molecule and crystal surface which is the activation energy for desorption calculated from the measured desorption rate as a function of time and temperature. Because molecular desorption can be a competitive pathway with dissociative chemisorption, the desorption parameters obtained from TPD spectra are crucial for building predictive models of dissociative chemisorption.

Van der Waals interactions between a gas molecule and a surface with respect to distance away from the surface along the direction from the surface normal, z, appear stronger than molecule-molecule interactions and have a 9:3 potential instead of the usual gas-phase Lennard-Jones 12:6 potential,[99]

$$V_{LJ}(z) = \varepsilon\left[\left(\frac{\sigma}{z}\right)^{9} - \left(\frac{\sigma}{z}\right)^{3}\right] \qquad \text{Equation 1.5}$$

because of the integration of the Lennard-Jones potential interactions across all the atoms of the surface plane. Equation 1.5 gives an approximate representation of the Lennard-Jones potential on a gas molecule with respect to surface atoms, where ε is the bonding energy holding the gas molecule to the surface, σ is the distance at which the potential becomes zero, and z is the distance of the molecule normal to the surface. As a gas molecule moves further away from the surface, the attractive force due to van der Waals and the repulsive force due to Pauli-exclusion decrease more slowly than would be the case for pair-wise Lennard-Jones interactions between two molecular species in the gas phase.

The thermal desorption of small alkanes have been studied on a wide variety of surfaces, such as the (111) face of gold,[100] silver,[101] copper,[102] palladium,[103-104] platinum,[82, 102, 104-108] and silicone,[109] the (100) face of copper[110-111] and magnesium oxide,[112-114] and the (0001) face of ruthenium,[115] aluminum oxide,[116] and graphite.[117-119] In the majority of these studies, the Redhead method was used,[120] in which the pre-exponential factor of the molecular desorption rate equation was assumed to be fixed at $v = 10^{13}\ s^{-1}$ in order to calculate the desorption energy. Desorption energies calculated using the Redhead method were known to be estimates with an uncertain error, because the exact pre-exponential factors were unknown. Under the assumption that pre-exponential factors were coverage independent, Campbell introduced a simple inversion-optimization analysis method of TPD spectra that seems to yield accurate pre-exponential factors broadly consistent with theoretical expectations.[121] In this study, Campbell reported that both the desorption energies and pre-exponential factors for desorption scaled linearly among alkanes with an increase in carbon chain length.

1.8 Graphene Growth

Graphene is a pure carbon 2D material with extraordinary electronic,[122] chemical,[123] and physical properties,[124-125] and has been important subject of study due to the potential of its applications.[126-127] Research into the epitaxial growth of graphene on transition metal surfaces by chemical vapor deposition (CVD) has led to an ability to manufacture large scale flexible graphene films on copper foil surfaces.[128] CVD has been studied across numerous flat single crystal transition metal surfaces, such as the (111) face of copper,[128-129] platinum,[90, 130-134] iridium,[135-137] rhodium,[138] palladium,[139-140] gold,[129] and nickel,[132, 141-142] as well as the (0001) face of ruthenium,[132, 143-147] rhenium,[148] and cobalt.[149-150] In order to obtain the highest quality graphene by CVD, the nucleation and growth of graphene has been studied under different temperatures and conditions.[90, 135] For the majority of epitaxial studies of graphene on transition metal surfaces, graphene has been grown using small chain hydrocarbons [C_nH_m, $n \leq 3$, $m = n$, $2n$, $2n + 2$], with ethylene being highly favored due to its availability, high dissociative sticking coefficient, and ability to form homogeneous, monolayer graphene at high temperatures.[135, 147]

The utility of large alkanes and hydrocarbons in the CVD of graphene has not been thoroughly investigated. Michely successfully formed graphene on Ir(111) with coronene ($C_{24}H_{12}$) by the temperature programmed growth (TPG) method, where the molecules were adsorbed at room temperature and then rapidly heated to a fixed temperature above 800 K.[135] Michely reported that TPG formed high quality graphene, which had few defects, but the saturation coverage of the physisorbed molecules limits the graphene coverage. Coronene was found to form higher coverages of graphene than ethylene via the TPG technique, which was attributed to the difference in size of the two reagent molecules. Ethylene CVD was studied in the same report and formed graphene of quality equal to TPG across the entire crystal surface at

surface temperatures of at least 1170 K. However, no CVD studies were done with coronene for comparison, which is a major oversight, because there is no information on the quality of graphene grown by large molecule CVD. In the case of saturated hydrocarbon CVD, methane is already known to form graphene on transition metals at temperatures greater than 800 K,[151-153] and the activation energy for alkane dissociative chemisorption decreases with size, making larger alkanes more reactive..[41] This may allow for graphene CVD to be accomplished at lower surface temperatures with alkanes larger than methane. This feature would be attractive for industrial scaling of graphene growth to minimize costs of heating reactors. However, while the kinetics of larger alkanes may be favorable for graphene growth, the current study points out some problems arising from graphene growth by large alkane CVD. This study reports on an octane isomer, 2,2,3,3-tetramethylbutane (TMB), and its quality of graphene growth on Pt(111). Auger electron spectroscopy (AES) was used to measure the carbon composition of the Pt(111) surface at different gas exposures up to a saturated monolayer of coverage. These data were then compared to known coverage versus exposure data for ethylene on Pt(111) at identical substrate temperatures.[90]

References

1. Haynes, W. M.; Lide, D. R.; Bruno, T. J., *Crc Handbook of Chemistry and Physics : A Ready-Reference Book of Chemical and Physical Data*, 2015.
2. Fechete, I.; Wang, Y.; Vedrine, J. C., The Past, Present and Future of Heterogeneous Catalysis. *Catal. Today* **2012**, *189*, 2-27.
3. Shinagawa, T.; Takanabe, K., Towards Versatile and Sustainable Hydrogen Production through Electrocatalytic Water Splitting: Electrolyte Engineering. *ChemSusChem* **2017**, *10*, 1318-1336.
4. Degenstein, N. J.; Subramanian, R.; Schmidt, L. D., Partial Oxidation of N-Hexadecane at Short Contact Times: Catalyst and Washcoat Loading and Catalyst Morphology. *Applied Catalysis a-General* **2006**, *305*, 146-159.
5. Wei, J. M.; Iglesia, E., Structural and Mechanistic Requirements for Methane Activation and Chemical Conversion on Supported Iridium Clusters. *Angew. Chem.* **2004**, *43*, 3685-3688.
6. Donald, S. B.; Harrison, I., Dynamically Biased Rrkm Model of Activated Gas-Surface Reactivity: Vibrational Efficacy and Rotation as a Spectator in the Dissociative Chemisorption of Ch_4 on Pt(111). *Phys. Chem. Chem. Phys.* **2012**, *14*, 1784-1796.
7. Donald, S. B.; Harrison, I., Methane Dissociative Chemisorption Dynamics and Detailed Balance on Pt(111): Tunneling Effects. *J. Chem. Phys.* **2013**, to be submitted.
8. Navin, J. K.; Donald, S. B.; Harrison, I., Angle-Resolved Thermal Dissociative Sticking of Light Alkanes on Pt(111): Transitioning from Dynamical to Statistical Behavior. *J. Phys. Chem. C* **2014**, *118*, 22003-22011.
9. Ertl, G., Reactions at Surfaces: From Atoms to Complexity (Nobel Lecture). *Angewandte Chemie International Edition* **2008**, *47*, 3524-3535.
10. Ertl, G., Primary Steps in Catalytic Synthesis of Ammonia. *Journal of Vacuum Science and Technology A* **1983**, *1*, 1247-1253.
11. Ertl, G.; Weiss, M.; Lee, S. B., Reprint Of: The Role of Potassium in the Catalytic Synthesis of Ammonia. *Chemical Physics Letters* **2013**, *589*, 18-20.
12. Hansen, J. B. a. H. N., Methanol Synthesis. In *Handbook of Heterogeneous Catalysis*, G. Ertl, H. K., F. Schüth and J. Weitkamp, Ed. 2008.
13. Rahimpour, M. R.; Jafari, M.; Iranshahi, D., Progress in Catalytic Naphtha Reforming Process: A Review. *Applied Energy* **2013**, *109*, 79-93.
14. Speight, J. G., *Chemistry and Technology of Petroleum (3rd Edition)*; CRC Press: New York, NY, USA, 1999.
15. Rase, H. F., *Handbook of Commercial Catalysts : Heterogeneous Catalysts*; CRC Press: Boca Raton :, 2000, p 488 p. :.
16. Ozkan, U., *Design of Heterogeneous Catalysts New Approaches Based on Synthesis, Characterization and Modeling*; Wiley-VCH, 2009; Vol. Weinheim :.
17. Lloyd, L., *Handbook of Industrial Catalysts*; Springer: New York, 2007; Vol. New York.
18. ZumMallen, M. P.; Schmidt, L. D., Oxidation of Methanol over Polycrystalline Rh and Pt: Rates, Oh Desorption, and Model. *Journal of Catalysis* **1996**, *161*, 230-246.
19. Karp, E. M.; Silbaugh, T. L.; Crowe, M. C.; Campbell, C. T., Energetics of Adsorbed Methanol and Methoxy on Pt(111) by Microcalorimetry. *Journal of the American Chemical Society* **2012**, *134*, 20388-20395.
20. Diekhoner, L.; Butler, D. A.; Baurichter, A.; Luntz, A. C., Parallel Pathways in Methanol Decomposition on Pt(111). *Surface Science* **1998**, *409*, 384-391.
21. Kidney, A. J.; Parrish, W. R., Fundamentals of Natural Gas Processing. In *Fundamentals of Natural Gas Processing*, CRC Press: 2006.
22. Speight, J. G., *The Chemistry and Technology of Petroleum*, 4th ed. ed.; CRC Press/Taylor & Francis: Boca Raton :, 2007.
23. Cushing, G. W.; Navin, J. K.; Valadez, L.; Johánek, V.; Harrison, I., An Effusive Molecular Beam Technique for Studies of Polyatomic Gas-Surface Reactivity and Energy Transfer. *Rev. Sci. Instr.* **2011**, *82*, 044102.
24. Van Willigen, W., Angular Distribution of Hydrogen Molecules Desorbed from Metal Surfaces. *Phys. Lett. A* **1968**, *28*, 80-81.
25. Stewart, G. R., Measurement of Low-Temperature Specific Heat. *Rev. Sci. Instrum.* **1983**, *54*, 1-11.
26. Labinger, J. A.; Bercaw, J. E., Understanding and Exploiting C-H Bond Activation. *Nature* **2002**, *417*, 507-514.
27. Bligaard, T.; Norskov, J. K.; Dahl, S.; Matthiesen, J.; Christensen, C. H.; Sehested, J., The Bronsted-Evans-Polanyi Relation and the Volcano Curve in Heterogeneous Catalysis. *Journal of Catalysis* **2004**, *224*, 206-217.

28. Wei, J. M.; Iglesia, E., Mechanism and Site Requirements for Activation and Chemical Conversion of Methane on Supported Pt Clusters and Turnover Rate Comparisons among Noble Metals. *J. Phys. Chem. B* **2004**, *108*, 4094-4103.
29. Wei, J. M.; Iglesia, E., Isotopic and Kinetic Assessment of the Mechanism of Reactions of Ch_4 with Co_2 or H_2o to Form Synthesis Gas and Carbon on Nickel Catalysts. *J. Catal.* **2004**, *224*, 370-383.
30. Nielsen, B. O.; Luntz, A. C.; Holmblad, P. M.; Chorkendorff, I., Activated Dissociative Chemisorption of Methane on Ni(100) - a Direct Mechanism under Thermal Conditions. *Catal. Lett.* **1995**, *32*, 15-30.
31. Abbott, H. L.; Harrison, I., Methane Dissociative Chemisorption on Ru(0001) and Comparison to Metal Nanocatalysts. *Journal of Catalysis* **2008**, *254*, 27-38.
32. Wu, M.-C.; Goodman, D. W., High-Resolution Electron Energy-Loss Measurements of Sticking Coefficients of Methane Decomposition on Ru(0001). *Surf. Sci.* **1994**, *306*, L529.
33. Jachimowski, T. A.; Hagedorn, C. J.; Weinberg, W. H., Direct and Trapping-Mediated Dissociative Chemisorption of Methane on Ir(111). *Surf. Sci.* **1997**, *393*, 126-134.
34. Johnson, D. F.; Weinberg, W. H., Quantification of the Influence of Surface-Structure on C-H Bond Activation by Iridium and Platinum. *Science* **1993**, *261*, 76-78.
35. Weinberg, W. H.; Sun, Y. K., Quantification of Primary Versus Secondary C-H Bond-Cleavage in Alkane Activation - Propane on Pt. *Science* **1991**, *253*, 542-545.
36. Luntz, A. C.; Winters, H. F., Dissociation of Methane and Ethane on Pt(110) - Evidence for a Direct Mechanism under Thermal Conditions. *J. Chem. Phys.* **1994**, *101*, 10980-10989.
37. Luntz, A. C.; Bethune, D. S., Activation of Methane Dissociation on a Pt(111) Surface. *J. Chem. Phys.* **1989**, *90*, 1274-1280.
38. Juurlink, L. B. F.; Smith, R. R.; Killelea, D. R.; Utz, A. L., Comparative Study of C-H Stretch and Bend Vibrations in Methane Activation on Ni(100) and Ni(111). *Phys. Rev. Lett.* **2005**, *94*, 208303.
39. Maroni, P.; Papageorgopoulos, D. C.; Sacchi, M.; Dang, T. T.; Beck, R. D.; Rizzo, T. R., State-Resolved Gas-Surface Reactivity of Methane in the Symmetric C-H Stretch Vibration on Ni(100). *Phys. Rev. Lett.* **2005**, *94*, 246104.
40. Seets, D. C.; Wheeler, M. C.; Mullins, C. B., Trapping-Mediated and Direct Dissociative Chemisorption of Methane on Ir(110): A Comparison of Molecular Beam and Bulb Experiments. *J. Chem. Phys.* **1997**, *107*, 3986-3998.
41. Cushing, G. W.; Navin, J. K.; Donald, S. B.; Valadez, L.; Johanek, V.; Harrison, I., C-H Bond Activation of Light Alkanes on Pt(111): Dissociative Sticking Coefficients, Evans-Polanyi Relation, and Gas-Surface Energy Transfer. *J. Phys. Chem. C* **2010**, *114*, 17222-17232.
42. Johnson, D. F.; Weinberg, W. H., Quantitative-Determination of the Activity of Defect Sites on a Single-Crystalline Surface - C-H Bond Activation of C-13 Labeled Ethane on Ir(111). *J. Chem. Phys.* **1994**, *101*, 6289-6300.
43. Hagedorn, C. J.; Weiss, M. J.; Kim, T. W.; Weinberg, W. H., Trapping-Mediated Dissociative Chemisorption of Cycloalkanes on Ru(001) and Ir(111): Influence of Ring Strain and Molecular Geometry on the Activation of C-C and C-H Bonds. *Journal of the American Chemical Society* **2001**, *123*, 929-940.
44. Johnson, D. F.; Weinberg, W. H., Quantification of the Selective Activation of C-C Bonds in Short-Chain Alkanes - Reactivity of Ethane, Propane, Isobutane, N-Butane and Neopentane on Ir(11). *Journal of the Chemical Society-Faraday Transactions* **1995**, *91*, 3695-3702.
45. Kelly, D.; Weinberg, W. H., Trapping-Mediated Dissociative Chemisorption of C3h8 and C3d8 on Ir(110). *J. Chem. Phys.* **1996**, *105*, 271-278.
46. Kelly, D.; Weinberg, W. H., Direct Dissociative Chemisorption of Methane, Ethane, Propane, and Cyclopropane on Ir(110). *J. Vac. Sci. Technol. A* **1997**, *15*, 1663-1666.
47. Jachimowski, T. A.; Weinberg, W. H., Trapping-Mediated Dissociative Chemisorption of Cyclopropane on Ru(001) Via C-C Bond Cleavage. *Surface Science* **1997**, *370*, 71-76.
48. Jachimowski, T. A.; Weinberg, W. H., Trapping-Mediated Dissociative Chemisorption of Ethane and Propane on Ru(001). *Surf. Sci.* **1997**, *372*, 145-154.
49. Ceyer, S. T., New Mechanisms for Chemistry at Surfaces. *Science* **1990**, *249*, 133-139.
50. Beebe, T. P.; Goodman, D. W.; Kay, B. D.; Yates, J. T., Kinetics of the Activated Dissociative Adsorption of Methane on the Low Index Planes of Nickel Single-Crystal Surfaces. *J. Chem. Phys.* **1987**, *87*, 2305-2315.
51. Luntz, A. C.; Winters, H. F., Dissociation of Methane and Ethane on Pt(110): Evidence for a Direct Mechanism under Thermal Conditions. *Journal of Chemical Physics* **1994**, *101*, 10980-10989.
52. Sault, A. G.; Goodman, D. W., Dissociative Adsorption of Alkanes on Ni(100): Comparison with Molecular Beam Results. *Journal of Chemical Physics* **1988**, *88*, 7232-7239.

53. Winters, H. F., The Activated, Dissociative Chemisorption of Methane on Tungsten. *J. Chem. Phys.* **1975**, *62*, 2454-2460.
54. Winters, H. F., The Kinetic Isotope Effect in the Dissociative Chemisorption of Methane. *J. Chem. Phys.* **1976**, *64*, 3495-3500.
55. Brass, S. G.; Reed, D. A.; Ehrlich, G., Vibrational-Excitation and Surface Reactivity - Examination of the N_3 and $2\nu_3$ Modes of Ch_4
J. Chem. Phys. **1979**, *70*, 5244-5250.
56. Yates, J. T.; Zinck, J. J.; Sheard, S.; Weinberg, W. H., Search for Vibrational Activation in the Chemisorption of Methane. *J. Chem. Phys.* **1979**, *70*, 2266-2272.
57. Sault, A. G.; Goodman, D. W., Dissociative Adsorption of Alkanes on Ni(100) - Comparison with Molecular-Beam Results. *J. Chem. Phys.* **1988**, *88*, 7232-7239.
58. Brass, S. G.; Ehrlich, G., Internal Molecular Motions and Activated Chemisorption: Ch_4 on Rhodium. *Journal of Chemical Physics* **1987**, *87*, 4285-4293.
59. Larsen, J. H.; Chorkendorff, I., From Fundamental Studies of Reactivity on Single Crystals to the Design of Catalysts. *Surf. Sci. Rep.* **1999**, *35*, 165-222.
60. Seets, D. C.; Reeves, C. T.; Ferguson, B. A.; Wheeler, M. C.; Mullins, C. B., Dissociative Chemisorption of Methane on Ir(111): Evidence for Direct and Trapping-Mediated Mechanisms. *J. Chem. Phys.* **1997**, *107*, 10229-10241.
61. Rettner, C. T.; Pfnur, H. E.; Auerbach, D. J., On the Role of Vibrational-Energy in the Activated Dissociative Chemisorption of Methane on Tungsten and Rhodium. *J. Chem. Phys.* **1986**, *84*, 4163-4167.
62. Scoles (Ed.), G., *Atomic and Molecular Beam Methods*; Oxford Univ. Press: New York, 1988; Vol. 1.
63. King, D. A.; Wells, M. G., Reaction Mechanism in Chemisorption Kinetics: Nitrogen on the {100} Plane of Tungsten. *Proc. R. Soc. London Ser. A-Math. Phys. Eng. Sci.* **1974**, *339*, 245-269.
64. Schoofs, G. R.; Arumainayagam, C. R.; Mcmaster, M. C.; Madix, R. J., Dissociative Chemisorption of Methane on Pt(111). *Surf. Sci.* **1989**, *215*, 1-28.
65. Newell, H. E.; Oakes, D. J.; Rutten, F. J. M.; McCoustra, M. R. S.; Chesters, M. A., Impact-Induced Dissociation of Methane and Ethane on Pt(111) and Pt0.25rh0.75(111). *Faraday Discuss.* **1996**, *105*, 193-207.
66. Valden, M.; Pere, J.; Hirsimaki, M.; Suhonen, S.; Pessa, M., Activated Adsorption of Methane on Clean and Oxygen-Modified Pt{111} and Pd{110}. *Surf. Sci.* **1997**, *377*, 605-609.
67. Higgins, J.; Conjusteau, A.; Scoles, G.; Bernasek, S. L., State Selective Vibrational ($2\nu_3$) Activation of the Chemisorption of Methane on Pt (111). *J. Chem. Phys.* **2001**, *114*, 5277-5283.
68. Weaver, J. F.; Krzyzowski, M. A.; Madix, R. J., Direct Dissociative Chemisorption of Alkanes on Pt(111): Influence of Molecular Complexity. *J. Chem. Phys.* **2000**, *112*, 396-407.
69. Bisson, R.; Sacchi, M.; Dang, T. T.; Yoder, B.; Maroni, P.; Beck, R. D., State-Resolved Reactivity of $Ch_4(2\nu_3)$ on Pt(111) and Ni(111): Effects of Barrier Height and Transition State Location. *J. Phys. Chem. A* **2007**, *111*, 12679-12683.
70. Juurlink, L. B. F.; Killelea, D. R.; Utz, A. L., State-Resolved Probes of Methane Dissociation Dynamics. *Prog. Surf. Sci.* **2009**, *84*, 69-134.
71. Utz, A. L., Mode Selective Chemistry at Surfaces. *Current Opinion in Solid State and Materials Science* **2009**, *13*, 4-12.
72. Lee, M. B.; Yang, Q. Y.; Tang, S. L.; Ceyer, S. T., Activated Dissociative Chemisorption of Ch4 on Ni(111) - Observation of a Methyl Radical and Implication for the Pressure Gap in Catalysis. *J. Chem. Phys.* **1986**, *85*, 1693-1694.
73. Lee, M. B.; Yang, Q. Y.; Ceyer, S. T., Dynamics of the Activated Dissociative Chemisorption of Ch4 and Implication for the Pressure Gap in Catalysis - a Molecular-Beam High-Resolution Electron-Energy Loss Study. *J. Chem. Phys.* **1987**, *87*, 2724-2741.
74. Beck, R. D.; Maroni, P.; Papageorgopoulos, D. C.; Dang, T. T.; Schmid, M. P.; Rizzo, T. R., Vibrational Mode-Specific Reaction of Methane on a Nickel Surface. *Science* **2003**, *302*, 98-100.
75. Juurlink, L. B. F.; McCabe, P. R.; Smith, R. R.; DiCologero, C. L.; Utz, A. L., Eigenstate-Resolved Studies of Gas-Surface Reactivity: Ch_4 ($1\nu_3$) Dissociation on Ni(100). *Phys. Rev. Lett.* **1999**, *83*, 868-871.
76. Killelea, D. R.; Campbell, V. L.; Shuman, N. S.; Utz, A. L., Bond-Selective Control of a Heterogeneously Catalyzed Reaction. *Science* **2008**, *319*, 790-793.
77. Killelea, D. R.; Campbell, V. L.; Shuman, N. S.; Smith, R. R.; Utz, A. L., Surface Temperature Dependence of Methane Activation on Ni(111). *J. Phys. Chem. C* **2009**, *113*, 20618-20622.
78. Schmid, M. P.; Maroni, P.; Beck, R. D.; Rizzo, T. R., Surface Reactivity of Highly Vibrationally Excited Molecules Prepared by Pulsed Laser Excitation: Ch_4 ($2\nu_3$) on Ni(100). *J. Chem. Phys.* **2002**, *117*, 8603-8606.

79. Smith, R. R.; Killelea, D. R.; DelSesto, D. F.; Utz, A. L., Preference for Vibrational over Translational Energy in a Gas-Surface Reaction. *Science* **2004**, *304*, 992-995.
80. Kelly, D.; Weinberg, W. H., Trapping-Mediated Dissociative Chemisorption of Propane on Ir(110). *J. Vac. Sci. Technol. A* **1996**, *14*, 1588-1592.
81. Hamza, A. V.; Steinruck, H. P.; Madix, R. J., The Dynamics of the Dissociative Adsorption of Alkanes on Ir(110). *Journal of Chemical Physics* **1987**, *86*, 6506-6514.
82. Weaver, J. F.; Carlsson, A. F.; Madix, R. J., The Adsorption and Reaction of Low Molecular Weight Alkanes on Metallic Single Crystal Surfaces. *Surf. Sci. Rep.* **2003**, *50*, 107-199.
83. Rettner, C. T.; Pfnur, H. E.; Auerbach, D. J., Dissociative Chemisorption of Ch4 on W(110) - Dramatic Activation by Initial Kinetic-Energy. *Phys. Rev. Lett.* **1985**, *54*, 2716-2719.
84. Holmblad, P. M.; Wambach, J.; Chorkendorff, I., Molecular-Beam Study of Dissociative Sticking of Methane on Ni(100). *J. Chem. Phys.* **1995**, *102*, 8255-8263.
85. Stewart, G. M.; McDonald, J. D., Intramolecular Vibrational Relaxation from C–H Stretch Fundamentals. *Journal of Chemical Physics* **1983**, *78*, 3907-3915.
86. DeWitt, K. M.; Valadez, L.; Abbott, H. L.; Kolasinski, K. W.; Harrison, I., Using Effusive Molecular Beams and Microcanonical Unimolecular Rate Theory to Characterize Ch_4 Dissociation on Pt(111). *Journal Of Physical Chemistry B* **2006**, *110*, 6705-6713.
87. Navin, J. K.; Donald, S. B.; Tinney, D. G.; Cushing, G. W.; Harrison, I., Communication: Angle-Resolved Thermal Dissociative Sticking of Ch_4 on Pt(111): Further Indication That Rotation Is a Spectator to the Gas-Surface Reaction Dynamics. *J. Chem. Phys.* **2012**, *136*, 061101.
88. Donald, S. B.; Navin, J. K.; Harrison, I., Methane Dissociative Chemisorption and Detailed Balance on Pt(111): Dynamical Constraints and the Modest Influence of Tunneling. *J. Chem. Phys.* **2013**, *139*, 15.
89. DeWitt, K. M.; Valadez, L.; Abbott, H. L.; Kolasinski, K. W.; Harrison, I., Effusive Molecular Beam Study of C_2h_6 Dissociation on Pt(111). *J. Phys. Chem. B* **2006**, *110*, 6714-6720.
90. Cushing, G. W.; Johanek, V.; Navin, J. K.; Harrison, I., Graphene Growth on Pt(111) by Ethylene Chemical Vapor Deposition at Surface Temperatures near 1000 K. *J. Phys. Chem. C* **2015**, *119*, 4759-4768.
91. Johnson, D. F.; Weinberg, W. H., Quantification of the Selective Activation of C-H Bonds in Short-Chain Alkanes - the Reactivity of Ethane, Propane, Isobutane, N-Butane, and Neopentane on Ir(111). *J. Chem. Phys.* **1995**, *103*, 5833-5847.
92. Nattino, F.; Migliorini, D.; Bonfanti, M.; Kroes, G. J., Methane Dissociation on Pt(111): Searching for a Specific Reaction Parameter Density Functional. *J. Chem. Phys.* **2016**, *144*, 16.
93. Migliorini, D., et al., Surface Reaction Barriometry: Methane Dissociation on Flat and Stepped Transition-Metal Surfaces. *J. Phys. Chem. Lett.* **2017**, *8*, 4177-4182.
94. Vines, F.; Lykhach, Y.; Staudt, T.; Lorenz, M. P. A.; Papp, C.; Steinruck, H. P.; Libuda, J.; Neyman, K. M.; Gorling, A., Methane Activation by Platinum: Critical Role of Edge and Corner Sites of Metal Nanoparticles. *Chemistry-a European Journal* **2010**, *16*, 6530-6539.
95. Qi, Q. H.; Wang, X. J.; Chen, L.; Li, B. T., Methane Dissociation on Pt(111), Ir(111) and Ptir(111) Surface: A Density Functional Theory Study. *Appl. Surf. Sci.* **2013**, *284*, 784-791.
96. Wang, X. L.; Yuan, Q. H.; Li, J.; Ding, F., The Transition Metal Surface Dependent Methane Decomposition in Graphene Chemical Vapor Deposition Growth. *Nanoscale* **2017**, *9*, 11584-11589.
97. Anghel, A. T.; Wales, D. J.; Jenkins, S. J.; King, D. A., Pathways for Dissociative Methane Chemisorption on Pt{110}-(1x2). *Phys. Rev. B* **2005**, *71*, 113410.
98. Anghel, A. T.; Wales, D. J.; Jenkins, S. J.; King, D. A., Pathways for Dissociative Ethane Chemisorption on Pt{110} (1x2) Using Density Functional Theory. *Chem. Phys. Lett.* **2005**, *413*, 289-293.
99. Steele, W. A., Physical Interaction of Gases with Crystalline Solids .1. Gas-Solid Energies and Properties of Isolated Adsorbed Atoms. *Surf. Sci.* **1973**, *36*, 317-352.
100. Wetterer, S. M.; Lavrich, D. J.; Cummings, T.; Bernasek, S. L.; Scoles, G., Energetics and Kinetics of the Physisorption of Hydrocarbons on Au(111). *J. Phys. Chem. B* **1998**, *102*, 9266-9275.
101. Pawelacrew, J.; Madix, R. J., Lateral Interactions in the Desorption-Kinetics of Weakly Adsorbed Species - Unexpected Differences in the Desorption of C-4 Alkenes and Alkanes from Ag(110) Due to Oriented Pi-Bonding of the Alkenes. *Surf. Sci.* **1995**, *339*, 8-22.
102. Lei, R. Z.; Gellman, A. J.; Koel, B. E., Desorption Energies of Linear and Cyclic Alkanes on Surfaces: Anomalous Scaling with Length. *Surf. Sci.* **2004**, *554*, 125-140.
103. Kao, C. L.; Madix, R. J., The Adsorption Dynamics of Molecular Methane, Propane, and Neopentane on Pd(111): Theory and Experiment. *J. Phys. Chem. B* **2002**, *106*, 8248-8257.

104. Kao, C. L.; Madix, R. J., The Adsorption Dynamics of Small Alkanes on (111) Surfaces of Platinum Group Metals. *Surf. Sci.* **2004**, *557*, 215-230.
105. Bishop, A. R.; Girolami, G. S.; Nuzzo, R. G., Structural Models and Thermal Desorption Energetics for Multilayer Assemblies of the N-Alkanes on Pt(111). *J. Phys. Chem. B* **2000**, *104*, 754-763.
106. Salmeron, M.; Somorjai, G. A., Adsorption and Bonding of Butane and Pentane on the Pt(111) Crystal-Surfaces - Effects of Oxygen Treatments and Deuterium Pre-Adsorption. *J. Phys. Chem.* **1981**, *85*, 3835-3840.
107. Weaver, J. F.; Ikai, M.; Carlsson, A.; Madix, R. J., Molecular Adsorption and Growth of N-Butane Adlayers on Pt(111). *Surf. Sci.* **2001**, *470*, 226-242.
108. Kao, C. L.; Weaver, J. F.; Madix, R. J., The Prediction of Trapping Probabilities for Ethane by Molecular Dynamics Simulations: Scaling from Pt(111) to Pd(111). *Surf. Sci.* **2002**, *505*, 115-123.
109. Simons, J. K.; Frigo, S. P.; Taylor, J. W.; Rosenberg, R. A., Adsorption of Saturated Hydrocarbons on the Si(111)-7x7 Surface Studied by Photoelectron and Photon Stimulated Desorption Spectroscopies. *Surf. Sci.* **1996**, *346*, 21-30.
110. Sexton, B. A.; Hughes, A. E., A Comparison of Weak Molecular Adsorption of Organic-Molecules on Clean Copper and Platinum Surfaces. *Surf. Sci.* **1984**, *140*, 227-248.
111. Teplyakov, A. V.; Gurevich, A. B.; Yang, M. X.; Bent, B. E.; Chen, J. G. G., Nexafs and Tpd Studies of Molecular Adsorption of Hydrocarbons on Cu(100): Segmental Correlations with the Heats of Adsorption. *Surf. Sci.* **1998**, *396*, 340-348.
112. Tait, S. L.; Dohnalek, Z.; Campbell, C. T.; Kay, B. D., N-Alkanes on Mgo(100). I. Coverage-Dependent Desorption Kinetics of N-Butane. *J. Chem. Phys.* **2005**, *122*, 164707.
113. Tait, S. L.; Dohnalek, Z.; Campbell, C. T.; Kay, B. D., N-Alkanes on Mgo(100). Ii. Chain Length Dependence of Kinetic Desorption Parameters for Small N-Alkanes. *J. Chem. Phys.* **2005**, *122*, 164708.
114. Tait, S. L.; Dohnalek, Z.; Campbell, C. T.; Kay, B. D., Methane Adsorption and Dissociation and Oxygen Adsorption and Reaction with Co on Pd Nanoparticles on Mgo(100) and on Pd(111). *Surf. Sci.* **2005**, *591*, 90-107.
115. Brand, J. L.; Arena, M. V.; Deckert, A. A.; George, S. M., Surface-Diffusion of Normal-Alkanes on Ru(001). *J. Chem. Phys.* **1990**, *92*, 5136-5143.
116. Slayton, R. M.; Aubuchon, C. M.; Camis, T. L.; Noble, A. R.; Tro, N. J., Desorption-Kinetics and Adlayer Sticking Model of N-Butane, N-Hexane, and N-Octane on Al2o3(0001). *J. Phys. Chem.* **1995**, *99*, 2151-2154.
117. Paserba, K. R.; Gellman, A. J., Effects of Conformational Isomerism on the Desorption Kinetics of N-Alkanes from Graphite. *J. Chem. Phys.* **2001**, *115*, 6737-6751.
118. Paserba, K. R.; Gellman, A. J., Kinetics and Energetics of Oligomer Desorption from Surfaces. *Phys. Rev. Lett.* **2001**, *86*, 4338-4341.
119. Gellman, A. J.; Paserba, K. R., Kinetics and Mechanism of Oligomer Desorption from Surfaces: N-Alkanes on Graphite. *J. Phys. Chem. B* **2002**, *106*, 13231-13241.
120. Dejong, A. M.; Niemantsverdriet, J. W., Thermal-Desorption Analysis - Comparative Test of 10 Commonly Applied Procedures. *Surf. Sci.* **1990**, *233*, 355-365.
121. Tait, S. L.; Dohnalek, Z.; Campbell, C. T.; Kay, B. D., N-Alkanes on Pt(111) and on C(0001)/Pt(111): Chain Length Dependence of Kinetic Desorption Parameters. *Journal of Chemical Physics* **2006**, *125*, 234308.
122. Castro Neto, A. H.; Guinea, F.; Peres, N. M. R.; Novoselov, K. S.; Geim, A. K., The Electronic Properties of Graphene. *Reviews of Modern Physics* **2009**, *81*, 109-162.
123. Allen, M. J.; Tung, V. C.; Kaner, R. B., Honeycomb Carbon: A Review of Graphene. *Chem. Rev.* **2010**, *110*, 132-145.
124. Xin, G. Q.; Yao, T. K.; Sun, H. T.; Scott, S. M.; Shao, D. L.; Wang, G. K.; Lian, J., Highly Thermally Conductive and Mechanically Strong Graphene Fibers. *Science* **2015**, *349*, 1083-1087.
125. Tsoukleri, G.; Parthenios, J.; Papagelis, K.; Jalil, R.; Ferrari, A. C.; Geim, A. K.; Novoselov, K. S.; Galiotis, C., Subjecting a Graphene Monolayer to Tension and Compression. *Small* **2009**, *5*, 2397-2402.
126. Geim, A. K.; Novoselov, K. S., The Rise of Graphene. *Nature Materials* **2007**, *6*, 183-191.
127. Geim, A. K., Graphene: Status and Prospects. *Science* **2009**, *324*, 1530-1534.
128. Li, X. S., et al., Large-Area Synthesis of High-Quality and Uniform Graphene Films on Copper Foils. *Science* **2009**, *324*, 1312-1314.
129. Martinez-Galera, A. J.; Brihuega, I.; Gomez-Rodriguez, J. M., Ethylene Irradiation: A New Route to Grow Graphene on Low Reactivity Metals. *Nano Lett.* **2011**, *11*, 3576-3580.
130. Fujita, T.; Kobayashi, W.; Oshima, C., Novel Structures of Carbon Layers on a Pt(111) Surface. *Surf. Interface Anal.* **2005**, *37*, 120-123.
131. Gao, M.; Pan, Y.; Huang, L.; Hu, H.; Zhang, L. Z.; Guo, H. M.; Du, S. X.; Gao, H. J., Epitaxial Growth and Structural Property of Graphene on Pt(111). *Appl. Phys. Lett.* **2011**, *98*, 033101.

132. Gao, M.; Pan, Y.; Zhang, C. D.; Hu, H.; Yang, R.; Lu, H. L.; Cai, J. M.; Du, S. X.; Liu, F.; Gao, H. J., Tunable Interfacial Properties of Epitaxial Graphene on Metal Substrates. *Appl. Phys. Lett.* **2010**, *96*, 053109.
133. Land, T. A.; Michely, T.; Behm, R. J.; Hemminger, J. C.; Comsa, G., Stm Investigation of Single Layer Graphite Structures Produced on Pt(111) by Hydrocarbon Decomposition. *Surf. Sci.* **1992**, *264*, 261-270.
134. Otero, G., et al., Ordered Vacancy Network Induced by the Growth of Epitaxial Graphene on Pt(111). *Phys. Rev. Lett.* **2010**, *105*.
135. Coraux, J.; N'Diaye, A. T.; Engler, M.; Busse, C.; Wall, D.; Buckanie, N.; Heringdorf, F.; van Gastei, R.; Poelsema, B.; Michely, T., Growth of Graphene on Ir(111). *New Journal of Physics* **2009**, *11*, 023006.
136. Pletikosic, I.; Kralj, M.; Pervan, P.; Brako, R.; Coraux, J.; N'Diaye, A. T.; Busse, C.; Michely, T., Dirac Cones and Minigaps for Graphene on Ir(111). *Phys. Rev. Lett.* **2009**, *102*, 056808.
137. N'Diaye, A. T.; Coraux, J.; Plasa, T. N.; Busse, C.; Michely, T., Structure of Epitaxial Graphene on Ir(111). *New Journal of Physics* **2008**, *10*.
138. Sicot, M.; Bouvron, S.; Zander, O.; Rudiger, U.; Dedkov, Y. S.; Fonin, M., Nucleation and Growth of Nickel Nanoclusters on Graphene Moireacute on Rh(111). *Appl. Phys. Lett.* **2010**, *96*, 3.
139. Murata, Y.; Starodub, E.; Kappes, B. B.; Ciobanu, C. V.; Bartelt, N. C.; McCarty, K. F.; Kodambaka, S., Orientation-Dependent Work Function of Graphene on Pd(111). *Appl. Phys. Lett.* **2010**, *97*, 3.
140. Mok, H. S.; Ebnonnasir, A.; Murata, Y.; Nie, S.; McCarty, K. F.; Ciobanu, C. V.; Kodambaka, S., Kinetics of Monolayer Graphene Growth by Segregation on Pd(111). *Appl. Phys. Lett.* **2014**, *104*, 4.
141. Rokuta, E.; Hasegawa, Y.; Itoh, A.; Yamashita, K.; Tanaka, T.; Otani, S.; Oshima, C., Vibrational Spectra of the Monolayer Films of Hexagonal Boron Nitride and Graphite on Faceted Ni(755). *Surf. Sci.* **1999**, *428*, 97-101.
142. Bengaard, H. S.; Norskov, J. K.; Sehested, J.; Clausen, B. S.; Nielsen, L. P.; Molenbroek, A. M.; Rostrup-Nielsen, J. R., Steam Reforming and Graphite Formation on Ni Catalysts. *J. Catal.* **2002**, *209*, 365-384.
143. Loginova, E.; Bartelt, N. C.; Feibelman, P. J.; McCarty, K. F., Evidence for Graphene Growth by C Cluster Attachment. *New Journal of Physics* **2008**, *10*, 093026.
144. Sutter, E.; Albrecht, P.; Camino, F. E.; Sutter, P., Monolayer Graphene as Ultimate Chemical Passivation Layer for Arbitrarily Shaped Metal Surfaces. *Carbon* **2010**, *48*, 4414-4420.
145. Marchini, S.; Gunther, S.; Wintterlin, J., Scanning Tunneling Microscopy of Graphene on Ru(0001). *Phys. Rev. B* **2007**, *76*, 075429.
146. Wang, B.; Bocquet, M. L.; Marchini, S.; Gunther, S.; Wintterlin, J., Chemical Origin of a Graphene Moire Overlayer on Ru(0001). *Phys. Chem. Chem. Phys.* **2008**, *10*, 3530-3534.
147. Sutter, P. W.; Flege, J. I.; Sutter, E. A., Epitaxial Graphene on Ruthenium. *Nature Materials* **2008**, *7*, 406-411.
148. Miniussi, E., et al., Thermal Stability of Corrugated Epitaxial Graphene Grown on Re(0001). *Phys. Rev. Lett.* **2011**, *106*, 4.
149. Eom, D.; Prezzi, D.; Rim, K. T.; Zhou, H.; Lefenfeld, M.; Xiao, S.; Nuckolls, C.; Hybertsen, M. S.; Heinz, T. F.; Flynn, G. W., Structure and Electronic Properties of Graphene Nanoislands on Co(0001). *Nano Lett.* **2009**, *9*, 2844-2848.
150. Kazi, H.; Cao, Y.; Tanabe, I.; Driver, M. S.; Dowben, P. A.; Kelber, J. A., Multi-Layer Graphene on Co(0001) by Ethanol Chemical Vapor Deposition. *Materials Research Express* **2014**, *1*, 9.
151. De Arco, L. G.; Zhang, Y.; Kumar, A.; Zhou, C. W., Synthesis, Transfer, and Devices of Single- and Few-Layer Graphene by Chemical Vapor Deposition. *Ieee Transactions on Nanotechnology* **2009**, *8*, 135-138.
152. Kim, J.; Seo, J.; Jung, H. K.; Kim, S. H.; Lee, H. W., The Effect of Various Parameters for Few-Layered Graphene Synthesis Using Methane and Acetylene. *Journal of Ceramic Processing Research* **2012**, *13*, S42-S46.
153. Kim, H.; Kim, E.; Lee, W. J.; Jung, J., Effects of Hydrogen in the Cooling Step of Chemical Vapor Deposition of Graphene. *Electronic Materials Letters* **2013**, *9*, 417-420.

Section 2 – Experimental Setup

Section **Page**

2.1 Instrumental Setup

All experiments were performed using an ultra-high vacuum (UHV) surface analysis chamber which consists of four main sections. The crystal used in each experiment is attached to a mount located in the main chamber. Gas dosing and surface composition measurements are the primary function of this section. A manipulator attached to the main chamber allows for 4-axis movement of the crystal in the x, y, z, and r directions. Reagent gases are stored and prepared using a gas manifold separated by a series of valves from the main chamber. A twice differentially pumped quadrupole mass spectrometer chamber allows for quantitative, line-of-sight mass spectrometry experiments.

2.1.1 Main Chamber

The main UHV chamber maintains a base pressure of 1×10^{-10} Torr, reaching base pressures as low as 7×10^{-11} Torr depending on the reagent gas and the strength of adsorption to the chamber walls, which are electro-polished 316 stainless steel. UHV pressures within the chamber are measured using a 370 Stabil-Ion Bayard-Alpert gauge from Granville-Phillips. The measurable pressure range of this gauge is between 1×10^{-4} and 2×10^{-11} Torr, with an accuracy of ± 4%[1] with respect to nitrogen gas. For pressures higher than the range of the ion gauge, two MKS model 615 Baratron capacitance manometers, of 1×10^{-4} to 1 Torr and 1×10^{-1} to 1000 Torr ranges and ± 0.25%[2] accuracy with respect to N_2, are used with a model 670 signal conditioner.

The main chamber achieves UHV through a series of pumps. A TMH-261 Pfeiffer turbo-molecular pump (TMP), with a TC600 computer and DCU200 controller, has a nominal pumping speed of 210 L/s. An Edwards B2M5 mechanical pump is linked in series as a roughing

pump on the exhaust side of the TMP. A power switch links the TMP and mechanical pump such that one cannot switch on without the other, reducing the risk of oil vapor backflow into the chamber upon venting or initializing the pumps. A double-ended Physical Electronics ion pump with a 210 L/s pumping speed can be activated at pressures less than 1×10^{-6} Torr. Titanium sublimation pump filaments are housed on the far end of the ion-pump. UHV valves from VAT allow for separating the TMP and/or the ion pump from the main chamber, which is beneficial for certain experiments, especially in instances where radical or ionized species can interfere with results. An infrared heat lamp is installed on the chamber and is used when baking out the chamber and outgassing filament. Schematics for the chamber are shown by Figures 2.1 and 2.2 and were drawn by Navin.[3]

Analytical measurements are done using a variety of instruments attached to the main chamber. The primary method of probing the crystal surface is Auger electron spectroscopy, which is performed using a Physical Electronics model 15-255 GAR double-pass cylindrical mirror analyzer with internal electron gun. An alternate surface probe is the Physical Electronics 40-548 x-ray source and 50-096 x-ray source power supply and controller for x-ray photoelectron spectroscopy (XPS). The residual gas composition of the UHV chamber is measured using a Stanford Research Systems RGA 200, which is capable of measuring m/z values between a range of 1 and 200 amu. The RGA 200 is capable of measuring a single mass with respect to time with high enough signal to noise for helium leak detection. For more quantitative mass spectrometry for temperature programmed desorption (TPD) or reaction (TPR) experiments, a quadrupole mass spectrometer (QMS) from Extrel Mass Spectrometers with a m/z range of 1 to 500 amu is located within the differentially pumped region, which will be explained in more detail later.

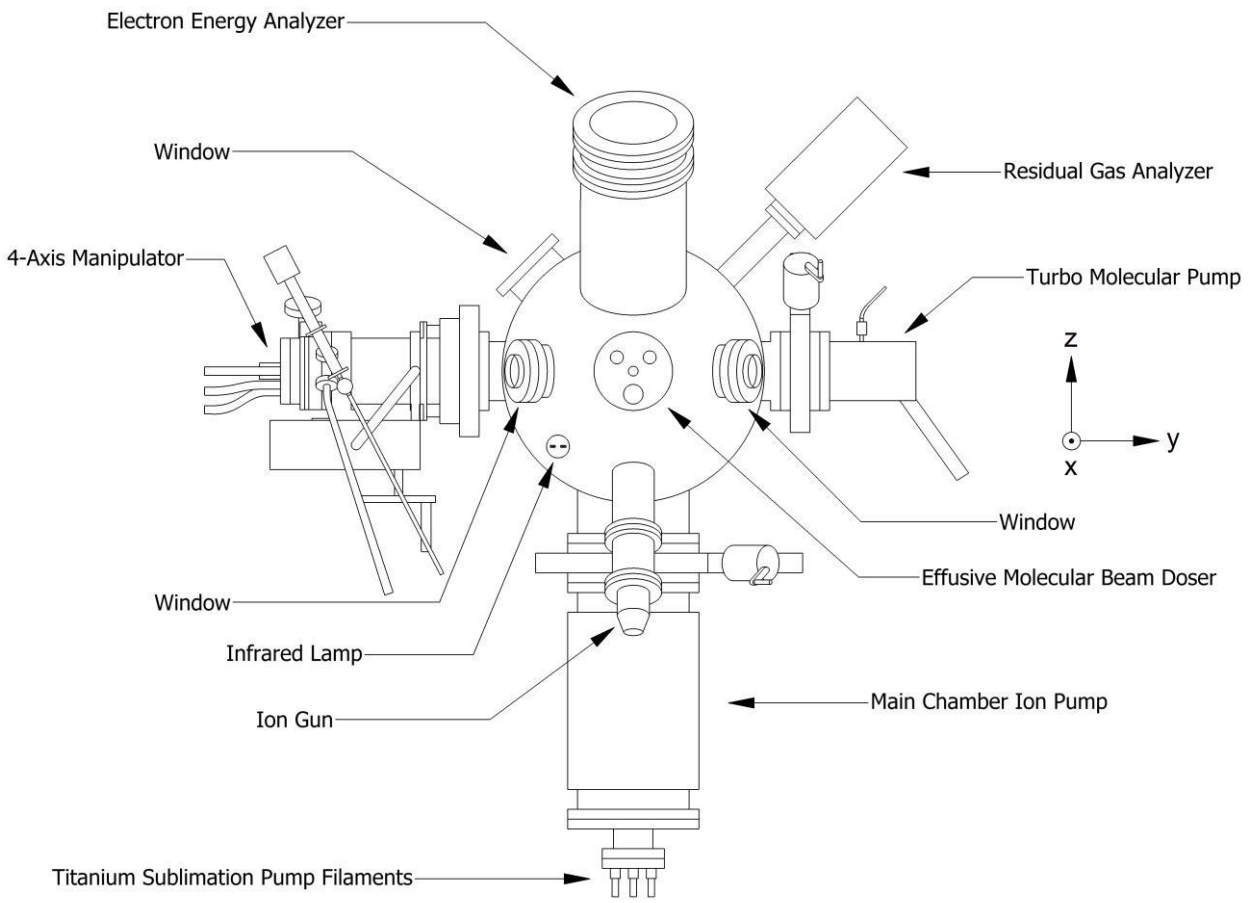

Figure 2.1: A schematic of the main UHV chamber as observed from the front

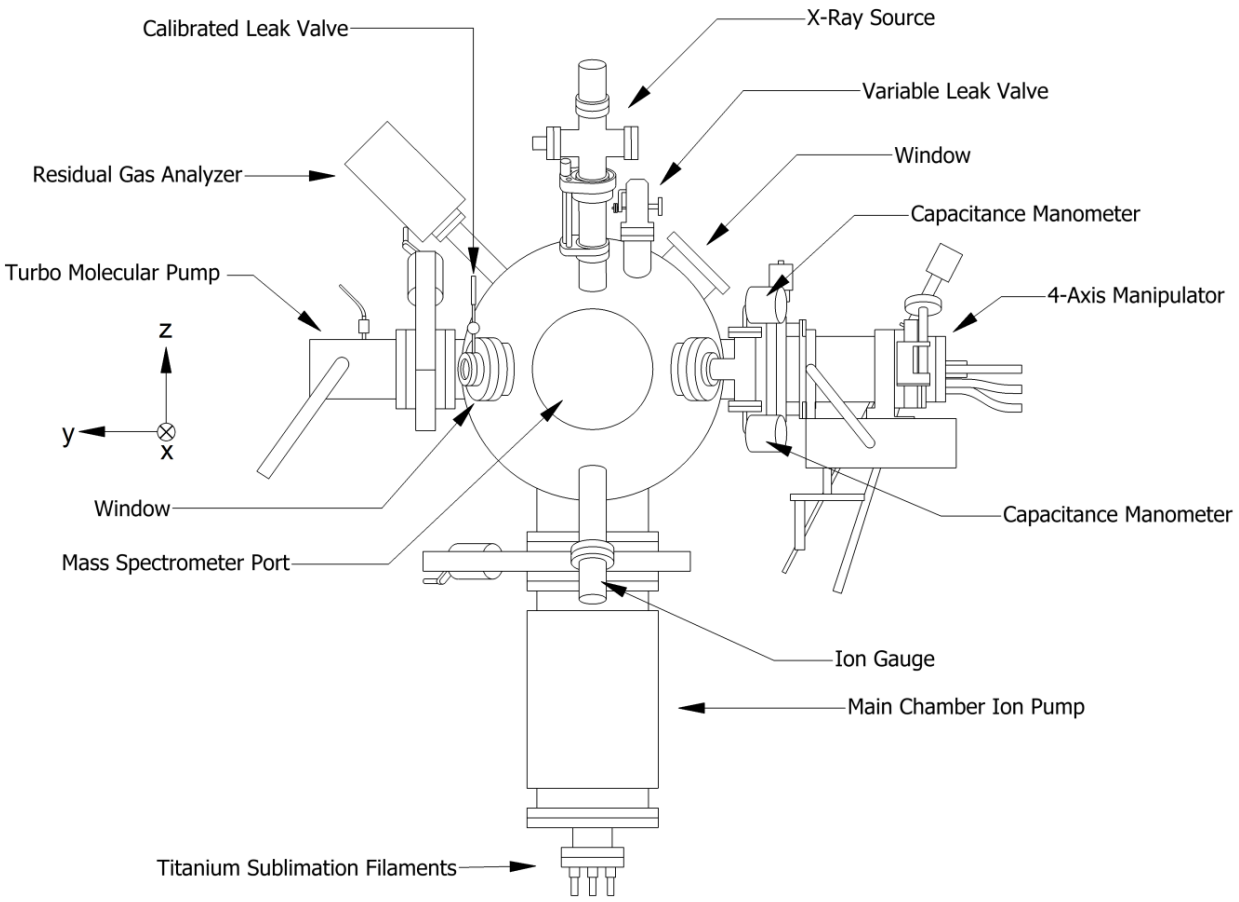

Figure 2.2: A schematic of the main UHV chamber as observed from the back

Gas reagents are able to enter into the main UHV chamber using three separate dosers. For experiments where accurate gas flow rates are not necessary, a variable leak from Duniway Stockrooms allows for precise reagent gas pressure control within the main chamber without changing the manifold pressure. When the precise gas fluence from the manifold into the chamber is essential, ambient dosing is done using an Accu-Flow nitrogen-calibrated leak from Vacuum Technology Incorporated and directed gas dosing is done using a heated effusive molecular beam doser with a cosine angular distribution of molecules. Argon sputtering for surface cleaning is performed using a Physical electronics 04-161 ion gun with a RBD Instruments 32-165 ion gun power supply.

The orientation of the chamber, according to the schematics in Figures 2.1 and 2.1, is with the x-y plane parallel to the floor and the z-axis pointed towards the ceiling. The TMP, crystal manipulator, effusive molecular beam doser, QMS are all located on the same central x-y plane, separated by 90 degrees. Three windows and the capacitance manometers lie at a 45 degree angle between these instruments and pumps on the same plane. The TMP, crystal manipulator, ion pump with TSP, RGA 200, and a window all lie on the same z-y plane. The ion pump with TSP, QMS, effusive molecular beam doser, ion gun, electron gun and analyzer, x-ray source, and ion gauge are located on the same x-z plane. The variable leak valve is located between the crystal manipulator and QMS near the x-ray source at the top of the chamber. The calibrated leak valve is also at the top of the chamber and between the TMP and QMS. The infrared bakeout lamp is located between the crystal manipulator and the ion pump on the lower half of the chamber.

2.1.2 Mass Spectroscopy Chamber

The twice differentially pumped line-of-sight QMS is separated from the main UHV chamber by two stainless steel cones with 1/8" diameter apertures which have a maximum conductance of 1 L/s each. The first differentially pumped region, which is between the two cones, is pumped by a Physical Electronics ion pump with a nominal pumping speed of 20 L/s. The section of the chamber in which the QMS resides is pumped by a double sided Gamma Vacuum model 200L ion pump with a nominal speed of 200 L/s. TSP filaments are housed on the far side of this ion pump. The exact pressure of this region is not directly measured, but is estimated to be approximately 4000 times lower than main UHV chamber. This is verified by comparing residual gas spectra from the RGA 200 in the main chamber and the QMS of the mass spectrometer chamber.

The differentially pumped region between the cone apertures has electrically floating plates with respect to the chamber walls which are connected to the mass spectrometer ionizer controller through feedthroughs on the side of the chamber. In experiments where ions form prior to reaching the QMS ionizer, these floating plates can be biased to guide these ions to the mass filter. The mounting flange for the QMS has a 1.33" window which sights through the central axis of the spectrometer. Figure 2.3 shows a schematic arranged by Navin[3] for the mass spectrometer chamber.

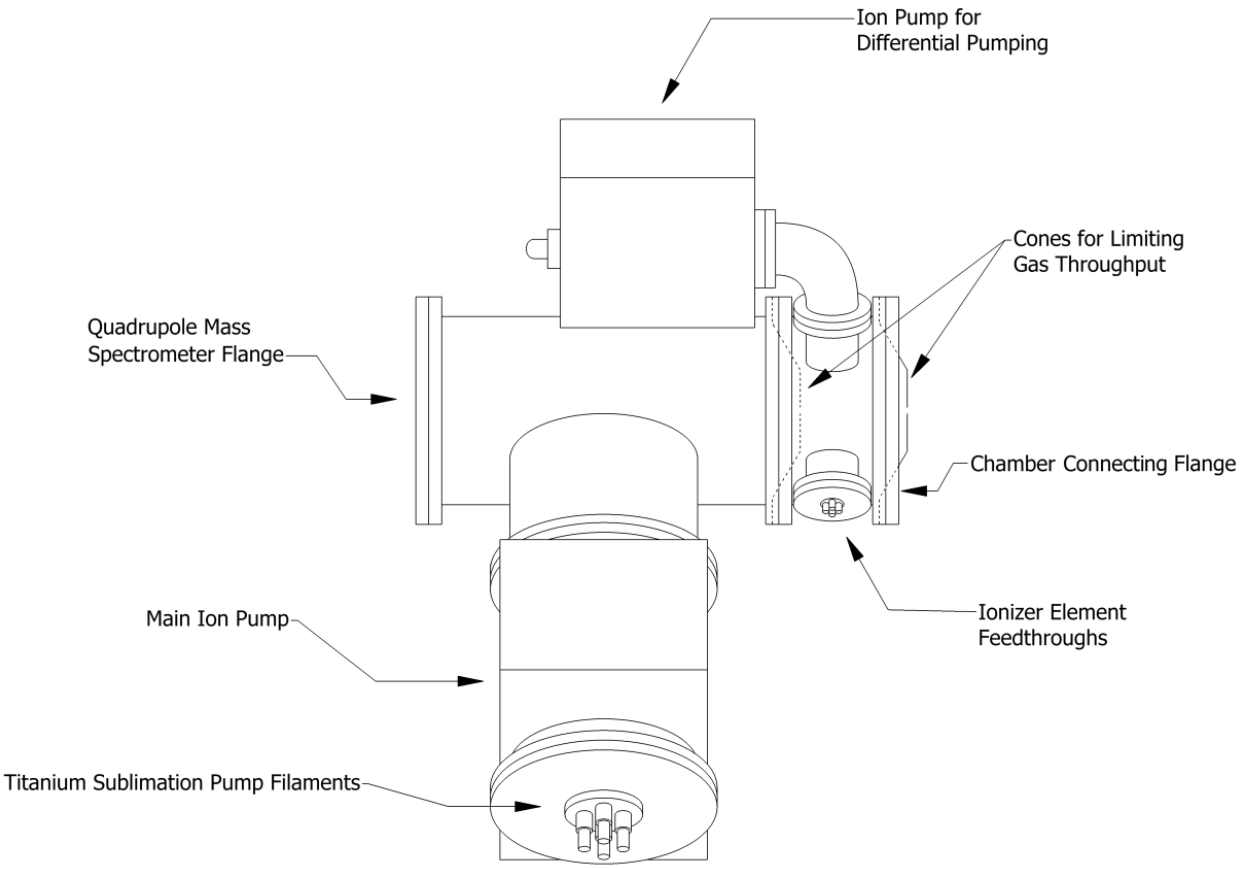

Figure 2.3: A schematic of the twice differentially pumped mass spectrometer chamber

2.1.3 Gas Manifold

Reagent gases are stored and prepared for experiments in the gas manifold separated from the main UHV chamber by the variable leak, calibrated leak, and effusive molecular beam dosers. The manifold is attached to an aluminum mounting plate for support. Several stainless steel gas cylinders are each separated from the central tubing of the manifold by two VCR valves in series. By separating the storage vessels with two valves, the reagent gas pressure in the manifold can be more easily controlled when compared to a single valve. Two Granville-Phillips 275 Convectron, Pirani vacuum gauges are equipped above and below the gas manifold and can measure pressures between 1×10^{-4} and 1000 Torr. However, because the pressure reading from Pirani vacuum gauges are calibrated to N_2 and change based on the gas being measured, a MKS Instruments 122B capacitance manometer, with a range of 1×10^{-4} to 1 Torr, is used to measure absolute pressures for experiments.

The gas manifold is pumped separately from the main chamber using a Pfeiffer TSU 065D pumping station. Although the base pressure of the manifold is below the measureable range of the capacitance manometer and Pirani vacuum gauges, by opening the manifold to the main UHV chamber and measuring the pressure change, it is possible to indirectly measure the manifold pressure. Using this method, the base pressure of the gas manifold was determined to be less than 1×10^{-7} Torr, as there was a negligible change ($< 1 \times 10^{-12}$) in the main chamber pressure upon opening the manifold to the main chamber. Two valves separate the gas manifold from the manifold pumping station, with one of the Pirani vacuum gauges located between the two. Figure 2.4 shows the front and back schematic of the gas manifold and Figure 2.5 shows the connections leading to the calibrated leak and effusive beam dosers.[3]

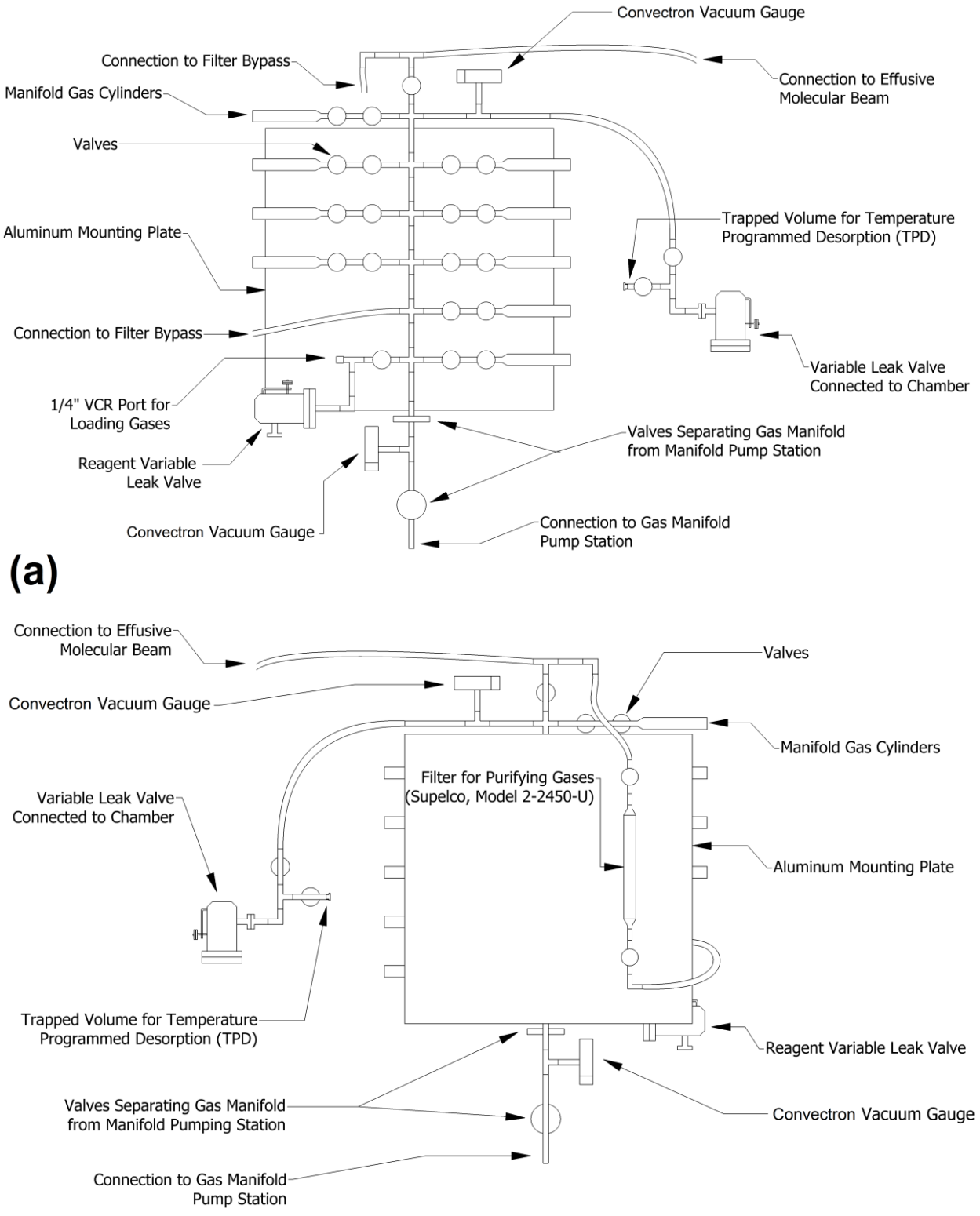

Figure 2.4: schematics of the front (a) and back (b) of the gas manifold

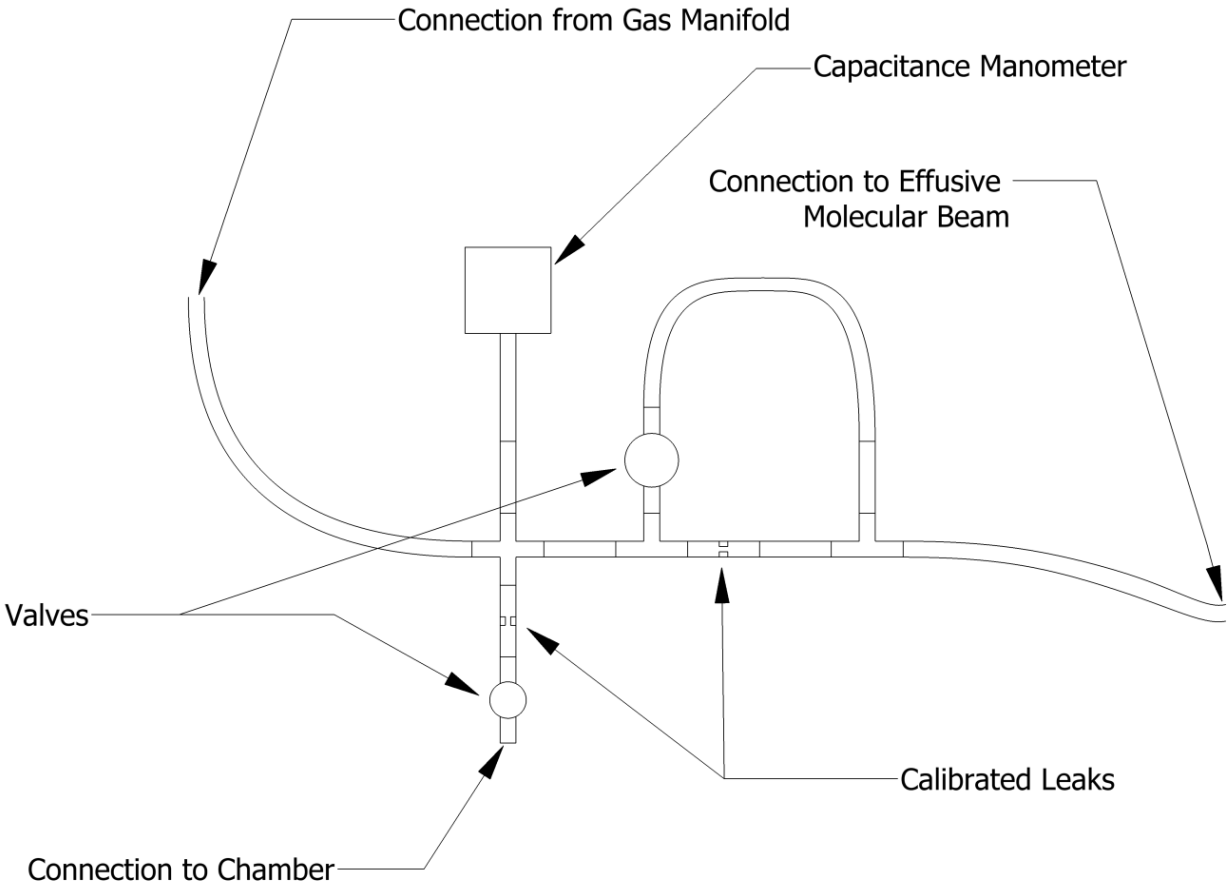

Figure 2.5: a schematic of the connections between the gas manifold and the calibrated leak and heated effusive molecular beam dosers

A variable leak valve allows reagent gases from external storage devices, such as lecture bottles and glass bulbs, as well as vapors from liquid or solid storage vessels, to flow at a controlled rate into the gas manifold. A 1/4" VCR blank functions as a secondary port for loading gases and is favored over the main variable leak loading port when refilling gas storage cylinders on the manifold, as these cylinders are typically filled to pressures between 100 and 1000 Torr.

The variable leak doser connected to the main UHV chamber is separated from the gas manifold by a single valve. Between the doser and this valve is a small trapped volume which can be isolated by its own valve. This trapped volume is used for temperature programmed desorption experiments.

A gas-filtering bypass leading to the calibrated leak and effusive beam dosers is equipped with a 2-2450-U Supelco gas filter, which allows for the purification of non-polar or low-reactivity gases like methane, nitrogen, and noble gases. A highly reactive mixture of powdered oxides of copper, nickel, manganese, cobalt, and aluminum in the filter is capable of removing a wide variety of molecules, such as H_2O, O_2, CO_2, CO, NH_3, alcohols, large alkanes, alkenes, amines, aromatics, ethers, halogens, and sulfur species.[4-5] A calibrated leak is positioned in the line leading to the effusive beam doser to facilitate the dosing of molecules with relatively high dissociative sticking coefficients (DSC) which normally require extremely short dosing periods. A bypass with a single valve can be opened when dosing molecules with relatively low DSCs, where dosing periods are extremely long.

2.1.4 Crystal Manipulator

The single crystal used for experiments in the main UHV chamber is attached to a mount which is directly connected to a 4-axis manipulator. The crystal can be moved in the x, y, and z direction and can be rotated around the z-axis via a DPRF 450 rotary flange obtained from McAllister Technological Services.

In order to manage the temperature of the crystal, cooling is supplied by an Oxford Instruments Ultrastat cryostat which runs through the center of the outermost flange to a cold finger within the chamber. The cryostat functions with a flow of liquid nitrogen or helium. Five electrical feedthroughs are attached to the manipulator around the cryostat. Two feedthroughs connect thick copper wires to the crystal mount and are used for resistive heating. Two feedthroughs connect Type K alumel/chromel thermocouples attached to the mount and backside of the crystal and allow for measurement of the crystal temperature. The final feedthrough connects a thermocouple which measures the temperature of the cryostat cold finger.

The rotary flange is twice differentially pumped to allow for angular manipulation of the crystal while maintaining UHV conditions within the main chamber. The main chamber is separated from atmosphere by three separate Viton o-rings, because typical UHV copper gaskets are immobile. The two inner regions between the gaskets are differentially pumped. The innermost region is pumped by a Physical Electronics ion pump with a nominal pumping speed of 2 L/s. The outer region is pumped by the Edwards B2M5 mechanical pump attached to the exhaust side of the main chamber TMP.

A set of gears allow for the rotational manipulation around the z-axis with half a degree of precision. The rotary flange supported on an aluminum block with a second set of gears for linear motion along the z-axis with a precision of 1 mm. Bellows allow for the flange to move

closer or further away from the main chamber as part of the movement along the z-axis. These bellows connect on one side to a flange attached to the main UHV chamber and on the other side to another set of bellows, near the rotary flange, and an x-y manipulator stage, which allow flexibility as the crystal mount is moved along each of the x, y, and z axes. Hand dials allow for crystal manipulation along the x and y dimensions with precision down to one-thousandth of an inch. Figures 2.6 and 2.7 show the schematics of the manipulator and crystal mount.[3]

2.1.5 Crystal Mount

The bulk of the crystal mount consists of oxygen-free, high conductivity copper (OFHC). The platinum crystal attached to the mount has a 10 mm diameter x 1.5 mm thickness with a surface oriented to within 0.1^{o} of the (111) face. The crystal was obtained from Surface Preparation Laboratory, Zaandam, The Netherlands with a 99.999% base purity. The crystal mount is attached to the manipulator and cryostat cold finger by a large diameter copper rod at the base. Four rectangular copper support structures at each corner of the mount, separated from the copper bulk by insulating sapphire pieces, are secured in place with stainless steel screws and insulating Macor washers from McAllister Technical Services. Two 75% W and 25% Re rods are positioned in grooves on a pair of these copper supports and run parallel to the copper rod leading to the manipulator. The Pt crystal is spot welded to these rods for support and resistive heating. Two copper rods connect the support structures and tungsten rods to the manipulator and allow a voltage for resistive heating between the tungsten and crystal. Thermocouple leads are attached to a stainless steel structure at the base of the mount which connect to feedthroughs on the manipulator. Alumina sleeves insulate the thermocouple leads from the steel structure. The thermocouple wires extend up and are spot-welded together onto backside of the crystal.

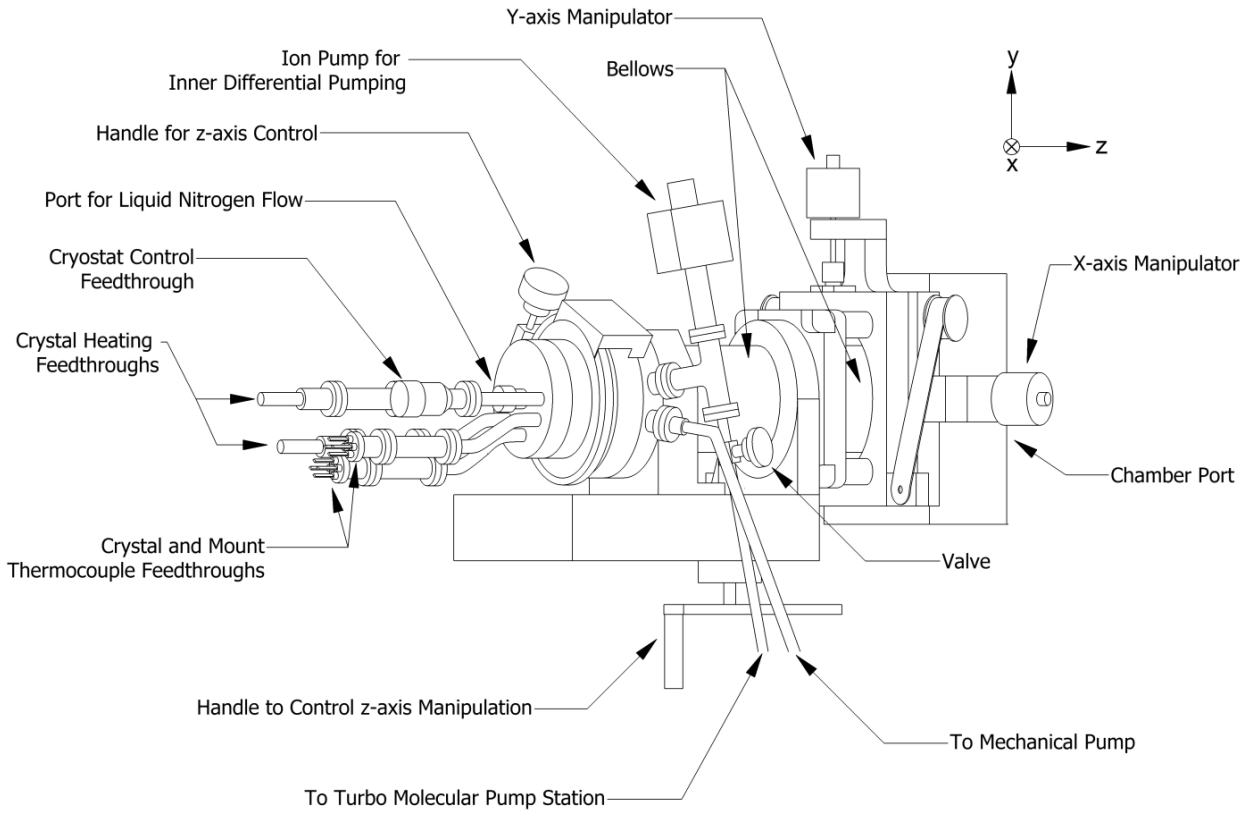

Figure 2.6: a schematic for the crystal mount manipulator

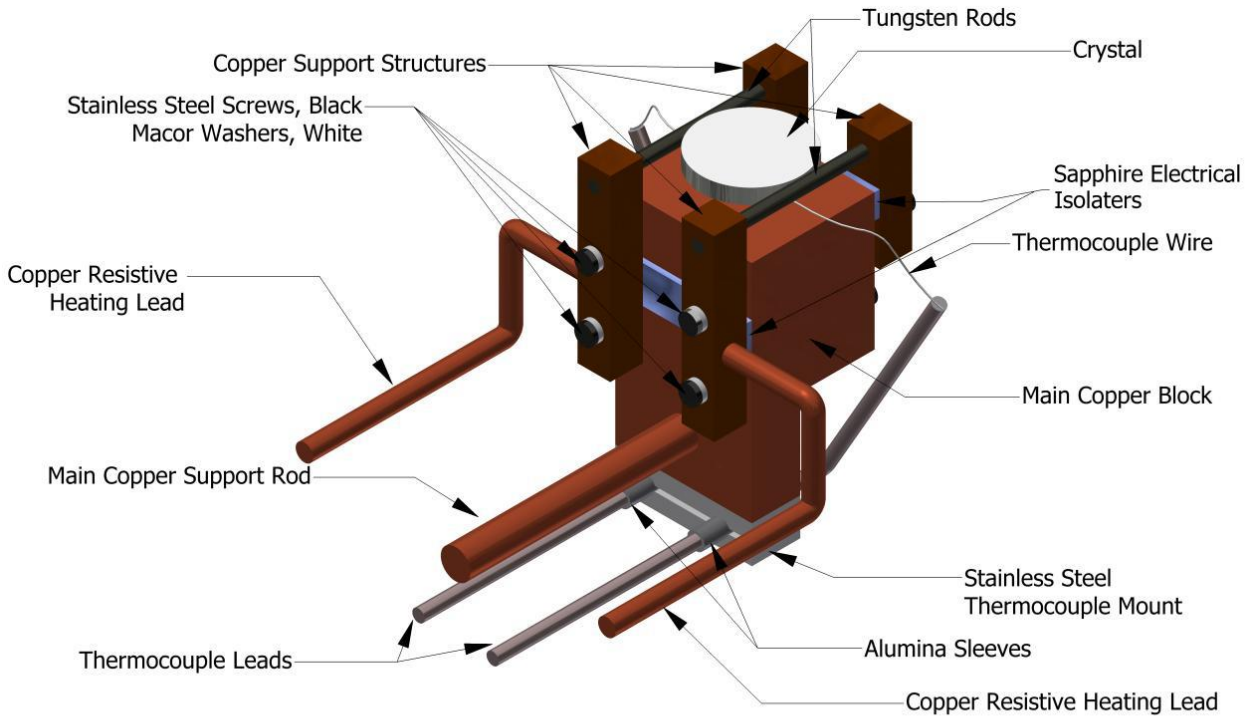

(a)

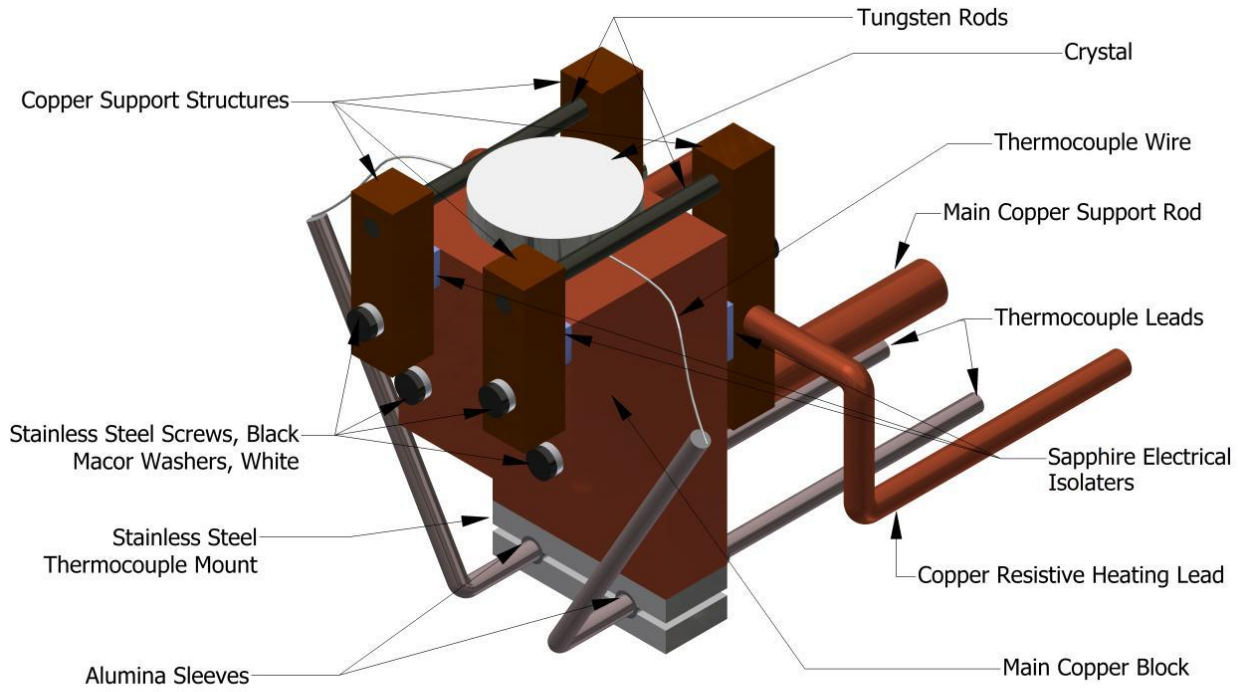

(b)

Figure 2.7: schematics of the crystal mount from (a) the perspective of the crystal mount and (b) the front of the crystal mount

2.1.6 Crystal Temperature Control

Resistive crystal heating is controlled by a programmable 906S Eurotherm temperature controller which is connected to a XFR 12-100 DC power supply from Xantrex. PID parameters for five separate temperature ranges allow the Eurotherm computer to smoothly control the rate of heating to a target set temperature set-point. In the case of TPD experiments where a linear temperature ramp rate is required for good spectra, Eurotherm programs provide more accuracy than manual voltage control. The Eurotherm is programmable to hold the crystal at stable temperatures or can perform temperature ramp rates with ± 0.1 K precision.

Boundary	Temperature (K)
1	115
2	132
3	620
4	920

Table 2.1: The boundary temperatures which separate the five PID temperature regions

Region	PB	TI	TD	HO1	LO1
1	24.0	11.0	0.0	15	0
2	10.0	7.5	1.3	5	0
3	8.6	6.9	0.8	34	0
4	14.3	3.7	0.0	40	10
5	14.3	3.7	0.0	45	16

Table 2.2: PID parameters set for the five temperature regions, where the voltage allotment is based on percent difference (PB), the time integral (TI) of the difference, and the time derivative (TD) of the difference from the set-point. HO1 and LO1 are the maximum and minimum allowed currents respectively

The crystal is cooled by an Oxford Ultrastat system which includes a cryostat within the crystal mount manipulator, a cryogen transfer arm, which connects a liquid nitrogen or helium

tank to the cryostat, and an Oxford ITC 503 temperature controller. When liquid nitrogen is used with this set-up the crystal temperature can be varied from 98 to 1200 K.

2.1.7 Effusive Molecular Beam Doser

The heated effusive molecular beam doser is attached to a 4.5” 304 stainless steel flange. A 0.250” ID diameter 304 stainless steel tube runs down the center of the flange face and is terminated at both ends by 1/4" male VCR glands. Above this central tube are two OFHC electrical feedthroughs for resistive filament heating. A 1.33” mini-conflat flange houses the feedthroughs for the themocouples which measure the nozzle temperature of the doser. The doser connects directly to the internal male VCR gland, while the external male VCR permits connection to the gas manifold.

The doser consists of a stainless steel nozzle, an inner ceramic sleeve, and an outer ceramic sleeve. The nozzle is made from 304 stainless steel, has an inner diameter of 0.250” with an 8” length, and is terminated by a 0.003” thick stainless steel disk with a 0.5 mm laser drilled hole through the center. The rear of the tube connects to a 1/4" inch female VCR nut. The ceramic sleeves are Aremcolox 502-1400 FF machined alumina tubes from Aremco. The inner ceramic tube, which directly touches the nozzle tube, is threaded and has an inner diameter of 0.26” and outer diameter of 0.50” with a 6” length. The threaded grooves, which extend 5” down the tube, are wrapped in 0.25 mm 99.95% purity tungsten wire from Goodfellow for resistive heating. The outer ceramic tube has an internal diameter of 0.555” and an outer diameter of 0.610” and a 6” length. The tungsten wires for resistive heating are spot-welded to the OFHC feedthroughs on the vacuum flange. Type K alumel/chromel thermocouples are spot welded along the base towards the front of the nozzle for temperature measurement. A TE10A power

thyristor and a 2416 temperature controller from Eurotherm allow for control of the doser temperature. Figures 2.8 and 2.9 shows the schematics for the doser flange and nozzle.[3]

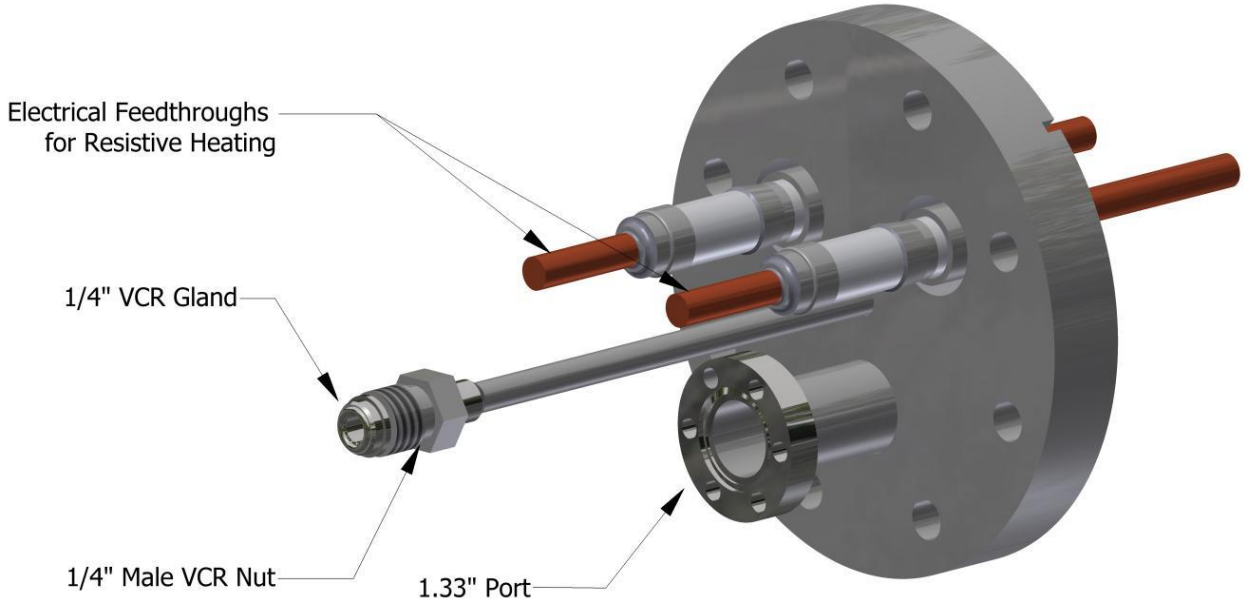

(a)

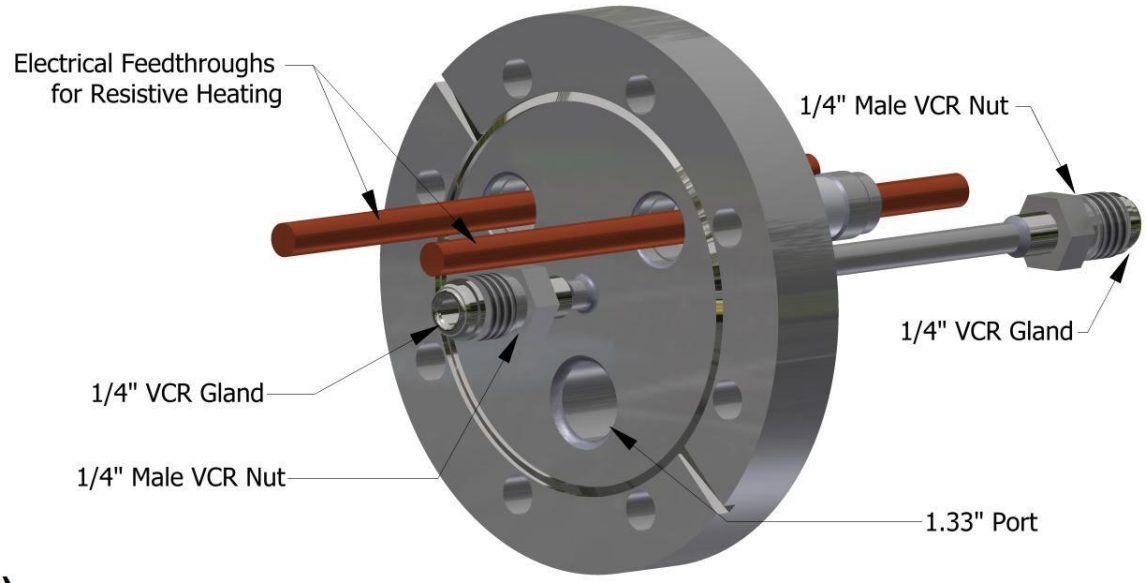

(b)

Figure 2.8: schematics of the (a) external and (b) internal design of the flange which supports the heated effusive molecular beam doser

Figure 2.9: a schematic of the three-layer design of the heated effusive molecular beam doser along with a close up view of the nozzle

2.1.8 Reagent Gases

The alkanes used in the experiments discussed herein were Grade 4.0 n-butane (≥ 99.99%), research grade purity isobutane (≥ 99.995%), and Grade 2.0 n-pentanes (≥ 99%) from Matheson Tri Gas, analytical standard n-hexane (≥ 99.7%), HPLC Grade n-octane (≥ 99%), 2,2,3,3-tetramethylbutane (≥ 94%), and HPLC Grade nonane (≥ 99%) from Sigma-Aldrich, and 2,2-dimethylpropane (≥ 99.3%) from Organic Technologies. n-Butane and isobutane were used without further purification. Cycles of free-pump-thaw were done with n-pentane, n-hexane, n-octane, n-nonane, 2,2-dimethylpropane (neopentane), and 2,2,3,3-tetramethylbutane (TMB) for increased purity. Gas sensitivity factors (relative to N2) for the Bayard-Alpert gauge were found to be 4.9, 4.3, 6.0, 5.7, 6.6, 7.75, 9.0, and 8.0 for n-butane, isobutane, n-pentane, neopentane, n-hexane, n-octane, 2,2,3,3-tetramethylbutane, and n-nonane, respectively, according to the reported trends of a case study by NASA.[6-7] Studies with methanol were performed using HPLC grade (≥ 99.9%) methanol from Sigma Aldrich. The gas sensitivity factor relative to N2 for methanol is 1.8.

2.2 Instrumental Theory

2.2.1 Auger Electron Spectroscopy

The primary purpose of Auger electron spectroscopy (AES) is for measuring the elemental composition of a surface. This is accomplished by the interaction of an electron beam with the core electrons of a sample. When a high energy electron, typically greater than 1500 eV, and 3000 eV in the case of these experiments, collides with an atom, a core electron ejects from the atom leaving a vacancy. In order to maintain stability of the atom, an electron at a higher energy level within the atom relaxes to the core vacancy. The energy of this relaxing electron

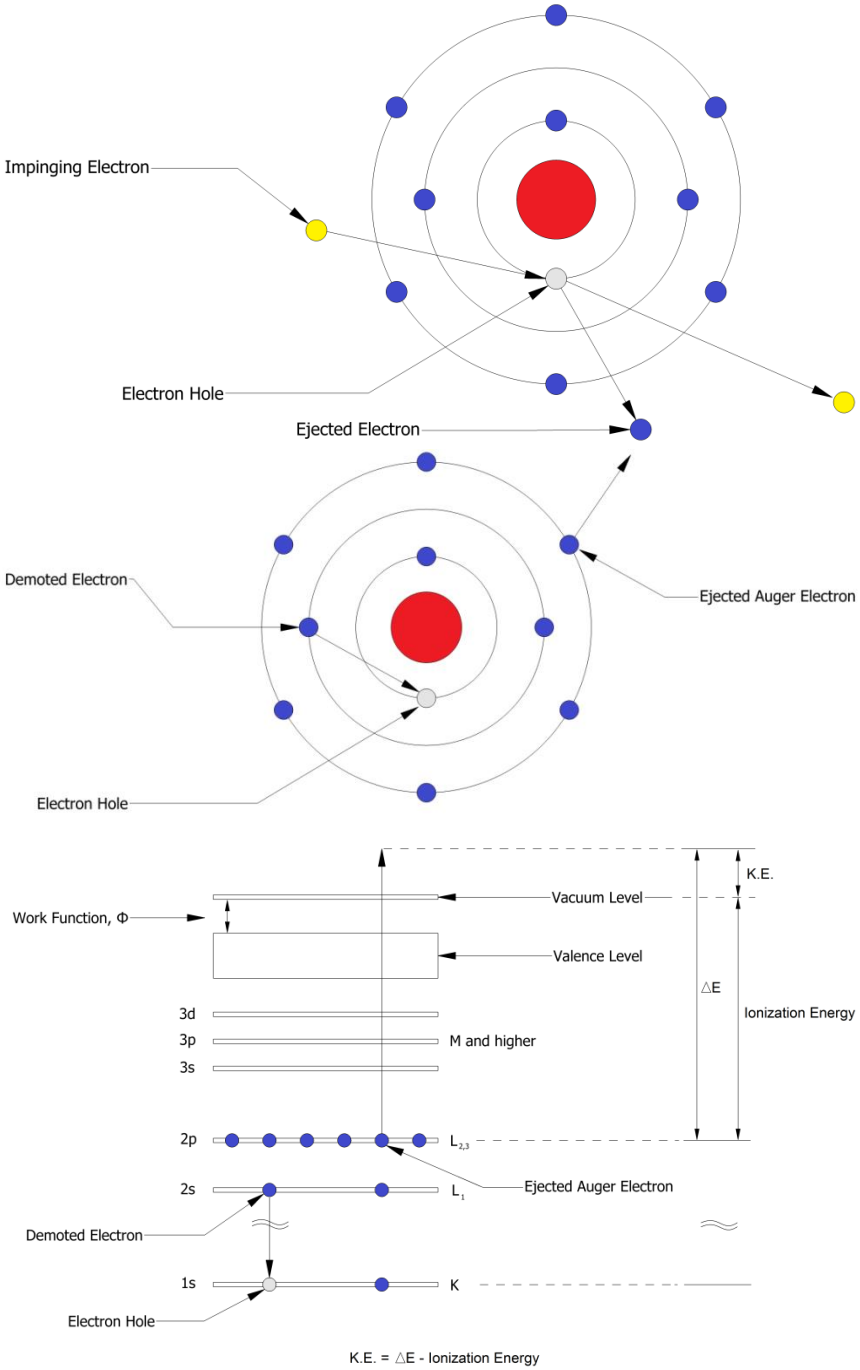

Figure 2.10: Diagrams showing the mechanism for the ejection of Auger electrons due to the collision of a high energy electron

transfers to another electron at a higher level, causing it to eject as a secondary electron. This secondary electron is known as the Auger electron, which is characteristic of the element from which it comes. There can be some overlap in elements which share Auger electron energies when the energy gaps between electron energy levels and ionization energies of elements are similar. It should be noted that due to the mechanism through which the Auger electron is formed, it is impossible to measure hydrogen and helium by AES. Elements with three or more electrons and multiple electron orbitals can be detected using AES. Additionally, surfaces can only be probed to a depth of about 10 nm, at which point secondary electrons cannot exit the bulk with sufficient energy to reach or be detected by the electron analyzer.

2.2.2 Double Pass Cylindrical Mirror Analyzer

Electrons in these experiments were detected using a double pass cylindrical mirror analyzer (CMA). In order to understand the function of a double pass CMA, a description of the a single pass CMA follows. A single pass CMA consists of an inner (IC) and outer cylinder (OC), both of which have DC bias voltages. The center of the IC contains an electron shield and prevents the passage of electrons directly through the center of the CMA. The only path available to the electrons is between the IC and OC. Depending on the relative voltages on both the IC and OC, only electrons of specific energies can reach the electron multiplier through the pinhole at the terminal end of the cylinders. A double pass CMA consists of two single pass CMAs in tandem, such that electrons terminating through the pinhole of the first CMA must pass through the second CMA in order to reach the electron multiplier at the far end. This results in higher resolution of electron energies at the cost of total signal.

2.2.3 Electron Ionization Quadrupole Mass Spectrometry

The primary use for mass spectrometry is measuring the masses of molecules in a system. There are multiple methods of measuring masses which are dependent on the type of mass analyzer and ionizer. In order to achieve separation of masses, the molecules must first be ionized and then directed through a series of electric and/or magnetic fields, which allow ions of specific mass-charge ratios to impact a microchannel plate detector. The ionizer is the primary part of the instrument which determines the potential applications of the mass spectrometer. In order to obtain an ion with the exact mass of the parent molecule, soft ionization techniques, which deal minimal damage to the molecule during ionization, are required. While such techniques are useful for measuring masses of known molecules, they are poor tools for identifying the structure and elemental composition of unknown molecules, as several molecules can share the same masses. Hard ionization techniques, most notably electron ionization, are used to break the parent molecule into characteristic fragments.

In the case of electron ionization, electrons bombard molecules before they enter the mass analyzer and create multiple ions of different mass-charge ratios. Characterization of molecules comes from the relative probabilities a certain ion is formed from the electron beam. The base peak, the most common ion formed during electron ionization which typically does not have the mass of the parent molecule, can give insight into the identity of the measured molecule. The relative ratios of other mass-charge peaks to the base peak gives a fingerprint of a molecule, which can reveal both structure and elemental composition, as both influence the fragmentation patterns of a molecule.

Quadrupole mass analyzers have four parallel metal rods. Each opposing rod are electrically connected and have both DC and AC bias voltages. One pair of rods has a negative

DC voltage and functions as a low mass filter. The other pair has a positive DC voltage and functions as a high mass filter. In both cases, the AC voltage modulates the voltage experienced by ions in the mass filter, such that the ions are more strongly or weakly accelerated towards or away from the low and high mass filters. The combination of these rods allow only ions of specific mass-to-charge ratios to oscillate through these electric fields to the detector. All other masses collide with the rods and neutralize.[8]

Optics	Voltage
Ion Region	14 V
Extractor	-30 V
Lens 1 and 3	-90 V
Lens 2	10 V
Entrance Lens	-13 V
Exit Lens	-300 V

Table 2.3: QMS optics parameters set for temperature programmed desorption and temperature programmed reaction experiments

References

1. Granville-Phillips *Granville-Phillips® Series 370 Stabil-Ion® Vacuum Gauge and Controller Advanced Vacuum Measurement Solutions*; 2013.
2. MKS_Instruments_Inc. *Mks Baratron® Types 615a/616a/617a High Accuracy Sensor Heads, Manual*; 2009.
3. Navin, J. K. Light Alkane Reactivity on Pt(111) Investigated Using Effusive Molecular Beam Methods. University of Virginia, 2014.
4. Sigma-Aldrich, Bulletin 918 - Selecting Purifiers for Gas Chromatography. **2000**.
5. Sigma-Aldrich, Supelpure®-O Oxygen/Moisture Trap, Safety Data Sheet. **2014**.
6. Bartmess, J. E.; Georgiadis, R. M., Empirical-Methods for Determination of Ionization Gauge Relative Sensitivities for Different Gases. *Vacuum* **1983**, *33*, 149-153.
7. Summers, R. L., *Nasa Technical Note Tn D-5285: Empirical Observations on the Sensitivity of Hot Cathode Ionization Type Vacuum Gauges*; NASA: Washington, D.C., 1969.
8. Finnigan, R. E., Quadrupole Mass Spectrometers. *Anal. Chem.* **1994**, *66*, 969A-975A.

Section 3 – Experimental Methods

Section **Page**

3.1 Crystal Preparation

Prior to running experiments, the Pt(111) surface was measured using AES in order to qualitatively search for contaminants. The most common contaminants which remain on a Pt(111) surface at ultrahigh vacuum pressures are carbon and oxygen. If the contamination is due to carbon monoxide, heating the Pt(111) crystal to 600 K causes all CO on the surface to desorb. If both C and O are detected by AES after flashing the sample to 600 K, the contamination is typically due to atomic oxygen or CH fragments. Flashing to 1100 K leads to the removal of atomic oxygen as it either recombines with C or O to form CO or O_2 respectively and desorbs from the surface. The latter reaction only occurs at temperatures greater than 900 K on Pt(111). If oxygen remains in AES spectra after flashing to 1100 K, the oxygen is most likely bound to Si or Ca, which are present in the oils used when cutting the single crystal, and will not leave the surface until the Si or Ca leaves. Atomic C, Si, and Ca do not leave the surface at any temperature and instead diffuse more easily into the bulk of the crystal at high surface temperatures. In the case of carbon, there is negligible C diffusion into the bulk until 1100 K.[1] In order to remove C, Si, and Ca from the surface, oxygen cleaning and argon ion sputtering become necessary.

3.1.1 Oxygen Cleaning

When carbon was detected on the Pt(111) surface, the carbon was oxidized to CO by dosing O_2 onto the surface. At surface temperatures greater than the molecular desorption temperature of O_2 ($T_s > 150$ K) and lower than the recombinative desorption of O_2 ($T_s < 900$ K), O_2 can dissociatively chemisorb to produce atomic O on the crystal surface which may react with other adsorbates (e.g. C, CO) to produce volatile products. The carbon and oxygen react to form

CO at temperatures which leads to prompt desorption. The surface temperature used for oxidation of carbon was 800 K, as that temperature allowed for a high reaction rate with minimal possibility of atomic O leaving the surface as $O_{2(g)}$ without first reacting with carbon. The oxygen was dosed onto the surface through a multicapillary array doser at pressures of approximately 5×10^{-7} Torr for 15 minutes to 2 hours depending on the amount of carbon present. However, when there is significant carbon buildup on the Pt(111) surface, two problems arise which make oxidation less efficient for cleaning the surface. The first problem is that the surface atoms are blocked by the carbon, preventing the oxygen from finding a Pt adsorption site. Secondly, carbon atoms which have multiple covalent bonds, of singular or multiple orders, to other carbon atoms on the surface are difficult to oxidize in a timely manner. Because of these problems, a surface with large amounts of carbon contamination is more efficiently cleaned using the same method to remove Si and Ca by means of argon ion sputtering.

3.1.2 Argon Ion Sputtering

Ion sputtering of a surface involves a collimated beam of ions at high energy which impact the surface atoms, causing a cascade of secondary atomic collisions at both the surface and the bulk of the crystal. These collisions rearrange and displace atoms in the bulk and lead to the ejection of surface atoms. Ion sputtering inevitably leads to damage and numerous defect sites on the crystal surface, however the impact of this damage can be minimized by annealing the crystal at high temperatures. Additionally, the ions used in sputtering have the potential to become contaminants themselves, and thus inert single atoms are preferred for surface cleaning. When silicon or calcium was detected by AES, or indirectly detected in oxides by lingering oxygen peak in AES after heating the surface above 1000K, or significant carbon was detected,

argon ion sputtering was done to clean the surface of these atoms. The surface temperature for argon ion sputtering was chosen based on the contaminant. In the case of carbon, which primarily resided on the surface and not in the bulk, relatively low temperatures were chosen to prevent carbon diffusion into the bulk. Although there is insignificant carbon diffusion into the bulk until 1100 K, the surface temperature of 600 K was chosen to effectively freeze the carbon on the surface while also allowing other contaminants, such as CO and argon, to freely desorb from the surface. However, in the case of Si and Ca, the main source of the contamination comes from the bulk and not the surface, and therefore argon ion sputtering is more efficient at high surface temperatures for cleaning those elements. The surface temperatures chosen for cleaning Si and Ca were 1000 and 1100 K, respectively, to maximize their rates of diffusion to the surface.[2] The ion gun was set to a beam voltage of 1000 eV for all contaminants. The background pressure of argon was approximately 5×10^{-6} Torr, not exceeding 5×10^{-5} Torr, while the Ar^+ ion gun was run.

3.2 Dissociative Sticking Coefficient Measurements

3.2.1 Overview

When dissociative chemisorption occurs for an alkane at surface temperatures greater than 400 K, only covalently bound alkyl and atomic carbon remain on the surface. As long as no oxygen contamination exists on the surface, any CO that desorbs from the surface originated from the background pressure and not as a secondary product of carbon on the surface. The recombinative desorption of H_2 is significantly faster than the recombination of an alkyl with a hydrogen atom at temperatures above 400 K, and so all carbon is assumed to remain on the surface regardless of secondary reactions. Because carbon diffuses negligibly into the platinum

bulk at surface temperatures below 1100 K, as long as dissociative chemisorption occurs below this threshold, the amount of carbon on the surface is equal to the number of carbons which reacted by dissociative chemisorption. With a known gas flux, dosing time, and surface carbon coverage, the reaction probability for dissociative chemisorption, also referred to as the dissociative sticking coefficient (DSC), can be calculated. Dissociative sticking coefficients are a function of both gas and surface temperature and, depending on the molecule, differ with respect to the angle of incidence of the impinging gas molecule. In other words, an ambient gas at a specific temperature may have a different DSC than a directed gas incident on the surface at a single particular angle.

3.2.2 Ambient Gas Flux

An ambient gas is any gas which is part of the background pressure and is not directed at a sample. The molecules in an ambient gas, due to collisions with the walls of the chamber, are assumed to be at the temperature of the chamber walls and randomly approach a substrate from all angles with respect to the surface normal. Ambient gas fluxes are important even in the case of a directed dosing experiment, because any molecule which does not react on initial collision with crystal surface becomes part of the background pressure and can collide with the surface additional times as an ambient gas.

Gas flux is the rate at which gas molecules collide with a surface per unit area per unit time. The background flux of an ambient gas is given by,[3]

$$F_{bkg} = \frac{d^2N}{dAdt} = \frac{p}{\sqrt{2\pi m k_B T_C}} \qquad \text{Equation 3.1}$$

where N is the number of gas molecules, A is the area of gas-surface collisions, t is time, p is the background pressure, m is the mass of the molecule, k_B is the Boltzmann constant, and T_C is the temperature of the chamber walls, which is assumed to be room temperature.

3.2.3 Effusive Beam Flux

An effusive molecular beam functions on the principal of effusion, which involves a gas escaping through a thin aperture. In order for a gas to effuse, it must be in molecular flow, where the gas molecules collide with the surfaces of their container more often than other gas molecules and the mean free path is significantly larger than the size of the aperture. The gas molecules are not forced out of the doser by intermolecular collisions, and are emitted with a pressure-independent distribution given by,

$$\frac{dN}{dt} = \int \frac{d^2N}{d\Omega dt} d\Omega = \frac{p_n A_n}{\sqrt{2\pi m k_B T_n}} \int \frac{j(\vartheta)}{\pi} d\Omega = \frac{p_n A_n W}{\sqrt{2\pi m k_B T_n}} \qquad \text{Equation 3.2}$$

where p_n is the pressure behind the nozzle, A_n is the area of the aperture, T_n is the temperature of the nozzle, $d\Omega$ is an increment of solid angle, and $j(\vartheta)$ is the flux angular function, which is equal to $\cos(\vartheta)$ for an infinitely thin orifice.[4] When integrated over the forward hemisphere of solid angle, W is the transmission coefficient which is dependent on the geometry of the aperture. If the wall thickness of the nozzle aperture gets thicker, $j(\vartheta)$, becomes more forward peaked than cosine.[5]

Although the flux varies as $\cos(\vartheta)$ as it leaves an infinitely thin walled nozzle, when projected onto a flat surface the distribution becomes even sharper. The directed beam flux, F_{dir}, onto a flat surface perpendicular to the doser can be calculated with a known perpendicular

distance, d, between the nozzle and surface. Because $d\Omega = dA\cos(\vartheta)/r^2 = dA\cos^3(\vartheta)/d^2$, where r is the distance from the nozzle center to the increment of area dA struck by molecules leaving the surface with polar angle ϑ, the directed beam flux takes the form of,[3]

$$F_{dir} = \frac{d^2N}{dAdt} = \frac{p_n A_n}{\sqrt{2\pi m k_B T_n}} \frac{j(\vartheta)}{\pi} \frac{\cos^3(\vartheta)}{d^2} = \frac{dN}{dt} \frac{j(\vartheta)}{W\pi} \frac{\cos^3(\vartheta)}{d^2} \qquad \text{Equation 3.3}$$

For our effusive molecular beam doser, j(ϑ) approximately equals cos(ϑ). The flux distribution onto a flat surface is therefore roughly $\cos^4(\vartheta)$, decreasing by the square of the perpendicular distance from the nozzle aperture. Hence, we can get DSCs as a function of angle, ϑ, after dosing an alkane by measuring C coverage by AES as a function of position across the surface.

In order to minimize the background flux onto the crystal surface during a directed beam experiment, the background gases are continuously pumped. An equilibrium is reached between the gas throughput into the chamber and the pumping speed, C_c, of the turbomolecular pump.

$$C_c p = \frac{d(pV)}{dt} = k_B T_C \frac{dN}{dt} \qquad \text{Equation 3.4}$$

After solving for p in Equation 3.4 and substituting in Equation 3.2 yields

$$p = \frac{k_B T_C}{C_C} \frac{dN}{dt} = \frac{k_B T_C}{C_C} \frac{p_n A_n W}{\sqrt{2\pi m k_B T_n}} \qquad \text{Equation 3.5}$$

and hence,

$$p_n = \frac{p C_c \sqrt{2\pi m k_B T_n}}{k_B T_C A_n W} \qquad \text{Equation 3.6}$$

The p_n needs to be known to determine F_{dir} in Equation 3.3, but in order to fix p_n one needs the parameters of Equation 3.6, notably including the chamber pumping speed and pressure. The pumping speed can be calculated separately with the aid of a calibrated leak. However, because the Bayard-Alpert gauge within the main chamber is turned off to prevent decomposition of

alkanes on the filament during actual DSC experiments, the pressure of the chamber, $p = p(p_m)$, is determined separately as a function of the pressure in the manifold, p_m, read by a capacitive manometer, which is approximately equal to, or slightly more than, the nozzle pressure. With a known pumping speed, the ratio of directed beam flux to background gas flux can be determined. In the case of methane, which has the fastest pumping speed of all the alkanes, the ratio at a dosing distance of 12.7 mm is 3 to 1 for directed and background fluxes respectively at $\vartheta = 0$.

3.2.4 Dissociative Sticking Coefficients

In effusive molecular beam dissociative chemisorption experiments with alkanes, C is assumed to remain on the surface, independent of secondary reactions. The rate of carbon deposition onto a crystal surface is equal to the product of the molecular dissociative sticking coefficient and the gas flux onto the surface, times the number of carbon atoms per molecule, *n*,[3]

$$\frac{d^2N_C}{dAdt} = \frac{d^2N}{dAdt} S(T_g, T_s) \cdot n \qquad \text{Equation 3.7}$$

$$\frac{d\theta_C}{dt} = \frac{F \cdot S(T_g, T_s) \cdot n}{\sigma_{Pt}} \qquad \text{Equation 3.8}$$

The carbon coverage in monolayers with respect to platinum, θ_c, is given by Equation 3.8, where $\sigma_{Pt} = 1.50 \times 10^{15}$ cm^{-1} is the areal density of Pt(111). By integrating Equation 3.8 with respect to carbon coverage and time, the total coverage over a known dosing period can be calculated.

$$\theta_C = \frac{F \cdot S(T_g, T_s) \cdot n \cdot t}{\sigma_{Pt}} \qquad \text{Equation 3.10}$$

In the case of the background flux of an ambient gas, the dissociative sticking coefficient is therefore the total carbon coverage in platinum monolayers multiplied by the areal density of

platinum and divided by the product of the flux of gas-surface collisions per unit time, the number of carbons in the alkane, and the total time.

$$S_{bkg}(T_g = T_c, T_s) = \frac{\theta_C \sigma_{Pt}}{nF_{bkg}t} \qquad \text{Equation 3.11}$$

Equation 3.11 assumes that the dissociative sticking coefficient remains independent of carbon coverage, which is true for low carbon coverages. As long as the total carbon coverage is below 0.4 ML, where 1 ML = σ_{Pt}, Equation 3.10 remains true and is linear with the dissociative sticking coefficient as the slope of the line. However, as more of the surface becomes covered in carbon, the dissociative sticking coefficient and rate of carbon deposition decrease. In the case of Equation 3.10, the plot of θ_c and F*t loses its linearity and plateaus at a saturation carbon coverage.

$$S(T_g, T_s) = S_0(T_g, T_s)\left(1 - \frac{\theta_C}{\theta_{C,sat}}\right)^m \qquad \text{Equation 3.12}$$

$$\frac{d\theta_C}{dt} = \frac{F \cdot S_0(T_g, T_s) \cdot n}{\sigma_{Pt}}\left(1 - \frac{\theta_C}{\theta_{C,sat}}\right)^m \qquad \text{Equation 3.13}$$

The saturated carbon coverage, when all binding sites are occupied by carbon and no more molecules may react with the surface, is given by $\theta_{c,sat}$. S_0 is the initial dissociative sticking coefficient at zero carbon coverage. The number of binding sites which an alkane occupies is given by m. In the realm of low carbon coverage, $\theta_c/\theta_{c,sat}$ are assumed to be approximately zero. At higher coverages, alkanes are assumed to require a single binding site (m = 1) to react.

$$\theta_C = \theta_{C,sat} - \theta_{C,sat} Exp\left(-\frac{F \cdot S(T_g, T_s) \cdot n \cdot t}{\sigma_{Pt} \cdot \theta_{C,sat}}\right) \qquad \text{Equation 3.14}$$

$$S(T_g, T_s) = \frac{\sigma_{Pt} \cdot \theta_{C,sat}}{F \cdot n \cdot t} ln\left(\frac{\theta_{C,sat} - \theta_C}{\theta_{C,sat}}\right) \qquad \text{Equation 3.15}$$

For the sake of simplicity, as it is more accurate in practice to fit data to a linear model than a non-linear model, gas fluxes were limited such that the total carbon coverage remained between 0.1 and 0.4 ML with respect to platinum when practically possible. Within this range, there was significant enough signal to be within the detection limit of AES but low enough carbon coverage to be within the linear region of carbon coverage and for the Equation 3.10 approximation to hold true.

In effusive molecular beam experiments, the total carbon deposition is the sum of carbon deposition from the direct beam flux and the background flux.

$$\theta_C = \theta_{C,dir} + \theta_{C,bkg} = \frac{F_{dir} \cdot S_{dir}(T_g, T_s) \cdot n \cdot t}{\sigma_{Pt}} + \frac{F_{bkg} \cdot S_{bkg}(T_c, T_s) \cdot n \cdot t}{\sigma_{Pt}} \quad \text{Equation 3.16}$$

By rearranging the parameters in Equation 3.16, the dissociative sticking coefficient with respect to the directed gas flow from the heated effusive molecular beam doser is defined as:

$$S_{dir}(T_g, T_s) = \frac{1}{R}\left(\frac{\theta_C \sigma_{Pt}}{n \cdot t \cdot F_{bkg}} - S_{bkg}(T_c, T_s) \right) \quad \text{Equation 3.17}$$

R is the ratio of the direct effusive beam flux to the background flux onto the Pt(111) crystal surface, n is the number of carbon atoms in the reacting gas molecule, and σ_{Pt} = 1.50 x 10^{15} cm^{-1} is the areal density of Pt(111). Molecules that miss or do not react after initial collision with the Pt(111) surface are assumed to collide with and thermalize to the chamber wall at temperature, T_c, before being pumped or colliding with the Pt(111) surface again with a dissociative sticking coefficient of $S_{bkg}(T_c,T_s)$. With the aperture of the doser at distance d from the center of the Pt(111) surface, the ratio R varies spatially across the surface as

$$R = \frac{F_{dir}}{F_{bkg}} = \frac{C_c \sqrt{2m} \cos^3(\vartheta)\, j(\vartheta)}{W \sqrt{\pi k_B T_c}\, d^2} \quad \text{Equation 3.18}$$

where $\vartheta = \tan^{-1}(x/d)$ is the angle away from the beam center axis for flux that hits the surface at a radial distance x from its center. The flux angular function, $j(\vartheta)$, and transmission coefficient, W, for effusion from an aperture of finite wall thickness approach $\cos(\vartheta)$ and 1, respectively, in the limit of a vanishingly thin aperture wall.[6]

With the measurement of $S_{dir}(T_g,T_s)$ and $S_{bkg}(T_c,T_s)$ at multiple surface temperatures, the activation energy for dissociative chemisorption can be determined using an Arrhenius equation.

$$S(T) = S_0(T)e^{\frac{-E_a}{RT}} \qquad \text{Equation 3.19}$$

In order to obtain accurate values for the activation energy, the system must be in thermal equilibrium, where the gas temperature and the surface temperature are equal. In the case where a molecule has a relatively long physisorption lifetime and sufficiently small energy steps between rovibrational modes, the molecule can thermalize to the surface temperature and will always be in thermal equilibrium with the surface regardless of the initial gas temperature. However, for many small molecules, a pseudo thermal equilibrium can only be obtained by heating the gas in the molecular beam doser to the surface temperature prior to dosing the molecules. DSC experiments done outside of thermal equilibrium can give information regarding the gas-surface energy transfer for a molecule, but the data cannot be used for directly calculating transition state barriers. In instances where a molecule approaches sticking coefficients of 1 or has more than one temperature dependent reaction mechanism, the accuracy of the Arrhenius equation decreases where the linearity in the correlation between DSC and temperature decreases. In order to obtain more accurate activation energies and pre-exponential factors, a precursor-mediated thermal trapping model was used, and is discussed in more detail in a separate section below.

3.2.5 Auger Analysis

The total carbon deposited onto the Pt(111) surface after the dosing period was measured using Auger electron spectroscopy (AES). Measurements were taken from 200 to 300 eV, in which range the 237 eV platinum and 272 eV carbon peaks are found. The relative ratios of these peaks give the total carbon coverage in monolayers with respect to platinum.[7]

$$\theta_C = 0.608 \frac{\int N_{C_{272}}(E)dE}{\int N_{Pt_{237}}(E)dE} \qquad \text{Equation 3.20}$$

The integral of the C272 peak divided by the integral of the Pt237 peak is proportional to the total carbon coverage. In order to obtain integrated intensities for these peaks, CasaXPS software was used to analyze the undifferentiated AES spectra. Early analysis of AES spectra used four peak lineshapes of 30% Lorentzian and 70% Gaussian, GL(30), at 219, 237, 248, and 272 eV in order to achieve accurate fitting.

Auger Peak	Position Constrained	FWHM (eV)	Integrated Peak Area Ratio to Pt_{237}
Pt_{219}	Yes	11.7	0.15
Pt_{237}	Yes	12.5	1.00
Pt_{248}	Yes	11.2	0.48
C_{272}	No	15	-

Table 3.4: Lineshape constraints used for AES analysis in CasaXPS

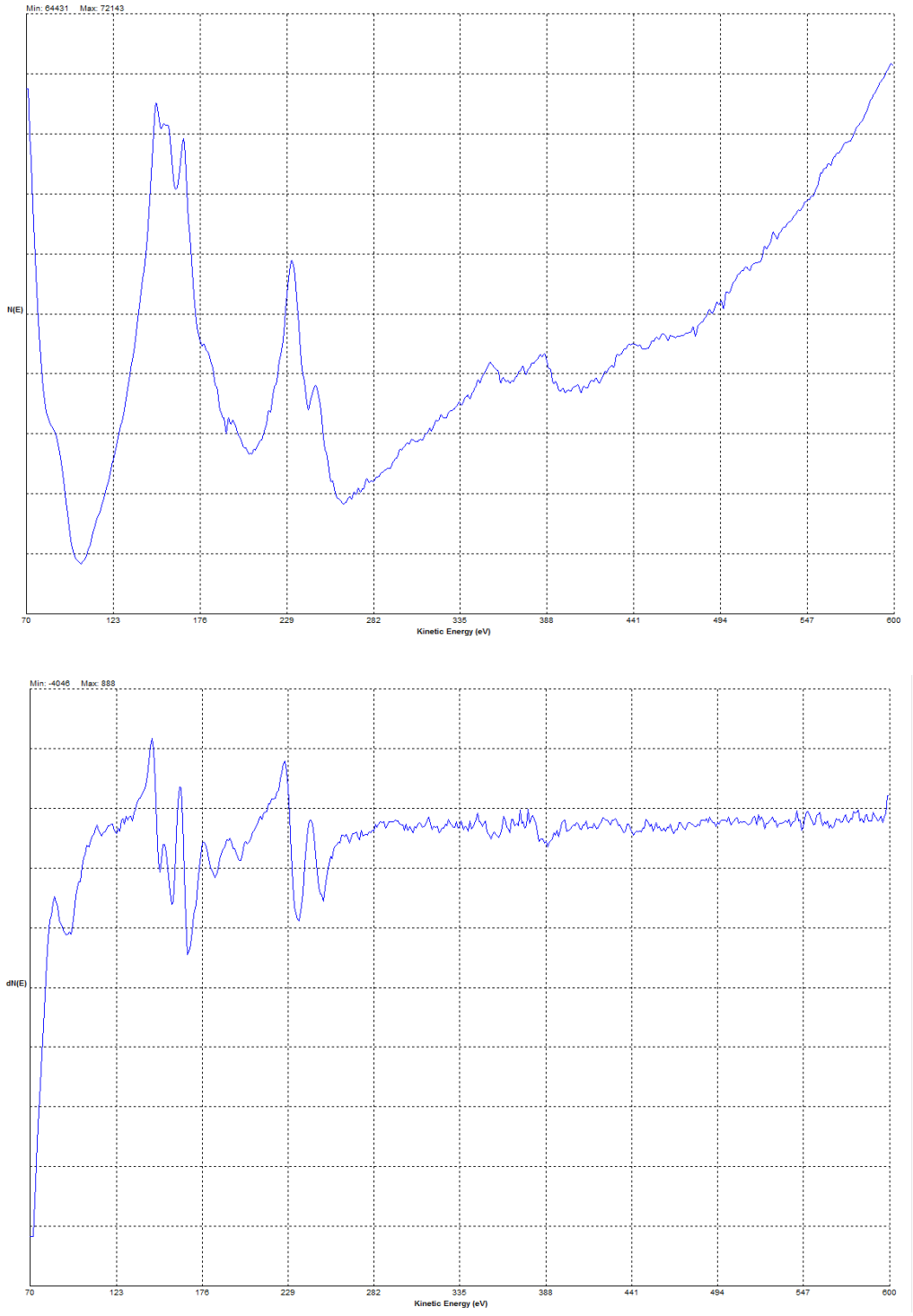

Figure 3.1: (Top) Undifferentiated and (Bottom) differentiated AES spectra of a clean Pt(111) surface; the Auger peaks at 150, 158, 167, 182, 195, 237, 248, 357, 385, 440, and 462 eV are characteristic of platinum

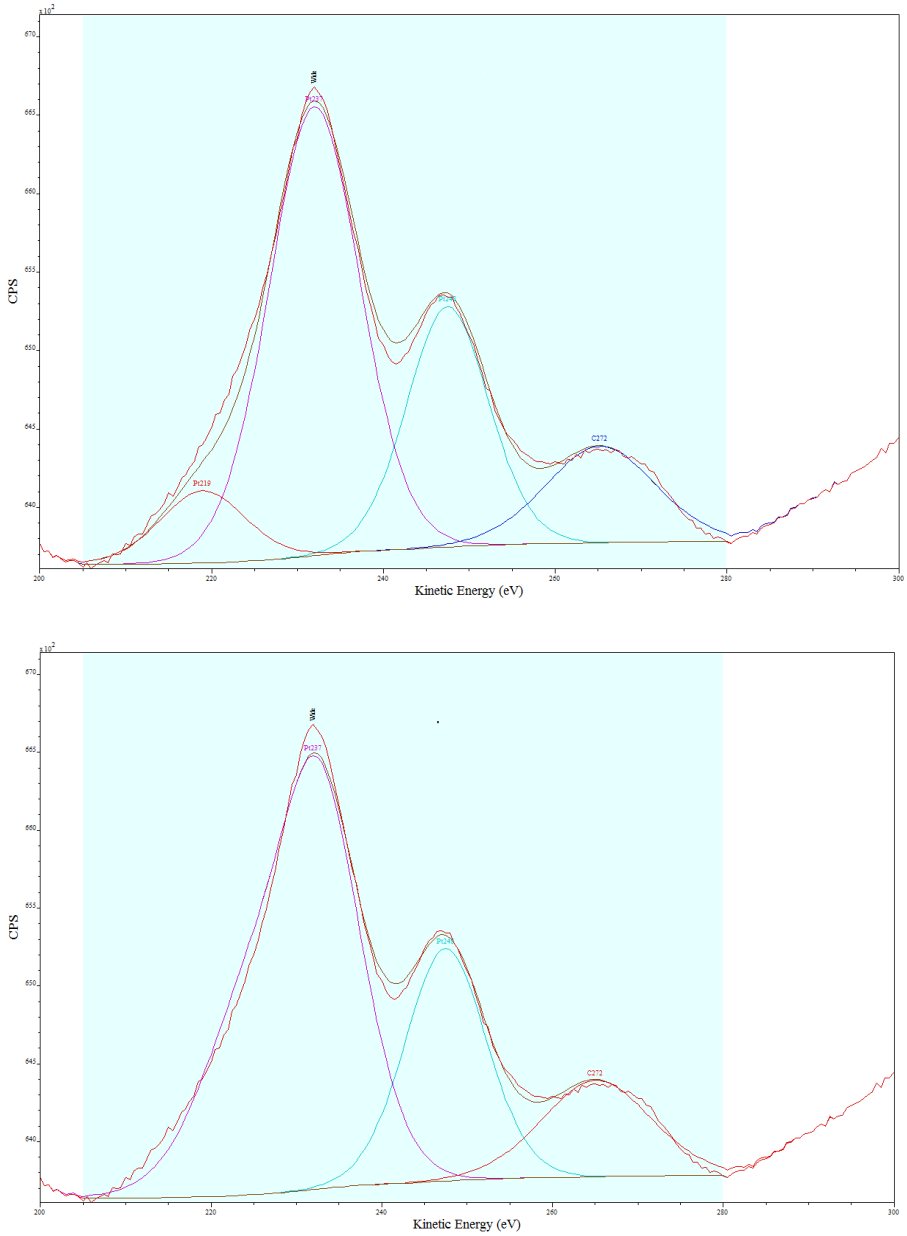

Figure 3.2: Auger spectra from 200 to 300 eV with (Top) symmetrical GL(30) lineshape functions at 219, 237, 248, and 272 eV and with (Bottom) asymmetrical A(0.1,0.9,0)GL(30) lineshape functions at 237, 248, and 272 eV

Table 3.4 shows the constraints used for each of these symmetrical lineshapes. The 237, 248, and 272 eV lineshapes were chosen for the Pt_{237}, Pt_{248}, and C_{272} Auger peaks respectively. The 219 eV lineshape was intended to address the low energy asymmetrical nature of the Pt_{237} peak. Later AES analysis removed this 219 eV lineshape and instead introduced an asymmetrical lineshape function for the Pt_{237} peak which corrected for the asymmetry in the low energy tail. This adjusted 237 eV lineshape still kept the Gaussian-Lorentzian function with the same parameters and constraints as in the original function, except it was multiplied by a CasaXPS asymmetrical function the parameters, A(a,b,0)GL(30), where a and b adjust for baseline rise and peak width increase at the low energy tail respectively. There was negligible difference between the total carbon coverage calculated using the unadjusted, symmetrical Pt_{237} lineshape and the asymmetrical lineshape. In the case of the spectra shown in Figure 3.2, the four symmetrical lineshape fit resulted in a carbon coverage of 1.62 ML, which was 3.3% larger than the 1.57 ML fit from the asymmetrical line.

3.2.6 Ambient Gas DSC Measurements

Before any dissociative sticking coefficient experiment could be done with a new molecule, the Bayard-Alpert gauge within the main chamber had to be calibrated with respect to the gas manifold Baratron for the gas effusing through the calibrated leak at the rear of the main chamber. The calibration setup emulated the experimental environment, such that all filaments, including ion pumps, were shut off or closed off from the main chamber to avoid decomposition of the molecules on the filaments, with exception to the ion gauge. The purposes for this calibration include the necessity to turn off the ion gauge during experiments, as it has a filament which can decompose reagent gases and create free radicals in the chamber. The flow of gases

through the calibrated leak into the main chamber does not remain constant with different molecules at the same manifold pressure. Molecules of different sizes effuse through the leak at different rates and are pumped out of the chamber at different pumping speed. Additionally, the ion gauge, which is calibrated to nitrogen, gives separate pressure readings for different gas molecules, although this can be accounted for using appropriate ion gauge sensitivity constants. With the gas in molecular flow from the manifold into the main chamber and out through the pumps, a calibration curve between the manifold baratron pressure, which is an absolute pressure, and the main chamber ion gauge pressure was obtained, such that the main chamber pressure could be determined by the manifold baratron alone while also accounting for the pumping speed of the molecule.

Before each dissociative chemisorption experiment, the Pt(111) crystal was cleaned of all contaminants and all filaments, including the Bayard-Alpert gauge, and ion pumps were shut off. The crystal mount was positioned such that the crystal face was not in line-of-sight to the calibrated leak, usually facing straight up towards the roof of the chamber. The surface temperature was then set on the Eurotherm temperature controller and held constant for the duration of the experiment. The reagent gas was then allowed to flow through the manifold into the main chamber through the calibrated leak. A LabView program recorded the manifold Baratron pressure as a function of time. After the desired flux was achieved, the calibrated leak was closed, the LabView program was terminated, and the reagent gas was pumped from both the main chamber and the manifold. All ion pumps were turned back on in order to facilitate the pumping of any remaining gas. With continuous pumping during the experiment, once the valve to the calibrated leak was closed, the pressure of the reagent gas dropped by two orders of magnitude (from ~1 x 10^{-7} to ~1 x 10^{-9} Torr) in the main chamber within a few seconds. It is

assumed that a negligible amount of molecules reacted after the calibrated leak was closed. The carbon coverage deposited on the surface after the dosing period was measured using AES by averaging multiple scans (e.g. 25) across the 200 to 300 eV region where the 237 eV platinum and 272 eV KLL carbon Auger peak reside, which took ~5 minutes to complete.

Dissociative sticking experiments were performed at surface temperatures less than or equal to 1000 K in order to minimize the diffusion of C into the Pt bulk. Surface temperatures below 400 K were used for some experiments, despite the potential for CO contamination during the course of the experiment. In general, it was difficult to obtain the same level of reproducibility for dissociative sticking coefficient experiments at surface temperatures of 300 K as compared to higher temperatures. The flux of alkane molecules were limited such that θ_c was in the range of 0.1 to 0.4 ML, where 1 ML = σ_{Pt}. The lower limit was chosen so that the AES had good signal-to-noise ratios. The upper limit was chosen to ensure that the measurements were of the initial sticking coefficient of the clean surface. Enhanced sticking due to step site defects was not observed due to the low defect level as fixed by the $< 0.1^o$ face alignment of our Pt(111) surface, with an upper bound of 0.0017 ML, and the detection limit of AES.

3.2.7 – Effusive Beam DSC Measurements

The procedure for effusive molecular beam experiments was very similar to that of the ambient gas measurements. For each a new molecule studied using the effusive beam doser, a conversion curve between the gas manifold Baratron and the main chamber ion gauge of the gas in molecular flow through the effusive doser was obtained at each separate nozzle temperature. The heated effusive molecular beam doser was set to the desired temperature before a set of experiments and allowed to equilibrate overnight. At the beginning of each experiment prior to

dosing gas, all filaments and ion pumps in the main chamber were turned off to prevent the formation of extraneous reactive species. The gas was then flowed from the manipulator through the effusive beam doser onto the Pt(111) crystal face which was positioned directly in front and normal to the nozzle aperture. The LabView program recorded the pressure of the manifold baratron with respect to time. After the desired flux of gas onto the crystal surface was achieved, the valve to the effusive doser was closed, the LabView program terminated, and the reagent gas pumped out from both the main chamber and manifold. The ion pumps were reinitiated to more swiftly evacuate any remaining reagent gas. In a similar manner to the ambient gas experiments, the main chamber pressure rapidly decreased as soon as the gas flow through doser ceased. It is assumed that an insignificant amount of molecules reacted after the valve to the effusive doser was closed before all of the reagent gas was pumped out. AES spectra were measured over a range of 200 to 300 eV to measure the relative values of the 237 eV and 272 eV platinum and carbon peaks respectively.

Experiments were performed at surface temperatures from 300 to 1000 K at different gas temperature. Directed gas temperatures ranged from 300 to 800 K. The latter limit was chosen to minimize the thermal decomposition of alkanes, especially larger alkanes which have relatively weak C-C bonds when compared to ethane and propane, within the doser which could form highly reactive radicals prior to interaction with the surface. Temperatures were chosen such that the studied molecules had both thermal equilibrium ($T_g = T_s = T$) and non-equilibrium (T_g != T_s) DSC values over a range of temperatures. The former provided data to calculate the activation energy, while the latter allowed for the analysis of gas-surface energy transfer for that molecule. For similar reasons as mentioned in the ambient gas DSC measurements section, the gas flux was

tuned such that the total carbon coverage was within the range of 0.1 and 0.4 ML with respect to platinum.

3.3 – Temperature Programmed Desorption

3.3.1 – Overview

A molecule is physisorbed to a surface when it is bound to the surface by electrostatic and van der Waals (dispersion) forces but has not formed a covalent bond with the surface atoms. The activation energy required to remove the molecule from the surface and return it to the gas phase is the desorption energy. Van der Waals interactions are the main force which bind alkanes non-covalently to a transition metal surface, due to the nonpolar nature of hydrocarbons and the difficulty of forming carbonium cations with the lack of a Lewis acid. Therefore, the desorption energy is a good approximation of the energy required to counteract the effect of van der Waals interactions on a molecule. Temperature programmed desorption (TPD) experiments measure the temperature at which molecules desorb from the surface. In general, the more polarizable the molecule, the strong the van der Waals interactions are on it, and therefore the higher the desorption temperature. Because polarizability increases with each additional electron in a molecule, it can be predicted that as alkanes increase in chain length, the van der Waals force increases as well. This has been demonstrated by Campbell,[8] in that the desorption energy of alkanes increase linearly with chain length.

The desorption temperature of a molecule from the Pt(111) surface is measured by cooling the crystal down to the coldest possible temperature and dosing a small amount, less than 0.1 ML with respect to platinum, of the molecule, such that the molecule physisorbs to the surface and does not desorb or react. Cooling methods limit the range of molecules for which the

desorption energy can be measured. In the case of liquid nitrogen cooling, any molecule which desorbs at temperatures below 100 K cannot be efficiently studied by TPD. Once the molecules adsorb to the surface, the substrate is heated while facing a QMS, set to measure the base peak mass of the molecule as a function of time and temperature. When the crystal reaches the minimum desorption temperature and molecules leave the surface, the signal measured from the QMS is proportional to the rate of desorption from the surface. Once all the molecules have desorbed from the surface, such that no signal appears in the QMS at temperatures equal to or above the desorption temperature, the crystal can be cooled back to the standby temperature. Because the desorption rate is proportional to the rate of temperature change, constant and linear temperature ramp rates across all desorption temperatures allow for simpler analysis and reproducible spectra. Eurotherm programs allow for such control of temperature ramp rates.

3.3.2 – Eurotherm Programs

The PID parameters of the 906S Eurotherm temperature controller are discussed in an earlier section. These parameters are essential for achieving a linear temperature ramp rate. A typical Eurotherm program for a temperature ramp rate would simply include a target temperature set point at a set rate in Kelvin per second, which under normal circumstances works fine. However, PID parameters adjust only the control of the voltage or current responsible for heating the sample. They have no knowledge or control of the cooling imposed on the crystal. While the cooling rate due to liquid nitrogen can be kept constant with flow rate controls, the Eurotherm controller must adjust for cooling by different amounts depending on the temperature of the crystal and the temperature of crystal mount without any information on either. In other words, the Eurotherm controller, regardless of PID parameters, will underestimate the amount of

power required to heat the crystal at the lowest surface temperatures. As a result of this, as the actual crystal temperature lags behind the working set point, the Eurotherm controller will then overestimate the amount of power it requires to heat the crystal in order to catch the working set point. This leads to a dampening oscillation, between underestimation and overestimation, until the controller achieves a linear temperature ramp rate.

There are several remedies to this problem. The simplest, yet most limiting, is to cool the sample to a temperature far below the desorption temperature, such that the temperature ramp rate reaches linearity before the desorption temperature. However, if the molecule desorbs at temperatures near to, within 50 K of, the coldest temperature, other methods for stabilizing the ramp rate must be used. Slow temperature ramp rates, $\leq$ 1 K/s, allow for more time for the working set point and the actual temperature to equilibrate. If a faster temperature ramp rate is desired, Eurotherm programs allow for timed pauses, which holds the working set point steady for the duration and gives the actual crystal temperature a chance to catch up, as well as multiple ramp rates, which can be used to slowly heat the crystal up to the desired ramp rate without allowing the working set point to move significantly ahead of the actual crystal temperature. With the combination of well-tuned Eurotherm programs, it was possible to reliably obtain a linear ramp rate of 2 K/s within 10 K of the coldest crystal temperature.

3.3.3 – Procedure

All molecules in this study reversibly desorbed, leaving a negligible amount of carbon covalently bound to the surface at the end of each TPD experiment. In the instances where the total carbon contamination on the surface was less than 0.1 ML with respect to platinum or immeasurable by AES prior to an experiment, oxygen TPD were performed to clean carbon off

the surface. Oxygen TPD as a cleaning technique follows a similar procedure to alkane TPD experiments described below, but the end result is different. If carbon contamination is present on the surface, CO will be detected from surface temperatures of 300 to 500 K during O_2 TPD. If the surface is clean, and no silicon or calcium are present on the surface, recombinative desorption of O_2 will be detected above 900 K. When the latter was detected, the surface was determined to be prepared for alkane TPD experiments.

Before any TPD experiments were done, the Pt(111) crystal was cooled to approximately 100 K by liquid nitrogen. Despite the cryostat reaching temperatures of 77 K, the distance of the cold finger from the crystal greatly decreased the rate of cooling at crystal temperatures below 100 K such that background gas contaminants, most notably CO, would saturate the surface prior to reaching a temperature of 90 K or lower. Heating the crystal to 600 K was sufficient for removing all CO contaminants. However, heating the crystal to temperatures 300 K and above warmed up the crystal mount significantly enough that the rate of cooling on the crystal plateaued at higher temperatures, 105 K in the case of a fast ramp (> 1 K/s) to 600 K followed by immediate cooling.

Once the crystal surface was cleaned and cooled to the minimum temperature, all filaments and ion pumps were turned off in the main chamber to prevent the formation of highly reactive radicals on the filaments. The gas manifold was closed off from both the main chamber and the manifold pumping station. The gas of study was then allowed into the manifold until the desired pressure, as measured by the baratron, was reached. A valve to a trapped volume was closed such that a small amount of the gas remained as the rest of the gas in the manifold was pumped through the manifold pumping station. The cold crystal was positioned facing a cosine doser behind a variable leak valve. The gas from the trapped volume was the flowed through the

variable leak valve onto the Pt(111) surface until all of the molecules had either adsorbed to the surface, crystal mount, cryostat, or left the chamber through the TMP. In experiments where the main chamber ion gauge was left on, it took approximately a half minute for the chamber pressure to return to the base pressure (~1 x 10^{-10} Torr) after a dose from the trapped volume, even for higher pressures (~1 x 10^{-1} Torr in the manifold). The main chamber pressure spiked no higher than 1 x 10^{-6} Torr, depending on the pressure in the trapped volume and the degree to which the variable leak valve was opened, within this time period.

With the gas adsorbed to the Pt(111) surface, the crystal was positioned in front of the line-of-sight QMS. A LabView program designed to record the QMS signal for multiple single mass-to-charge ratios as a function of time and temperature was initiated. A previously prepared temperature ramp program from the Eurotherm was chosen and run. The ramp rate chosen differed based on the gas of study, but were typically among 1, 2, 5, and 10 K/s. For molecules which desorbed at temperature below 160 K, 1 and 2 K/s were the only continuously reliable ramp rates. The 5 K/s ramp rate was reproducibly stable by 160 K. The 10 K/s ramp rate was exclusively used for molecules which desorbed above 300 K, and was primarily used during oxygen TPD. The target temperature was set to 600 K for alkane studies, terminating above the CO desorption temperature. Oxygen TPD and methanol TPR terminated at 1150 K, well above the temperature of O_2 recombinative desorption. Once the crystal reached the maximum temperature and a TPD spectrum was recorded, the surface was immediately cooled in preparation for another experiment.

3.3.4 – Spectra Analysis

The initial step in the analysis of TPD spectra (mass spectrum voltage ∝ desorption rate, versus time ∝ surface temperature) is the identification of the monolayer and multilayer desorption peaks, which have a maximum desorption rate at T_{peak}. The monolayer desorption peak of an alkane molecule has the highest T_{peak} in a TPD spectrum, provided that a physisorbed monolayer of the molecule can both form and desorb within the temperature range of the experimental equipment. In the cases where a molecule has a desorption temperature sufficiently higher than the lowest practical crystal temperature, multilayer TPD peaks, which are significantly lower (~80 K for alkanes) than the monolayer TPD peak, can be measured. The detection of a multilayer peak indicates that a saturated monolayer of the molecule has been obtained. By adjusting the gas exposure, which, in the case of this study, is proportional to the pressure in the trapped volume of the gas manifold, over the course of multiple TPD experiments, a calibration plot of integrated peak versus exposure is obtained. There is a linear relation between integrated peak and exposure until the molecule reaches a saturated monolayer, at which point the monolayer peak area completely plateaus and multilayer peak area begins to increase. Once a calibration plot for peak area and exposure has been obtained, the peak areas can be converted to ML with respect to a saturated monolayer or with respect to platinum, if the molecular coverage with respect to platinum is measured at a physisorbed coverage equal to or below the saturation coverage.

The flux of molecules which desorbs from the surface is identical to the flux of molecules onto the surface as an ambient gas, which is Equation 1.2 with a cosine angular distribution,

$$F\left(T_s\right)=\frac{d^2N}{dAdt}\frac{\cos\left(\vartheta\right)}{\pi}=\frac{1}{4}\left\langle v\right\rangle\rho\frac{\cos\left(\vartheta\right)}{\pi} \qquad \text{Equation 3.21}$$

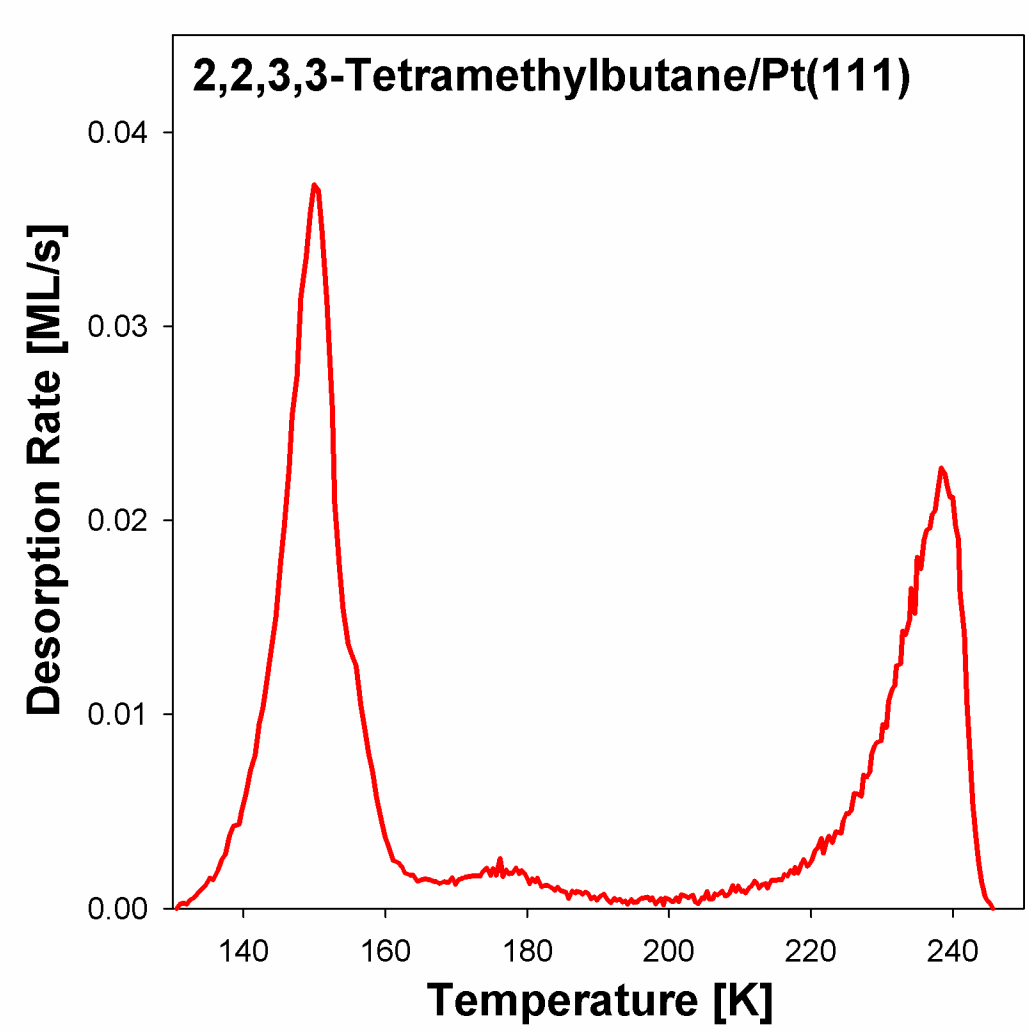

Figure 3.3: An example TPD spectrum of 2,2,3,3-tetramethylbutane, measured at a heating ramp rate of 5 K/s, showing the monolayer peak at T_{peak} = 238 K and the multilayer peak at T_{peak} = 150 K.

where N is the number of molecules, A is the surface area, t is time, $\langle v \rangle$ is the mean velocity of the molecules, ρ is the density of molecules, and ϑ = 0 is the normal angle. A line-of-sight QMS, which is behind two apertures from the surface, negates the necessity to account for the angular distribution. This is because all of the desorbed molecules which arrive at the detector are assumed to have desorbed from the single angle (ideally ϑ = 0) and therefore have no angular distribution in flux. The signal from the QMS is the density of molecules which hit the QMS ionization region. The flux is proportional to the product of the density of molecules and their mean velocity. Desorbing molecules, which are in thermal equilibrium with the surface, have a mean velocity of $\langle v \rangle = (3\pi/8)\sqrt{8k_B T/\pi m}$. This means that the desorption flux proportional to $\rho\sqrt{T}$. For this reason, in addition to correcting the spectra for the background signal, the QMS signal at each point of surface temperature was multiplied by the square root of the surface temperature, $\sqrt{T}$, in order to obtain the temperature dependent desorption flux of molecules desorbing from the surface. The desorption rate of the molecules can be used to determine rate constants for desorption using the Polanyi-Wigner desorption rate equation, given by:[8]

$$\frac{-d\theta}{dt} = \nu_d e^{\frac{-E_D(\theta)}{RT_s}} \theta \qquad \text{Equation 3.22}$$

where θ is the molecular coverage at time, t, $E_D(\theta)$ is the coverage dependent desorption energy, ν_d is the pre-exponential factor, R is the gas constant, and T_s is the surface temperature.

The inversion-optimization analytical method of calculating the desorption pre-exponential factor from the TPD spectrum followed the method described by Campbell.[8] After correcting the TPD spectra for background and thermal velocity, the spectra were inverted to the linearized form of the Polanyi-Wigner equation.

$$\ln\left(\frac{-d\theta/dt}{\theta}\right)=\frac{-E_D(\theta)}{R}\frac{1}{T_s}+\ln\left(\nu_d\right) \qquad \text{Equation 3.23}$$

In the range where the desorption rate is non-zero, the experimental data arranged according to Equation 3.23 should be linear. A linear least squares fit to the linear region of the inverted data yields the desorption prefactor from the intercept and a constant, locally coverage independent desorption energy from the slope. However, as expressed in both Equation 3.22 and 3.23, the desorption energy is not necessarily coverage independent at all coverages and may indeed vary significantly with molecular coverage. Assuming that the desorption pre-exponential factor is not also coverage dependent, the Polanyi-Wigner equation was further rearranged to calculate the experimental coverage dependent desorption energies using the desorption rate, coverage, and surface temperature.

$$E_D\left(\theta\right)=-RT_s\ln\left(\frac{d\theta/dt}{\theta\cdot\nu_d}\right) \qquad \text{Equation 3.24}$$

A non-linear least squares fit of the experimental coverage dependent desorption energies to a coverage dependent desorption energy model,

$$E_D(\theta)=a+b\theta+ce^{\frac{-\theta}{d}} \qquad \text{Equation 3.25}$$

where *a* is the coverage independent desorption energy on the lattice, *b* is the increased desorption energy caused by positive molecule-molecule interactions (i.e. van der Waals), and *c* is the increased desorption energy from defect sites which falls off relative to *d*, can then be done. Following Campbell's lead, the desorption energy of a molecule was determined to be the coverage dependent desorption energy (Equation 3.25) at a half saturated monolayer. Simulated TPD were calculated using the coverage dependent desorption energy and a temperature dependent desorption rate equation,

$$\frac{d\theta}{dT_S} = -\frac{\nu}{\beta} e^{\frac{-E_D[\theta]}{RT_s}} \theta \qquad \text{Equation 3.26}$$

where β is the temperature ramp rate ($T_S = T_0 + \beta t$). By comparing the simulated TPD to experimental data, the accuracy of the calculated pre-exponential factor and coverage dependent desorption energy parameters was evaluated.

3.4 – Precursor Mediated Thermal Trapping Model

3.4.1 – One Dissociation Pathway

The precursor-mediate thermal trapping (PMTT) model assumes that gas molecules which collide with the Pt(111) with a known flux adsorb and thermalize to the surface temperature prior to either reacting or desorbing. The molecule can then reversibly desorb or undergo dissociative chemisorption, where a C-H bond is broken and the alkyl and hydrogen fragments bind covalently to the surface.

$$RH_{(g)} \underset{k_d(T)}{\overset{F(T_g)}{\rightleftharpoons}} RH_{(p)} \xrightarrow{k_r(T)} R_{(c)} + H_{(c)} \qquad \text{Equation 3.27}$$

The following kinetic equations result from the kinetic scheme above:

$$\frac{d\theta_{RH_{(p)}}}{dt} = F(T_g) - k_d(T)\theta_{RH_{(p)}} - k_r(T)\theta_{RH_{(p)}}$$
$$\frac{d\theta_{R_{(c)}}}{dt} = k_r(T)\theta_{RH_{(p)}} \qquad \text{Equation 3.28}$$

Applying the steady-state approximation to $RH_{(p)}$, assuming all molecules which physisorb to the surface rapidly react or desorb, the total rate of a molecule reacting with the surface is

$$\frac{d\theta_{R_{(c)}}}{dt} = \frac{k_r(T)}{k_d(T) + k_r(T)} F(T_g) \qquad \text{Equation 3.29}$$

where θ is the total molecular coverage which reacted with the surface and $F(T_g)$ is the reagent flux at gas temperature T_g. Arrhenius thermal rate constants are used for each reaction pathway,

$$k_i(T) = \nu_i e^{-\frac{E_i}{RT}} \qquad \text{Equation 3.30}$$

where ν_i is the pre-exponential factor, R is the gas constant, T is the temperature of the thermalized molecule, and E_i is the reaction activation energy with respect to the initial potential energy of the molecule, which in the case of this model is the physisorption minima of the potential energy curve. Equation 3.29 can then be related back to the dissociative sticking coefficient under thermal equilibrium conditions, where $T_g = T_s = T$, by

$$\frac{d\theta}{dt} = S(T)\, F(T_g) \qquad \text{Equation 3.31}$$

such that,

$$S(T) = \frac{k_r(T)}{k_d(T) + k_r(T)} \qquad \text{Equation 3.32}$$

in the case where coverage is low and scales linearly with the total exposure, $F(T_g)*t$, and

$$S(T) = \frac{k_r(T)}{k_d(T) + k_r(T)}\left(1 - \frac{\theta}{\theta_{max}}\right)^n \qquad \text{Equation 3.33}$$

when the molecular coverage is large enough that the chemisorbed coverage scales non-linearly with respect to the total exposure and number of binding sites, n, and approaches a plateau equal to the saturation coverage, θ_{max}. In the realm of low coverage, inserting Equation 3.30 into Equation 3.32 simplifies to,

$$S(T) = \left(1 + \frac{\nu_d}{\nu_r} e^{\frac{E_r - E_d}{RT}}\right)^{-1} \qquad \text{Equation 3.34}$$

The apparent activation energy of dissociative chemisorption for an impinging molecule is approximately $E_a = E_r - E_d$, which implies a molecule approaching from the vacuum has an

apparent activation energy equal to the difference in activation energies between the transition state barrier and the physisorbed molecule minus the difference in potential energy between the vacuum and the physisorbed molecule. A more accurate representation of the apparent activation energy can be shown from the derivative of the natural log of Equation 3.32 with respect to temperature.

$$E_a(T) = RT^2 \frac{d\ln(S(T))}{dT} \qquad \text{Equation 3.35}$$

When Equation 3.34 is inserted into Equation 3.35, the temperature dependent apparent activation energy is then equal to,

$$E_a(T) = (E_r - E_d)\left(1 + \frac{\nu_r}{\nu_d} e^{\frac{-(E_r - E_d)}{RT}}\right)^{-1} \qquad \text{Equation 3.36}$$

which is typically equal to ($E_r - E_d$) given the second bracketed term in Equation 3.36 is usually miniscule with $\nu_d >> \nu_r$ and ($E_r - E_d$) positive for activated dissociative chemisorption.

3.4.2 – Two Dissociation Pathway

Not all dissociative chemisorption reactions involve the dissociation of a C-H bond. If an alkane favors C-C bond dissociative chemisorption over C-H bond dissociation, as small c-alkanes do on Ru(0001),[9] the PMTT model does not differ from the equations shown in section 3.4.1. However, if C-H and C-C bond dissociative chemisorption are competitive reaction pathways, as Weinberg observed for alkanes on Ir(111),[10] then a more complex PMTT model must be constructed.

$$\begin{aligned} &RRH_{(g)} \underset{k_d(T)}{\overset{F(T_g)}{\rightleftharpoons}} RRH_{(p)} \\ &RRH_{(p)} \xrightarrow{k_{r\,C\text{-}H}(T)} RR_{(c)} + H_{(c)} \\ &RRH_{(p)} \xrightarrow{k_{r\,C\text{-}C}(T)} R_{(c)} + RH_{(c)} \end{aligned} \qquad \text{Equation 3.37}$$

This model assumes that an impinging molecule physisorbs to the surface and thermalizes to the surface temperature. The molecule then either desorbs or reacts by one of who dissociation pathways. Using the kinetic scheme equations shown in Equation 3.37, the following holds true:

$$\begin{aligned} \frac{d\theta_{RH_{(p)}}}{dt} &= F(T_g) - \left(k_d(T) - k_{r\,C\text{-}H}(T) - k_{r\,C\text{-}C}(T)\right)\theta_{RH_{(p)}} \\ \frac{d\theta_{RR_{(c)}}}{dt} &= k_{r\,C\text{-}H}(T)\,\theta_{RH_{(p)}} \\ \frac{d\theta_{RH_{(c)}}}{dt} &= k_{r\,C\text{-}C}(T)\,\theta_{RH_{(p)}} \end{aligned} \qquad \text{Equation 3.38}$$

Using a steady-state approximation, the total rate of a molecule reacting with the surface is

$$\frac{d\theta_{R_{(c)}}}{dt} = \frac{k_{r\,C\text{-}H}(T) + k_{r\,C\text{-}C}(T)}{k_d(T) + k_{r\,C\text{-}H}(T) + k_{r\,C\text{-}C}(T)} F(T_g) \qquad \text{Equation 3.39}$$

where θ is the total molecular coverage which reacted with the surface by either C-H or C-C bond dissociation. Considering Equation 3.31, the coverage independent DSC at low molecular coverage is

$$S(T) = \frac{k_{r\,C\text{-}H}(T) + k_{r\,C\text{-}C}(T)}{k_d(T) + k_{r\,C\text{-}H}(T) + k_{r\,C\text{-}C}(T)} \qquad \text{Equation 3.40}$$

and coverage dependent DSC is

$$S(T) = \frac{k_{r\,C\text{-}H}(T) + k_{r\,C\text{-}C}(T)}{k_d(T) + k_{r\,C\text{-}H}(T) + k_{r\,C\text{-}C}(T)} \left(1 - \frac{\theta}{\theta_{max}}\right)^n \qquad \text{Equation 3.41}$$

when the linear approximation of the molecular coverage with respect to exposure and the number of binding sites no longer applies. Inserting Equation 3.40 into Equation 3.35 gives an apparent activation energy equal to

$$E_a(T) = \frac{\left(E_{r,C-H} - E_d\right)\nu_{C-H} e^{\frac{E_{r,C-C}}{RT}} + \left(E_{r,C-C} - E_d\right)\nu_{C-C} e^{\frac{E_{r,C-H}}{RT}}}{\nu_{C-H} e^{\frac{E_{r,C-C}}{RT}} + \nu_{C-C} e^{\frac{E_{r,C-H}}{RT}}} A \qquad \text{Equation 3.42}$$

where

$$A = \frac{\nu_d e^{\frac{E_{r,C-H}+E_{r,C-C}}{RT}}}{\nu_d e^{\frac{E_{r,C-H}+E_{r,C-C}}{RT}} + \nu_{C-H} e^{\frac{E_d+E_{r,C-C}}{RT}} + \nu_{C-C} e^{\frac{E_{r,C-H}+E_d}{RT}}} \qquad \text{Equation 3.43}$$

In the case where $\nu_{C\text{-}C} >> \nu_{C\text{-}H}$, Equations 3.42 and 3.43 simplify to

$$E_a(T) = \left(\frac{\nu_{C-H}}{\nu_{C-C}} e^{\frac{E_{r,C-C}-E_{r,C-H}}{RT}} \left(E_{r,C-H} - E_d\right) + \left(E_{r,C-C} - E_d\right)\right) A \qquad \text{Equation 3.44}$$

and

$$A = \frac{\nu_d e^{\frac{E_{r,C-H}+E_{r,C-C}}{RT}}}{\nu_d e^{\frac{E_{r,C-H}+E_{r,C-C}}{RT}} + \nu_{C-C} e^{\frac{E_{r,C-H}+E_d}{RT}}} = \left(1 + \frac{\nu_{C-C}}{\nu_d} e^{\frac{E_d - E_{r,C-C}}{RT}}\right)^{-1} \qquad \text{Equation 3.45}$$

and if $\nu_{C\text{-}H}/\nu_{C\text{-}C} \simeq 0$,

$$E_a(T) = \left(E_{r,C-C} - E_d\right)\left(1 + \frac{\nu_{C-C}}{\nu_d} e^{\frac{E_d - E_{r,C-C}}{RT}}\right)^{-1} \qquad \text{Equation 3.46}$$

which is identical to the PMTT model for a one dissociation reaction pathway as shown by Equation 3.36 above. From the derivation of Equation 3.46 it can be predicted that in the case where either $\nu_{C\text{-}C} >> \nu_{C\text{-}H}$ or $\nu_{C\text{-}H} >> \nu_{C\text{-}C}$, that the apparent activation energy will equal Equation 3.36 for the reaction pathway with the significantly larger pre-exponential factor. However, when the pre-exponential factors for two dissociation reaction pathways are close enough in

value such that neither $\nu_{C-H}/\nu_{C-C} \simeq 0$ nor $\nu_{C-C}/\nu_{C-H} \simeq 0$ are accurate approximations, then the apparent activation energy equals Equation 3.42.

In the case where temperature is low and $E_{r,C-H} >> E_{r,C-C}$, Equation 3.42 also approximates to Equation 3.43 indicating that the reactive pathway with the lowest reaction energy is favored at low temperatures. When both $\nu_{C-H} >> \nu_{C-C}$ and $E_{r,C-C} >> E_{r,C-H}$, then a C-C bond dissociation reaction pathway should not be observed and Equation 3.33 should be the apparent activation energy. However, if either $\nu_{C-C} >> \nu_{C-H}$ or $E_{r,C-H} >> E_{r,C-C}$ but not both is true, then C-C bond dissociation should be observed at higher or lower temperatures respectively with a temperature dependent activation energy equal to Equation 3.42. Weinberg's observations of alkanes on Ir(111)[10] indicate that C-C bond dissociative chemisorption occurs at higher temperatures, which predicts $\nu_{C-C} > \nu_{C-H}$ and $E_{r,C-C} > E_{r,C-H}$ according to the PMTT model.

References

1. Hamilton, J. C.; Blakely, J. M., Carbon Segregation to Single-Crystal Surfaces of Pt,Pd and Co. *Surf. Sci.* **1980**, *91*, 199-217.
2. Tripa, C. E.; Zubkov, T. S.; Yates, J. T.; Mavrikakis, M.; Norskov, J. K., Molecular N-2 Chemisorption-Specific Adsorption on Step Defect Sites on Pt Surfaces. *J. Chem. Phys.* **1999**, *111*, 8651-8658.
3. Cushing, G. W.; Navin, J. K.; Valadez, L.; Johánek, V.; Harrison, I., An Effusive Molecular Beam Technique for Studies of Polyatomic Gas-Surface Reactivity and Energy Transfer. *Rev. Sci. Instr.* **2011**, *82*, 044102.
4. Cushing, G. W.; Navin, J. K.; Valadez, L.; Johánek, V.; Harrison, I., An Effusive Molecular Beam Technique for Studies of Polyatomic Gas-Surface Reactivity and Energy Transfer. *Rev. Sci. Instr.* **2011**, revision submitted.
5. Scoles, G., *Atomic and Molecular Beam Methods*; Oxford University Press, 1988.
6. Pauly, H., Other Low-Energy Beam Souces. In *Atomic and Molecular Beam Methods*, Scoles, G., Ed. Oxford Univ. Press: New York, 1988; Vol. 1, pp 83-123.
7. Deng, R. P.; Herceg, E.; Trenary, M., Identification and Hydrogenation of C-2 on Pt(111). *J. Am. Chem. Soc.* **2005**, *127*, 17628-17633.
8. Tait, S. L.; Dohnalek, Z.; Campbell, C. T.; Kay, B. D., N-Alkanes on Pt(111) and on C(0001)/Pt(111): Chain Length Dependence of Kinetic Desorption Parameters. *J. Chem. Phys.* **2006**, *125*, 234308.
9. Hagedorn, C. J.; Weiss, M. J.; Kim, T. W.; Weinberg, W. H., Trapping-Mediated Dissociative Chemisorption of Cycloalkanes on Ru(001) and Ir(111): Influence of Ring Strain and Molecular Geometry on the Activation of C-C and C-H Bonds. *J. Am. Chem. Soc.* **2001**, *123*, 929-940.
10. Johnson, D. F.; Weinberg, W. H., Quantification of the Selective Activation of C-H Bonds in Short-Chain Alkanes - the Reactivity of Ethane, Propane, Isobutane, N-Butane, and Neopentane on Ir(111). *J. Chem. Phys.* **1995**, *103*, 5833-5847.

Section 4 – Branched Alkane Temperature Programmed Desorption

Section **Page**

4.1 Isobutane

TPD spectra for the desorption of isobutane and n-butane from Pt(111) have been previously measured by Koel.[1] Both isomers were found to have the same peak temperature, T_{peak}, at 175 K, and were calculated to have the same desorption energy (45 kJ/mol). However, the activation energies for molecular desorption were determined using the Redhead method, which assumes a pre-exponential factor of 1×10^{13} s^{-1}. The Redhead method has been shown to yield inaccurate desorption energies compared to the inversion-optimization analysis by Campbell.[2] Campbell also predicted that isobutane should have a kinetic rate pre-exponential factor for desorption several orders of magnitude larger (ca. 1×10^{15} s^{-1}) than the value assumed for the Redhead analysis. Because the PMTT model requires desorption energies and pre-exponential factors in order to yield dissociative chemisorption rate constants from fits to experimental DSC data, isobutane TPD spectra were measured and analyzed using Campbell's inversion method.

In accordance to Koel, isobutane was found to desorb reversibly, such that no carbon remained on the surface within the detection limit of AES. Isobutane TPD spectra (Figure 4.1) had a T_{peak} of 175 K, which did not shift in temperature with respect to total molecular coverage. The molecular coverage, in monolayers (ML) with respect to the areal density of platinum, of a saturated monolayer was determined by a monolayer coverage versus exposure plot (Figure 4.2). The molecular coverage of the isobutane monolayer correlated linearly with exposure, given by the trapped volume pressure, and suddenly plateaued, remaining constant at the saturated monolayer molecular coverage of $\theta_{max} = 0.104$ ML with respect to platinum, as the remaining impinging molecules formed a multilayer at a lower T_{peak} (ca. 100 K). The molecular coverage of the saturated monolayer was measured using AES at the 275 eV C KLL Auger peak after dosing

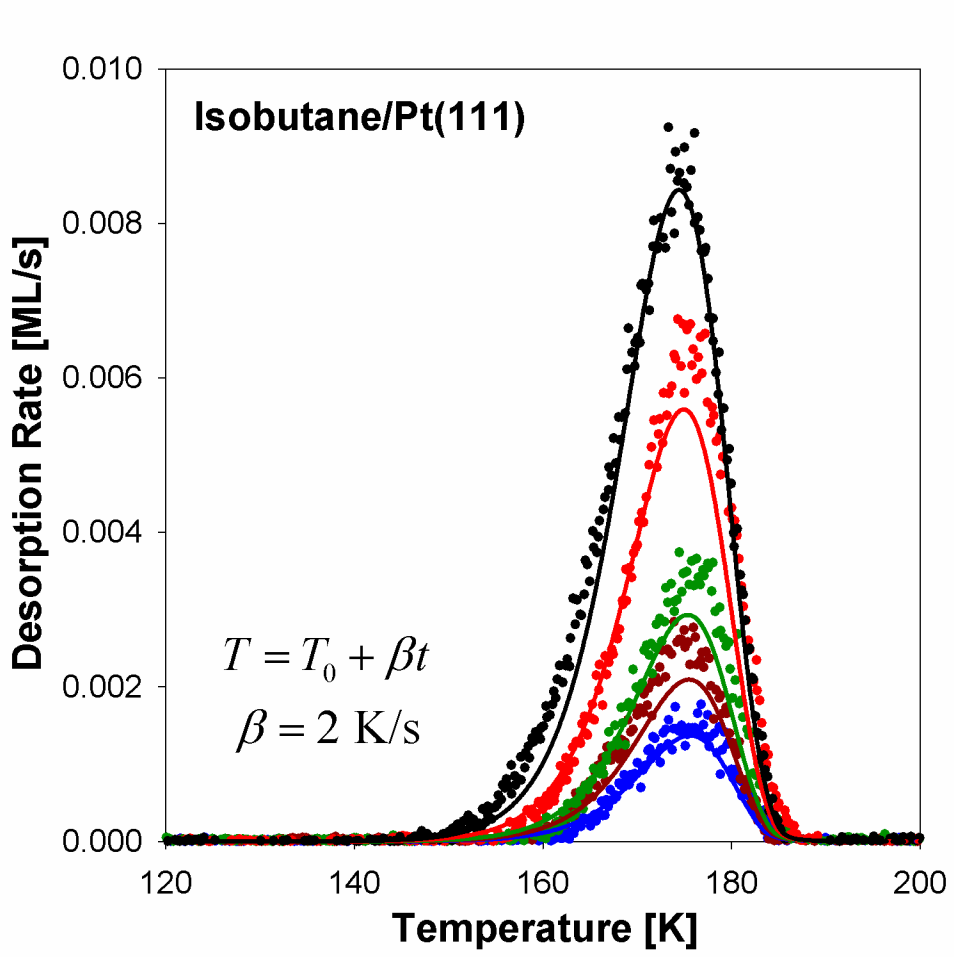

Figure 4.1: TPD spectra of isobutane on Pt(111) for five coverages (0.0089, 0.0137, 0.0194, 0.0380, 0.0592 ML with respect to Pt) measured at a heating ramp of 2K/s; the dots indicate experimental spectra, while the lines are simulated TPD using the desorption kinetic rate parameters calculated from the inversion analysis of the TPD

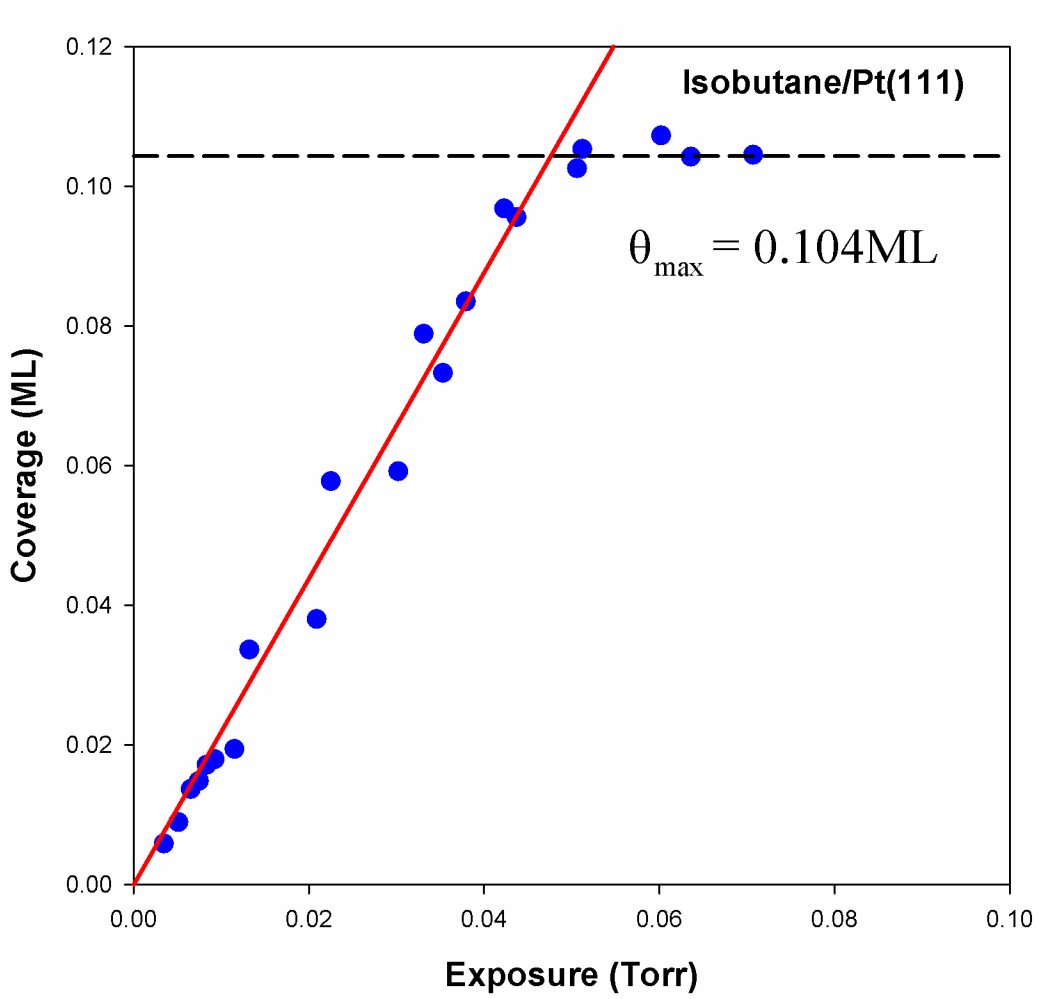

Figure 4.2: Monolayer molecular coverage, in ML with respect to the areal density of platinum, versus exposure plot of isobutane on Pt(111), given by the trapped volume pressure in Torr; the red lines are linear least square fits to the data below the saturation limit and to the data at the plateau; the intersection of the two red lines was used to determine the saturation coverage of the monolayer (θ_{max}), indicated by the dashed black line at 0.104 ML.

an amount of molecules (trapped volume pressure: 4.76 x 10^{-2} Torr) such that a saturated monolayer was obtained with a negligible multilayer. The isobutane multilayer, which has a significantly weaker binding energy to the surface than the monolayer, has a T_{peak} approximately at 100 K, which is below the practical lower limit of surface temperatures for a crystal cooled using a liquid nitrogen cold finger. Because the primary focus of this study is the analysis of monolayer TPD spectra, and because of the difficulties in reliably obtaining clear multilayer spectra using liquid nitrogen and a heating ramp of 2 K/s, the measurement and analysis of multilayer peaks for isobutane are not reported.

The inversion analysis of isobutane TPD spectra for calculating the desorption kinetic pre-exponential factor was performed by combining the TPD data from all initial experimental molecular coverages and analyzing the combined data as a whole, as opposed to analyzing each TPD spectrum individually. Figure 4.3 shows the molecular coverage on the Pt(111) surface with respect to surface temperature as measured using a heating ramp of 2 K/s. The temperature range from 160 to 185 K best represented the range over which desorption occurred for all initial coverages, as well as the range over which the coverage desorption energy was approximately constant for all molecular coverages, which will be explained in further detail later in this section. This temperature range was used in the inversion analysis for calculating the desorption pre-exponential factor, where the isobutane TPD spectra were inverted according to the Polanyi-Wigner equation (Equation 3.22). The inverted TPD spectra are linear across the range of desorbing molecules, as shown by Figure 4.4. A linear least squares fit of the inverted data between 160 and 185 K to the inverted Polanyi-Wigner equation yielded a desorption pre-exponential factor of $\ln(\nu_d) = 33.7 \pm 0.2$, $\nu_d = 4.37 \times 10^{14}$ s^{-1}, ranging from 3.43 x 10^{14} to 5.57 x 10^{14} s^{-1} due to uncertainty. The slope of the fit yielded $E_d = 50.5 \pm 0.3$ kJ/mol. Because the

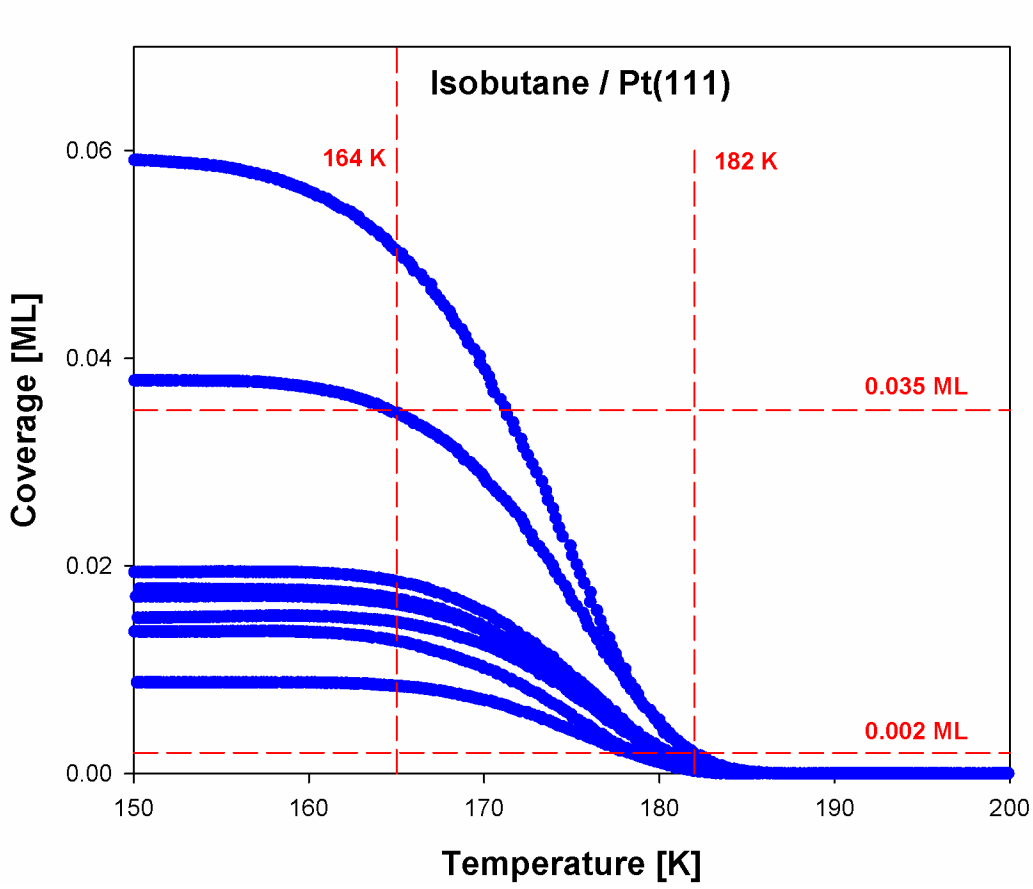

Figure 4.3: Total molecular coverage versus surface temperature plots of isobutane on Pt(111) for several initial coverages, heated at 2 K/s. The vertical dashed red lines indicate the surface temperature range boundaries through which isobutane desorbs from the surface

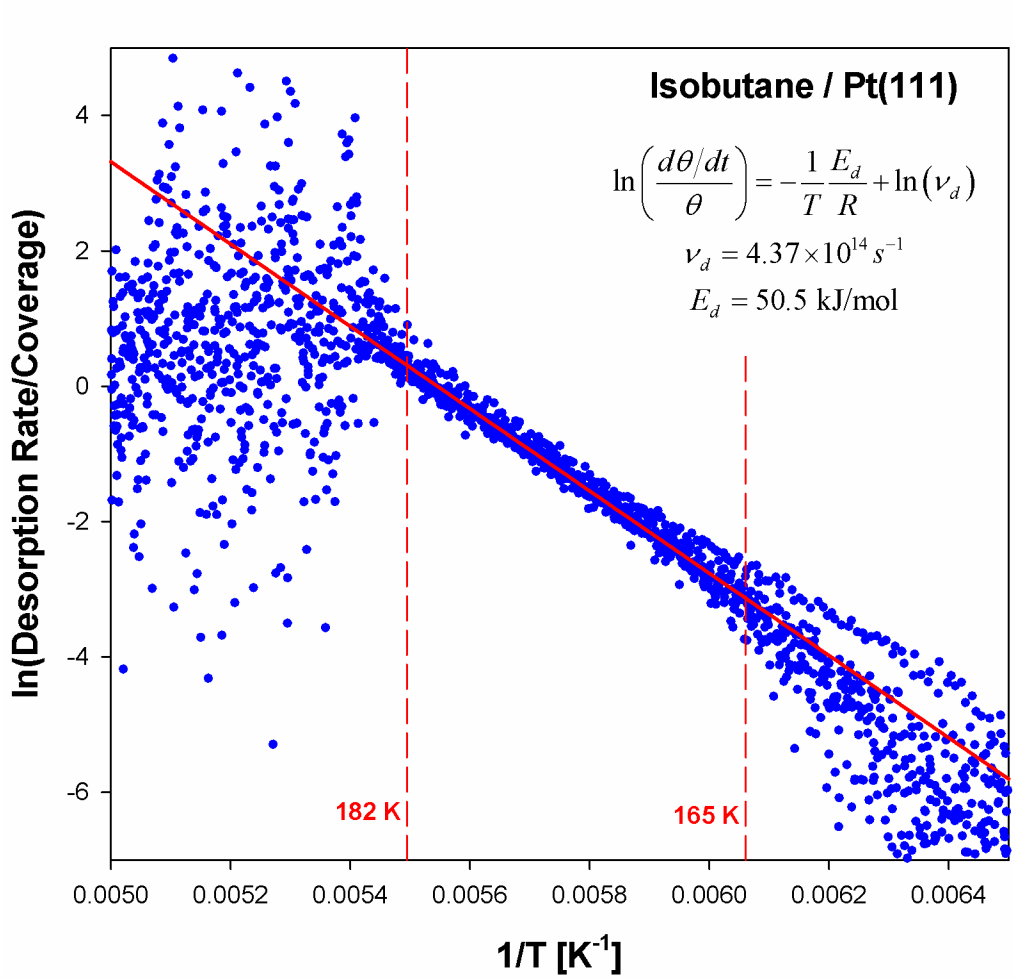

Figure 4.5: An inversion-optimization analysis plot for isobutane on Pt(111) of the natural log of the desorption rate divided by the total molecular coverage at surface temperature T versus 1/T; the vertical dotted red lines mark the surface temperature region through which isobutane desorbed from the surface; the solid red line is a linear least squares fit to the data (blue dots) from 160 to 185 K, from which the desorption pre-exponential factor, $\ln(\nu_d) = 33.7 \pm 0.2$, was derived

coverage dependent desorption energy was constant across this temperature range for all TPD spectra, the pre-exponential factor calculated from this fit can also be assumed to be constant in this temperature range.

Experimental desorption energies at each point of molecular coverage were calculated from the measured desorption rates, molecular coverages, and temperatures using a transform of the Polanyi Wigner equation (Equation 3.24) and the desorption pre-exponential factor obtained using the inversion analysis above. A nonlinear least squares fit of the experimentally derived desorption energies of isobutane on Pt(111) to the coverage dependent desorption energy model (Equation 3.25) yielded a = 50.6 ± 0.1 kJ mol^{-1}, b = -6.31 ± 5.58 kJ mol^{-1} ML^{-1}, c = 1.87 ± 0.13 kJ mol^{-1}, and d = (5.61 ± 0.74) x 10^{-5} ML. Figure 4.5 shows the fit in comparison to the experimental data. The desorption energies were approximately constant at all coverages (Figure 4.5), with little deviation above 0.2 θ_{max}. Significant deviation from *a* ($E_{D,0}$ = 50.6 ± 0.1 kJ/mol), due to increased binding energy from defect sites, were only measured at coverages lower than 0.001 θ_{max}. The value of *b* indicates that there are minor molecule-molecule repulsive force which reduce the desorption energy with increasing molecular coverage. The value of *d* is the fraction of defect sites on the Pt(111) crystal surface, which is sufficiently low such that defect sites have a negligible impact on these TPD studies. The standard deviation of each parameter relates to whole fit across each point of coverage, including the coverage range where defect sites play a significant role. In order to evaluate the average error between two coverages, the standard deviation equation (σ_{fit}) was used,

$$\sigma_{fit} = \sqrt{\frac{\sum \left(x_{exp} - x_{fit} \right)^2}{N - 1}} \qquad \text{Equation 4.1}$$

where x_{exp} is the expected, or experimental, value, x_{fit} is the value produced by the fit, and N is

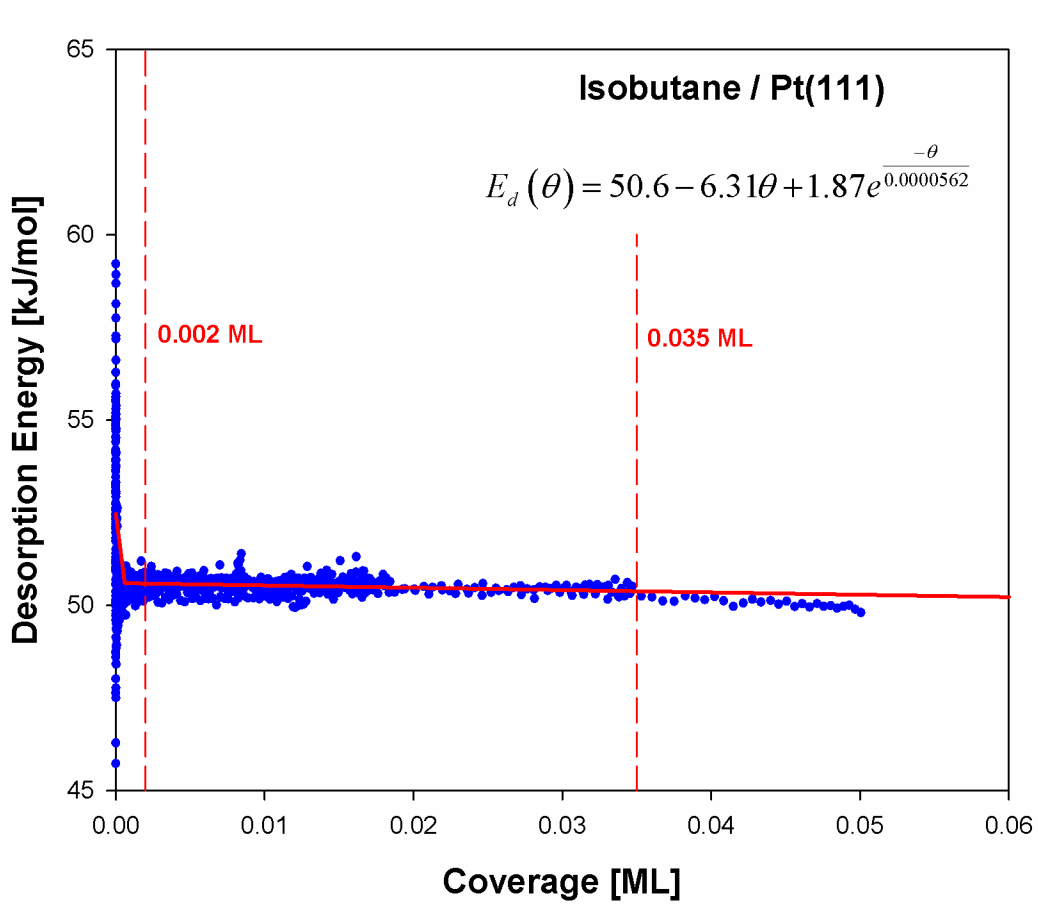

Figure 4.5: The coverage dependent desorption energy plot of isobutane on Pt(111); the solid red line is the least squares fit of the experimental data (blue dots) to the coverage dependent desorption energy model (Equation 3.25)

the number of statistical degrees of freedom. The standard deviation is $E_D(\theta) \pm 1.5$ kJ/mol across all coverages, but decreases to $E_D(\theta) \pm 0.9$ kJ/mol, $E_D(\theta) \pm 0.3$ kJ/mol and $E_D(\theta) \pm 0.2$ kJ/mol for coverages greater than 0.00001, 0.0001 and 0.001 ML, which are approximately 1/10x, 1x and 10x of the coverage of defect sites, respectively. Because the majority of TPD experiments had coverages significantly greater than 0.001 ML (0.01 θ_{max}), $\sigma_{fit} = \pm 0.2$ kJ/mol best represents the standard deviation of the experimental desorption energies. The desorption energy was calculated to be 50.2 ± 0.2 kJ/mol at a half saturated monolayer of coverage (0.5 θ_{max} = 0.052 ML). Simulated TPD spectra were calculated by inserting the fitted model parameters and the experimentally derived pre-exponential factor into the temperature-dependent desorption rate equation (Equation 3.26). Figure 4.1 shows the experimental TPD with simulated spectra, calculated using the same initial molecular coverages as the experimental data.

The desorption energy of 50.2 ± 0.2 kJ/mol calculated in this study for isobutane on Pt(111) is significantly (10%) greater than the 45 kJ/mol reported by Koel,[1] which can be attributed to the relative inaccuracy of the Redhead analysis in comparison to the inversion analysis. The desorption energy matches well with Campbell's prediction for the desorption energy of a four carbon alkane on Pt(111) of 53.5 kJ/mol, differing from the expected value by 6.6%. This study, Koel,[1] and Campbell[2] all agree that the T_{peak} of isobutane and n-butane is 175 K. When the same analysis method is used for both isobutane and n-butane, the desorption energies and pre-exponential factors do not differ significantly between the isomers. The desorption energy of isobutane reported by this study is 1.4% smaller than the experimental value of 50.9 kJ/mol for n-butane by Campbell.[2] The desorption pre-exponential factors of n-butane (5.01×10^{14} s^{-1}) and isobutane (4.37×10^{14} s^{-1}) differ by a larger percentage (15%) than

the desorption energies, but considering the range of error of pre-exponential factors, the difference is relatively small.

4.2 2,2-Dimethylpropane (Neopentane)

Neopentane was determined to desorb from Pt(111) reversibly, such that no carbon remained on the surface in any amount measurable by AES. The TPD spectra had a T_{max} at 175 K, overlapping the temperature of butane and isobutane, as shown by Figure 4.6 below. The molecular coverage, in ML with respect to the areal density of platinum, of a saturated monolayer was determined by a monolayer coverage versus exposure plot (Figure 4.7). AES spectra of the 275 eV C KLL Auger peak for an exposure of 4.94×10^{-2} Torr in the trapped volume, which resulted in a saturated monolayer with no significant multilayer, yielded a molecular coverage of $\theta_{max} = 0.110$ ML. Monolayer coverage correlated linearly with respect to exposure, given by the pressure in Torr of the trapped volume. Monolayer TPD spectra for exposures greater than 4.94×10^{-2} Torr did not yield consistent molecular coverages. This was due to a reconstruction multilayer peak at 145 K, which affected the area of the monolayer peak around 150 K, overestimating the molecular coverage for some spectra. The multilayer peak at 145 K did not scale with increasing coverage, which was determined to be due to two possible occurrences. In the case where the neopentane multilayer forms layer-by-layer wetting, the 145 K peak may be due to the fraction of monolayer neopentane molecules orientated nonoptimally with the surface. Neopentane can orient to the surface such that one or three methyl groups are far from the surface. Considering the surface integrated Lennard Jones potential (Equation 1.5) the neopentane orientation with more methyl groups further from the surface is expected to have a weaker physisorption energy and a lower T_{peak} than the other orientation. The peak at 145 K

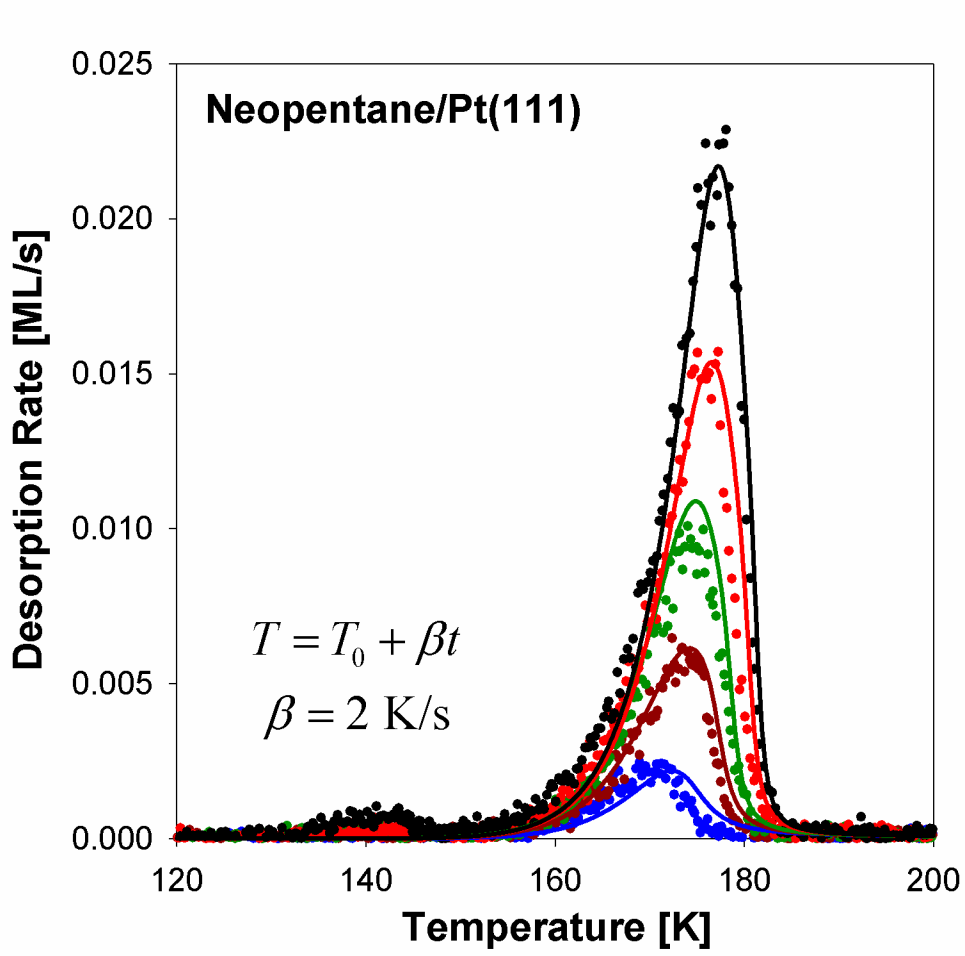

Figure 4.6: TPD spectra of neopentane on Pt(111) for five initial molecular coverages (0.0108, 0.0261, 0.0441, 0.0603, and 0.0804 ML with respect to Pt) heated at 2K/s; the dots indicate experimental spectra, while the solid lines are the simulated TPD

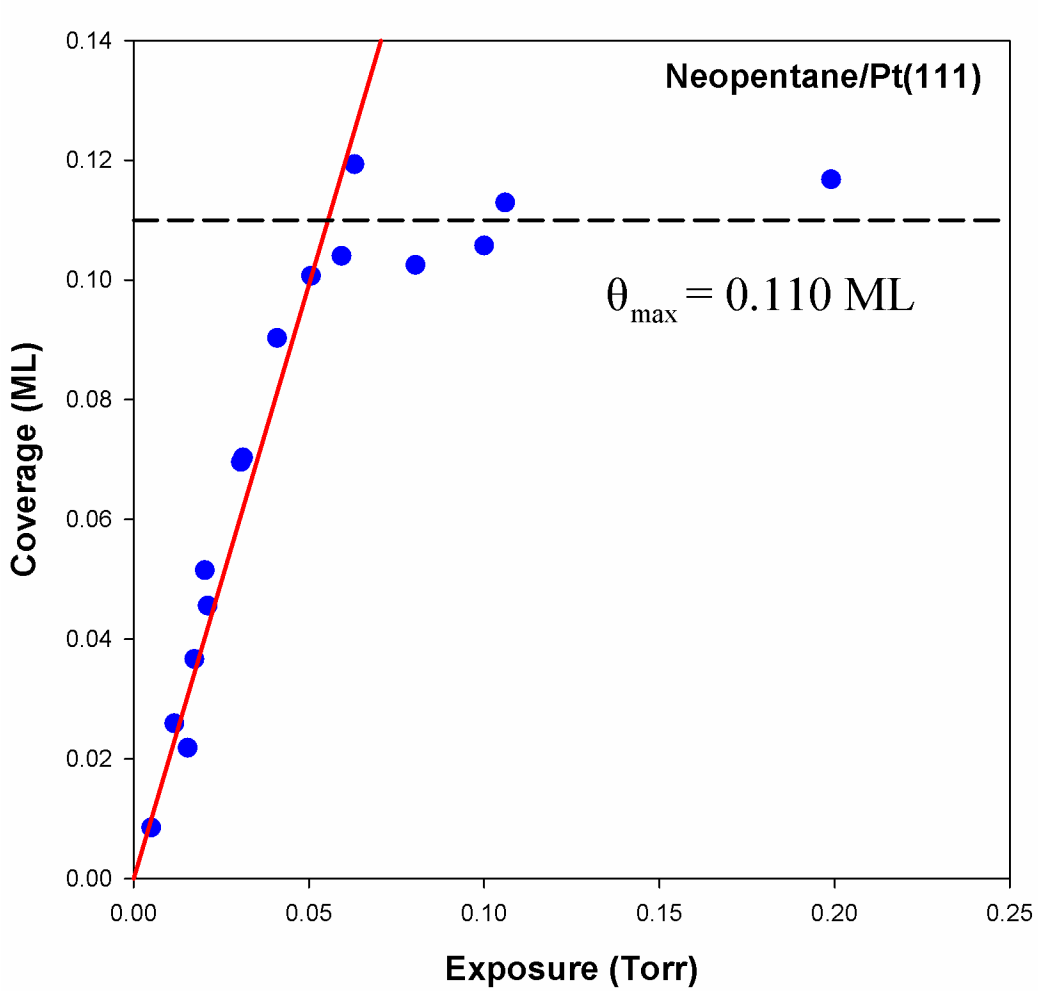

Figure 4.7: Monolayer molecular coverage, in ML with respect to the areal density of platinum, versus exposure plot of neopentane on Pt(111), given by the trapped volume pressure in Torr; the red lines are linear least square fits to the data below the saturation limit and to the data at the plateau; the intersection of the two red lines was used to determine the saturation coverage of the monolayer, indicated by the dashed black line at θ_{max} = 0.110 ML.

may also be due to the formation of multilayer islands by Stranski-Krastanov growth, provided that they only form at low multilayer coverages and have higher binding energy than layer-by-layer multilayer growth. The full multilayer peak, which did scale with increasing coverage, of neopentane was determined to be in the same temperature range as the multilayer peak of isobutane and n-butane. The multilayer peak of neopentane was not fully investigated due to the same difficulties as described in Section 4.1 for isobutane.

The inversion analysis of neopentane TPD spectra for calculating the desorption kinetic pre-exponential factor was performed by combining the TPD data from all initial experimental molecular coverages and analyzing the combined data as a whole, as opposed to analyzing each TPD spectrum individually. Figure 4.8 shows the molecular coverage of neopentane on the Pt(111) surface with respect to surface temperature as measured using a heating ramp of 2 K/s. As will be discussed in further detail later, the coverage dependent desorption energy did not remain constant over any significant coverage or temperature range. For this reason, the temperature range from 155 to 180 K was chosen because it best represented the range for all initial molecular coverages over which desorption occurred until approximately 2% of θ_{max} remained on the surface, at which point defect sites significantly increases the coverage dependent desorption energy. This temperature range is also the range through which the desorption energy varies the least with respect to coverage, and is therefore the best available region for extracting a constant pre-exponential factor. The inversion plot of neopentane TPD spectra, which is linear from 155 to 180 K, is shown by Figure 4.9. A linear least squares fit of the inverted data between 155 and 180 K to the inverted Polanyi-Wigner equation (Equation 3.23) yielded a desorption pre-exponential factor of $\ln(\nu_d) = 34.0 \pm 0.5$, $\nu_d = 6.10 \times 10^{14}\ s^{-1}$, ranging from 3.60×10^{14} to $1.04 \times 10^{15}\ s^{-1}$ due to uncertainty. The slope of the fit yielded a

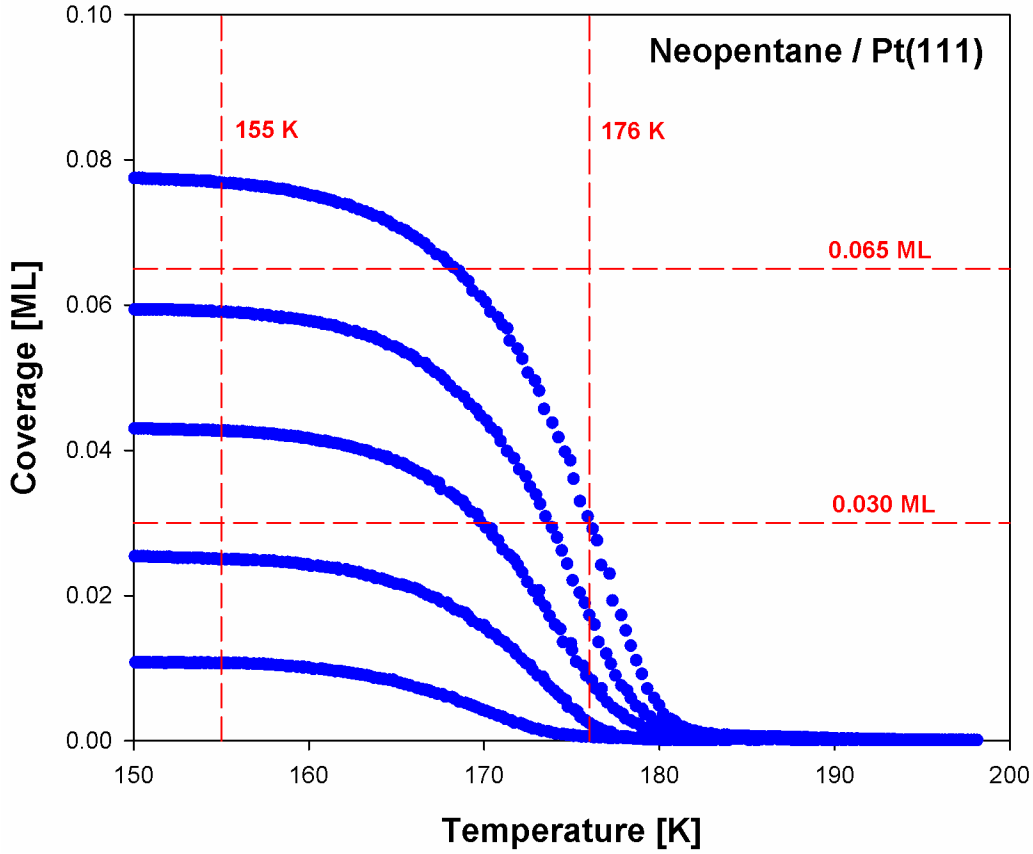

Figure 4.8: Total molecular coverage versus surface temperature plots of neopentane on Pt(111) for several initial coverages, heated at 2 K/s. The vertical dashed red lines indicate the surface temperature range boundaries through which neopentane desorbs from the surface

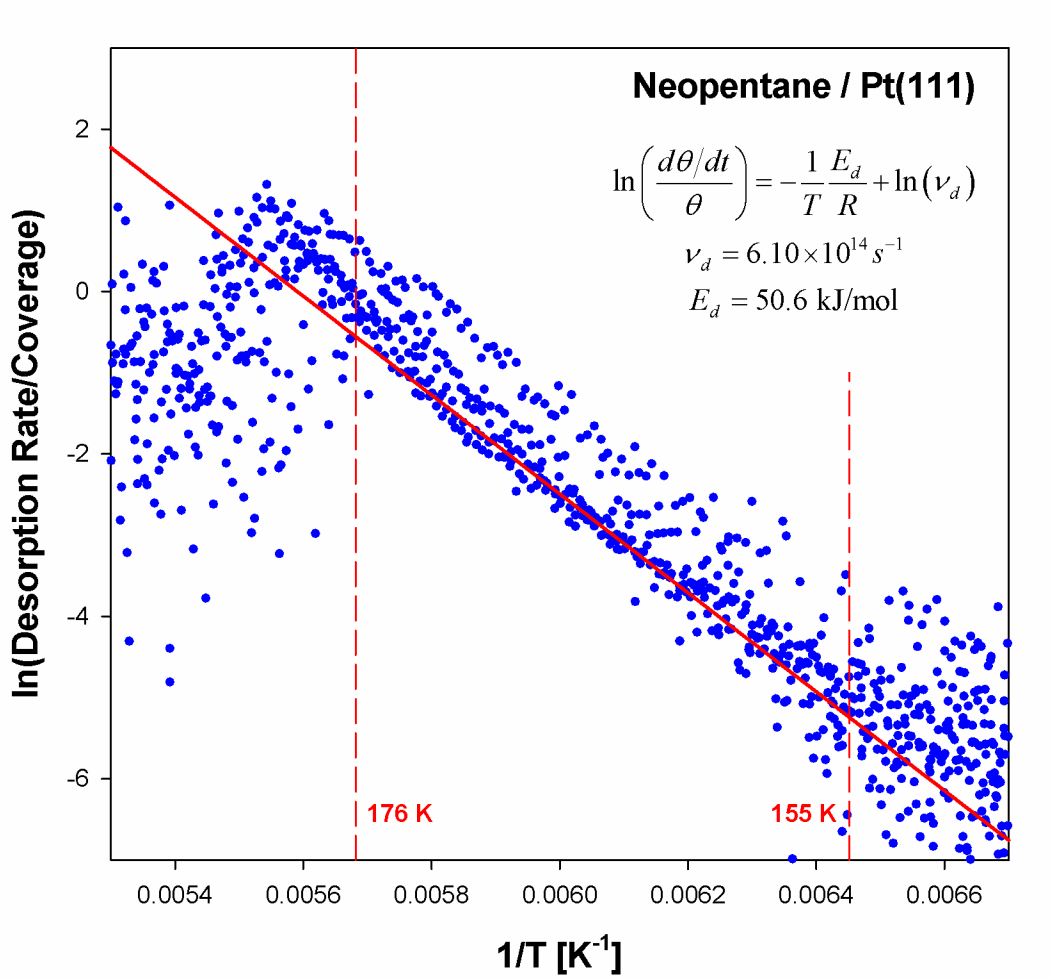

Figure 4.9: An inversion-optimization analysis plot for neopentane on Pt(111) of the natural log of the desorption rate divided by the total molecular coverage at surface temperature T versus 1/T; the vertical dotted red lines mark the surface temperature region through which neopentane desorbed from the surface; the solid red line is a linear least squares fit to the data (blue dots) from 155 to 180 K, from which the desorption pre-exponential factor, $\ln(\nu_d) = 34.0 \pm 0.5$, was derived

desorption energy of 50.6 ± 0.7 kJ/mol. The inversion analysis was performed on individual neopentane TPD spectra from 155 to 180 K to evaluate if there was a significant coverage dependence on the pre-exponential factor. However, the pre-exponential factors derived from individual spectra did not significantly deviate from the $\ln(\nu_d) = 34.0 \pm 0.5$ calculated from the combined TPD data, indicating no substantial coverage dependence for the pre-exponential factor.

A non-linear least squares fit of the experimental data for neopentane on Pt(111) to the coverage dependent desorption energy model (Equation 3.25) yielded values of a = 49.5 ± 0.1 kJ mol^{-1}, b = 20.4 ± 3.1 kJ mol^{-1} ML^{-1}, c = 5.96 ± 0.19 kJ mol^{-1}, and d = (1.03 ± 0.10) x 10^{-3} ML. The value of *b* indicates that neopentane has non-negligible molecule-molecule attraction on the surface which increases the physisorption energy with respect to molecular coverage, as shown by the coverage dependent desorption energy plot for neopentane on Pt(111) in Figure 4.10 below. The low value of *d* indicates that the low fraction of surface defects had a negligible impact on the desorption energy. The standard deviation according to Equation 4.1 is $E_D(\theta) \pm 1.4$ kJ/mol across all coverages, but decreases to $E_D(\theta) \pm 1.2$ kJ/mol and $E_D(\theta) \pm 0.6$ kJ/mol for coverages greater than 0.0001 and 0.001 ML, which are approximately 1x and 10x of the coverage of defect sites, respectively. Because the majority of TPD experiments had coverages significantly greater than 0.001 ML (0.01 θ_{max}), $\sigma_{fit} = \pm 0.6$ kJ/mol best represents the standard deviation of the experimental desorption energies. The physisorption energy was calculated to be 50.6 ± 0.6 kJ/mol at a half saturated monolayer of coverage (0.5 θ_{max} = 0.055 ML). Simulated TPD spectra were calculated by inserting the fitted model parameters and the experimentally derived pre-exponential factor into the temperature dependent desorption rate equation (Equation

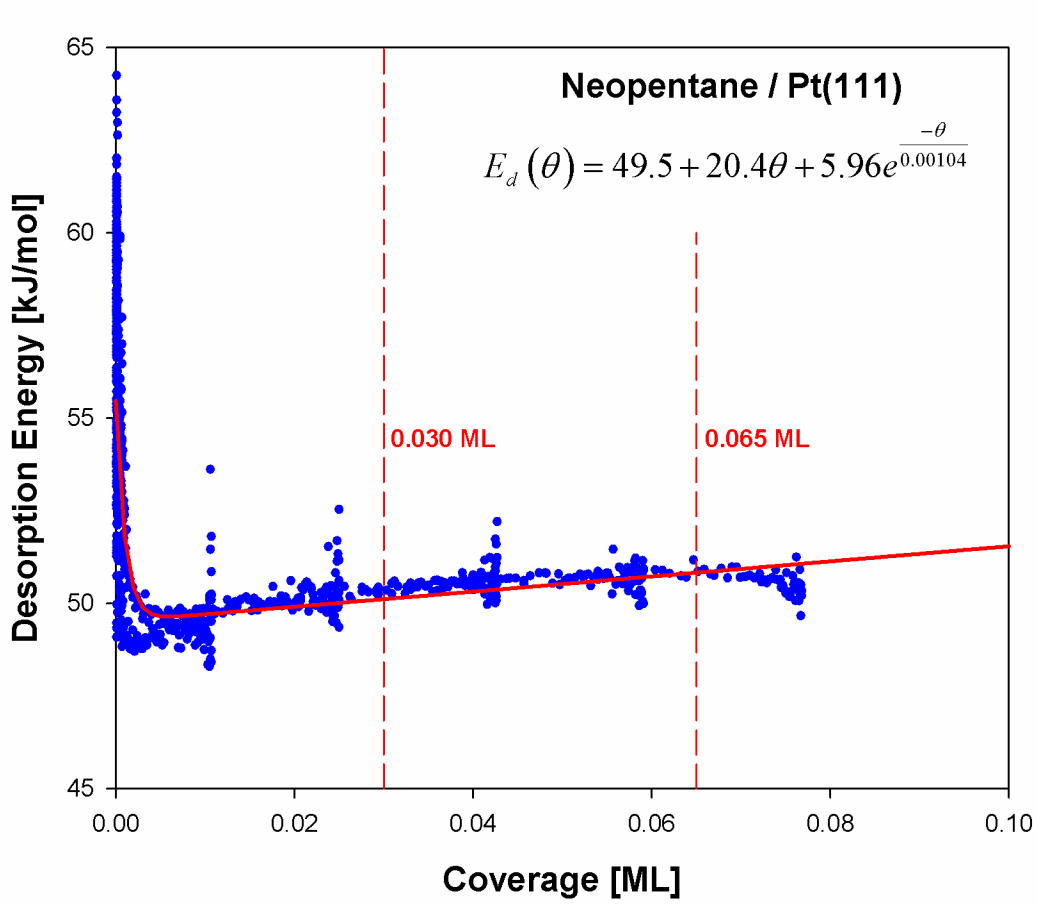

Figure 4.10: The coverage dependent desorption energy plot of neopentane on Pt(111); the solid red line is the least squares fit of the experimental data (blue dots) to the coverage dependent desorption energy model (Equation 3.25)

3.26). Figure 4.6 shows the experimental TPD with simulated spectra, calculated using the same initial molecular coverages as the experimental data.

The desorption energy for neopentane (50.6 ± 0.6 kJ/mol) is significantly lower than the value of 66.2 kJ/mol (24%) predicted by Campbell for pentane and is closer to the 53.5 kJ/mol (5.7%) prediction for butane.[2] The surface integrated Lennard Jones potential (Equation 1.5) predicts that neopentane should have a lower desorption energy than n-pentane, because of the geometry of neopentane. No matter the orientation, at least one methyl group will be far from the surface relative to the other methyl groups and will have negligible van der Waals interactions, giving neopentane a physisorption energy closer to butane than n-pentane. No experimental desorption pre-exponential factor has been measured for n-pentane, but Campbell estimated that it should be between 2.51 x 10^{15} and 1.58 x 10^{20} s-1, which is larger than both average ν_d = 6.10 x 10^{14} s^{-1} and maximum ν_d = 1.04 x 10^{15} s^{-1} reported by this study lies. However, it is similar to the ν_d = 5.01 x 10^{14} s^{-1} pre-exponential factor of n-butane.[2] Neopentane has a similar desorption energy and pre-exponential factor to n-butane and isobutane, which indicates that the desorption kinetics of neopentane on Pt(111) is more comparable to both n-butane and isobutane than n-pentane.

4.3 2,2,3,3-Tetramethylbutane (TMB)

4.3.1 Overview

TMB was found to reversibly desorb from the Pt(111) surface, such that the amount of carbon remaining on the surface after dosing a saturated monolayer of physisorbed molecules at 100 K and running a TPD experiment was indistinguishable from noise by AES spectra of the

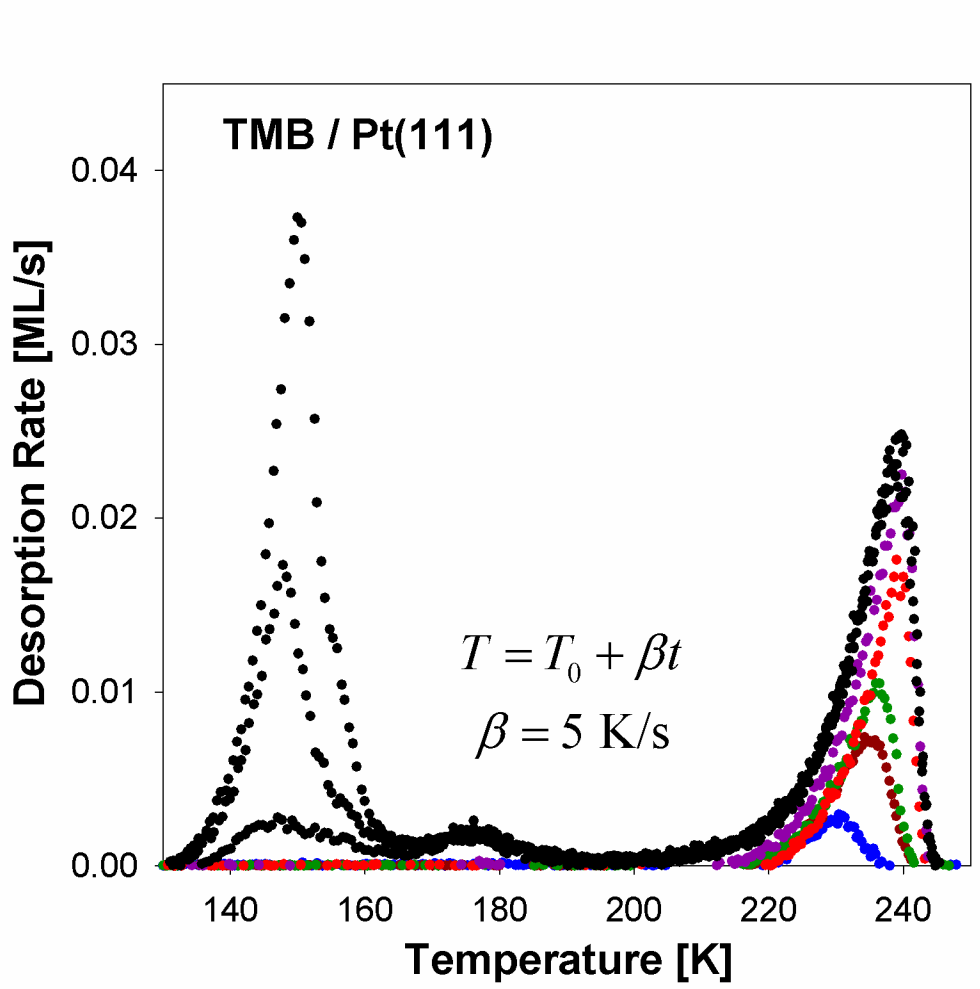

Figure 4.11: 2,2,3,3-tetramethylbutane on Pt(111) TPD spectra with monolayer molecular coverages of 0.00576, 0.0151, 0.0187, 0.0285, 0.0434 and 0.0557 ML with respect to Pt heated at 5 K/s; the sharp deformations of the multilayer peaks at 150 K are due to a nonlinear heating ramp below 160 K; the 5 K/s heating ramp stabilized by 160 K for all experiments; the multilayer peak at 175 K was determined to be molecular reorganization on the surface at low multilayer coverages

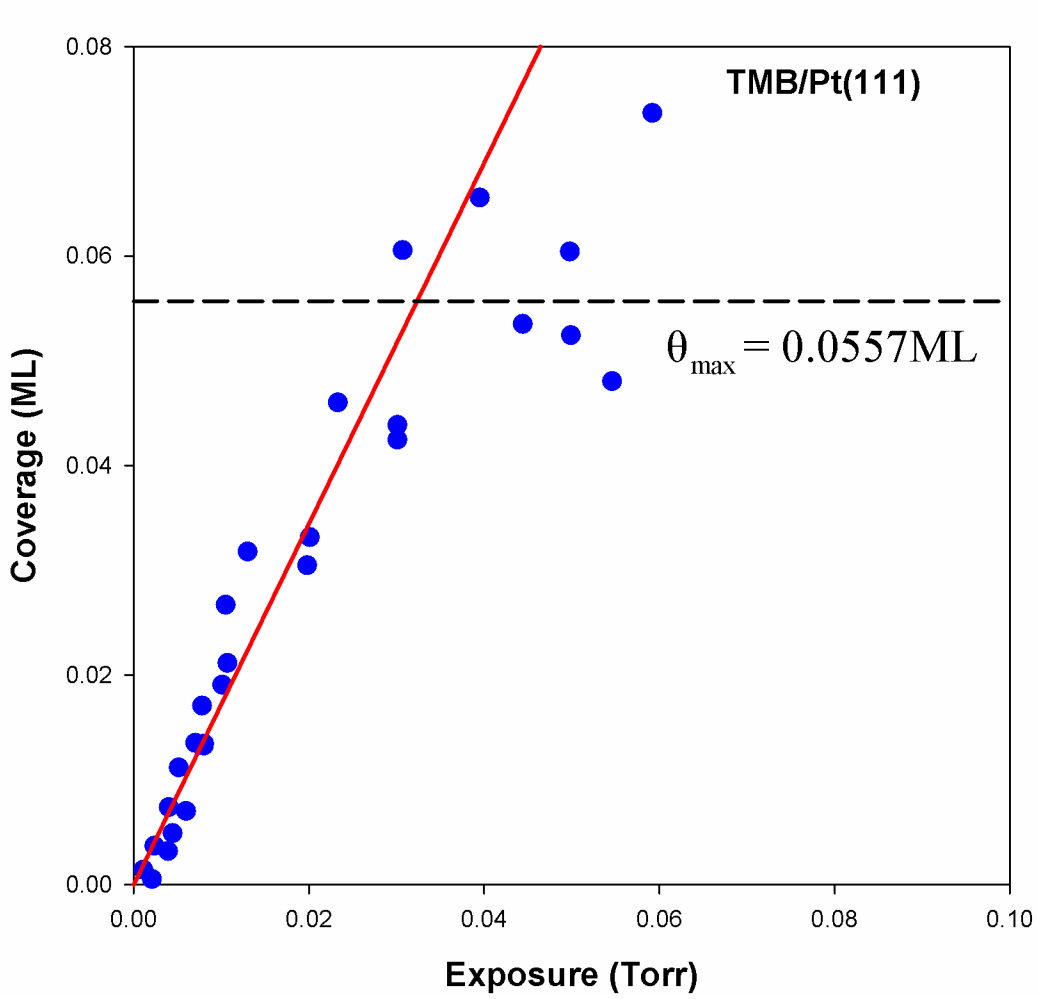

Figure 4.12: Monolayer molecular coverage, in ML with respect to the areal density of platinum, versus exposure plot of 2,2,3,3-tetramethylbutane on Pt(111), given by the trapped volume pressure in Torr; the red lines are linear least square fits to the data below the saturation limit and to the data at the plateau; the intersection of the two red lines was used to determine the saturation molecular coverage of the monolayer, indicated by the dashed black line at θ_{max} = 0.0557 ML.

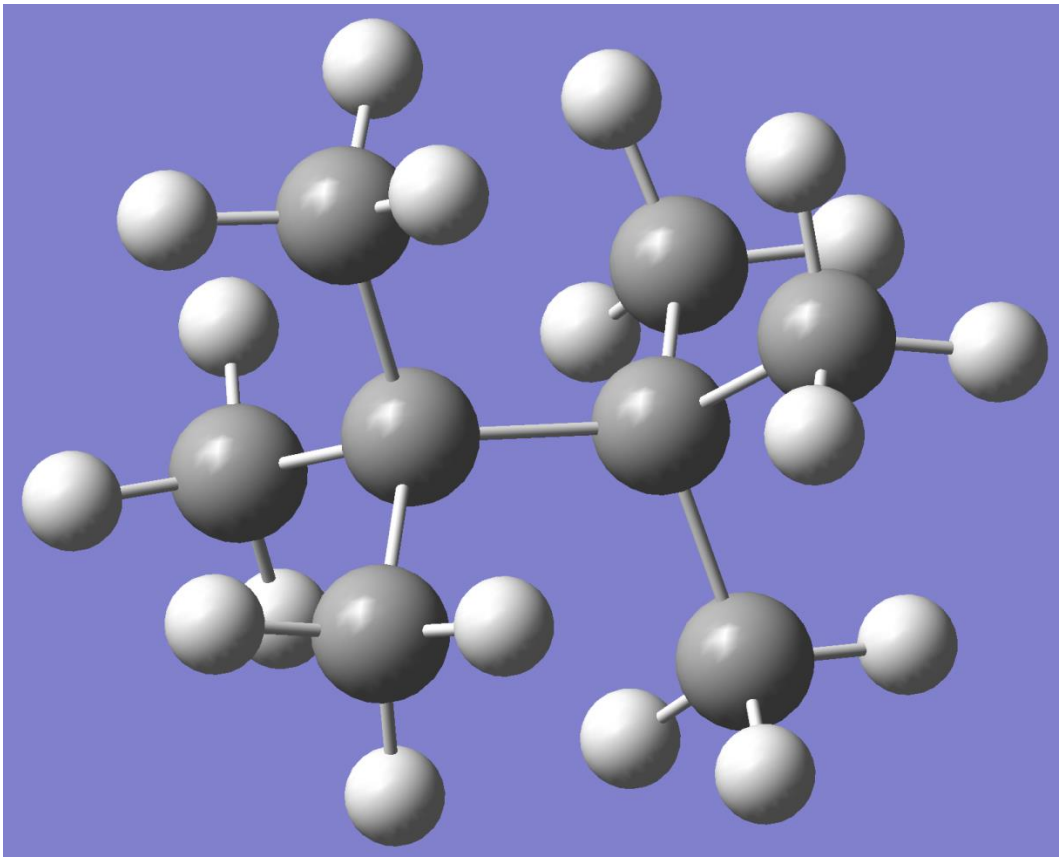

Figure 4.13: The optimized geometry of 2,2,3,3-tetramethylbutane (TMB) in the gas phase. The dark gray spheres are carbon atoms, and the smaller white spheres are hydrogen atoms. While TMB has a symmetry number of 6 (equivalent to ethane), due to the tetrahedral geometry and length of C-C bonds, TMB is semi-spherical (width $\simeq$ height $\simeq$ length $\simeq$ 4.5Å).

275 eV C KLL Auger peak. The surface temperature of maximum desorption rate (T_{peak}) shifted with respect to total molecular coverage, with T_{peak} = 230 K at a coverage of 0.103 θ_{max} (0.00576 ML, with respect the areal density of platinum), increasing to 238 K at a saturated monolayer, θ_{max} = 0.0557 ML (Figure 4.11). The molecular coverage of a saturated monolayer was measured by AES after dosing an exposure of 3.80 x 10^{-2} Torr from the trapped volume, which was determined to yield a saturated monolayer with no significant multilayer according to the coverage versus exposure plot (Figure 4.12). The monolayer coverage of exposures greater than 3.80 x 10^{-2} Torr from the trapped volume were not easily reproducible due to changes in the baseline between the multilayer peak at ~150 K and the leading edge of the monolayer peak between 210 and 220 K. In a similar manner to neopentane, the desorption energy of TMB is expected to change significantly depending on the orientation of the molecule with the surface. The monolayer coverage is assumed to be due to the lowest energy position of TMB with respect to the surface, where the central C-C bond between the two quaternary carbon atoms is parallel to the surface, such that only three methyl groups extend far from the surface, assuming a staggered conformation of the methyl groups according to the optimized geometry (Figure 4.13). The highest energy, and therefore lowest desorption energy, orientation of TMB with the surface has four carbon atoms near and four carbon atoms far from the surface, such that the central C-C bond between the two quaternary carbons is normal to the surface. While this relatively high energy orientation with the surface is not expected to occur in favor of the lower energy conformations under normal circumstances at 100 K, it may be forced upon a fraction of molecules in the saturated monolayer due to close proximity of other physisorbed molecules and limited packing space. The multilayer peak at 175 K, which is the T_{peak} of isobutane, n-butane, and neopentane, appeared after a saturated monolayer was formed but did not scale with

increasing exposure. It was determined that this peak and the rise in the baseline between 150 and 220 K was due to molecular reorganization on the surface at low multilayer coverages. The 175 peak may be attributed to the fraction of molecules in the monolayer forced into the highest energy configuration with respect to the surface. The 175 K may also indicate the formation of multilayer islands by Stranski-Krastanov growth when the multilayer coverage is small, which is expected when molecule-molecule van der Waals interactions are relatively strong. However, the presence of a multilayer peak, which did scale with exposure, at 150 K indicated that layer-by-layer growth was favored at large multilayer coverages. The abnormal shapes of the 150 K multilayer peaks in Figure 4.11 are due to a nonlinear heating ramp at temperatures below 160 K. The 5 K/s heating ramp stabilized by 160 K for every experiment, but was consistently nonlinear through the 150 K multilayer peak.

4.3.2 Desorption Pre-exponential Factor

The inversion analysis of TMB TPD spectra for calculating the desorption kinetic pre-exponential factor was first performed by combining the TPD data from all initial experimental molecular coverages and analyzing the combined data as a whole, as opposed to analyzing each TPD spectrum individually. Figure 4.14 shows the molecular coverage of TMB on the Pt(111) surface with respect to surface temperature as measured using a heating ramp of 5 K/s. It should be noted that the coverage versus temperature curves varied significantly with respect to the initial molecular coverage. The smallest initial coverages ($\theta_{max} < 0.5$) all fully desorbed just beyond 238 K, whereas the larger initial coverages ($\theta_{max} > 0.5$) did not fully desorb until about 243 K. The desorption energies, which will be discussed in more detail further in this section, varied by 5 kJ/mol from the smallest to the largest initial coverage, as shown in Figure 4.15

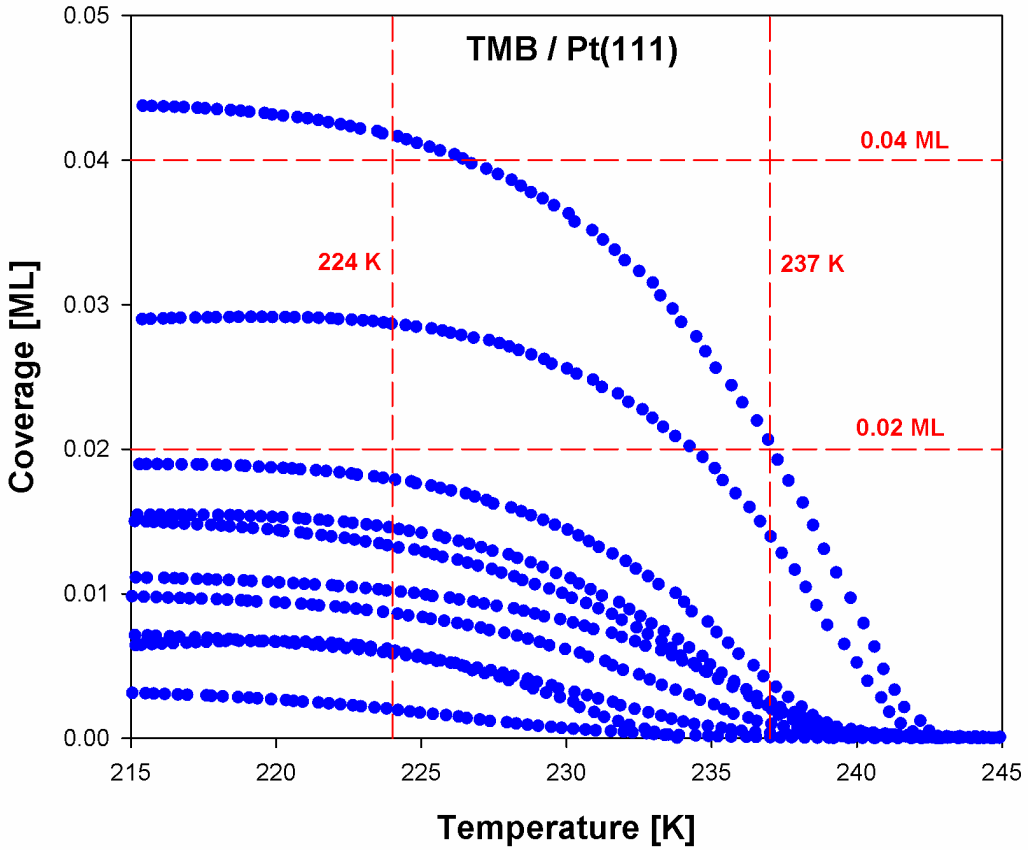

Figure 4.14: Total molecular coverage versus surface temperature plots of 2,2,3,3-tetramethylbutane (TMB) on Pt(111) for several initial coverages, heated at 5 K/s. The vertical dashed red lines indicate the surface temperature range boundaries through which TMB desorbs from the surface and the desorption energy is approximately constant for coverages between 0.4 θ_{max} and 0.7 θ_{max}, where θ_{max} = 0.0557 ML with respect to platinum

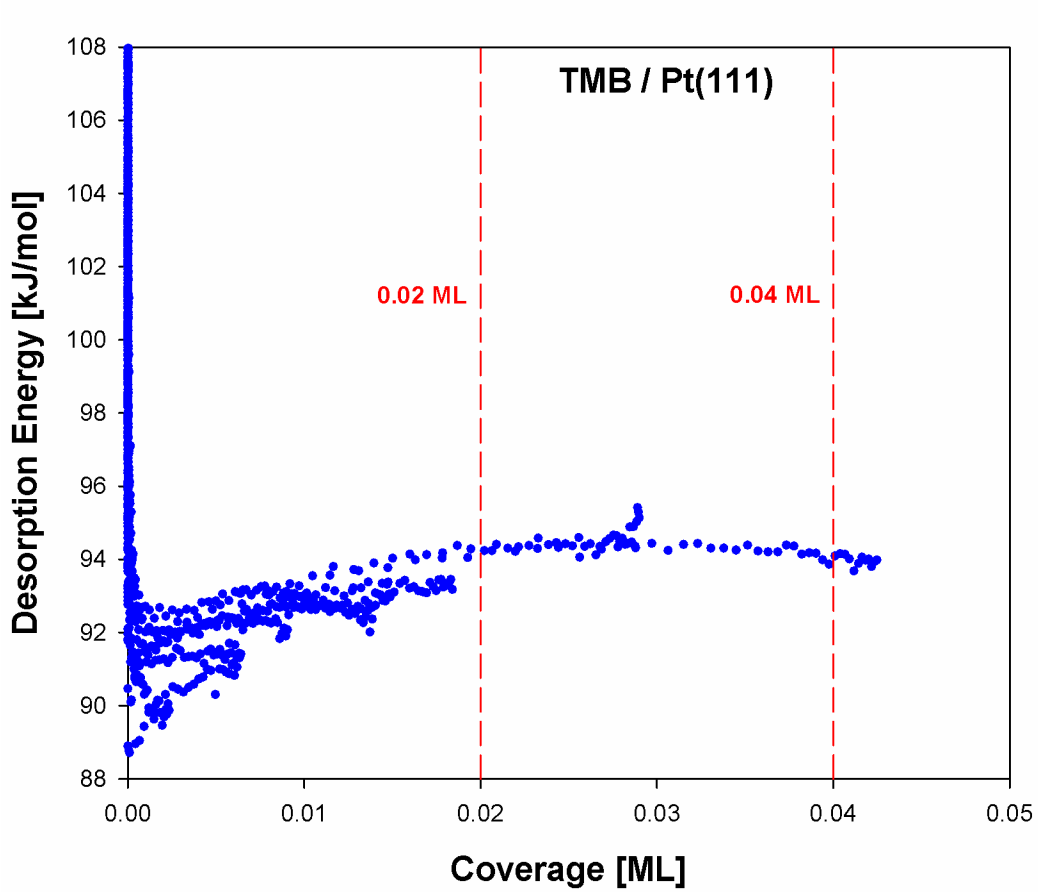

Figure 4.15: Experimental desorption of TMB on Pt(111) energies, assuming a pre-exponential factor of $\nu_d = 4.89 \times 10^{20}\ s^{-1}$, with respect to surface molecular coverage calculated from combined TPD spectra and using Equation 3.24

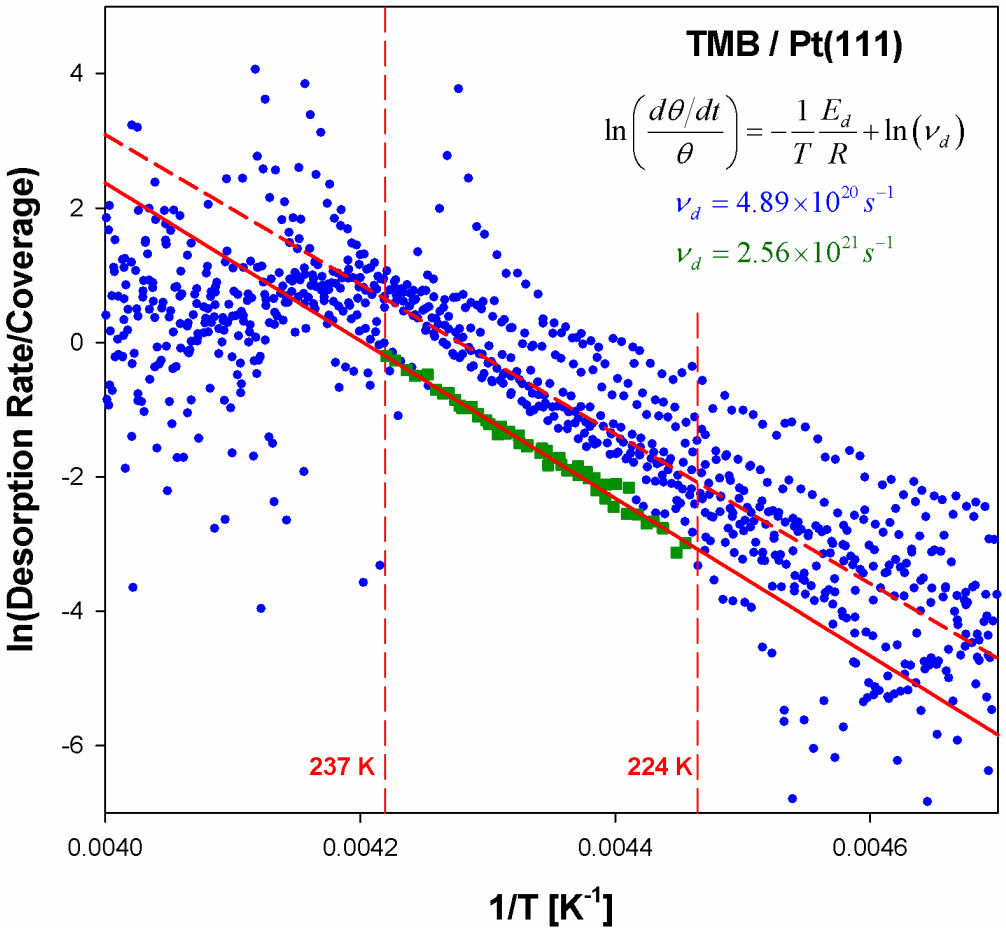

Figure 4.16: An inversion of all TPD spectra of 2,2,3,3-tetramethylbutane (TMB) on Pt(111) according to the inverted Polanyi-Wigner equation (Equation 3.23); the vertical dashed red lines mark the surface temperature region (224 to 237 K) through which the desorption energy of TMB was estimated to be constant for coverages between 0.4 θ_{max} and 0.7 θ_{max}; the solid red line is a linear least squares fit of only the 0.4 θ_{max} and 0.7 θ_{max} data (green squares) from 224 to 237 K, which yielded $\ln(\nu_d) = 49.3 \pm 0.9$; the dashed red line is a linear least squares fit of all data (blue dots) between 224 to 237 K, which yielded $\ln(\nu_d) = 47.6 \pm 1.7$

below. The coverage range through which the desorption energy varied the least was determined to be between 0.4 θ_{max} and 0.7 θ_{max}, which is larger than the initial coverages of a significant portion of the experimental TPD spectra. For the experimental data which had coverages between 0.4 θ_{max} and 0.7 θ_{max}, the temperature range was 224 to 237 K. A linear least squares fit of the inverted TMB data, which lay both between 224 and 237 K and between 0.4 θ_{max} and 0.7 θ_{max}, to the inverted Polanyi-Wigner equation (Equation 3.23) yielded a desorption pre-exponential factor of $\ln(\nu_d) = 49.3 \pm 0.9$, $\nu_d = 2.56 \times 10^{21}\ s^{-1}$, ranging from 1.04×10^{21} to $6.31 \times 10^{21}\ s^{-1}$ by error. Figure 4.16 below shows the fit along with the data (green squares) between 0.4 θ_{max} and 0.7 θ_{max} in comparison with all of the experimental data (blue dots). Unlike isobutane and neopentane, whose inverted TPD data was relatively tight packed in the linear range, TMB shows significant deviation in $\ln\left(\frac{d\theta/dt}{\theta}\right)$ with respect to molecular coverage. This indicates that $\ln(\nu_d)$ may vary significantly with coverage for TMB on Pt(111), and that the $\ln(\nu_d) = 49.3 \pm 0.9$ value reported above may only be representative of large molecular coverages.

In order to evaluate a pre-exponential factor which best represents all molecular coverages for TMB on Pt(111), the inversion analysis was repeated from 224 to 237 K was using all of the data, including data below 0.4 θ_{max}. The majority (90%) of the data from the combined spectra had coverages greater than 0.01 θ_{max} from 224 to 237 K, and a significant portion (60%) of the data in this temperature region had coverages above 0.1 θ_{max} (0.006 ML), where $E_D(\theta)$ varied the least. The temperature range from 224 to 237 K was kept for this analysis, as the inverted TPD data were linear through this range for the majority of spectra, with exception to the smallest initial coverages. It should be noted that if the inverted Polanyi-Wigner equation (Equation 3.23) is approximately linear through a temperature region, the desorption energy is constant through that region. However, the value of the desorption energy and pre-exponential

factor can change significantly if the slope of these linear regions varies among different initial coverages. A linear least squares fit of the inverted TMB combined spectra data, between 224 and 237 K, to the inverted Polanyi-Wigner equation yielded a desorption pre-exponential factor of $\ln(\nu_d) = 47.6 \pm 1.7$, $\nu_d = 4.89 \times 10^{20}\ s^{-1}$, ranging from 9.27×10^{19} to $2.57 \times 10^{21}\ s^{-1}$ due to uncertainty. The pre-exponential value calculated from all TPD data ($\ln(\nu_d) = 47.6 \pm 1.7$) and the value calculated from data between 0.4 θ_{max} and 0.7 θ_{max} ($\ln(\nu_d) = 49.3 \pm 0.9$) overlap in their upper and lower ranges of uncertainty, respectively. There are a few implications of this overlap. Most simply, both pre-exponential factors contain the true, constant desorption pre-exponential factor which represents all coverages for TMB on Pt(111), within their overlapping regions of error. However, if there is a coverage dependence of the pre-exponential factor, the value extracted from 0.4 θ_{max} and 0.7 θ_{max} data ($\ln(\nu_d) = 49.3 \pm 0.9$) best represents that range of coverage, and the value extracted from all data represents no single coverage, but may be viewed as an approximation of the average pre-exponential factor among all coverages. In future sections, the pre-exponential factor is assumed to be coverage dependent, and so $\ln(\nu_{d,avg}) = 47.6 \pm 1.7$, $\nu_{d,avg} = 4.89 \times 10^{20}\ s^{-1}$, will be defined as the average pre-exponential factor for future discussion. For clarity, the pre-exponential yielded between 0.4 θ_{max} and 0.7 θ_{max} will be defined as $\ln(\nu_{d,con}) = 49.3 \pm 0.9$, $\nu_{d,con} = 2.56 \times 10^{21}\ s^{-1}$, because it is the value derived from the portion of the E_D vs coverage plot where E_D is constant.

4.3.3 Coverage Dependent Pre-exponential Factor

Previous TPD experiments by this lab and Campbell[2] assumed that the pre-exponential factors for desorption of alkanes did not depend on the molecular coverage. This was not found to be the case for TMB. The inversion analysis was performed for each TMB TPD spectrum

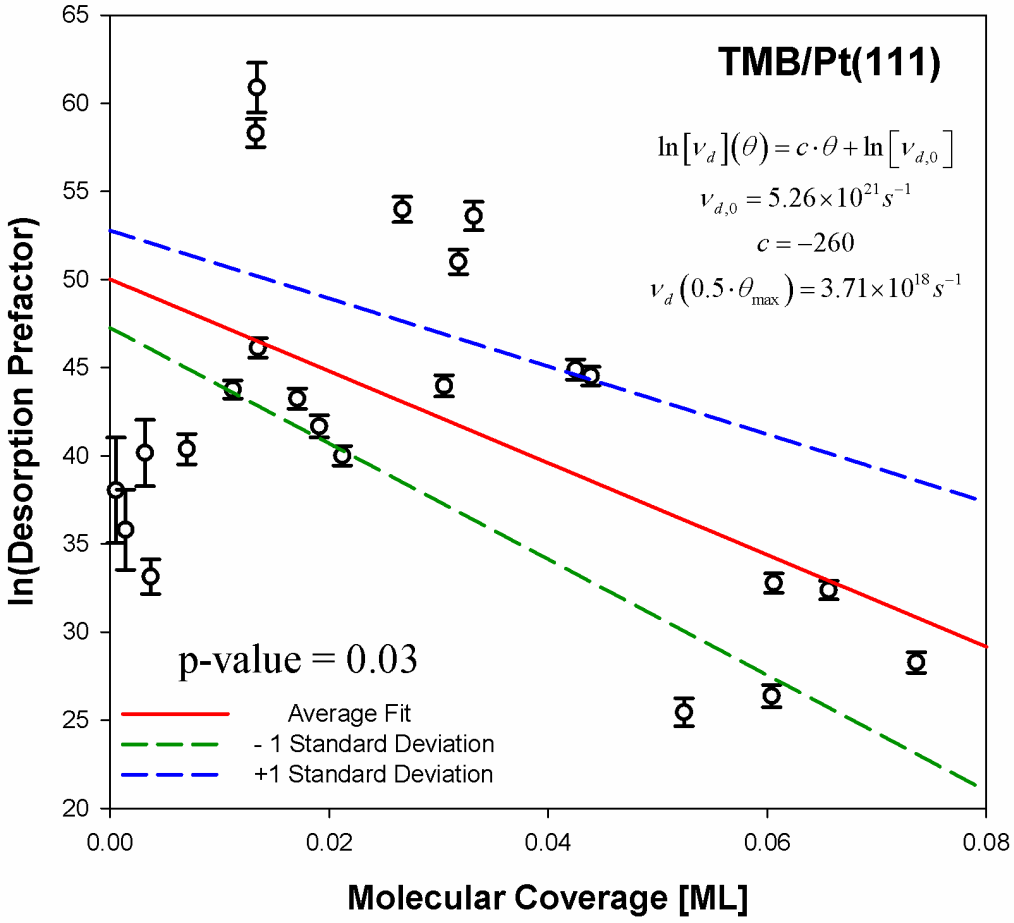

Figure 4.17: A plot of the coverage dependent desorption pre-exponential factors; $\ln(\nu_d)$, with error bars, (open dot) were calculated using the inversion optimization method for each individual TPD spectra; a weighted linear least squares fit (solid red line) is shown along with the upper (dashed blue line) and lower (dashed green line) bounds of the fit; the intercept was determined to be $\ln(\nu_{d,0}) = 50.0 \pm 2.8$, and the slope was $c = -260 \pm 70$

Table 4.1: The desorption pre-exponential factors and desorption energies with the lowest standard error for each TPD spectrum with initial coverages in ML with respect to the areal density of platinum, as determined from a linear least squares fit of each spectrum to the inverted Polanyi-Wigner equation between T_{min} and T_{max}

Coverage [ML]	$\ln(\nu_d)$	E_D [kJ/mol]	T_{min} [K]	T_{max} [K]
0.000528	38.0 ± 3.0	72.9 ± 5.6	214	239
0.001419	35.8 ± 2.3	68.2 ± 4.2	209	234
0.003191	40.2 ± 1.9	77.4 ± 3.5	212	238
0.003699	33.1 ± 1.0	63.2 ± 1.8	215	235
0.007023	40.4 ± 0.9	77.6 ± 1.6	209	238
0.0112	43.8 ± 0.5	84.1 ± 1.0	211	237
0.0133	58.3 ± 0.8	112 ± 1.5	222	235
0.0134	60.9 ± 1.4	117 ± 2.7	222	235
0.0135	46.1 ± 0.6	89.3 ± 1.0	216	239
0.0171	43.2 ± 0.6	84.5 ± 1.1	212	241
0.0191	41.7 ± 0.6	80.6 ± 1.2	211	238
0.0212	40.0 ± 0.6	78.2 ± 1.0	215	232
0.0267	54.0 ± 0.7	104 ± 1.4	222	236
0.0305	44.0 ± 0.6	85.2 ± 1.2	220	238
0.0318	51.0 ± 0.7	99.6 ± 1.3	221	235
0.0332	53.6 ± 0.8	106 ± 1.5	223	238
0.0425	44.9 ± 0.6	89.1 ± 1.1	221	237
0.0439	44.5 ± 0.5	88.2 ± 1.0	217	238
0.0524	25.5 ± 0.8	51.0 ± 1.5	209	238
0.0604	26.4 ± 0.6	53.5 ± 1.1	205	234
0.0606	32.8 ± 0.5	65.1 ± 1.0	214	235
0.0656	32.4 ± 0.5	64.9 ± 1.0	211	235
0.0736	28.3 ± 0.6	57.1 ± 1.1	213	232

individually. The temperature range chosen for each inverted spectrum was the range through which the inverted Polanyi-Wigner equation was linear and between which the linear least squares fit had the lowest standard error. Table 4.1 lists the temperature range, pre-exponential factor, and standard deviations for each TPD spectrum. A plot of the natural log of the pre-exponential factor versus coverage is shown in Figure 4.17. The desorption pre-exponential factors increased in value with respect to decreasing coverage with a p-value of 0.02, indicating a 98% confidence that the data are not equivalent in value. The coverage dependent pre-exponential factors ranged from $\ln(\nu_d) = 60.9 \pm 1.4$, 2.81×10^{26} s^{-1}, at a molecular coverage of 0.241 θ_{max} to $\ln(\nu_d) = 32.4 \pm 0.5$, 1.18×10^{14} s^{-1}, at θ_{max}. The desorption pre-exponential factors were found to correlate with molecular coverage as,

$$\nu_d(\theta) = \nu_{d,0} e^{-c\cdot\theta}$$
$$\ln\left(\nu_d(\theta)\right) = \ln\left(\nu_{d,0}\right) - c\cdot\theta \qquad \text{Equation 4.2}$$

where is $\nu_{d,0}$ the initial desorption pre-exponential factor at zero coverage and *c* is a constant. The error-weighted linear least squares fit of the pre-exponential data to Equation 4.2 yielded $\ln(\nu_{d,0}) = 50.0 \pm 2.8$ and $c = -260 \pm 70$. This correlation indicates that for every 0.001 ML of TMB adsorbed to the surface, $\ln(\nu_d)$ on average decreases by ~0.3, and ν_d decreases by ~26%. The upper and lower bounds of the fit are shown in Figure 4.17 as dashed lines. The initial desorption pre-exponential factor at zero coverage is $\nu_{d,0} = 5.26 \times 10^{21}$ s^{-1} and varies from 3.34×10^{20} to 8.28×10^{22} s^{-1} due to the range of uncertainty. It should be noted that $\ln(\nu_{d,0}) = 50.0 \pm 2.8$ is approximately equal to $\ln(\nu_{d,con}) = 49.3 \pm 0.9$, and that $\ln(\nu_{d,avg}) = 47.6 \pm 1.7$ falls within the range of uncertainty of $\ln(\nu_{d,0})$. However, the pre-exponential factors derived from initial coverages between 0.4 θ_{max} and 0.7 θ_{max} data are relatively large compared to other coverages (Figure 4.17) and skew $\ln(\nu_{d,0})$ to higher values, assuming a linear fit is appropriate for modeling

the coverage dependent pre-exponential factor. This indicates that $\nu_{d,con}$ does not well represent the pre-exponential at all coverages, despite being derived from the constant E_D coverage range in the desorption energy versus coverage plot (Figure 4.14) above. Because $\nu_{d,avg}$ is positioned at the lower range of uncertainty in the value of $\nu_{d,0}$, it is reasonable to assert $\nu_{d,avg}$ is the constant pre-exponential factor, of the choice between $\nu_{d,avg}$ and $\nu_{d,con}$, which best represents all coverages. The pre-exponential factor at a half saturated monolayer was determined to be $\ln[\nu_d(0.5\ \theta_{max})] = 42.8 \pm 4.6$, $\nu_d(0.5\ \theta_{max}) = 3.71 \times 10^{18}\ s^{-1}$, ranging from 3.56×10^{16} to $3.87 \times 10^{20}\ s^{-1}$ due to uncertainty. The pre-exponential factor derived from the inversion of all TPD spectra, $\ln(\nu_{d,avg}) = 47.6 \pm 1.7$, falls into the higher range of $\ln[\nu_d(0.5\ \theta_{max})] = 42.8 \pm 4.6$, indicating that $\ln(\nu_{d,avg})$ best represents coverages below $0.5\ \theta_{max}$, with exception to initial coverages which are near zero coverage. This is reasonable because the majority of experiments were performed with initial coverages between $0.1\ \theta_{max}$ and $0.5\ \theta_{max}$, indicating that an average value should best fit coverages within that range. When choosing between $\nu_{d,avg}$ and $\nu_d(0.5\ \theta_{max})$ as the constant pre-exponential factor for modeling the desorption energy and simulating TPD, it important to consider the propagation of errors. The value of $\nu_{d,avg}$ was obtained directly from a fit of all experimental TMB TPD data, and the reported error bars are the standard deviation in the certainty of the fit. The value of $\nu_{d,0}$ was calculated from an error-weighted linear least squares fit to a series of linear least squares fits to experimental data. The propagation of error from these two sequential fits is not trivial to ascertain and leaves the full extent of the uncertainty of $\nu_{d,0}$ ambiguous relative to $\nu_{d,avg}$. Without clear identification of the absolute range of uncertainty in $\nu_{d,0}$ and $\nu_d(0.5\ \theta_{max})$, the constant pre-exponential factor chosen for TMB for the purpose of modeling the coverage dependent desorption energy and simulating TPD was $\ln(\nu_{d,avg}) = 47.6 \pm$

1.7, $\nu_{d,avg}$ = 4.89 x 10^{20} s^{-1}, due to the known standard deviation and it being a representation of the majority of experimental TPD, which were measured between 0.1 θ_{max} and 0.5 θ_{max}.

Differences in desorption pre-exponential factors, given the same molecule and environment, are due to the relative change in entropy of the physisorbed molecules [i.e. $\nu_d = k_b T/h \cdot \exp(\Delta S/R)$]. Larger pre-exponential factors with decreasing molecular coverage indicates that the molecules have more entropy when fewer molecules are physisorbed. This indicates that molecule-molecule van der Waals interactions are significant enough to limit the range of motion of molecules near the surface as coverage increases. Transition state theory indicates that, for a similar set of reactions, a change in pre-exponential factor is proportional to the ratio of the entropy of the transition state to the initial state (i.e. $\nu_d = k_b T/h \cdot Q_{transition} / Q_{initial}$, where Q are the partition functions). As the desorption pre-exponential factor decreases with increasing coverage, the molecule-molecule van der Waals interactions cause an earlier transition state. An earlier transition state appears more similar to the initial state, would have a smaller difference in the relative entropy between the initial and the transition state, and therefore a smaller pre-exponential factor.

4.3.4 Unlimited Desorption Energy Scaling Model (Constant ν_d)

Using the average pre-exponential factor, $\nu_{d,avg}$ = 4.89 x 10^{20} s^{-1}, the experimental desorption energies were calculated at each point of coverage using Equation 3.24 using the desorption rates, coverages, and temperatures from the TPD spectra. A least squares fit of the desorption energies to Equation 3.25, shown by Figure 4.19, yielded values of a = 93.4 ± 0.2 kJ mol^{-1}, b = 35.5 ± 11.3 kJ mol^{-1} ML^{-1}, c = 1.41 ± 0.25 kJ mol^{-1}, and d = (6.43 ± 2.00) x 10^{-4} ML. The standard deviation according to Equation 4.1 is $E_D(\theta)$ ± 8.6 kJ/mol across all coverages, but

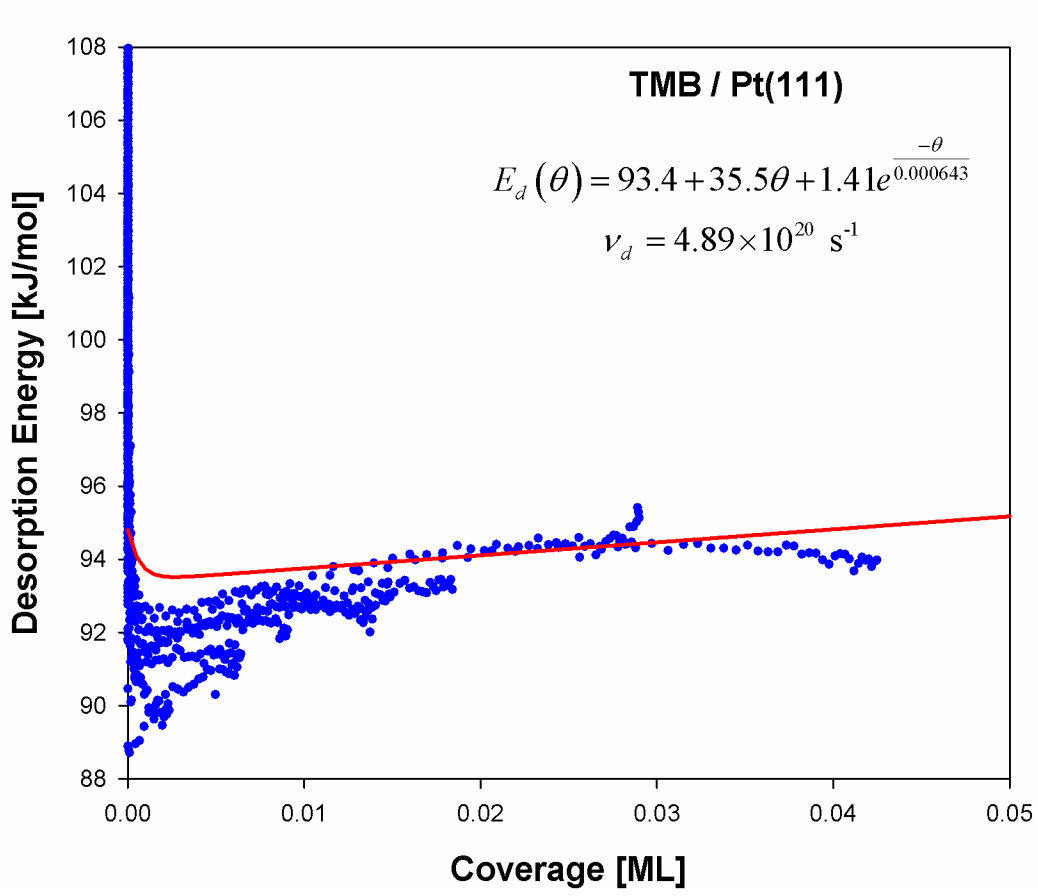

Figure 4.18: The coverage dependent desorption energy plot of 2,2,3,3-tetramethylbutane on Pt(111); the solid red line is the least squares fit of the experimental data (blue dots) to the coverage dependent desorption energy model (Equation 3.25)

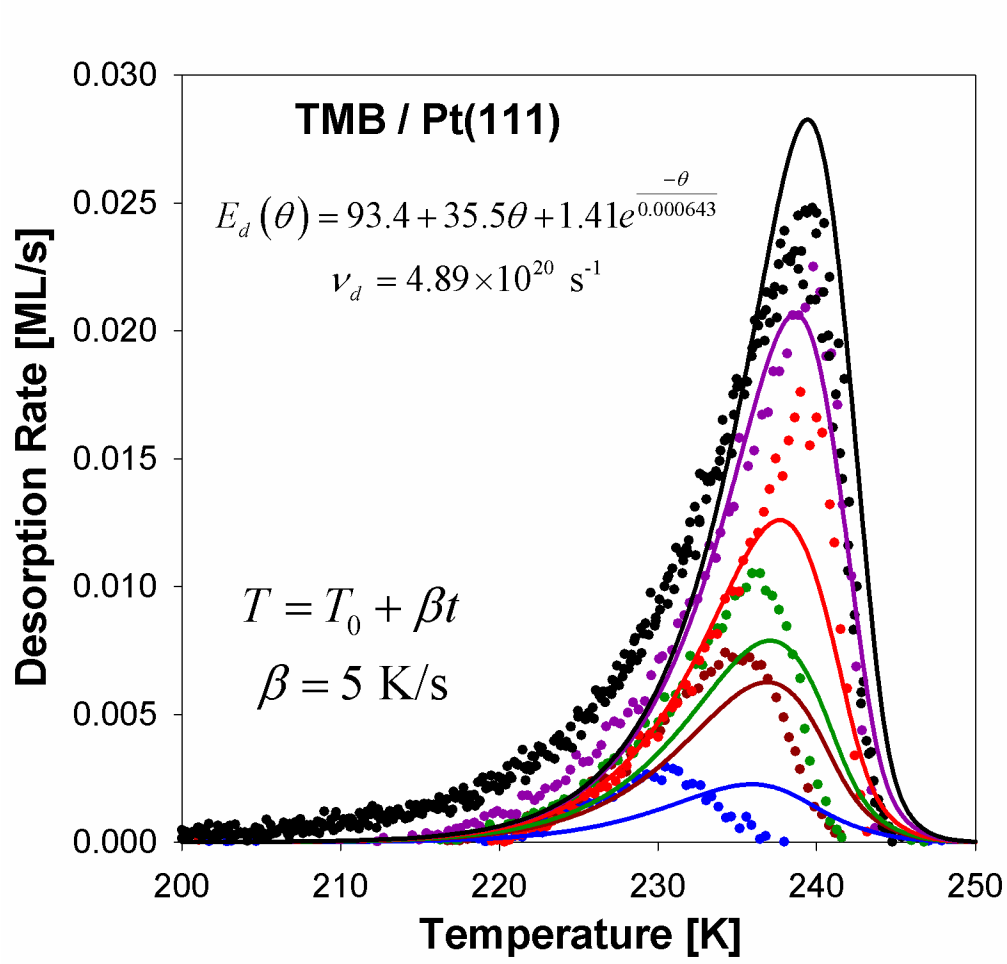

Figure 4.19: 2,2,3,3-tetramethylbutane on Pt(111) TPD spectra with coverages of 0.0058, 0.0151, 0.0187, 0.0285, 0.0434 and 0.0557 ML with respect to Pt heated at 5 K/s; the dots indicate experimental spectra, while the lines are the simulated TPD using the coverage dependent desorption energy parameters yielded from a fit to Equation 3.25

decreases to $E_D(\theta) \pm 4.8$ kJ/mol, $E_D(\theta) \pm 2.3$ kJ/mol and $E_D(\theta) \pm 2.3$ kJ/mol for coverages greater than 0.00001, 0.0001 and 0.001 ML, which are approximately 1/10x, 1x and 10x of the coverage of defect sites, respectively. Because the majority of TPD experiments had coverages significantly greater than 0.001 ML (0.02 θ_{max}), $\sigma_{fit} = \pm 2.3$ kJ/mol best represents the standard deviation of the experimental desorption energies. The desorption energy at a half saturated monolayer (0.5 θ_{max} = 0.0279 ML) was calculated to be 94.4 ± 2.3 kJ/mol. As shown by Figure 4.19, the simulated TPD calculated using the coverage dependent desorption energy model parameters did not overlap well with the experimental TPD. While the simulated TPD apparently fit the larger coverages well, the simulated TPD of smaller coverages were shifted significantly to a higher T_{peak}. In order to quantify the goodness of fit of the simulated TPD with respect to the experimental TPD, Equation 4.1 was used to determine the σ_{fit} of the temperature dependent desorption rates. Because desorption rates are small fractions of θ_{max}, the standard deviation is easier to view as a percentage of the maximum desorption rate, σ_{fit}/x_{max}, at each particular coverage. The percent standard deviation was calculated for each simulated TPD spectrum at each coverage, which were 29.5%, 14.5%, 11.9%, 8.0%, 4.7%, and 10.2% for molecular coverages of 0.103, 0.271, 0.336, 0.512, 0.779, and 1.00 θ_{max}, respectively.

One of the major causes of the deviation for the simulated TPD from the experimental TPD is the overestimation of E_D at low coverages and the constant scaling of the desorption energy with respect to coverage. For the value of *a*, $E_{D,0}$, to decrease and fit the lowest coverages (ca. 0.103 θ_{max}), the value of *b* would have to increase to match the shape of the desorption energy versus coverage curve of Figure 4.19. However, the coverage scaling with respect to *b* is constant to an infinite coverage, and cannot replicate the plateauing nature of the curve. Desorption energies at coverages greater than 0.04 ML (0.7 θ_{max}) decrease significantly, which

this coverage dependent desorption energy model cannot account for. For this reason, the TPD for θ_{max} cannot be well simulated without simultaneously poorly simulating all other coverages using this model. The major difficulty of fitting the coverage dependent desorption energy of TMB to Equation 3.25 can be seen in Figure 4.19. Initially, at very lower coverages, the strong molecule-molecule interactions of TMB significantly increased the desorption energy as coverage increased. However, the reduced pre-exponential factor at high coverages caused the coverage dependent desorption energy to plateau and slightly decrease as the monolayer coverage approached a saturated molecular coverage.

4.3.5 Limited Coverage Dependent Desorption Energy Scaling Model (Constant νd)

In order to account for the plateauing of the coverage dependent desorption energy without adding the extra layer of complexity of a coverage depending pre-exponential factor, Equation 3.25 was adjusted to account for the deficits of strong molecule-molecule interactions on the desorption energy at high coverages.

$$E_D(\theta) = a + be^{\frac{-\theta}{c}} + d\theta e^{\frac{-\theta}{f}} \qquad \text{Equation 4.3}$$

where *a* is the coverage independent desorption energy on the lattice, *b* is the increased desorption energy from defect sites which falls off relative to *c*, and *d* is the increased desorption energy caused by molecule-molecule van der Waals interactions which fall off relative to *f*.

A least squares fit of the experimental TMB on Pt(111) coverage dependent desorption energies to Equation 4.3 yielded a = 92.2 ± 2.4 kJ mol^{-1}, b = 15.5 ± 2.3 kJ mol^{-1}, c = (1.63 ± 0.07) x 10^{-4} ML, d = 150 ± 615 kJ mol^{-1} ML^{-1}, and f = 0.043 ± 0.248 ML for TMB, as shown in Figure 4.20. It should be noted that the large uncertainty in *d* and *f* are primarily due to the large standard deviation in the experimental desorption energies at extremely low coverage. In order to

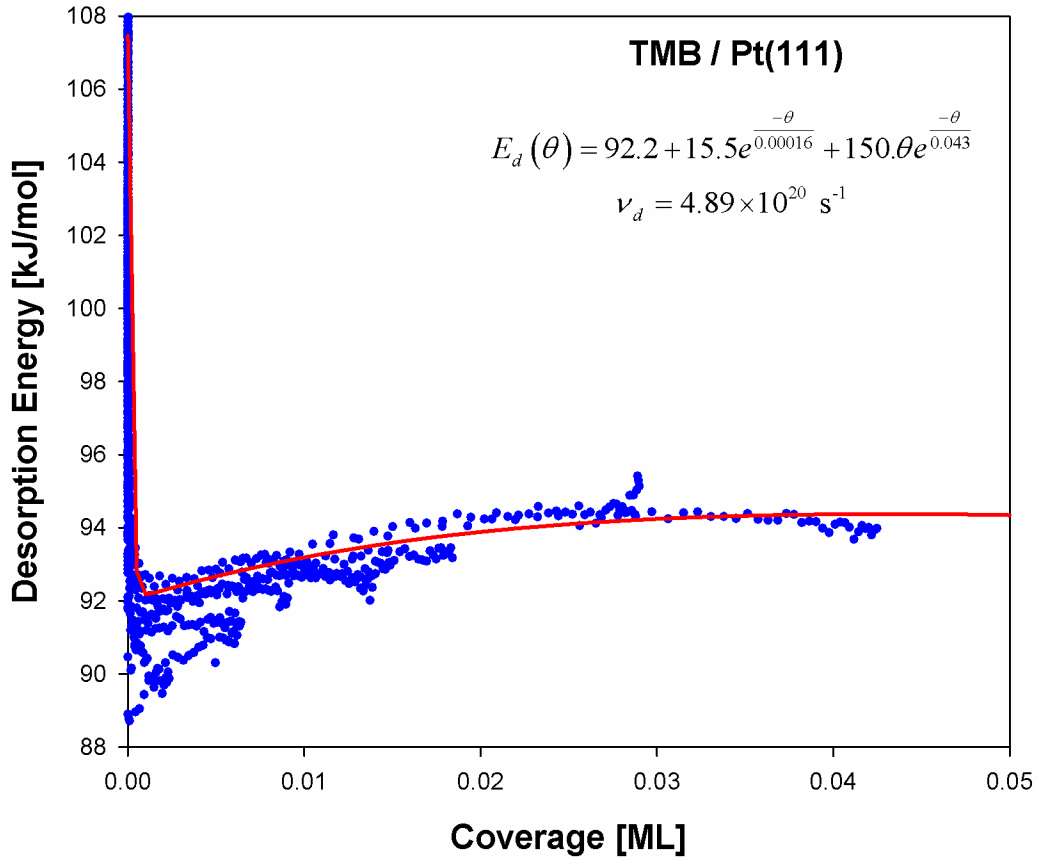

Figure 4.20: The coverage dependent desorption energy plot of 2,2,3,3-tetramethylbutane on Pt(111); the solid red line is the least squares fit of the experimental data (blue dots) to Equation 4.3

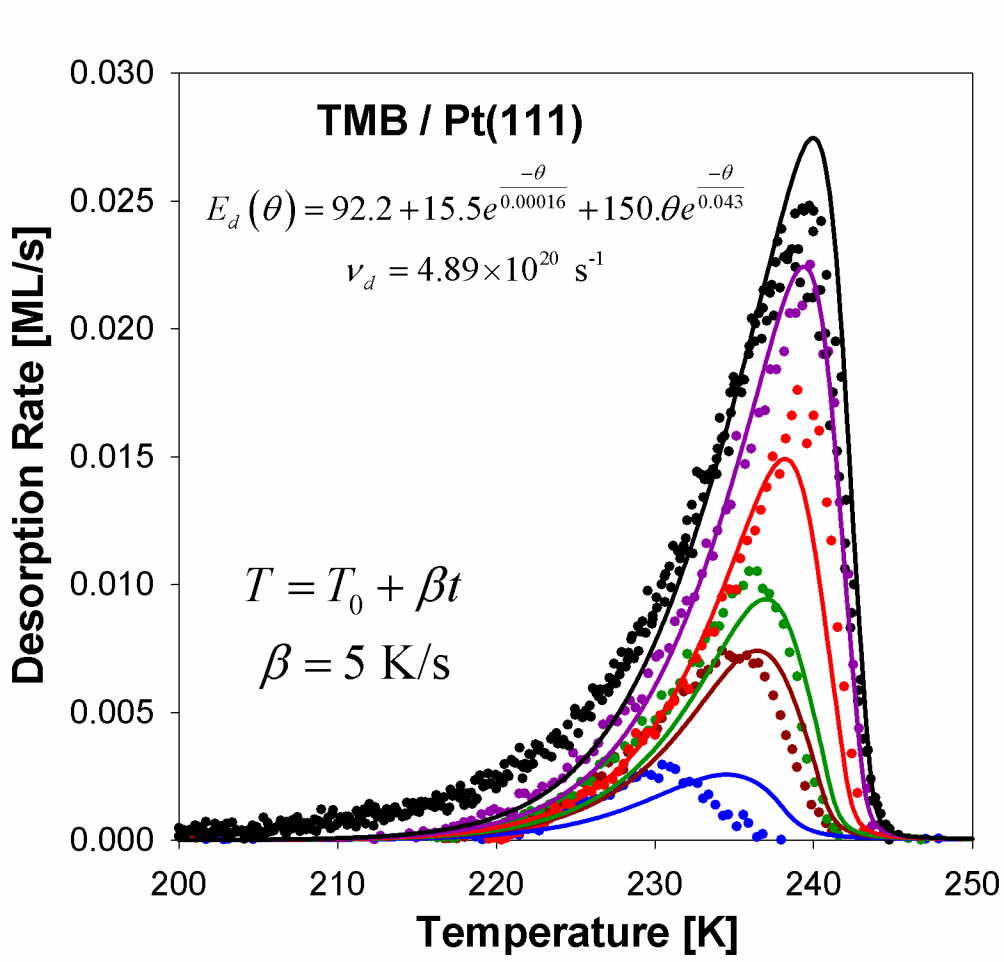

Figure 4.21: 2,2,3,3-tetramethylbutane on Pt(111) TPD spectra with coverages of 0.0058, 0.0151, 0.0187, 0.0285, 0.0434 and 0.0557 ML with respect to Pt heated at 5 K/s; the dots indicate experimental spectra, while the lines are the simulated TPD using the coverage dependent desorption energy parameters yielded from a fit to Equation 4.3

get a better picture of how the standard deviation changes with respect to coverage, σ_{fit} was calculated for the limited-scaling coverage dependent desorption energy model with respect to the experimental data across different coverage ranges. The standard deviation is $E_D(\theta) \pm 28.7$ kJ/mol across all coverages, but decreases to $E_D(\theta) \pm 3.9$ kJ/mol, $E_D(\theta) \pm 2.1$ kJ/mol and $E_D(\theta) \pm 1.9$ kJ/mol for coverages greater than 0.00001, 0.0001 and 0.001 ML, which are approximately 1/10x, 1x and 10x of the coverage of defect sites, respectively. Because the majority of TPD spectra had initial molecular coverages significantly greater than 0.001 ML (0.02 θ_{max}), the standard deviation of $E_D(\theta) \pm 1.9$ kJ/mol well represents the uncertainty of $E_D(\theta)$ for all coverages significantly larger than the number of defect sites. The desorption energy was determined to be 94.4 ± 1.9 kJ/mol at a half saturated monolayer of coverage ($0.5\ \theta_{max} = 0.0279$ ML). Figure 4.21 shows monolayer TPD spectra of TMB on Pt(111) with the simulated TPD calculated using Equation 3.26 with the fits to Equation 4.3 above.

The simulated TPD spectra using the fit to Equation 4.3 better matched the experimental TPD but still could not well reproduce the TPD spectra of the lowest coverages. The percent standard deviations, σ_{line}/x_{max}, were calculated for simulated TPD spectra at each coverage, where x_{max} is the maximum measured desorption rate of the experimental TPD spectrum. The simulated TPD generated from the fit to Equation 4.3 yielded percent standard deviations of 22.4%, 8.9%, 7.0%, 7.3%, 2.8%, and 6.5% for molecular coverages of 0.103, 0.271, 0.336, 0.512, 0.779, and 1.00 θ_{max}, respectively.

The percent standard deviations of the simulated TPD from the experimental TPD allow for simple comparison between the unlimited-scaling and limited-scaling coverage dependent desorption energy models. The average percent uncertainty using the parameters derived from the limited-scaling model (9.2%) was lower than the average percent uncertainty from the

unlimited-scaling model (13.2%). The simulated TPD calculated using the limited-scaling model universally fit the experimental TPD at every coverage better than the simulated TPD calculated from the unlimited-scaling model. However, neither model was able to simulate TPD well for the smallest or largest molecular coverages.

4.3.6 Coverage Dependent Desorption Energy and Pre-exponential Factor Model

In order to evaluate the impact of the coverage dependent desorption kinetic rate pre-exponential factor on the coverage dependent desorption energy and simulated TPD spectra, the experimentally measured desorption energies, $E_D(\theta)$, were calculated using $\nu_d(\theta)$ (Equation 4.1) at each point in coverage. In the case were the desorption pre-exponential factor decreases with increasing molecular coverage, the desorption energy was also found to decrease with increasing coverage (Figure 4.22). The desorption energy, according to the Polanyi-Wigner equation (Equation 3.24), scales by both the molecular coverage and the desorption pre-exponential factor. However, because the pre-exponential factor is orders of magnitude larger than the coverage, a small change in $\ln(\nu_d)$ has a more significant impact on E_D than a change in the molecular coverage. A least squares fit of the unlimited-scaling model (Equation 3.25) to the desorption energy yielded a = 98.0 ± 0.2 kJ mol^{-1}, b = -475. ± 13 kJ mol^{-1} ML^{-1}, c = 0.389 ± 0.286 kJ mol^{-1}, and d = (6.6 ± 8.7) x 10^{-4} ML. The negative value of *b* indicates that the reduction in entropy, associated with the decrease in pre-exponential factor, plays a more significant role in decreasing the desorption energy than increased molecule-molecule van der Waals interactions do to increase the desorption energy at large coverages.

In order to get a better picture of how the standard deviation changes with respect to coverage, σ_{fit} was calculated across different coverage ranges. The standard deviation is $E_D(\theta)$ ±

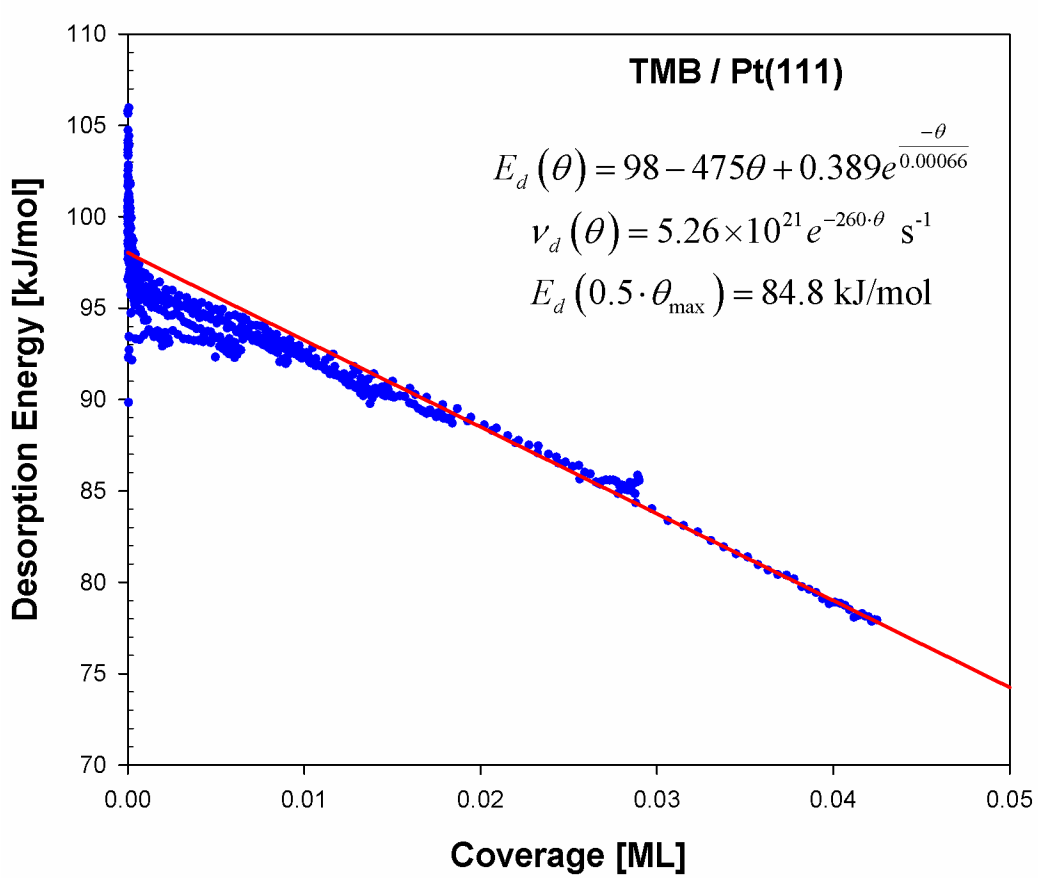

Figure 4.22: The coverage dependent desorption energy, which was calculated using the coverage dependent desorption pre-exponential factor (Equation 4.2), plot of 2,2,3,3-tetramethylbutane on Pt(111); the solid red line is the least squares fit of the experimental data (blue dots) to Equation 3.25

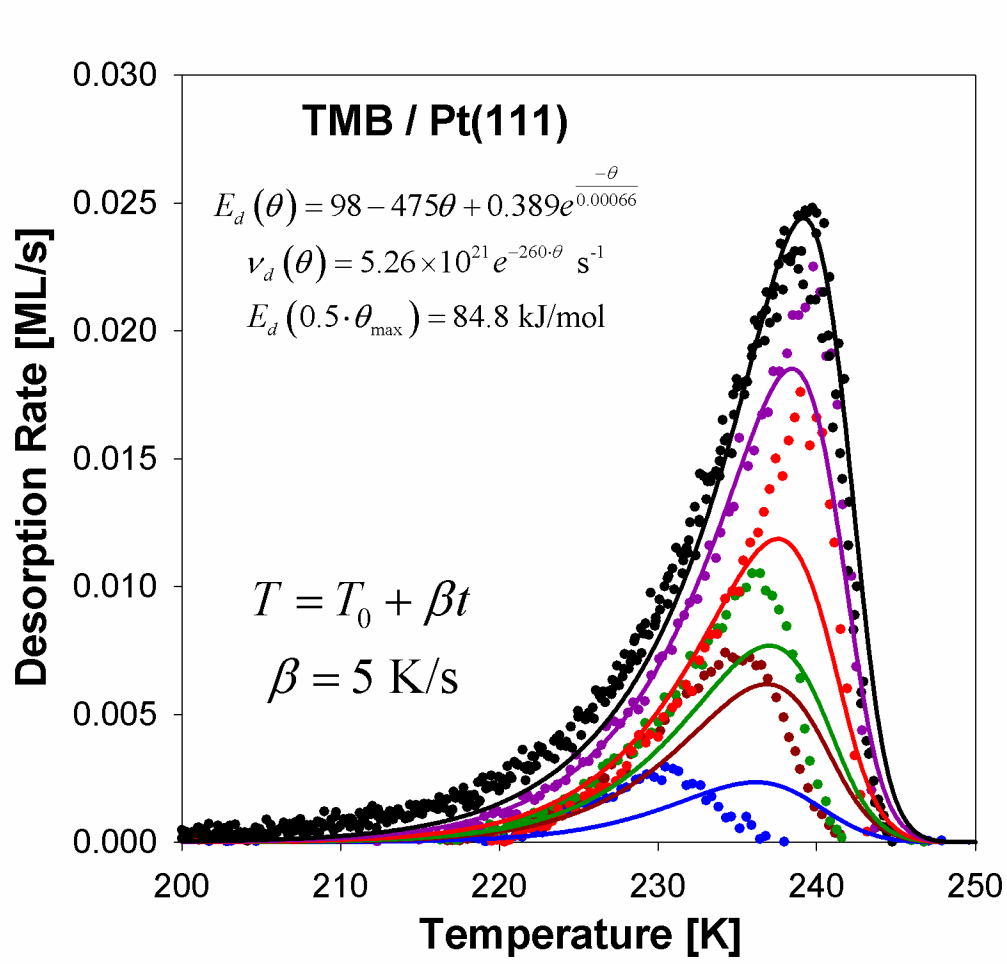

Figure 4.23: 2,2,3,3-tetramethylbutane on Pt(111) TPD spectra with coverages of 0.0058, 0.0151, 0.0187, 0.0285, 0.0434 and 0.0557 ML with respect to Pt heated at 5 K/s; the dots indicate experimental spectra, while the lines are the simulated TPD using a fit of the coverage dependent desorption energies, calculated using the coverage dependent desorption pre-exponential factor (Equation 4.2), to Equation 3.25

9.7 kJ/mol across all coverages, but decreases to $E_D(\theta) \pm 5.3$ kJ/mol, $E_D(\theta) \pm 2.3$ kJ/mol and $E_D(\theta) \pm 2.3$ kJ/mol for coverages greater than 0.00001, 0.0001 and 0.001 ML, which are approximately 1/10x, 1x and 10x of the coverage of defect sites, respectively. Because the majority of TPD spectra had initial molecular coverages significantly greater than 0.001 ML ($0.02\ \theta_{max}$), the standard deviation of $E_D(\theta) \pm 2.1$ kJ/mol well represents the uncertainty of $E_D(\theta)$ for all coverages significantly larger than the number of defect sites. The desorption energy at a half saturated monolayer of coverage ($0.5\ \theta_{max} = 0.0279$ ML) was determined to be 84.8 ± 2.3 kJ/mol.

Simulated TPD spectra for TMB on Pt(111) assuming a coverage dependent pre-exponential factor are shown in Figure 4.23. Similar to the previous simulations using a constant desorption pre-exponential factor, the simulated TPD spectra best fit larger coverages and poorly reproduced smaller coverages. The percent standard deviation (σ_{fit}/x_{max}) of the fit were 30.3%, 14.1%, 11.6%, 9.3%, 5.3%, and 5.0% for molecular coverages of 0.103, 0.271, 0.336, 0.512, 0.779, and 1.00 θ_{max}, respectively. The average percent uncertainty (12.6%) of the coverage dependent pre-exponential factor model was better than the 13.2% of the unlimited-scaling model but worse than the 9.2% of the limited-scaling model. The limiting term $\exp(-\theta/f)$ of the limited-scaling model accounted for the decrease in desorption energy at high coverage better than the coverage dependent pre-exponential factor. Because of this, the limited-scaling model produced simulated TPD which fit all coverages with less deviation than either the unlimited-scaling model or the coverage dependent pre-exponential factor model.

It should be noted that fitting both the desorption energy and pre-exponential factor to coverage introduces an additional layer of error in this analysis when compared to simply assuming a constant desorption pre-exponential factor. The uncertainty in the measurements of

the pre-exponential factors, propagates with the uncertainty in the fit of $\ln(\nu_d)$ to molecular coverage (Equation 4.2). When the coverage dependent pre-exponential factor is used both for calculating the desorption energies as well as simulating TPD, it is expected for there to be a significantly larger standard deviation than reported here. The non-trivial calculation of the propagation of error through several model fits is beyond the scope of this study. The simpler, limited-scaling coverage dependent desorption energy model (Equation 4.3) well compensates for decreasing desorption energy values at high coverage due to a reduction in entropy. The coverage dependent pre-exponential factor model, which adds extra complexity through more parameters and propagation of standard deviation, is unideal for calculating accurate desorption energies and simulating TPD.

4.3.7 Summary

Three models were used to calculate the desorption energy of 2,2,3,3-tetramethylbutane (TMB) on Pt(111). The model which was used for both isobutane and neopentane (Equation 3.25) assumes that any increase (due to favorable molecule-molecule interactions) or decrease (due to unfavorable molecule-molecule interactions) in desorption energy with respect to molecular coverage remains constant up to a saturated monolayer. This is reasonable when the pre-exponential factor is also constant. However, TMB was found to have a coverage dependent desorption pre-exponential factor which causes the desorption energy to increase significantly at coverages less than $0.5\ \theta_{max}$, before plateauing and decreasing as molecular coverages approach θ_{max}. In the case of TMB, the unlimited scaling with respect to coverage of Equation 3.25 is inadequate for modeling TMB data. For this reason, a limiting term of $\exp(-\theta/f)$ was multiplied by the coverage dependent term in Equation 3.25 to form a limited-scaling coverage dependent

desorption energy model (Equation 4.3). The fits to the limited-scaling model matched better with experimental data than the fits to the unlimited-scaling model, regardless of whether or not a constant or coverage dependent pre-exponential factor was used. The model which combined the unlimited-scaling model and the coverage dependent pre-exponential factor not only fit experimental data worse than the limited-scaling model, but had ambiguous uncertainty due to complexity and the propagation of errors across multiple least squares fits. For this reason, the simple limited-scaling model was determined to yield parameters which best represented the true coverage dependent desorption energies for TMB on Pt(111). Table 4.2 shows the desorption energies calculated at $0.5\ \theta_{max}$ for all three models, as well as the pre-exponential factors and average percent standard deviations of simulated TPD.

The desorption energy of TMB/Pt(111), as calculated using Equation 4.3 (94.4 ± 1.9 kJ/mol), is less than that of octane, which can be attributed to the geometry of TMB. No matter the orientation of the molecule, at least two methyl groups must be further from the surface than any other group, reducing their van der Waals interactions significantly, according to the $1/r^3$ distance relation of the attractive element of the surface integrated Lennard Jones potential.[3-4] For this reason, it may be more reasonable to compare TMB to n-heptane or even n-hexane than n-octane when it comes to desorption from Pt(111). There have been no TPD experiments done for either n-octane or n-heptane on Pt(111) which yielded desorption rate constants for an apt comparison. Campbell predicted that the desorption pre-exponential factors should be between 7.94×10^{15} and $6.31 \times 10^{21}\ s^{-1}$ for n-octane and 5.01×10^{15} and $2.51 \times 10^{21}\ s^{-1}$ for n-heptane.[2] The calculated desorption pre-exponential factors for TMB, $\nu_{d,0} = 4.69 \times 10^{21}\ s^{-1}$ from Equation 3.2 and $\nu_{d,avg} = 4.89 \times 10^{20}\ s^{-1}$ from Figure 4.16, are within the ranges of n-octane, with $\nu_{d,avg}$ also being within the range of n-heptane. Campbell also predicted that the desorption energies for n-

heptane and n-octane should be approximately 91.6 and 104 kJ/mol, respectively. The 94.4 ± 1.9 kJ/mol desorption energy of TMB matches well with the prediction for n-heptane. From these data, the desorption kinetics are affected by the branched geometry of TMB, in a similar manner to neopentane behaving like n-butane and isobutane, and functions less like its isomer n-octane and more like n-heptane when physisorbed on Pt(111).

Table 4.2: A list of the desorption pre-exponential factors, desorption energies at a half saturated monolayer, and percent deviations of simulated TPD with respect to experimental TPD for three coverage dependent desorption energy models: unlimited coverage scaling with a constant pre-exponential factor, unlimited coverage scaling with a coverage-dependent pre-exponential factor, and limited coverage scaling with a constant pre-exponential factor.

Coverage Scaling	**ν_d [s^{-1}]**	**$E_D(0.5\ \theta_{max})$ [kJ/mol]**	**Simulated TPD Percent Deviation**
Unlimited	4.89×10^{20}	94.4 ± 2.3	13.2%
Unlimited	$\nu_d(0.5\ \theta_{max}) = 3.71 \times 10^{18}$	84.8 ± 2.3	12.6%
Limited	4.89×10^{20}	94.4 ± 1.9	9.2%

Table 4.3: A list of the desorption energies and pre-exponential factors for isobutane, neopentane, and TMB.

Alkane	**$E_D(0.5\ \theta_{max})$ [kJ/mol]**	**$Log_{10}(\nu_d)$**
Isobutane	50.2 ± 0.2	14.6 ± 0.1
Neopentane	50.6 ± 0.6	14.7 ± 0.2
TMB	94.4 ± 1.9	20.7 ± 0.7

4.4 Summary of Branched Alkanes

The desorption energies of isobutane, neopentane, and 2,2,3,3-tetramethylbutane (TMB) were determined to be 51.6 ± 0.2, 53.5 ± 0.6, and 94.4 ± 1.9, respectively, at a half monolayer of coverage. As the size of the alkane increased, the desorption energy increased. This was expected, as the increased number of electrons in the molecules causes them to be more polarizable, and therefore have stronger van der Waals interactions with other molecules and the surface. The coverage dependence of $E_D(\theta)$ also increases with the larger alkanes, where both neopentane and TMB had a small range of coverage where $E_D(\theta)$ remained constant relative to isobutane. The desorption pre-exponential factors also increased with alkane size. The pre-exponential factors of isobutane, neopentane, and TMB were determined to be $\log_{10}(\nu_d) = 14.6 \pm 0.1$, 14.7 ± 0.2, and 20.7 ± 0.7, respectively. These values indicate that larger molecules, with more degrees of freedom, have more entropy in the desorption transition state relative to the physisorbed state than smaller molecules. In general, the desorption rate constants measured for branched alkanes in this study follow similar trends of linear alkanes, as reported by Campbell, where both E_D and ν_d increase in proportion with alkane chain length.[2] However, both TMB and neopentane have lower E_D and ν_d than their n-alkane isomer, because of their branched geometry and different van der Waals attraction to the surface that falls off as $1/z^3$. Table 4.3 below lists the desorption energies and pre-exponential factors for the branched alkanes.

References

1. Xu, C.; Koel, B. E.; Paffett, M. T., Adsorption and Desorption Behavior of N-Butane and Isobutane on Pt(111) and Sn/Pt(111) Surface Alloys. *Langmuir* **1994**, *10*, 166-171.
2. Tait, S. L.; Dohnalek, Z.; Campbell, C. T.; Kay, B. D., N-Alkanes on Pt(111) and on C(0001)/Pt(111): Chain Length Dependence of Kinetic Desorption Parameters. *Journal of Chemical Physics* **2006**, *125*, 234308.
3. Steele, W. A., Physical Interaction of Gases with Crystalline Solids .1. Gas-Solid Energies and Properties of Isolated Adsorbed Atoms. *Surf. Sci.* **1973**, *36*, 317-352.
4. Zaremba, E.; Kohn, W., Vanderwaals Interaction between an Atom and a Solid-Surface. *Phys. Rev. B* **1976**, *13*, 2270-2285.

Section 5 – Alkane Dissociative Sticking Coefficients

Section **Page**

5.1 Overview

As this lab previously reported,[1-2] the initial dissociative sticking coefficients (DSC) for n-alkanes increased in proportion to the surface temperature, gas temperature, and molecule size. An increase in DSC with respect to temperature indicates an activated process, where the potential energy barrier of the reaction is larger than the potential energy of the molecule at infinite distance from the surface. For the majority of alkanes reported in this study, dissociative chemisorption by initial C-H bond cleavage is an activated process. The exception is n-nonane, which increases in DSC to a plateau of 1 with a decrease in temperature. Figures 5.1 and 5.2 show the DSC of n-alkanes from methane to n-nonane with Arrhenius and PMTT fits, respectively. As the chain length of the alkane increases, the absolute DSC at each temperature increases and the slope of the DSC relative to temperature decreases. Because the activation energy (E_a) for dissociative chemisorption is proportional to the slope of the DSC, provided the system is in thermal equilibrium, the activation energies also decrease in magnitude with alkane size. Figures 5.1 and 5.2 also demonstrate the similarities in results between the linear least squares Arrhenius fit and the non-linear least squares PMTT fit. Provided that all of the DSC for a molecule are significantly lower than 1 and that the experimental data were gathered at thermal equilibrium, the Arrhenius and PMTT fits differ negligibly. The two alkanes for which the PMTT and Arrhenius fits did not match well were n-octane and n-nonane. Both molecules were measured to have DSC greater than 0.1 at all experimental temperatures. The Arrhenius fit permits DSC values greater than 1, and remains linear even as the DSCs approach 1. The PMTT model, on the other hand, cannot predict DSC values greater than 1, and will curve non-linearly and plateau at 1. The activation energies calculated from the Arrhenius linear regression fit to the DSCs also matched well with the activation energies derived from the PMTT model. Both

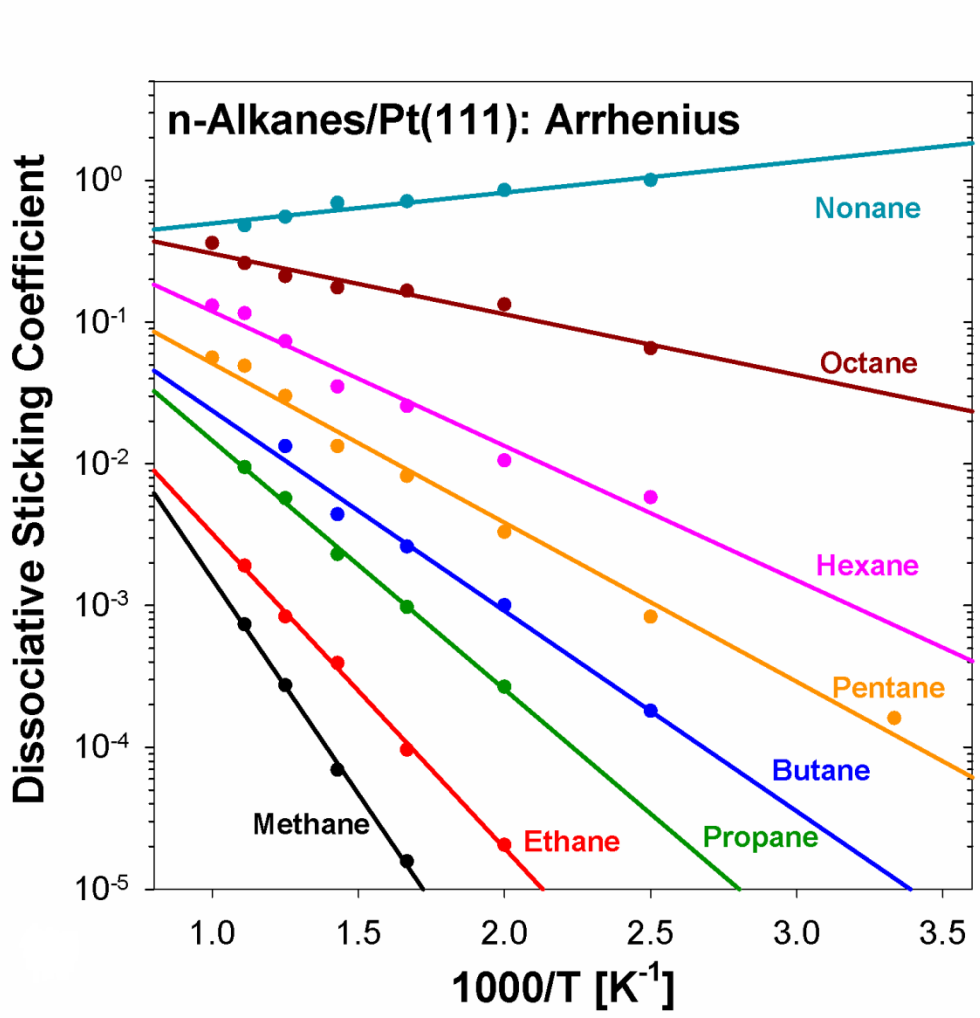

Figure 5.1: Experimental dissociative sticking coefficients for C_1 to C_9 n-alkanes (dots) and the linear regression fit for each set of data (solid lines)

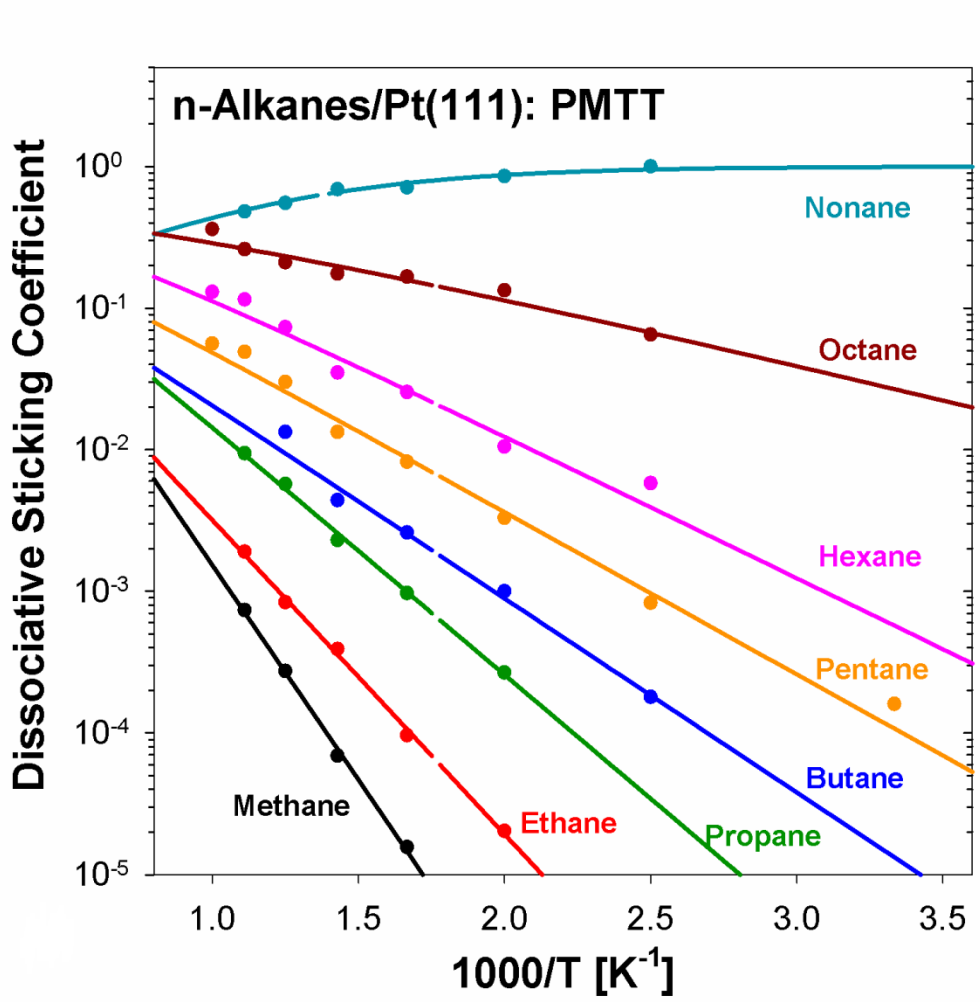

Figure 5.2: Experimental dissociative sticking coefficients for C_1 to C_9 n-alkanes (dots) and the PMTT fit for each set of data (solid lines)

analysis methods produced nearly identical results for the same molecule, with significant differences only occurring for n-octane and n-nonane. Because the PMTT fits for n-octane and n-nonane curve as the DSCs approach 1, the temperature dependent activation energies change non-negligibly when evaluated at different temperatures.

As alkane size and the number of rovibrational modes increased, the significance of normal translational energy on the angle resolved thermal dissociative sticking coefficients decreased. This can be seen in Figure 5.3 below. Three fits are shown for the thermal DSCs of methane, ethane and propane. The solid lines indicate Arrhenius linear regression fits for the experimental data. The dashed lines indicate theoretical predictions of the thermal DSC for each molecule at temperature T approaching either as a directed gas normal to the surface with no angular distribution (dashed line) or as an ambient gas with a cosine angular distribution (dot-dashed line).

The fits for methane experimental thermal DSC, which ranged from 1.6×10^{-5} to 7.4×10^{-3} from 600 to 900 K, had little overlap. The normal DSC were similar, but underestimated the experimental DSC. However, the ambient DSC were significantly lower than both the normal DSC and experimental DSC. These data indicate that translational energy normal to the surface is the most efficacious degree of freedom for methane overcoming the transition state barrier for dissociative chemisorption. This non-statistical behavior of methane, where energy in certain degrees of freedom are more favorable for reaction than others, is due to a relatively small number of vibrational modes, which have an efficacy of 0.4 relative to normal translational energy. As alkanes increase in size and the number of vibrational degrees of freedom increase, the molecules approach more statistical behavior. The normal DSC and ambient DSC predictions of ethane still deviate from the experimental DSCs, which range from 2.04×10^{-5} to 1.90×10^{-3}

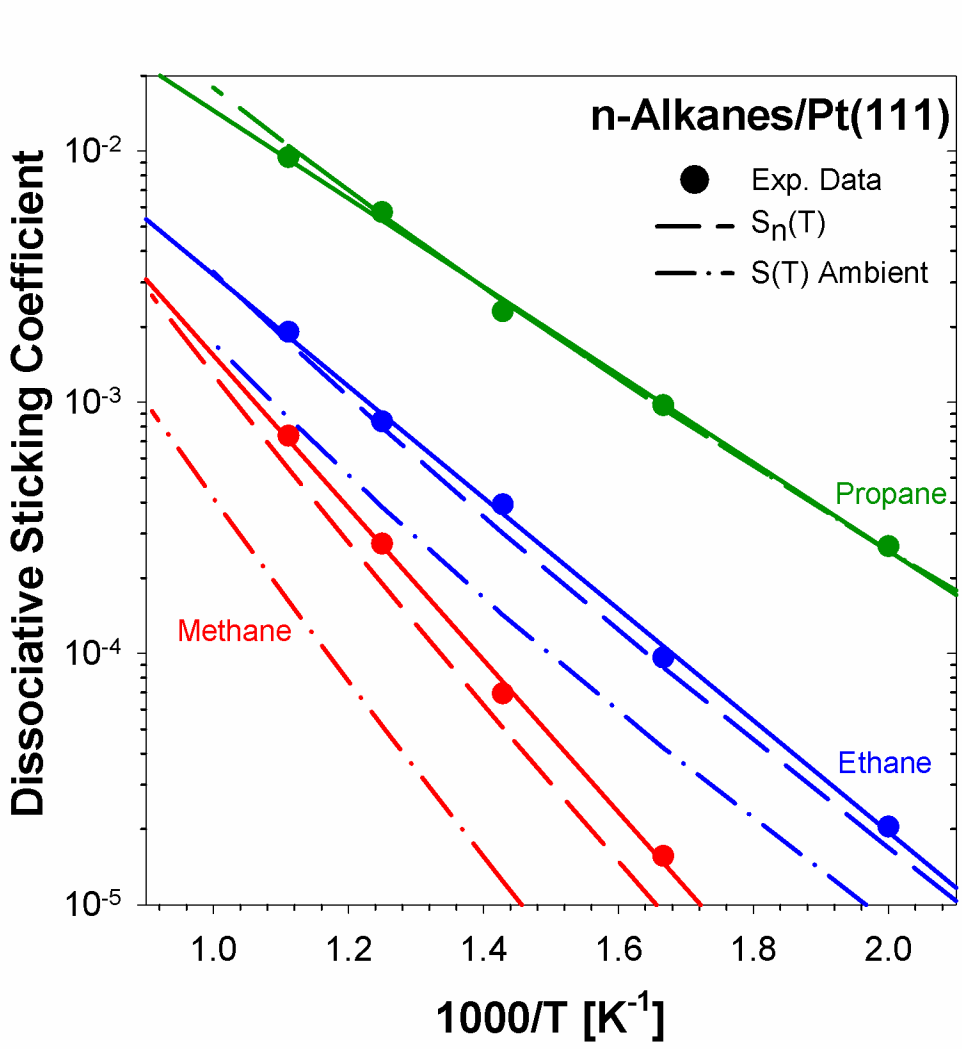

Figure 5.3: Experimental dissociative sticking coefficients (dots) for methane (red), ethane (blue), and propane (green) with Arrhenius style linear regression fits (solid lines). Theoretical predictions for normally directed gas (dashed lines) and ambient dosed gas (dot-dashed lines) are also given.

from 500 to 900 K. However, the ambient DSCs of ethane are substantially closer to the experimental DSCs when compared to methane. And by propane, whose experimental DSCs range from 2.67×10^{-4} to 9.44×10^{-3} from 500 to 900 K, the normal DSCs, ambient DSCs, and experimental DSCs nearly fully overlap. This is because with each increase in carbon chain length, alkane molecules gain 9 additional vibrational degrees of freedom. Even when accounting for the reduced efficacy of vibrational energy relative to normal translational energy, by propane, the sheer number of vibrational modes cause normal translational energy to be a negligible portion of the total energy of the molecule.

It should be noted that the ambient DSC shown in Figure 5.3 were theoretical values for a molecule at temperature, T, approaching the surface with the cosine angular distribution of an ambient gas. In reality, an ambient gas approaches the surface at the temperature of the chamber walls, T_c. If the temperature of the surface is not the same as the chamber walls, an ambient gas experiment is at thermal non-equilibrium, provided that gas-surface energy exchange is inefficient. However, as the number of vibrational modes increases with alkane size, the efficiency of gas-surface energy exchange increases. In additional to a flattening of the angle resolved DSCs with increased alkane size, as the total vibrational energy swamps out normal translational energy, the non-equilibrium DSCs approach the thermal equilibrium DSCs, as gas-surface energy exchange improves. There becomes a point, n-pentane and larger alkanes, where the gas-surface energy exchange is so fast that a molecule, which impinges at a temperature different from the surface, thermalizes to the surface temperature and reaches thermal equilibrium prior to reacting with the surface.

5.2 Methane, Ethane, n-Propane

The PMTT model was applied to the data for the previously reported data of methane, ethane, and n-pentane and compared to the Arrhenius fits. In the case of methane, the Arrhenius linear least squares fit of the experimental thermal DSCs, which were obtained at quasi-thermal equilibrium ($T_g = T_s$), yielded $E_a = 58.1 \pm 2.0$ kJ/mol and $S_0 = 1.67 \pm 0.57$. The non-linear least squares fit of experimental thermal DSCs to the PMTT model (Equation 3.34) yielded $E_r = 73.3 \pm 2.0$ kJ/mol and $\nu_d/\nu_r = 0.598 \pm 0.203$. The activation energy at 700 K had the most probable value of $E_a = 58.1$ kJ/mol and ranged from 56.1 to 60.1 kJ/mol due to the uncertainty in both E_r and ν_d/ν_r. The value and variance of E_a for methane is identical for both the Arrhenius fit and the PMTT model, indicating that the simpler Arrhenius form is as appropriate for calculating the apparent activation energy of methane as other, more complex models, provided that the data were obtained in thermal equilibrium. The reaction pre-exponential factor was calculated to be $\nu_r = 2.10 \times 10^{12}$ s^{-1}, ranging from 1.57×10^{12} to 3.15×10^{12} s^{-1} due to the uncertainty.

In the case of ethane, the Arrhenius linear least squares fit of the experimental thermal DSCs, which were obtained at quasi-thermal equilibrium ($T_g = T_s$), yielded $E_a = 42.5 \pm 1.2$ kJ/mol and $S_0 = 0.529 \pm 0.113$. The non-linear least squares fit of experimental thermal DSCs to the PMTT model (Equation 3.34) yielded $E_r = 71.3 \pm 1.2$ kJ/mol and $\nu_d/\nu_r = 1.89 \pm 0.40$. The activation energy at 700 K had the most probable value of $E_a = 42.4$ kJ/mol and ranged from 41.2 to 43.6 kJ/mol due to the uncertainty in both E_r and ν_d/ν_r. The value of E_a for ethane obtained from the PMTT model is 0.1 kJ/mol smaller than the value from the Arrhenius fit, which is a negligible difference. The variance is identical for both the Arrhenius fit and the PMTT model. Similar to methane, the simpler Arrhenius form is as appropriate for calculating the apparent activation energy of ethane as other, more complex models, provided that the data

were obtained in thermal equilibrium. The reaction pre-exponential factor of ethane was calculated to be $\nu_r = 2.11 \times 10^{13}$ s^{-1}, ranging from 1.74×10^{13} to 2.67×10^{13} s^{-1} due to the uncertainty.

In the case of n-propane, the Arrhenius linear least squares fit of the experimental thermal DSCs, which were obtained at quasi-thermal equilibrium ($T_g = T_s$), yielded $E_a = 33.5 \pm 1.0$ kJ/mol and $S_0 = 0.813 \pm 0.154$. The non-linear least squares fit of experimental thermal DSCs to the PMTT model (Equation 3.34) yielded $E_r = 75.0 \pm 1.1$ kJ/mol and $\nu_d/\nu_r = 1.23 \pm 0.24$. The activation energy at 700 K had the most probable value of $E_a = 33.4$ kJ/mol and ranged from 32.3 to 34.5 kJ/mol due to the uncertainty in both E_r and ν_d/ν_r. The value of E_a for n-propane obtained from the PMTT model is 0.1 kJ/mol smaller than the value from the Arrhenius fit, which is a negligible difference. The variance is identical for both the Arrhenius fit and the PMTT model. Similar to both methane and ethane, the simpler Arrhenius form is as appropriate for calculating the apparent activation energy of n-propane as other, more complex models, provided that the data were obtained in thermal equilibrium. The reaction pre-exponential factor of n-propane was calculated to be $\nu_r = 5.13 \times 10^{14}$ s^{-1}, ranging from 4.29×10^{14} to 6.37×10^{14} s^{-1} due to the uncertainty.

5.3 n-Butane

The DSCs for butane on Pt(111) were measured over a surface temperature range (T_s) from 300 to 1000 K. Ambient gas measurements $S_{bkg}(T_g = 295, T_s)$ were performed to account for any background sticking. The effusive beam nozzle was heated to 300, 600, and 800 K for directed gas measurements $S_n(T_g, T_s)$, not exceeding 800 K due to the risk of thermal cracking. In both the cases of increasing nozzle temperature and increasing surface temperature, $S_n(T_g, T_s)$

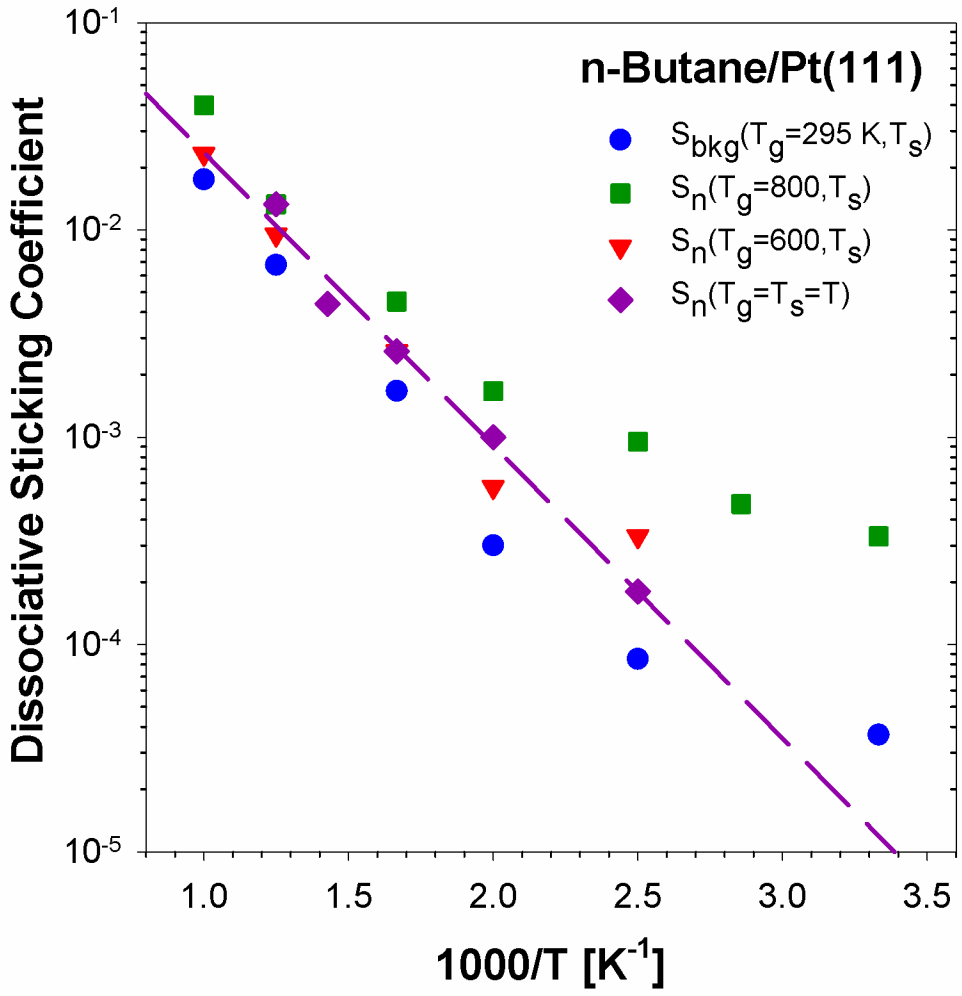

Figure 5.4: Butane dissociative sticking coefficients $S_{bkg}(T_g = 295\ K, T_s)$ and $S_n(T_g, T_s)$ on Pt(111). An Ea = 26.1 kJ/mol resulted from an Arrhenius style linear regression fit (dashed line) to the $S_n(T_g = T_s = T)$ data (purple diamonds). The PMTT fit for the n-pentane DSCs is not shown because it overlaps directly with the Arrhenius fit, with no distinguishable deviation. The PMTT model yielded E_a = 26.1 kJ/mol.

also increases, indicating that butane is an activated process. At surface temperatures below 700 K, the energy of the impinging molecule is greater than that of the surface, which can be observed by a decrease in the ratio of ambient sticking relative to the directed sticking at 800 K $S_{bkg}(T_g = 295\ K, T_s)/S_n(T_g = 800\ K, T_s)$ as surface temperature decreases. Conversely, at surface temperatures above 700 K, the ambient sticking and directed sticking are close to being equal, indicating that the surface is able to provide the energy for dissociation to the molecule, with little regard to the internal energy of the molecule as it collides with the surface. The range of DSCs for butane was determined to be from 2×10^{-5} to 4×10^{-2}.

The Arrhenius fit across thermal DSC data from 400 to 1000 K yielded an E_a of 26.2 ± 1.7 kJ/mol and S_0 of 0.485 ± 0.185 for n-butane on Pt(111). The non-linear least squares fit of experimental thermal DSCs to the PMTT model (Equation 3.34) yielded E_r = 77.1 ± 1.7 kJ/mol and ν_d/ν_r = 2.04 ± 0.78. The activation energy at 700 K had the most probable value of E_a = 26.1 kJ/mol and ranged from 24.2 to 27.8 kJ/mol due to the uncertainty in both E_r and ν_d/ν_r. The value of E_a for n-butane obtained from the PMTT model is 0.1 kJ/mol smaller than the value from the Arrhenius fit, which is a negligible difference. The variance is identical for both the Arrhenius fit and the PMTT model. Similar to smaller, linear alkanes, the simpler Arrhenius form is as appropriate for calculating the apparent activation energy of n-butane as other, more complex models, provided that the data were obtained in thermal equilibrium. The reaction pre-exponential factor of n-butane was calculated to be $\nu_r = 2.46 \times 10^{14}\ s^{-1}$, ranging from 1.78×10^{14} to $3.98 \times 10^{14}\ s^{-1}$ due to the uncertainty. Compared to the data of methane, ethane, and propane, butane has a significantly lower E_a, following the previously reported trend where the apparent activation energy varies significantly with alkane size.[1] The S_0 value is lower than that of methane and propane, but close in magnitude with ethane.

5.4 Isobutane

Heated effusive molecular beam dissociative sticking coefficient experiments for isobutane directed along the Pt(111) surface normal were performed at nozzle temperatures of 300, 500, and 700 K across a surface temperature range of 400 to 1000 K. Additional $T_g = T_s = T$ experiments were done at 400 and 600 K. The range of DSC was determined to be from 5×10^{-5} to 1×10^{-2}. An Arrhenius fit for the $T_g = T_s = T$ data from 400 to 700 K yielded an E_a of 28.3 ± 6.5 kJ/mol and a S_0 of 0.250 ± 0.369 for isobutane on Pt(111).

The non-linear least squares fit of experimental thermal DSCs to the PMTT model (Equation 3.34) yielded $E_r = 79.9 \pm 6.5$ kJ/mol and $\nu_d/\nu_r = 3.99 \pm 5.91$. The activation energy at 700 K had the most probable value of $E_a = 28.2$ kJ/mol and ranged from 22.1 to 34.8 kJ/mol due to the uncertainty in both E_r and ν_d/ν_r. The value of E_a for isobutane obtained from the PMTT model is 0.1 kJ/mol smaller than the value from the Arrhenius fit, which is a negligible difference. The variance of the E_a calculated from the PMTT model was not symmetrical, indicating that the uncertainty in pre-exponential factor skews the range of uncertainty in E_a. However, the average uncertainty due to the PMTT model fit is less than the symmetrical variance from the Arrhenius fit. Despite the slight differences in the average E_a value and uncertainty, the simpler Arrhenius form is as appropriate for calculating the apparent activation energy of isobutane as other, more complex models, provided that the data were obtained in thermal equilibrium. The reaction pre-exponential factor of isobutane was calculated to be $\nu_r = 1.08 \times 10^{14}$ s^{-1}, with a minimum value of 4.36×10^{13} due to the uncertainty. Because the ratio ν_d/ν_r becomes negative at one extreme of the variance from the PMTT fit, there is an ambiguous, unrealistic value (-2.25×10^{14}) for the maximum per-exponential factor.

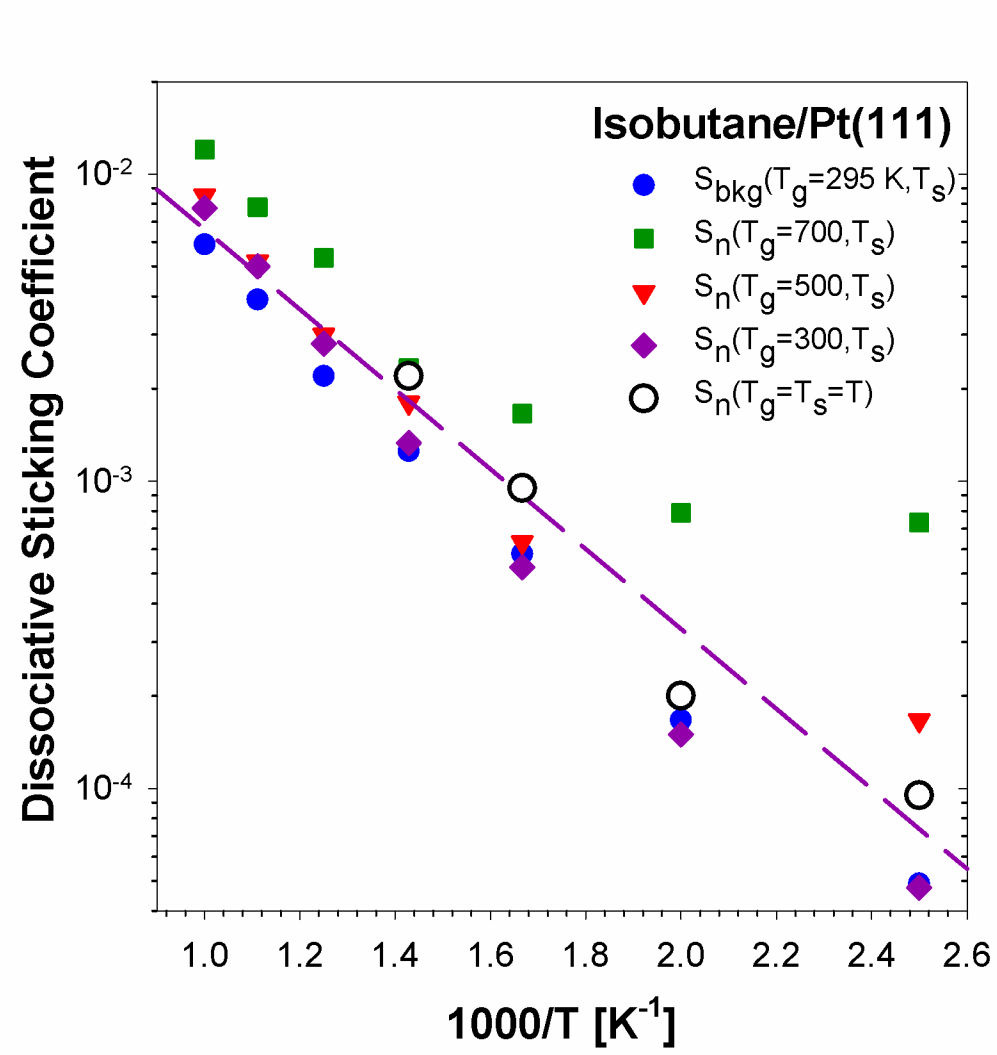

Figure 5.6: Isobutane dissociative sticking coefficients $S_{bkg}(T_g = 295\ K, T_s)$ and $S_n(T_g, T_s)$ on Pt(111). An $E_a = 28.3$ kJ/mol resulted from an Arrhenius style linear regression fit (dashed line) to the $S_n(T_g = T_s = T)$ data (open circles). The PMTT fit for the isobutane DSCs is not shown because it overlaps directly with the Arrhenius fit, with no distinguishable deviation. The PMTT model yielded $E_a = 28.2$ kJ/mol.

The E_a found for isobutane is higher than that of n-butane by 7.4%, which is greater than the 3.5% difference between the strongest C-H bond of isobutane and weakest C-H bond of n-butane. Considering the weakest C-H bond of isobutane is 2.7% lower than the weakest C-H bond of n-butane, it is clear that difference in E_a between the isomers is not strictly between the difference in gas-phase bond dissociation energies. The difference instead is likely because of less van der Waals stabilization of the transition state and products for isobutane relative to n-butane, due to the slightly lower E_d of n-butane, which will be explained in more detail later in Section 7.

5.5 n-Pentane

The ambient gas DSCs for pentane on Pt(111) were measured over a surface temperature range of 300 to 1000 K and compared to 600 K directed gas DSC measurements at surface temperatures of 400, 600, and 800 K. The ratio of the DSCs of ambient gas to the DSCs for directed gas at 600 K, $S_{bkg}(T_g = 295\ K, T_s)/ S_n(T_g = 600\ K, T_s)$, is close to 1 at each T_s, indicating that the molecule thermalizes to the surface temperature. From these data, it was determined that alkanes with van der Waals forces equal to or greater than n-pentane fully thermalize to the surface temperature regardless of the initial temperature or orientation of an impinging molecule. As the surface temperature increases, the DSC also increases, indicating that pentane is an activated process. The range of DSCs for pentane was determined to be from 2×10^{-4} to 6×10^{-2}. An Arrhenius analysis of ambient gas data from 400 to 1000 K yielded an E_a of 21.8 ± 1.0 kJ/mol and S_0 of 0.683 ± 0.159 for pentane on Pt(111).

The non-linear least squares fit of experimental thermal DSCs to the PMTT model (Equation 3.34) yielded E_r = 88.1 ± 1.2 kJ/mol and ν_d/ν_r = 1.40 ± 0.35. The activation energy at

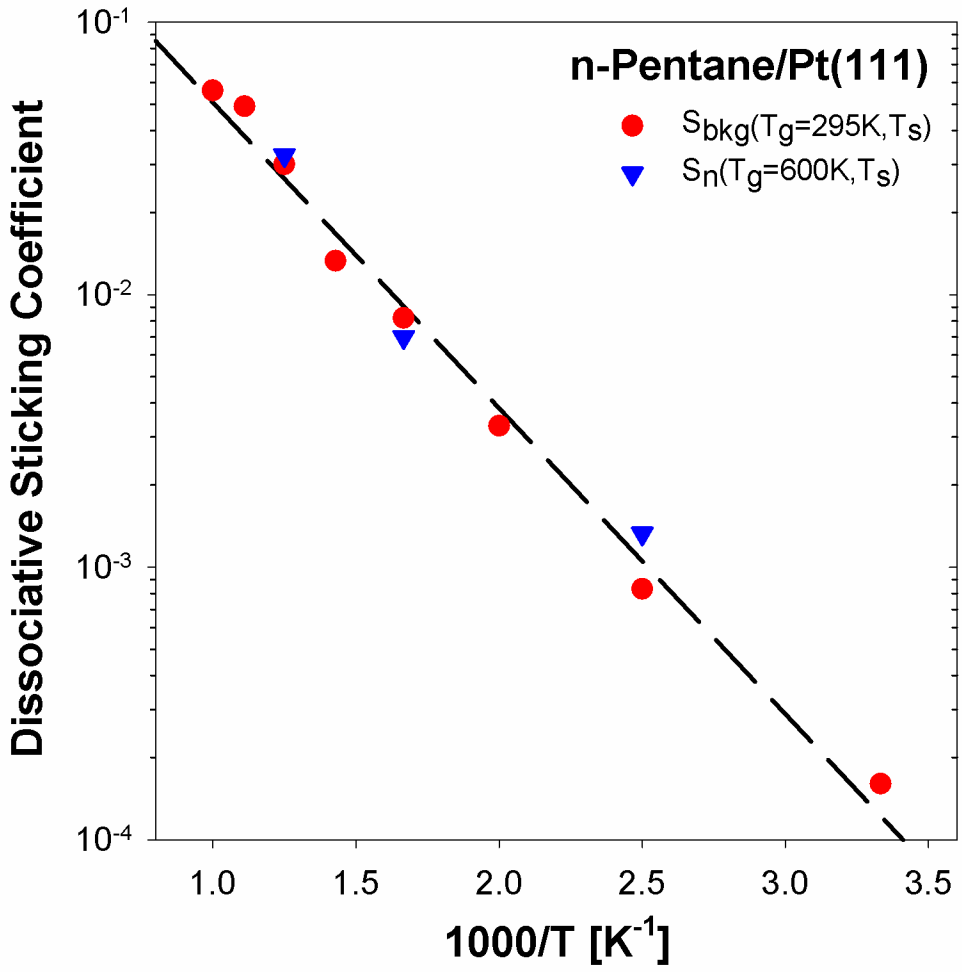

Figure 5.7: Pentane dissociative sticking coefficients $S_{bkg}(T_g = 295\ K, T_s)$ and $S_n(T_g = 600\ K, T_s)$ on Pt(111). The lack of apparent difference between the $S_{bkg}(T_g = 295\ K, T_s)$ and $S_n(T_g = 600\ K, T_s)$ data indicates that pentane thermalizes to the surface temperature. An $E_a = 21.6$ kJ/mol resulted from an Arrhenius style linear regression fit (dashed line) to the $S_n(T_g = 295\ K, T_s)$ data (red dots). The PMTT fit for the n-pentane DSCs is not shown because it overlaps directly with the Arrhenius fit, with no distinguishable deviation. The PMTT model yielded $E_a = 21.5$ kJ/mol.

700 K had the most probable value of E_a = 21.5 kJ/mol and ranged from 20.3 to 22.8 kJ/mol due to the uncertainty in both E_r and ν_d/ν_r. The value of E_a for n-pentane obtained from the PMTT model is 0.3 kJ/mol smaller than the value from the Arrhenius fit, which is a negligible difference considering the variance of both fits. The variance of the E_a calculated from the PMTT model was not symmetrical, indicating that the uncertainty in pre-exponential factor skews the range of uncertainty in E_a. Additionally, the average uncertainty due to the PMTT model fit is greater than the symmetrical variance from the Arrhenius fit. Despite the slight differences in the average E_a value and uncertainty, because both models overlap heavily through their range of uncertainty, the simpler Arrhenius form is as appropriate for calculating the apparent activation energy of n-pentane as other, more complex models, provided that the data were obtained in thermal equilibrium. The reaction pre-exponential factor of n-pentane was calculated to be $\nu_r = 1.13 \times 10^{16}$ s^{-1}, ranging from 9.06×10^{15} to 1.51×10^{16} s^{-1} due to the uncertainty.

5.6 2,2-Dimethylpropane (Neopentane)

Neopentane DSC on Pt(111) were measured using a heated effusive beam doser directed normal to the surface at nozzle temperatures of 300, 500, and 700 K over a surface temperature range from 400 to 1000 K. Additional $T_g = T_s = T$ experiments were done at 600 and 800 K. The range of DSCs was found to be from 7×10^{-4} to 2.5×10^{-2}, increasing with increasing temperature and indicating an activated mechanism. It is important to note that neopentane did not thermalize to the surface temperature in the same manner as n-pentane. The lower desorption energy, indicating weaker van der Waals interactions, of neopentane relative to n-pentane predicts that the ratio of the DSCs for ambient gas to directed gas at 700 K,

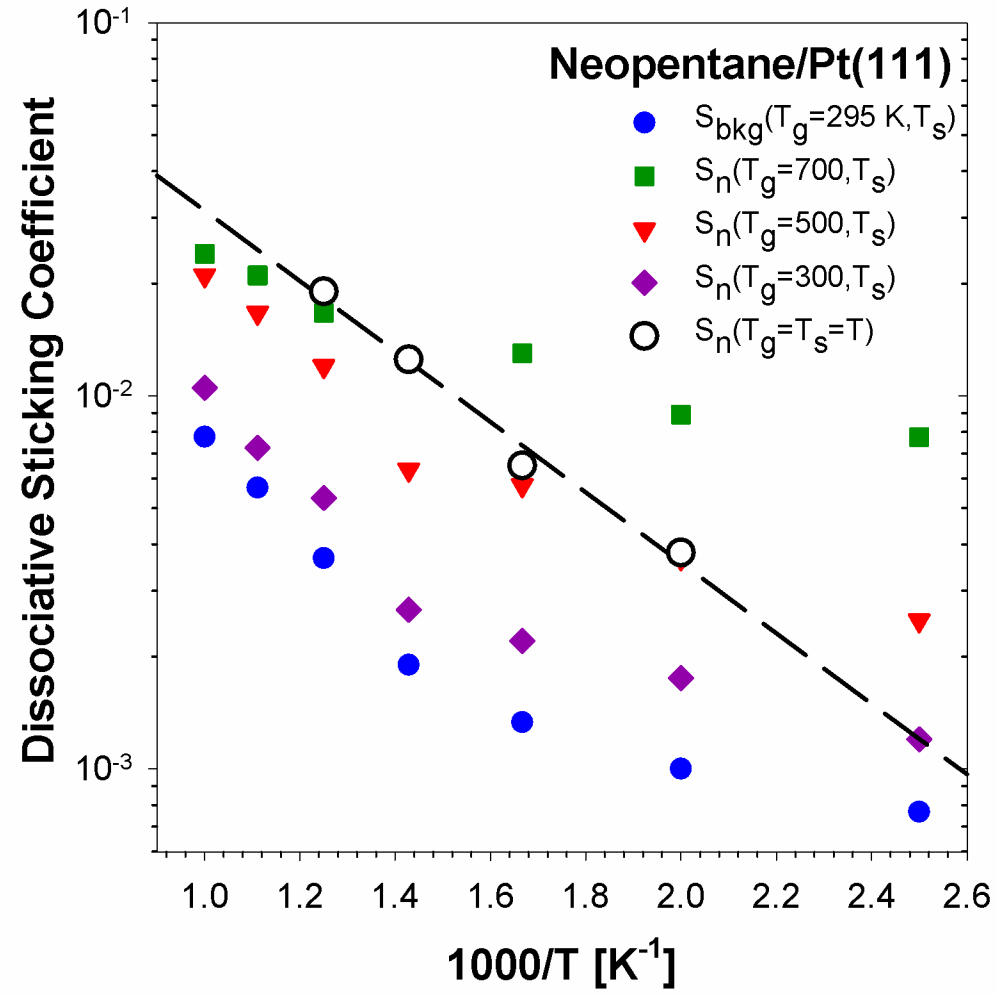

Figure 5.8: Neopentane dissociative sticking coefficients $S_{bkg}(T_g = 295\ K, T_s)$ and $S_n(T_g, T_s)$ on Pt(111). An E_a = 18.1 kJ/mol resulted from an Arrhenius style linear regression fit (dashed line) to the $S_n(T_g = T_s = T)$ data (open circles). The PMTT fit for the neopentane DSCs is not shown because it overlaps directly with the Arrhenius fit, with no distinguishable deviation. The PMTT model yielded E_a = 18.1 kJ/mol.

$S_{bkg}(T_g = 295\ K, T_s)/ S_n(T_g = 700\ K, T_s)$, should be less than 1 for neopentane, which was indeed the case. The ratio at each surface temperature is closer to yet still lower than that of n-butane, indicating that neopentane tends towards more dynamic behavior than other alkanes larger than propane. The high-symmetry and geometry of neopentane is analogous to methane and may be a key factor in the dynamic behavior of neopentane relative to n-pentane. An Arrhenius fit of the $T_g = T_s = T$ data from 500 to 800 K yielded an E_a of 18.2 ± 1.7 kJ/mol and S_0 of 0.278 ± 0.090 for neopentane on Pt(111).

The non-linear least squares fit of experimental thermal DSCs to the PMTT model (Equation 3.34) yielded E_r = 71.5 ± 1.8 kJ/mol and ν_d/ν_r = 3.45 ± 1.15. The activation energy at 700 K had the most probable value of E_a = 18.1 kJ/mol and ranged from 16.2 to 19.9 kJ/mol due to the uncertainty in both E_r and ν_d/ν_r. The value of E_a for neopentane obtained from the PMTT model is 0.1 kJ/mol smaller than the value from the Arrhenius fit, which is a negligible difference. The variance of the E_a calculated from the PMTT model was not symmetrical, indicating that the uncertainty in pre-exponential factor skews the range of uncertainty in E_a. Additionally, the average uncertainty due to the PMTT model fit is greater than the symmetrical variance from the Arrhenius fit. Despite the slight differences in the average E_a value and uncertainty, the simpler Arrhenius form is as appropriate for calculating the apparent activation energy of neopentane as other, more complex models, provided that the data were obtained in thermal equilibrium. The reaction pre-exponential factor of neopentane was calculated to be $\nu_r = 1.69 \times 10^{14}\ s^{-1}$, ranging from 1.27×10^{14} to $2.53 \times 10^{14}\ s^{-1}$ due to the uncertainty.

There are significant differences between the dissociative chemisorption of neopentane and n-pentane on Pt(111). The apparent activation energy of neopentane is 16.5% smaller than that of n-pentane. The desorption energy of neopentane is significantly smaller than that of n-pentane,

which predicts weaker van der Waals stabilization of the transition state and products and a lower activation energy (See Section 7). Additionally, Neopentane has far less efficient gas-surface energy exchange than n-pentane, as demonstrated by the non-equilibrium experiments. Regardless of the temperature of the impinging molecules, n-pentane thermalized to the surface temperature. The thermal equilibrium and non-equilibrium experiments for n-pentane produced identical DSCs. However, this was not the case for neopentane, which had significant differences in DSC between thermal equilibrium and non-equilibrium experiments. While n-pentane and neopentane have an identical number of vibrational modes, neopentane has several modes which are degenerate and has significant energy gaps between modes. The vibrational rigidity of neopentane relative to n-pentane plays a critical role in the relative gas-surface energy transfer of the two molecules

5.7 n-Hexane

As it was determined that the ambient and directed DSCs for pentane on Pt(111) were equivalent for alkane molecules with surface van der Waals interactions equal to or greater than that of n-pentane, only ambient gas DSC measurements for hexane on Pt(111) were done across surface temperatures of 400 to 1000 K. The DSCs were found to increase with increasing surface temperature, indicating an activated mechanism. The range of DSCs for hexane was determined to be from 6×10^{-3} to 1×10^{-1}. The Arrhenius fit for the ambient data yielded an E_a of 18.7 ± 1.8 kJ/mol and S_0 of 1.10 ± 0.37 for n-hexane on Pt(111).

The non-linear least squares fit of experimental thermal DSCs to the PMTT model (Equation 3.34) yielded $E_r = 99.0 \pm 2.0$ kJ/mol and $\nu_d/\nu_r = 0.789 \pm 0.307$. The activation energy at 700 K had the most probable value of $E_a = 18.3$ kJ/mol and ranged from 15.5 to 20.7 kJ/mol

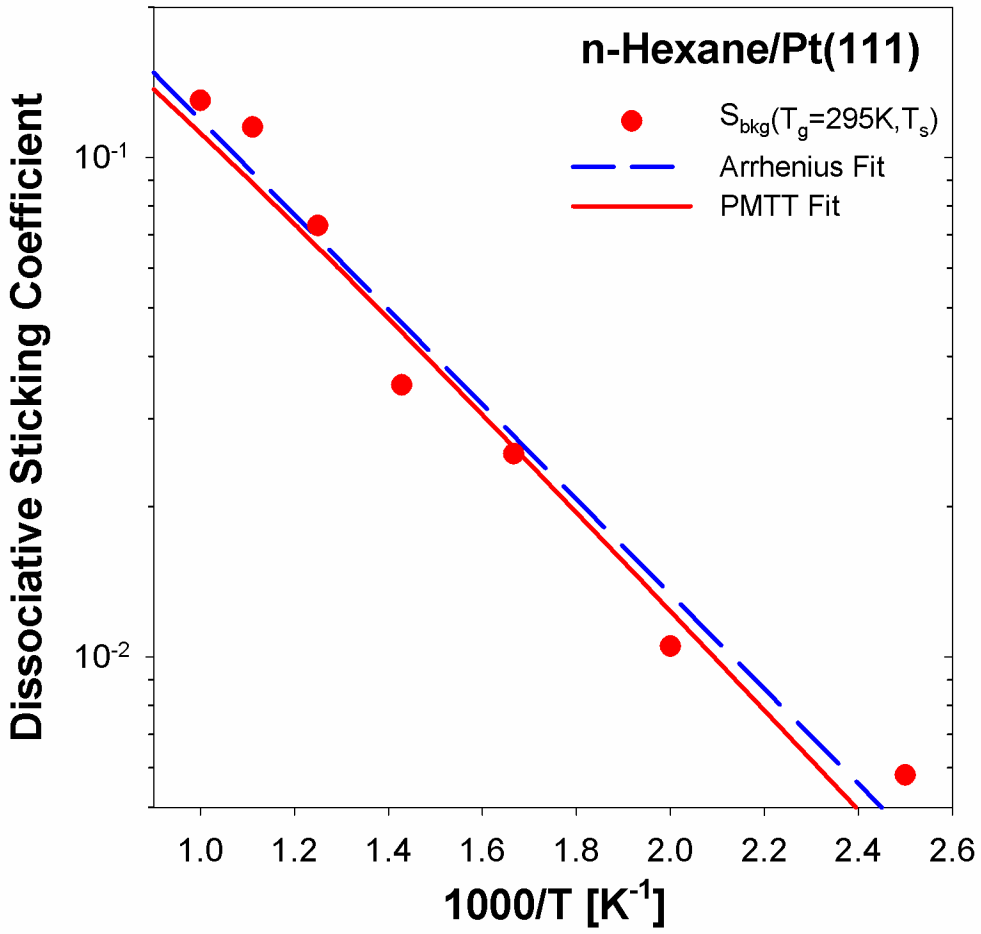

Figure 5.9: Hexane dissociative sticking coefficients $S_{bkg}(T_g = 295\ K, T_s)$ on Pt(111). An E_a of 18.7 ± 1.8 kJ/mol and E_a = 18.3 kJ/mol resulted from an Arrhenius style fit (dashed blue line) and PMTT fit (solid red line), respectively, to the $S_n(T_g = 295\ K, T_s)$ data (red dots).

due to the uncertainty in both E_r and ν_d/ν_r. The value of E_a for n-hexane obtained from the PMTT model is 0.4 kJ/mol smaller than the value from the Arrhenius fit, which is a negligible difference considering the range of uncertainty of the two fits. The variance of the E_a calculated from the PMTT model was not symmetrical, indicating that the uncertainty in pre-exponential factor skews the range of uncertainty in E_a. Additionally, the average uncertainty due to the PMTT model fit (± 2.6) was greater than the symmetrical variance from the Arrhenius fit (± 1.8). Despite the slight differences in the average E_a value and uncertainty, due to the significant overlap in the variance between the two fits, the simpler Arrhenius form was as appropriate for calculating the apparent activation energy of n-hexane as other, more complex models, provided that the data were obtained in thermal equilibrium. The reaction pre-exponential factor of n-hexane was calculated to be $\nu_r = 2.01 \times 10^{17}$ s^{-1}, ranging from 1.45×10^{17} to 3.29×10^{17} s^{-1} due to the uncertainty.

5.8 n-Octane

Ambient DSCs for octane on Pt(111) were measured across surface temperatures of 400 to 1000 K. The DSCs increased with increasing temperature, indicating an activated mechanism for dissociative chemisorption. The range of DSCs for octane was determined to be from 6×10^{-2} to 3×10^{-1}. An Arrhenius fit for the ambient data from 400 to 1000 K yielded an E_a of 8.14 ± 0.85 kJ/mol and an S_0 of 0.793 ± 0.134 for n-octane on Pt(111). Both of these values are significantly lower than that of n-hexane.

The non-linear least squares fit of experimental thermal DSCs to the PMTT model (Equation 3.34) yielded $E_r = 114 \pm 1$ kJ/mol and $\nu_d/\nu_r = 0.786 \pm 0.170$. The activation energy at 700 K had the most probable value of $E_a = 7.64$ kJ/mol and ranged from 6.16 to 9.03 kJ/mol due to the

uncertainty in both E_r and ν_d/ν_r. The value of E_a for n-octane obtained from the PMTT model is 0.5 kJ/mol smaller than the value from the Arrhenius fit, which is a negligible difference considering the range of uncertainty of the fits to both models. The variance of the E_a calculated from the PMTT model was not symmetrical, indicating that the uncertainty in pre-exponential factor skews the range of uncertainty in Ea. Additionally, the average uncertainty due to the PMTT model fit was greater than the symmetrical variance from the Arrhenius fit. Despite the slight differences in the average E_a value and uncertainty, because of the significant overlap in the variance between the fits of the two models, the simpler Arrhenius form was as appropriate for calculating the apparent activation energy of n-octane as other, more complex models, provided that the data were obtained in thermal equilibrium. The reaction pre-exponential factor of n-octane was calculated to be $\nu_r = 1.27 \times 10^{19}$ s^{-1}, ranging from 1.05×10^{19} to 1.62×10^{19} s^{-1} due to the uncertainty.

5.9 n-Nonane

Ambient DSCs for nonane on Pt(111) were measured across surface temperature of 400 to 900 K. S_{bkg} approaches 1 at lower temperatures and decreases with increasing temperature, indicating that initial dissociative chemisorption of nonane on Pt(111) is an unactivated process. The barrier for dissociative chemisorption for nonane is below the vacuum level energy, indicating that a reaction with the surface is more facile than desorption for a molecule trapped in the physisorption well. However, in the case of the competing reactions of dissociative chemisorption and reversible desorption, as surface temperature increases, the probability of desorption increases, lowering the reactivity of nonane with the surface. The range of DSCs for nonane, with the maximum value at 400 K and minimum value at 1000 K, was determined to be

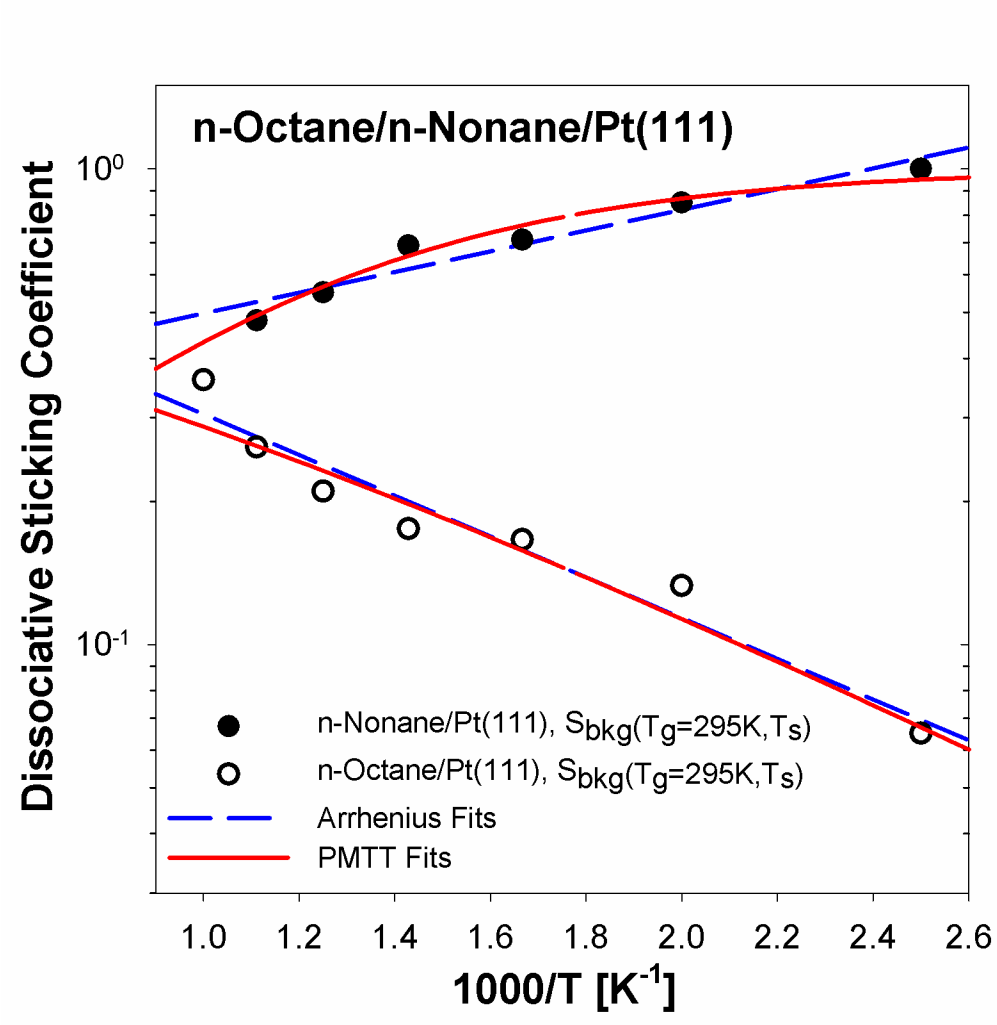

Figure 5.10: Octane dissociative sticking coefficients $S_{bkg}(T_g = 295\ K, T_s)$ on Pt(111) (black circles). An $E_a = 8.14 \pm 1.8$ kJ/mol and $E_a = 7.64$ kJ/mol resulted from an Arrhenius style fit (dashed blue line) and PMTT fit (solid red line), respectively, to the n-octane $S_{bkg}(T_g = 295\ K, T_s)$. Also, nonane dissociative sticking coefficients $S_{bkg}(T_g = 295\ K, T_s)$ on Pt(111) (open black circles). An $E_a = -4.21 \pm 0.55$ kJ/mol and $E_a = -6.24$ kJ/mol resulted from an Arrhenius style fit (dashed blue line) and PMTT fit (solid red line), respectively, to the n-nonane $S_{bkg}(T_g = 295\ K, T_s)$

from 1 x 10^0 to 5 x 10^{-1}. An Arrhenius fit for the ambient data from 400 to 900 K yielded an E_a of -4.21 ± 0.55 kJ/mol and a S_0 of 0.297 ± 0.034 for n-nonane on Pt(111).

The non-linear least squares fit of experimental thermal DSCs to the PMTT model (Equation 3.34) yielded E_r = 99.4 ± 2.3 kJ/mol and ν_d/ν_r = 11.3 ± 4.1. The activation energy at 700 K had the most probable value of E_a = -6.24 kJ/mol and ranged from -8.05 to -3.80 kJ/mol due to the uncertainty in both E_r and ν_d/ν_r. The value of E_a for n-nonane obtained from the PMTT model is 2.03 kJ/mol smaller than the value from the Arrhenius fit, which is significant considering the range of uncertainty of the fits to the two models. The variance of the E_a calculated from the PMTT model was not symmetrical, indicating that the uncertainty in pre-exponential factor skews the range of uncertainty in E_a. Additionally, the average uncertainty due to the PMTT model fit (± 2.13) was significantly greater than the symmetrical variance from the Arrhenius fit (± 0.55). Because of the significant differences in the average E_a value and uncertainty, the Arrhenius fit was not appropriate for calculating the apparent activation energy of n-nonane. This is because the Arrhenius fit permits DCSs greater than 1, when such values are unrealistic. Because n-nonane plateaus at a DSC of 1, the linear regression due to the Arrhenius fit, extrapolated to low temperatures, predicts DSCs for n-nonane which are greater than 1. However, the non-linear fit from the PMTT model properly accounts for the fact that DSCs cannot be greater than 1, and therefore fits the non-linear experimental data better than the Arrhenius fit. The reaction pre-exponential factor of n-nonane was calculated to be ν_r = 8.85 x 10^{18} s^{-1}, ranging from 6.49 x 10^{18} to 1.39 x 10^{19} s^{-1} due to the uncertainty.

5.10 Summary

The apparent activation energies overall decreased with each increase of alkane size. Both the Arrhenius and PMTT model fits yielded activation energies of approximately the same values and variance. Overall, the Arrhenius fits overestimate the activation energies and DSCs for alkanes, although the discrepancy between the Arrhenius and PMTT fits are small with the smallest alkanes. The first obvious deviation of the Arrhenius fit from the PMTT model was with n-hexane, which can be seen from Figure 5.9 above. The Arrhenius linear regression to the experimental DSCs overestimates the DSCs at high and low temperatures, and only overlaps with the PMTT model at around 600 to 700 K. Also, the activation energy of n-hexane calculated at 700 K using the PMTT model deviated by more than 0.1 kJ/mol, where the values of all smaller alkanes from both model fits were within 0.1 kJ/mol of each other. The deviation between the Arrhenius and PMTT fits increased for alkanes larger than n-hexane, as the DSCs approached closer to 1. By n-nonane, which has DSCs of 1 at low temperatures, the Arrhenius fit fails to provide good fit to the experimental data and yields an activation energy which is significantly different from the PMTT value calculated at 700 K. It should be noted that the PMTT model fits non-linear experimental DSCs, like those of n-octane and n-nonane better than the linear Arrhenius fit. However, because the activation energy is proportional to the derivative of the curve, there is a significant temperature dependence on the activation energy the more non-linear the DSC fit is. In the case of n-nonane, E_a varies from -10.1 to 0.00 kJ/mol at temperatures from 1000 to 100 K, respectively. Conversely, the Arrhenius fit predicts a constant E_a of -4.21, regardless of temperature. The Arrhenius fit and the PMTT model only overlap at a single temperature (591 K) and otherwise deviate from each other. Because the experimental data for n-hexane and smaller alkanes are approximately linear when arranged in an Arrhenius

plot, the temperature dependence of E_a, as calculated by the PMTT model, is negligible, and allows the Arrhenius and PMTT models to match well. Table 5.1 shows the apparent activation energies at 700 K, pre-exponential factors, and initial DSCs calculated from the Arrhenius and PMTT fits for each alkane in this study.

Table 5.1: The activation energies calculated from the Arrhenius and PMTT model (at 700 K) fits, as well as the initial DSCs and reaction pre-exponential factors for each alkane reported in this study.

Alkane	Arrhenius E_a [kJ/mol]	Arrhenius S_0	PMTT E_r [kJ/mol]	PMTT v_r [s^{-1}]	PMTT E_a [kJ/mol]
Methane	58.1 ± 2.0	1.67 ± 0.57	73.3 ± 2.0	2.10×10^{12}	58.1
Ethane	42.5 ± 1.2	0.529 ± 0.113	71.3 ± 1.2	2.11×10^{13}	42.4
n-Propane	33.5 ± 1.0	0.813 ± 0.154	75.0 ± 1.1	5.13×10^{14}	33.5
n-Butane	26.2 ± 1.7	0.485 ± 0.185	77.1 ± 1.7	2.46×10^{14}	26.1
Isobutane	28.3 ± 6.5	0.25 ± 0.369	79.9 ± 6.5	1.08×10^{14}	28.3
Neopentane	18.2 ± 1.7	0.278 ± 0.090	71.5 ± 1.7	1.69×10^{14}	18.2
n-Pentane	21.8 ± 1.0	0.683 ± 0.159	88.1 ± 1.1	1.13×10^{16}	21.7
n-Hexane	18.7 ± 1.8	1.10 ± 0.370	99.0 ± 2.0	2.01×10^{17}	18.7
n-Octane	8.14 ± 0.85	0.793 ± 0.134	114 ± 1	1.27×10^{19}	7.64
n-Nonane	-4.21 ± 0.55	0.297 ± 0.034	99.4 ± 23	8.85×10^{18}	-6.24

References

1. Cushing, G. W.; Navin, J. K.; Donald, S. B.; Valadez, L.; Johanek, V.; Harrison, I., C-H Bond Activation of Light Alkanes on Pt(111): Dissociative Sticking Coefficients, Evans-Polanyi Relation, and Gas-Surface Energy Transfer. *J. Phys. Chem. C* **2010**, *114*, 17222-17232.
2. Navin, J. K.; Donald, S. B.; Harrison, I., Angle-Resolved Thermal Dissociative Sticking of Light Alkanes on Pt(111): Transitioning from Dynamical to Statistical Behavior. *J. Phys. Chem. C* **2014**, *118*, 22003-22011.

Section 6 –Dissociative Chemisorption of 2,2,3,3-Tetramethylbutane

Section **Page**

6.1 Overview

2,2,3,3-Tetramethybutane (TMB) is an isomer of octane and a larger analog to neopentane, having only primary C-H bonds and being highly branched. Similar to neopentane, all C-H bonds are equivalent in terms of symmetry and all C-C bonds contain at least one tertiary carbon. The two central carbons of TMB have a bond energy of 322.6 kJ/mol which is one of the weakest C-C bond energies among simple alkanes, being 40 and 50 kJ/mol less than the weakest C-C bond in octane and butane respectively.[1] The low bond dissociation energy for this central C-C bond comes from the relative stability of tert-butyl radicals, which are the only products of the dissociation. TMB was studied in order to investigate the dissociative chemisorption reactivity of branched alkanes with weaker C-C bond dissociation energies relative to previously studied linear alkanes.

6.2 Dissociative Sticking Coefficients

Ambient gas dissociative sticking coefficient (DSC) experiments for TMB on Pt(111) were performed across a surface temperature range from 400 to 1000 K. The range of DSCs was found to be from 6.62×10^{-4} to 1.66×10^{-1}, increasing with higher temperatures and indicating an activated process. The data were arranged in an Arrhenius plot (Figure 6.1) and form two linear slopes with an intersection point at 560 K.

The separate linear slopes are indicative of two competing reaction mechanisms. An Arrhenius linear least squares fit from 300 to 500 K yielded an E_a of 10.0 ± 0.3 kJ/mol and a S_0 of 0.0368 ± 0.0039 for TMB on Pt(111), where the error bars are ± 1 standard deviation in the confidence of the fit. Another fit from 600 to 1000 K yielded an E_a of 39.7 ± 2.8 kJ/mol and a S_0 of 22.8 ± 9.2, indicating that a second reaction mechanism with a higher pre-exponential factor

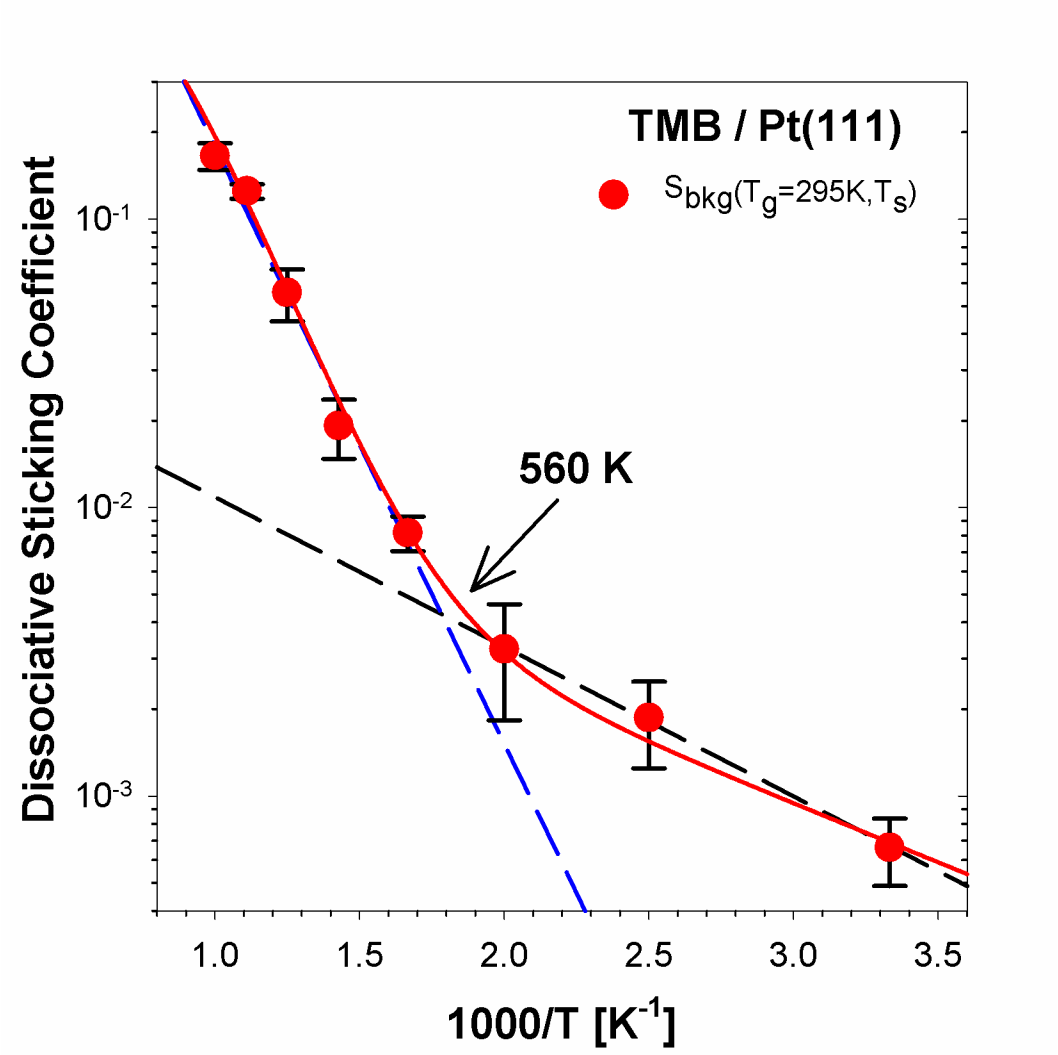

Figure 6.1: 2,2,3,3-Tetramethylbutane dissociative sticking coefficients $S_{bkg}(T_g = 295\ K, T_s)$ on Pt(111). Arrhenius style linear regression fits (dashed lines) to the $S_{bkg}(T_g = 295\ K, 300\text{-}500\ K)$ and $S_{bkg}(T_g = 295\ K, 600\text{-}1000\ K)$ data (red dots) resulted in an $E_a = 10.0 \pm 0.3$ kJ/mol and an $E_a = 39.7 \pm 2.8$ kJ/mol respectively. The intersection of the Arrhenius lines is indicated at 560 K. A PMTT model fit assuming two reaction pathways is also shown (solid red line) and resulted in an $E_a = 7.82$ kJ/mol and an $E_a = 40.0$ kJ/mol respectively.

than the first exists. The intersection of the two Arrhenius lines was calculated to be approximately 560 K. The temperature dependent DSCs were fit to a two-reaction pathway PMTT model (Equation 3.40), and the reaction energies and pre-exponential factors for the low and high temperature regions were calculated. The reaction energies were $E_{r,low}$ = 102 ± 4 kJ/mol and $E_{r,high}$ = 142 ± 6 kJ/mol for the low and high temperature reaction pathways respectively. The pre-exponential factors were calculated to be $\ln(\nu_{low})$ = 43.5 ± 1.6, ν_{low} = 7.72 x 10^{18} s^{-1}, ranging from 1.65 x 10^{18} to 3.67 x 10^{19} s^{-1} by error, and $\ln(\nu_{high})$ = 51.9 ± 0.8, ν_{high} = 3.62 x 10^{22} s^{-1}, ranging from 1.54 x 10^{22} to 7.78 x 10^{22} s^{-1} by error, for the low and high temperature regions respectively. The low temperature pre-exponential falls in line with those from previous experiments on alkane dissociative chemisorption by initial C-H bond cleavage. However, the high temperature pre-exponential is substantially larger than the pre-exponential for molecular desorption of ν_d = 4.89 x 10^{20} s^{-1} which indicates that the high temperature dissociation mechanism should have a transition state with more degrees of freedom than a molecule desorbing from the surface. The ratio of reaction pre-exponential factors to desorption pre-exponential factors were ν_{low}/ν_d = 0.0158 and ν_{high}/ν_d = 74.2 for the low and high surface temperature regions respectively. The reaction energies and pre-exponential factors were inserted into Equation 3.42 to calculate the activation energies at 400 and 700 K. The most probable apparent activation energy, calculated at 400 K, for the low temperature reaction was determined to be 8.88 kJ/mol, ranging from 3.47 to 18.0 kJ/mol due to the uncertainty of $E_{r,low}$, $E_{r,high}$, $\ln(\nu_{low})$, and $\ln(\nu_{high})$. This value differed from the Arrhenius fit (10.0 ± 0.3 kJ/mol) by 12.6%. The most probable apparent activation energy, calculated at 700 K, for the high temperature region was 40.0 kJ/mol, ranging from 6.63 to 52.3 kJ/mol due to the uncertainty of $E_{r,low}$, $E_{r,high}$, $\ln(\nu_{low})$, and $\ln(\nu_{high})$. and differed by 0.75% from the Arrhenius fit (39.7 ± 2.8 kJ/mol).

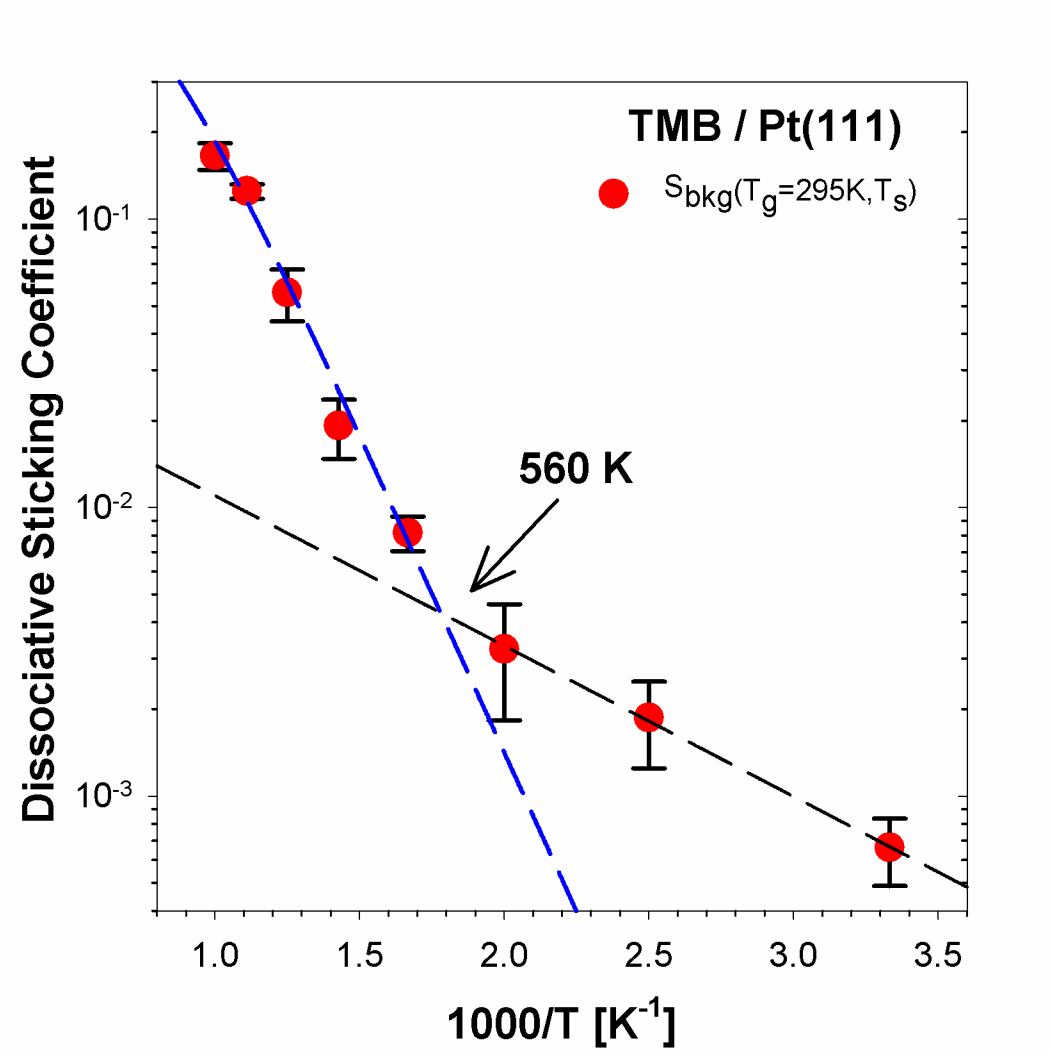

Figure 6.2: 2,2,3,3-Tetramethylbutane dissociative sticking coefficients versus 1000/T, where experimental data (red dots with error bars) from 300 to 500 K (black dashed line) and from 600 to 1000 K (blue dashed line) are fit separately to a single reaction pathway PMTT model. The only discernable difference from the Arrhenius fit is at high temperature, where the blue line curves as it approaches a plateau of 1.

Table 6.1: Activation energies and pre-exponential factors for the low and high temperature dissociative chemisorption mechanisms for TMB, calculated from the Arrhenius, one-reaction pathway PMTT model, and two-reaction pathway PMTT model fits.

Model	$E_{a,low}$ [kJ/mol]	$E_{a,high}$ [kJ/mol]	$\ln(\nu_{low})$	$\ln(\nu_{high})$
Arrhenius	10.0 ± 0.3	39.7 ± 2.8	-	-
One-Reaction Pathway PMTT	10.0 ± 0.3	41.1 $^{+ 1.6}_{- 7.0}$	44.3 ± 0.1	51.3 $^{+ 1.3}_{- 1.1}$
Two-Reaction Pathway PMTT	8.88 $^{+ 9.12}_{- 5.41}$	40.0 $^{+ 12.3}_{- 33.4}$	43.5 ± 1.6	51.9 ± 0.8

In order to evaluate the differences between a one and two reaction pathway PMTT model, as the former was exclusively used by Weinberg in his analysis of alkane DSCs on Ir(111),[2] the temperature dependent DCSs from 300 to 500 K and 600 to 1000 K were fit separately to a one reaction pathway PMTT model (Equation 3.32). The low temperature region had a reaction energy of $E_{r,low}$ = 104.4 ± 0.3 kJ/mol, a ν_d/ν_{low} = 26.9 ± 2.8, ν_{low} = 1.81 x 10^{19} s^{-1}, ranging from 1.64 x 10^{19} to 2.03 x 10^{19} s^{-1} by error, and a ν_{low}/ν_d of 0.0371. The reaction energy and pre-exponential were inserted into Equation 3.35 and yielded an apparent activation energy of 10.0 kJ/mol at 400 K, which ranged from 9.71 to 10.3 kJ/mol due to error. The high temperature region had a reaction energy of $E_{r,high}$ = 136.6 ± 2.7 kJ/mol, a ν_d/ν_{high} = 0.0269 ± 0.0108, ν_{high} = 1.82 x 10^{22} s^{-1}, ranging from 5.77 x 10^{21} to 6.84 x 10^{22} s^{-1} by error, and a ν_{high}/ν_d of 37.2. The apparent activation was calculated to be 41.1 kJ/mol at 700 K, which ranged from 34.1 to 42.7 kJ/mol due to error. In comparison to the data calculated from the two reaction pathway PMTT model, the one reaction pathway model in the low temperature region differed by 2% in reaction energy, 134% with the pre-exponential factors, and 12.6% in activation energy, and in the high temperature region differed by 4% in reaction energy, 49.7% with the pre-exponential factors, and 2.8% in activation energy in the high temperature region. In the case of the low temperature region, there was no difference between the Arrhenius equation derived apparent activation energy compared to the single reaction pathway PMTT model, evaluated at 400 K. At 700 K, the single reaction pathway PMTT yielded an apparent activation energy 3.4% off from the Arrhenius activation energy.

6.3 Dissociative Chemisorption by Initial C-H Cleavage

In the absence of per-deuterated TMB, the low and high temperature reaction mechanisms were identified by comparing the current data with previous studies. Figure 6.3 shows an Evans-Polanyi correlation between the apparent activation energies for initial C-H bond dissociative chemisorption and the activation energy for molecular desorption. The 400 K temperature dependent activation energy for TMB correlates with the activation energies of dissociative chemisorption by initial C-H bond cleavage of other alkanes, and supports an initial C-H bond dissociation mechanism at surface temperatures less than 560 K. The high temperature reaction, however, is a clear outlier, having an activation energy at 700 K equivalent to the activation energy for dissociative chemisorption by initial C-H bond cleavage of ethane. Figure 6.4 shows a plot of the pre-exponentials of dissociative chemisorption versus desorption. The low temperature dissociative chemisorption pre-exponential for TMB correlates with the pre-exponential factor for dissociative chemisorption by initial C-H bond cleavage of all other alkanes in this study. The high temperature dissociative chemisorption pre-exponential factor is significantly above the linear regression and is an outlier. The correlations in both Figure 6.3 and 6.4 indicate that the low temperature dissociative chemisorption reaction of TMB involves the cleavage of a C-H bond.

6.4 Trapping-Mediated Pyrolysis

Experiments on Ir(111), a more reactive surface relative to Pt(111), by Weinberg[2] demonstrated that alkanes with carbon-chain lengths equal to or larger than propane undergo two separate temperature dependent dissociative chemisorption reactions. For each alkane reported, the high temperature reaction became favored over the low temperature initial C-H bond

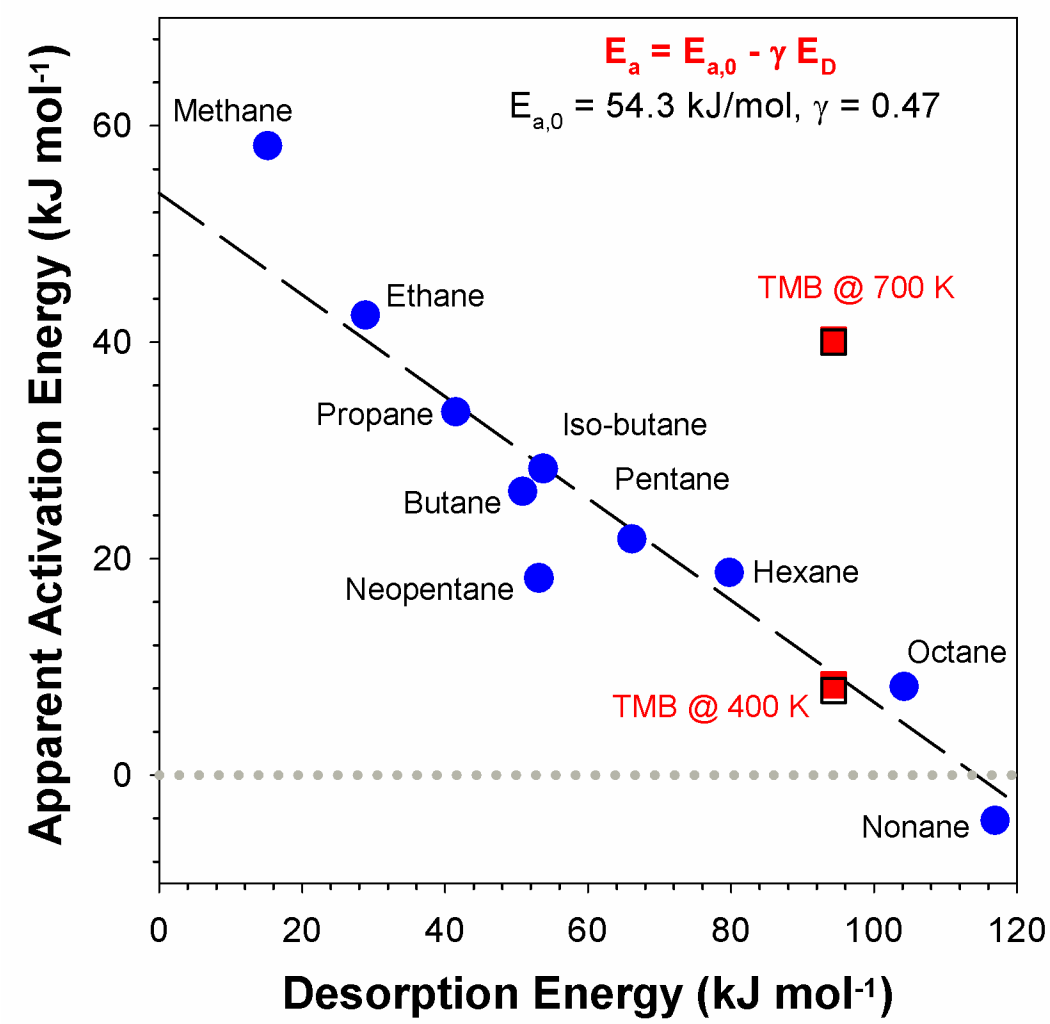

Figure 6.3: An Evans-Polanyi plot of apparent activation energy, evaluated at T = 700 K, of initial C-H bond dissociative chemisorption versus desorption energy for linear and branched alkanes from C1 to C9 (blue dots). The low and high temperature reaction activation energies for 2,2,3,3-Tetramethylbutane calculated from the Arrhenius plot (red squares) and PMTT model (empty squares) are overlaid.

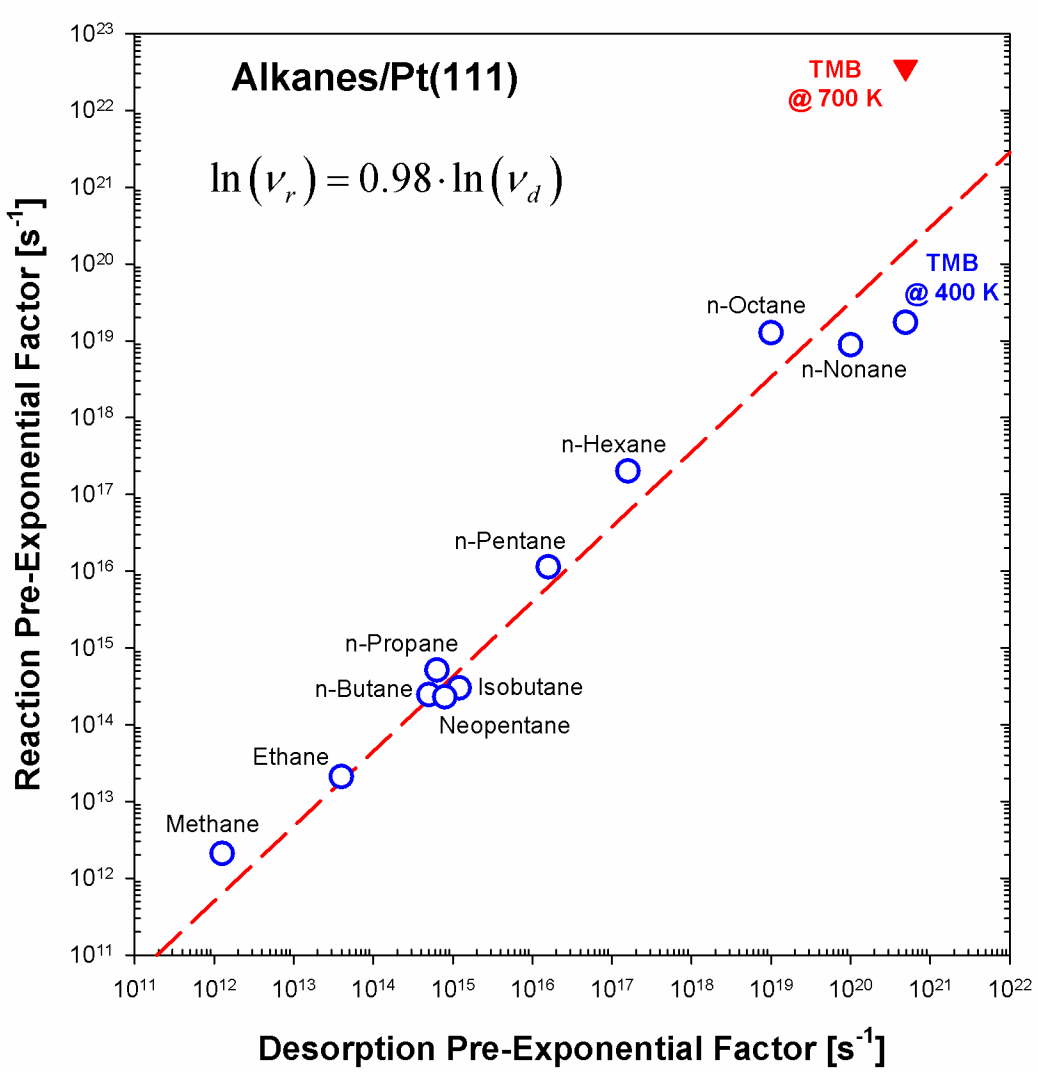

Figure 6.4: The pre-exponential factors of dissociative chemisorption (ν_r) versus desorption (ν_d) for alkanes from methane to n-nonane. The blue, open dots are the ν_r of dissociative chemisorption by initial C-H bond cleavage, whereas the red triangle is the ν_r of the high temperature dissociative chemisorption reaction of TMB. The blue dots correlate with a slope $d\ln(\nu_r)/d\ln(\nu_d) = 0.98$ and a correlation coefficient of 0.999 when the intercept is the origin.

dissociation mechanism at approximately 550 K, with exception to n-butane and isobutane which switched mechanisms at 630 K. With no significant kinetic isotope effect detected, the high temperature reaction was attributed to initial C-C dissociation. Weinberg's observations of alkane reactivity on Ir(111)[2] compare well with the current TMB study on Pt(111), because TMB also favors the high temperature mechanism at temperatures greater than 560 K. Based on these analogous observations, it is reasonable to attribute the high temperature reaction mechanism of TMB/Pt(111) to initial C-C bond dissociation. A comparison of Weinberg's neopentane/Ir(111) data to neopentane/Pt(111) and TMB/Pt(111) data is shown in Figure 6.5 below.

It is not self-evident that dissociative chemisorption by initial C-C bond cleavage should dominate the reactivity of TMB at high temperatures. The surface always has easier access to C-H bonds rather than any C-C bond. The relative weakness of the C-C bonds is negligible when considering the steric and torsional strain required to access the C-C bond prior to C-H cleavage. Additionally, the conformations required to have any C-C bond dissociate directly on the surface predicts a lower pre-exponential factor relative to C-H dissociation, which runs contrary to the $\nu_{C\text{-}H} = 7.72 \times 10^{18}\ s^{-1}$ and $\nu_{C\text{-}C} = 3.62 \times 10^{22}\ s^{-1}$ pre-exponential factors determined here for TMB/Pt(111). The relatively high pre-exponential factor argues for a "loose" or high entropy transition state for C-C dissociative chemisorption. The desorption pre-exponential factor of TMB, $\nu_d = 4.89 \times 10^{20}\ s^{-1}$, calculated using Campbell's method,[3] is significantly smaller than the C-C bond dissociation pre-exponential factor, $\nu_{C\text{-}C} = 3.62 \times 10^{22}\ s^{-1}$, determined using the two reaction pathway PMTT model, such that there is no overlap within the bounds of uncertainty. The ratio of the reaction and desorption pre-exponential factors is 74.2, ranging from 5.99 to 839 due to error. This indicates that the transition state for initial C-C bond dissociative chemisorption must have equivalent or more degrees of freedom than the transition state for a

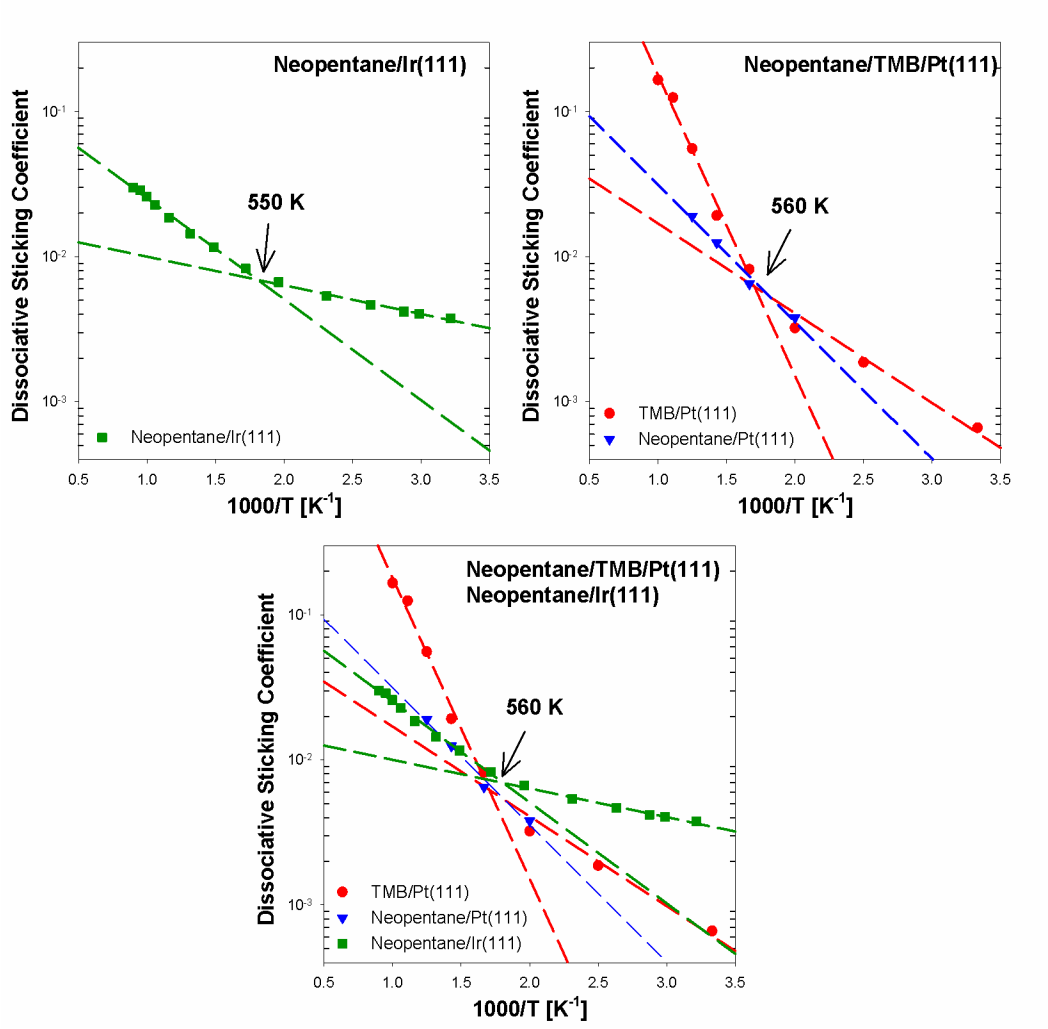

Figure 6.5: Neopentane/Ir(111), neopentane/Pt(111), and TMB/Pt(111) DSC plots, demonstrating the higher reactivity of the Ir(111) surface relative to Pt(111), considering the absolute DSCs. The two-reaction (C-H and C-C cleavage) regions of neopentane on Ir(111) are shown. A qualitative observation of TMB low temperature DSC roughly equaling neopentane DSC indicates that TMB undergoes dissociative chemisorption by C-H bond cleavage, standing with 3 methyl groups near the surface, similar to neopentane (Figure 6.6)

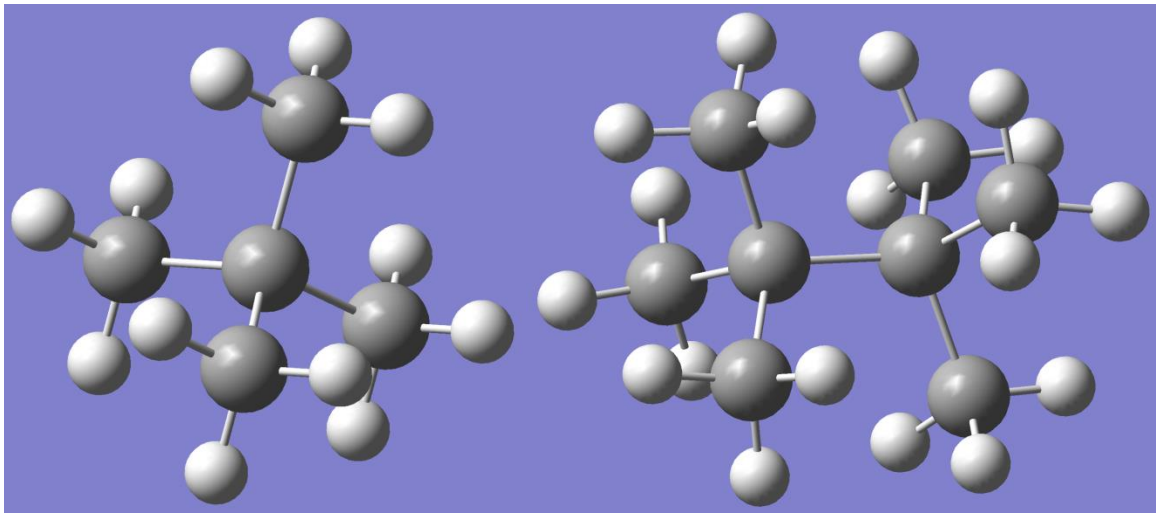

Figure 6.6: Molecular structures of neopentane (Right) and TMB (Left). Both molecules can present 3 methyl groups to the surface, which may be the favored alignment with the surface for dissociative chemisorption by initial C-H cleavage. The near equivalent absolute DSCs for dissociative chemisorption by initial C-H cleavage of TMB and Neopentane at 500 and 600 K support this supposition

molecule desorbing from the surface. The relatively weak central C-C bond of TMB suggests a C-C bond pyrolysis mechanism where the molecule undergoes a unimolecular reaction and decomposes into two t-butyl radicals. Although a pyrolysis mechanism satisfies the requirement of having more transition state degrees of freedom than C-H bond dissociative chemisorption and, perhaps, than molecular desorption, it is not obvious how the activation energy falls from the gas-phase bond dissociation energy of 322.6 kJ/mol to 40.0 kJ/mol when interacting with the surface. However, a molecule trapped in the physisorption well near the transition metal surface experiences a very different reaction environment relative to that in the gas phase. The relatively large desorption energy of TMB from Pt(111) (94.4 kJ/mol) leads to a long physisorption lifetime ($\tau_d = 1/\nu_d$, 1.31 ps at 560 K) which is sufficient for many gas/surface collisions. The presence of surface atoms provide the possibility for concerted stabilization of radical products formed during C-C bond breaking in collision-stimulated pyrolysis. If the surface orbitals are close enough and available to the electrons in the central C-C bond of TMB during the pyrolysis transition state, the transition metal surface can have a direct impact on stabilizing the transition state and products without significantly constraining the molecule. In this case, a significantly lower activation energy for pyrolysis near the surface than in the gas-phase is expected.

The equipment used to measure these dissociative sticking coefficients cannot monitor for short lived radical intermediates of the kind expected from a pyrolysis mechanism. However, even without conclusive detection of such radicals, there is evidence pointing towards C-C bond pyrolysis. It is unlikely for a reaction mechanism which has equal to or fewer transition state degrees of freedom than initial C-H bond dissociative chemisorption, such as constrained C-C bond dissociative chemisorption with surface atoms, to also have a pre-exponential factor several orders of magnitude larger in value. For a reaction which must have a transition state with at

least as many degrees of freedom as the transition state of desorption, a pyrolysis-like mechanism is more likely.

6.5 Transition State Theory Analysis

In order to evaluate the plausibility of pyrolysis as a reaction mechanism, and with pre-exponential factors as the main experimental evidence supporting such a mechanism, the ratio of the partition functions of C-C bond pyrolysis and molecular desorption were considered.

$$\nu_i = \frac{k_B T_i}{h} \frac{Q_i^{\neq}(T_i)}{Q_{R,i}(T_i)} \qquad \text{Equation 6.1}$$

where $Q_i^{\neq}$ is the transition state partition function and $Q_{R,i}$ is the reactant partition function. The ratio of the pre-exponential factors of C-C bond pyrolysis and molecular desorption for TMB is then,

$$\frac{\nu_r}{\nu_d} = \frac{T_r}{T_d} \frac{Q_r^{\neq}(T_r) Q_{R,d}(T_d)}{Q_d^{\neq}(T_d) Q_{R,r}(T_r)} \qquad \text{Equation 6.2}$$

The C-C bond dissociative chemisorption and desorption pre-exponential factors calculated from experimental data using the two reaction pathway PMTT model have a ratio of 74.2, with a lower bound of 5.99 and an upper bound of 839 due to the error in the pre-exponential factors, and were measured at $T_d \simeq 235$ K and $T_r \simeq 700$ K. The ratio of reaction to desorption pre-exponential factors as calculated using single reaction pathway PMTT model at 700 K is 37.2, ranging from 26.6 to 62.2 due to error in the fit for ν_d/ν_{high}. The single reaction pathway PMTT parameter ν_d/ν_{high} was determined exclusively from DSC data, and so $T_r = T_d$, and T_r is an undefined value between 600 and 1000 K. Because molecular desorption and dissociative

chemisorption by C-C bond pyrolysis both initiate with a molecule physisorbed to the surface, $Q_{R,r}$ and $Q_{R,d}$ only differ by T_r and T_d are equivalent when the temperatures are identical.

In the case of this analysis, the surface is in a x-y plane with the z-axis normal to the surface. Assuming TMB lies with the maximum possible number of atoms near the surface at the physisorption potential minima, the x-axis is defined lengthwise along the central C-C bond of TMB between the two quaternary carbons. The y and z axes then bisect the molecule at the midpoint of these two carbons, with the z-axis pointing away from the surface.

A TMB molecule physisorbed on Pt(111) has two dimensions of frustrated translation, limited and frustrated rotational degrees of freedom, all internal vibration modes, and a low frequency z-axis molecule-surface vibrational mode, where the z-axis is normal to the surface. Similar to ethane, as the molecules share the same symmetry point group, rotations for TMB is limited to the helicopter rotation about the z-axis (I_z = 167 amu*Å^2) and the log roll rotation around the x-axis (I_x = 179 amu*Å^2).[4] The energy requirement for cartwheel rotation around the y-axis (I_y = 167 amu*Å^2) is assumed to be negligibly less than the desorption energy, and therefore doesn't occur for a physisorbed molecule with lower symmetry than methane.

Typically the transition state for molecular desorption is taken as the freely moving gas-phase molecule far from the surface and has enhanced entropy compared to the physisorbed molecule, which is evidenced by a pre-exponential factor considerably greater than k_BT/h. The transition state for molecular desorption has two dimensions of free translation, with the third being along the reaction coordinate, z, three dimensions of free rotation, and all vibrational modes, with exception to the low-frequency gas-surface oscillation.

Because the C-C cleavage transition state must have more entropy at T_r = 700 K than the transition state of desorption at T_d = 235 K, TMB cannot be significantly constrained on the

surface during the reaction. The lowest energy distance from the surface of a molecule, without forming a covalent bond, is the physisorption potential well, and so this analysis assumes C-C bond pyrolysis occurs with the molecule still physisorbed. In this case, a molecule undergoing pyrolysis in a physisorbed collision complex maintains all degrees of freedom of a physisorbed molecule, with exception to the vibrational stretching mode of the dissociating bond. If the only molecular transformation from the reactant to the transition state is the loss of the central C-C bond stretching mode, as expected from an early transition state, the pre-exponential factor would be less than k_BT/h. A late transition state barrier with respect to the stretching of the central C-C bond of TMB allows the tertiary-butyl groups on either side of the central C-C bond to approach the trigonal-planar orientation of t-butyl radicals. A geometric shift from tetrahedral to trigonal-planar for TMB overall weakens the vibrational modes, and moderately increases the moments of inertia of the x, y, and z axes as the distance between the quaternary carbons increases with the lengthening of central bond and as the methyl groups move further from the x-axis as they move into plane with the quaternary carbons ($I_x \sim 203$ amu*Å^2, $I_y \sim 193$ amu*Å^2, $I_z \sim 193$ amu*Å^2). While an early transition state predicts a pre-exponential factor less than k_BT/h, the increased rotational and vibrational entropy with the lengthening of the central C-C bond permits a pre-exponential factor substantially larger than k_BT/h.

Assuming a late transition state for both molecular desorption and C-C bond dissociation, and assuming that frustrated translation and rotation do not differ significantly from free translation and rotation, the following equations are reasonable for the ratio of the transition state and the initial state partition functions,

Table 6.2: the ratio of dissociative chemisorption by initial C-C bond cleavage to desorption kinetic rate pre-exponential factors ($\nu_{r,C\text{-}C}/\nu_d$) of TMB calculated using Equation 6.2, where T_r = 300-1000 K and T_d = 235 K or T_r. The two reaction pathway PMTT model, fit to DSC data from 300 to 1000 K and where T_d = 235 K, yielded an average ratio of $\nu_{r,C\text{-}C}/\nu_d$ = 74.2. The single reaction pathway PMTT model, fit to DSC data from 600 to 1000 K and where $T_d = T_r$, yielded an average ratio of $\nu_{r,C\text{-}C}/\nu_d$ = 37.2.

T_r (K)	$\nu_{r,C\text{-}C}/\nu_d$ (T_d = 235 K)	$\nu_{r,C\text{-}C}/\nu_d$ ($T_d = T_r$)
300	322	275
400	325	233
500	283	178
600	231	131
700	183	94.9
800	142	68.6
900	110	49.7
1000	85.1	36.3

$$\frac{Q_r^{\neq}(T_r)}{Q_{R,r}(T_r)} = \frac{Q_{vib}^{*}(T_r)\,Q_{rot,xz}^{*}(T_r)}{Q_{vib,C-C}(T_r)\,Q_{vib}(T_r)\,Q_{rot,xz}(T_r)}$$
$$\frac{Q_d^{\neq}(T_d)}{Q_{R,d}(T_d)} = \frac{Q_{rot,xyz}(T_d)}{Q_{vib,z}(T_d)\,Q_{rot,xz}(T_d)} \qquad \text{Equation 6.3}$$

where $Q_{vib,C-C}$ is the vibrational stretching mode at 1311 cm^{-1} of the central C-C bond of TMB, $Q_{vib,z}$ is the low frequency surface-molecule z-axis oscillation, and Q* are the adjusted degrees of freedom assuming a shift towards trigonal planar geometry of the t-butyl groups due to a late transition state barrier for C-C bond dissociation. The values for the desorption and dissociative chemisorption partition functions shown in Equation 6.3 were calculated at T_d = 235 K and T_r = 300-1000 K, respectively, and at $T_r = T_d$ = 300-1000 K, using vibrational frequencies approximated using PM3 calculations.[5] Table 6.2 shows the predicted ratios of pre-exponential factors, according to Equation 6.2, across a range of T_r = 300-1000K in both the cases where T_d = 235 K and T_r. In general, the ratio of reaction to desorption kinetic rate pre-exponential factors decreases with increasing surface temperature. At a surface temperature of 1000 K, the calculated ratios closely match the experimentally derived ratios in both the case where T_d = 235 K and $T_r = T_d$. The experimental ratio of 74.2 yielded by the two reaction pathway PMTT model is 14.7% off from the predicted value of 85.1 from Equation 6.2 at T_r = 1000 K and T_d = 235 K. The experimental ratio of 37.2 yielded by the single reaction pathway PMTT model is 2.4% off from the predicted value of 36.3 from Equation 6.2 at T_r = 1000 K and T_d = 1000 K. The similarity between the experimental and theoretical pre-exponential factor ratios supports a C-C bond dissociative chemisorption mechanism where C-C bond pyrolysis occurs with the molecule trapped in the physisorption potential energy well near the Pt(111) surface. These calculations also predict a late transition state barrier for the dissociation of the central C-C bond of TMB,

such that the transition state occurs when the molecule behaves more like two linked t-butyl radicals than the initial TMB molecule.

6.6 Enthalpy of Reaction

While the pre-exponential factors for dissociative chemisorption and molecular desorption support a surface assisted pyrolysis mechanism, the previous discussion does little to explain the discrepancy between the 322.6 kJ/mol bond dissociation energy of the central C-C bond of TMB[6] and the 40.0 kJ/mol dissociative chemisorption transition state barrier on Pt(111). Kinetic isotope studies by Weinberg demonstrated that at high temperature, greater than 550 K, C-C bond dissociative chemisorption occurs for propane and larger alkanes on Ir(111),[2] but a full explanation of the mechanism and energetics was not explored. With exception to TMB in this study, no other non-cyclic alkane has been previously observed dissociating via a C-C bond on Pt(111). Alkane initial C-H bond dissociative chemisorption is already known to be more facile on Ir(111)[7] than on Pt(111),[8] which may explain why C-C bond dissociative chemisorption is not observed for n-alkanes on Pt(111) as it is on Ir(111). Enthalpies of reaction ($\Delta_r H$) of dissociative chemisorption by C-H and C-C bond cleavage give insight into the relative thermodynamic favorability of the two reaction pathways. The reaction enthalpy of dissociative chemisorption is the difference of reactant and product bond dissociation energies, D^0(A-B),

$$D^0(\text{A-B}) = \Delta_f H^0(\text{A}) + \Delta_f H^0(\text{B}) - \Delta_f H^0(\text{A-B}) \qquad \text{Equation 6.4}$$

where the bond dissociation energy is the heat of formation of moiety A, plus the heat of formation of moiety B, minus the heat of formation of A-B. The reaction enthalpy of alkane dissociative chemisorption on Pt(111) is then,

$$\Delta_r H = D^0(\text{R-A}) - D^0(\text{Pt-R}) - D^0(\text{Pt-A}) \qquad \text{Equation 6.5}$$

where R is an alkyl and A is either a hydrogen atom or a different alkyl. If the bond energies of alkane C-C and C-H bonds and Pt(111) Pt-C and Pt-H bonds are known, the heat of reaction for any alkane can be calculated. While the CRC Handbook reports bond dissociation energies for a wide variety of C-C and C-H bonds,[6] only a handful of experimental studies have reported Pt-C bond energies. It is expected that the energy of a Pt-C bond should vary no greater percentage than C-H bonds do among methyl, primary, secondary, and tertiary carbons, because Pt and H have the same electronegativity. However, the bond energies reported by Campbell for Pt-[CH_3] (197 kJ/mol) and Pt-[t-butyl] (216 kJ/mol), which have error of ± 20 which is systematic, differ such that the methyl-platinum bond is 20 kJ/mol weaker than the tertiary-platinum bond, which is contrary to the bond energy trends of C-H bonds.[9-11] The reason why the reported bond energy for Pt-[t-butyl] is greater than Pt-[CH_3] is because the t-butyl group has stronger van der Waals interactions with the surface than the methyl group. The influence of van der Waals interactions, which is well approximated by the desorption energy, accelerates impinging molecules to the surface and makes the reaction more exothermic equal to the desorption energy. Calorimetry experiments do not distinguish between covalent and van der Waals energetic contributions to the bond strength between the surface and a molecular fragment. The covalent bond energy, separate from any van der Waals contributions, of an alkane fragment to platinum is the measured bond energy minus the desorption energy,

$$D^{0-}(\text{Pt-A}) = D^{0}(\text{Pt-A}) - E_d(\text{A}) \qquad \text{Equation 6.6}$$

where a minus sign, D^{0-}, indicates the van der Waals subtracted bond energy. By substituting D^0 with D^{0-} in Equation 6.5, the reaction heat for dissociative chemisorption becomes,

$$\Delta_r H = D^{0}(\text{R-A}) - D^{0-}(\text{Pt-R}) - D^{0-}(\text{Pt-A}) - E_d(\text{R-A}) \qquad \text{Equation 6.7}$$

Table 6.3: Bond dissociation energies and van der Waals corrected bond dissociation energies are given for the weakest C-H, Pt-C, and Pt-H bonds for C_1-C_9 alkanes. The desorption energy is also shown for each alkane. Gas phase bond dissociation energies at 295 K for C-H bonds, $D^0(RH)$, were obtained from the CRC Handbook (†).[3] The Pt-C and Pt-H bond energies are derived from Pt-CH_3,[1] Pt-[t-butyl],[2] and cyclohexene[4] calorimetry studies by Campbell (‡). Desorption energies where either measured by (*) or extrapolated from (**) TPD experiments by Campbell.[5]

Alkane (RH)	$D^0(RH)^{\dagger}$	$D^0(PtR)$	$D^{0\text{-}}(PtR)$	$D^0(PtH)^{\ddagger}$	$D^{0\text{-}}(PtH)$	$E_d(RH)$	$E_d(R)$	$E_d(H)$
Methane	439.3	**194**‡	180	254	253	15.2*	14.3	0.9**
Ethane	420.5	200.	172	254	253	28.9*	28.0	0.9**
Propane	410.5	209	168	254	253	41.5*	40.6	0.9**
Butane	411.1	218	168	254	253	50.9*	50.0	0.9**
Pentane	415.1	235	170	254	253	66.2**	65.3	0.9**
Hexane	410	247	168	254	253	79.8*	78.9	0.9**
Octane	410	271	168	254	253	104.3**	103.4	0.9**
Nonane	410	284	168	254	253	117.0**	116.1	0.9**
Isobutane	400.4	**216**‡	163	254	253	53.7	52.8	0.9**
Neopentane	419.7	224	172	254	253	53.2	52.3	0.9**
TMB	419.7	265	172	254	253	94.4	93.5	0.9**

The Pt-[CH_3] and Pt-[t-butyl] bond energies adjust to 180 and 165 kJ/mol by subtracting the methyl and t-butyl group desorption energies of 14.3 and 50.7 kJ/mol, respectively.[10-11] It is already known that C-H bond dissociation energies weaken from 439 to 400 kJ/mol (8.9%) from methyl to tertiary C-H bonds due to the increased local electron density at the reactive carbon from adjacent carbon atoms,[6] and the van der Waals corrected methyl and tertiary Pt-C covalent bond energies differ by a similar percentage (8.3%). Because hydrogen and platinum have approximately equal electronegativity,[6] it is reasonable to assume that all Pt-R bonds differ from Pt-CH_3 by the same ratio that the R-H bond differs from CH_3-H. This approximation allows the Pt-C bond energies for any alkyl to be calculated by

$$D^{0-}\left(\text{Pt-R}\right) = D^{0-}\left(\text{Pt-CH}_3\right)\left(\frac{D^{0}\left(\text{R-H}\right)}{D^{0}\left(\text{CH}_3\text{-H}\right)}\right) \qquad \text{Equation 6.8}$$

using Campbell's data and gas phase bond dissociation energies for alkane C-H bonds from the CRC Handbook. The Pt-H bond energy of 254 kJ/mol was calculated from the -72 kJ/mol heat of formation of $2H_{(ads)}$ on Pt(111)[12] and the 435.77 kJ/mol room temperature gas phase bond dissociation energy of H_2.[6] Desorption energies of linear alkanes on Pt(111) were measured by Campbell and correlate with a slope of 0.9 with respect to the number of electrons in the molecules. Using E_d(R-H), from TPD experiments by Campbell and in this study, along with D^0(R-H), D^{0-}(Pt-R), and ΔD^{0-}(Pt-H), shown in Table 6.3 above, the heats of reaction for alkane dissociative chemisorption by initial C-H bond and C-C bond scission were calculated and are shown in Figure 6.7 with respect to desorption energy. Table 6.4 shows the reaction enthalpies and activation energies for dissociative chemisorption, including predictions for activation energies for dissociative chemisorption by initial C-C for alkanes other than TMB, assuming an correlation between $Ea_{,C\text{-}C}$ and E_D of approximately 0.5 as observed between $Ea_{,C\text{-}H}$ and E_D in Figure 6.3 and a maximum correlation of 1.0 for the upper range of activation energies.

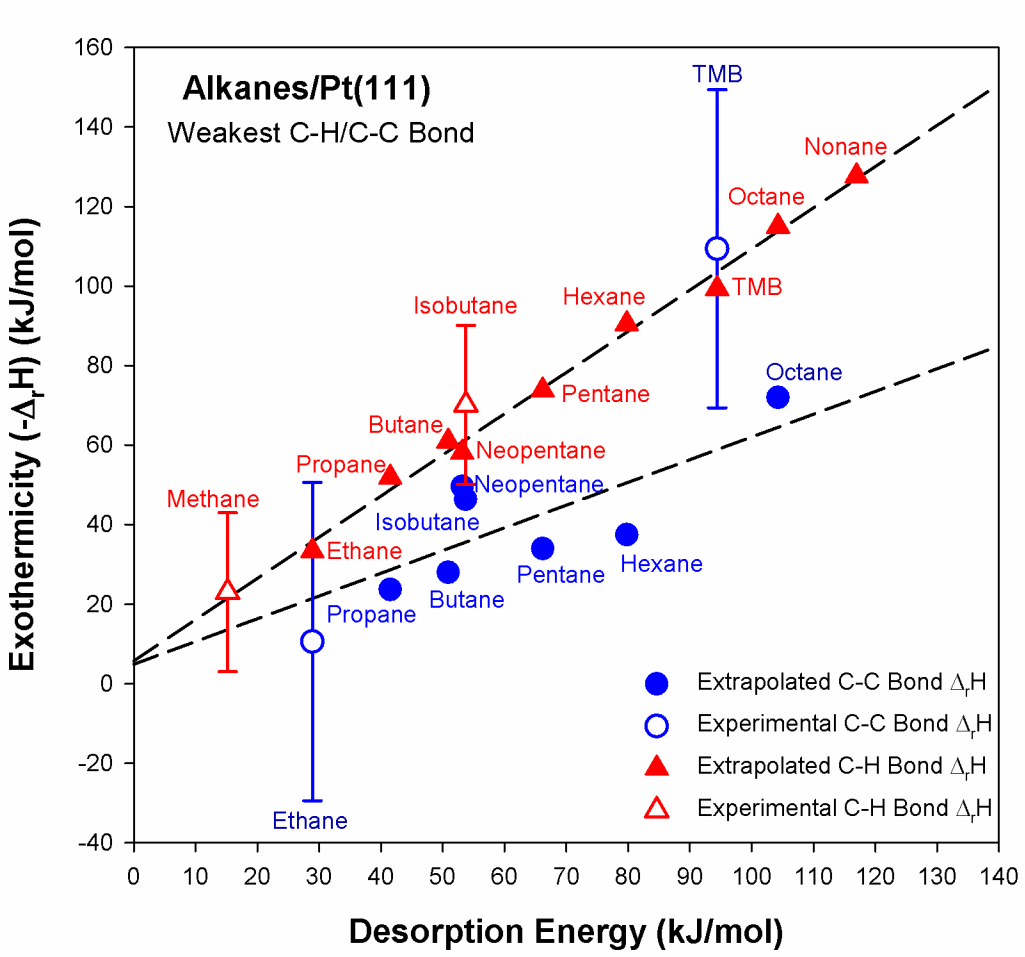

Figure 6.7: Exothermicity of dissociative chemisorption by initial C-H (red triangles) and C-C (blue circles) bond scission versus desorption energy for alkanes. Error bars are given for the experimental data (open symbols) by Campbell, but are excluded for the extrapolated heats of reaction for the alkanes without Pt(111) calorimetry experiments (filled symbols). All the error bars adjust the data in proportion to each other, because the error of each of the experimental data points is the same (± 20 for C-H and ± 20*2 for C-C) and systematic. Because of this, the relative positions of alkanes aligned along the slopes of $d\Delta_r H_{C-H}/dE_D$ and $d\Delta_r H_{C-C}/dE_D$ will not change due to error; the error will only change the intercepts $\Delta_r H_{C-H,0}$ and $\Delta_r H_{C-C,0}$ by ± 20 for C-H and ± 20*2 for C-C.

Table 6.4: Heats of reaction (Δ_rH_{C-H} and Δ_rH_{C-C}) and activation energies for dissociative chemisorption by initial C-H bond cleavage ($E_{a,C-H}$) are reported; estimated activation energies for dissociative chemisorption by initial C-C bond scission are also given assuming an Evans-Polanyi correlation, between $E_{a,C-C}$ and Δ_rH_{C-C}, with slopes of 0.5 ($E_{a,C-C,0.5}$) and 1.0 ($E_{a,C-C,max}$). The heats of reaction, Δ_rH_{C-H} and Δ_rH_{C-C}, have error of ± 20 and ± 20*2 which is systematic, because the source of error is identical for all reported heats. The bold numbers were calculated from experimental data; all other values are extrapolations from these values.

Alkane	ΔrH_{C-H}	$E_{a,C-H}$	ΔrH_{C-C}	$E_{a,C-C,0.5}$	$E_{a,C-C,max}$
Methane	**-9 ± 20**	58.1	**-**	-	-
Ethane	-33 ± 20	42.5	**-11 ± 40**	87	139
Propane	-52 ± 20	33.4	-24 ± 40	81	126
Butane	-61 ± 20	26.1	-28 ± 40	79	121
Isobutane	**-70 ± 20**	28.3	-34 ± 40	76	115
Pentane	-74 ± 20	21.6	-38 ± 40	74	112
Neopentane	-58 ± 20	18.1	-46 ± 40	70	103
Hexane	-90 ± 20	18.4	-50 ± 40	69	100
Octane	-115 ± 20	9.3	-72 ± 40	58	77
TMB	-99 ± 20	7.8	**-109 ± 40**	**40.0**	**40.0**

Both C-H and C-C reactions are exothermic for each alkane and correlate with desorption energy, such that dissociative chemisorption becomes more exothermic with an increase in desorption energy. In general, C-H bond dissociative chemisorption is more exothermic than C-C bond dissociative chemisorption for each alkane, with TMB as the exception.

$\Delta_r E_{C-H}$ and $\Delta_r E_{C-C}$ for TMB were calculated to be -99 ± 20 and -109 ± 40 kJ/mol, respectively. It should be noted that the error for both values comes from the same source, the uncertainty in the heat of formation of I_{ad} on Pt(111).[13] The Pt-[CH_3] and Pt-[t-butyl] bond energies were determined from calorimetry experiments where the heats of CH3I and (CH3)CI decomposition were measured, respectively. Because the measured heat released by the dissociative chemisorption of an alkyl iodide (R-I) is equal to the R-I bond energy minus the sum of Pt-R and Pt-I bond energies, the significant uncertainty in the Pt-I bond energy (± 20) propagates when calculating the Pt-R bond energy. The error in $\Delta_r E_{C-C}$ can be considered twice the error in $\Delta_r E_{C-H}$ for TMB. This means the maximum values of $\Delta_r E_{C-H}$ and $\Delta_r E_{C-C}$ for TMB are -79 and -69 kJ/mol, while the minimum values are -119 and -149 kJ/mol, respectively. On average, dissociative chemisorption by initial C-C bond scission is 10 kJ/mol more exothermic for TMB on Pt(111) than C-H bond dissociative chemisorption. At the extreme ends of the uncertainty, dissociative chemisorption by initial C-C bond cleavage ranges from being 10 kJ/mol less exothermic to 30 kJ/mol more exothermic than dissociative chemisorption by initial C-H bond scission for TMB. C-C bond cleavage is more exothermic than C-H bond dissociation across the majority (75%) of the range of error for TMB. In the case of all other alkanes, with exception to neopentane, dissociative chemisorption by initial C-C bond cleavage is consistently less exothermic than C-H bond cleavage across the full range of error. At the minimum extreme of the error for neopentane, dissociative chemisorption by C-C bond scission is 8 kJ/mol more

exothermic than C-H bond cleavage but is less exothermic than C-H bond cleavage for the majority (80%) of the range of error. Even accounting for the uncertainty in the alkyl bond energies with Pt(111), dissociative chemisorption by initial C-C bond scission is unusually exothermic for TMB when compared with other alkanes, and that can be attributed to the weak C-C bond between the two central quaternary carbons, which only TMB has among the alkanes considered in this study. Although the bond dissociation energy for the central C-C bond is significantly higher than the measured activation energy for C-C bond dissociative chemisorption, the enthalpies of reaction for TMB predict that C-C bond dissociation is on average more energetically favorable than C-H bond dissociation on Pt(111). Considering a late transition state barrier, the energy requirement for bond dissociation may decrease significantly from the gas-phase BDE due to the proximity of the surface and the strong bond potential between Pt(111) and the t-butyl radicals relative to the BDE.

References

1. Haynes, W. M., *Crc Handbook of Chemistry and Physics*, 94 ed.: Taylor & Francis Limited, 2013.
2. Johnson, D. F.; Weinberg, W. H., Quantification of the Selective Activation of C-C Bonds in Short-Chain Alkanes - Reactivity of Ethane, Propane, Isobutane, N-Butane and Neopentane on Ir(11). *Journal of the Chemical Society-Faraday Transactions* **1995**, *91*, 3695-3702.
3. Tait, S. L.; Dohnalek, Z.; Campbell, C. T.; Kay, B. D., N-Alkanes on Pt(111) and on C(0001)/Pt(111): Chain Length Dependence of Kinetic Desorption Parameters. *J. Chem. Phys.* **2006**, *125*, 234308.
4. Tait, S. L.; Dohnalek, Z.; Campbell, C. T.; Kay, B. D., N-Alkanes on Mgo(100). Ii. Chain Length Dependence of Kinetic Desorption Parameters for Small N-Alkanes. *J. Chem. Phys.* **2005**, *122*, 164708.
5. Jensen, J. H.; Kromann, J. C., The Molecule Calculator: A Web Application for Fast Quantum Mechanics-Based Estimation of Molecular Properties. *J. Chem. Educ.* **2013**, *90*, 1093-1095.
6. Haynes, W. M.; Lide, D. R.; Bruno, T. J., *Crc Handbook of Chemistry and Physics : A Ready-Reference Book of Chemical and Physical Data*, 2015.
7. Abbott, H. L.; Harrison, I., Dissociative Chemisorption and Energy Transfer for Methane on Ir(111). *J. Phys. Chem. B* **2005**, *109*, 10371-10380.
8. Bukoski, A.; Abbott, H. L.; Harrison, I., Microcanonical Unimolecular Rate Theory at Surfaces. Iii. Thermal Dissociative Chemisorption of Methane on Pt(111) and Detailed Balance. *J. Chem. Phys.* **2005**, *123*, 094707.
9. Karp, E. M.; Silbaugh, T. L.; Campbell, C. T., Energetics of Adsorbed Ch_3 on Pt(111) by Calorimetry. *J. Am. Chem. Soc.* **2013**, *135*, 5208-5211.
10. Silbaugh, T. L.; Giorgi, J. B.; Xu, Y.; Tillekaratne, A.; Zaera, F.; Campbell, C. T., Adsorption Energy of Tert-Butyl on Pt(111) by Dissociation of Tert-Butyl Iodide: Calorimetry and Dft. *J. Phys. Chem. C* **2014**, *118*, 427-438.
11. Karp, E. M.; Silbaugh, T. L.; Campbell, C. T., Energetics of Adsorbed Ch_3 and Ch on Pt(111) by Calorimetry: Dissociative Adsorption of Ch_3i. *J. Phys. Chem. C* **2013**, *117*, 6325-6336.
12. Lytken, O.; Lew, W.; Harris, J. J. W.; Vestergaard, E. K.; Gottfried, J. M.; Campbell, C. T., Energetics of Cyclohexene Adsorption and Reaction on Pt(111) by Low-Temperature Microcalorimetry. *J. Am. Chem. Soc.* **2008**, *130*, 10247-10257.
13. Labayen, M.; Furman, S. A.; Harrington, D. A., A Thermal Desorption Study of Iodine on Pt(111). *Surf. Sci.* **2003**, *525*, 149-158.

Section 7 – Evans-Polanyi Correlation

Section **Page**

7.1 Overview

The apparent activation energies of alkanes dissociative chemisorption by initial C-H bond cleavage on Pt(111) decrease significantly as the alkane size increases. When looking only at methane (58.1 kJ/mol), ethane (42.5 kJ/mol), n-propane (33.4 kJ/mol), and isobutane (28.3 kJ/mol), the differences in activation energy appear to be proportional to the differences among methyl (439.3 kJ/mol), primary (420.5 kJ/mol), secondary (410.5 kJ/mol), and tertiary (400.4 kJ/mol) C-H bond dissociation energies.[1] The activation energies of dissociative chemisorption and the weakest C-H bonds of these four alkanes correlate with a slope of 0.79 and a correlation coefficient of 0.99. However, this correlation deteriorates when other alkanes are considered. Figure 7.1 shows the apparent activation energies of dissociative chemisorption with respect to the weakest C-H bond in each alkane reported in this study, with exception to n-nonane, which does not have bond dissociation energies in the literature. Alkanes which share similar weakest C-H bond dissociation energies still differ significantly in activation energy, which indicates that some other stabilizing force plays a role in lowering the activation energy.

The Evans-Polanyi assumption is that the apparent activation energy should scale linearly with the heat of reaction for a series of related reactions, such that,

$$E_a = \gamma \Delta_r H + \beta \qquad \text{Equation 7.1}$$

where $\Delta_r H$ is the heat of reaction, $0 \leq \gamma \leq 1$, and β is a constant. A value of γ which is closer to 0 indicates an early transition state, which resembles the reactants. Conversely, a value of γ which is closer to 1 indicates a late transition state, which resembles the products. In the case where $\gamma \neq 0$, any force which makes a reaction more exothermic helps lower the activation energy. Van der Waals interactions are a force which accelerates molecules towards the surface, and stabilize the products of the reaction, thereby making the dissociative chemisorption of alkanes on Pt(111)

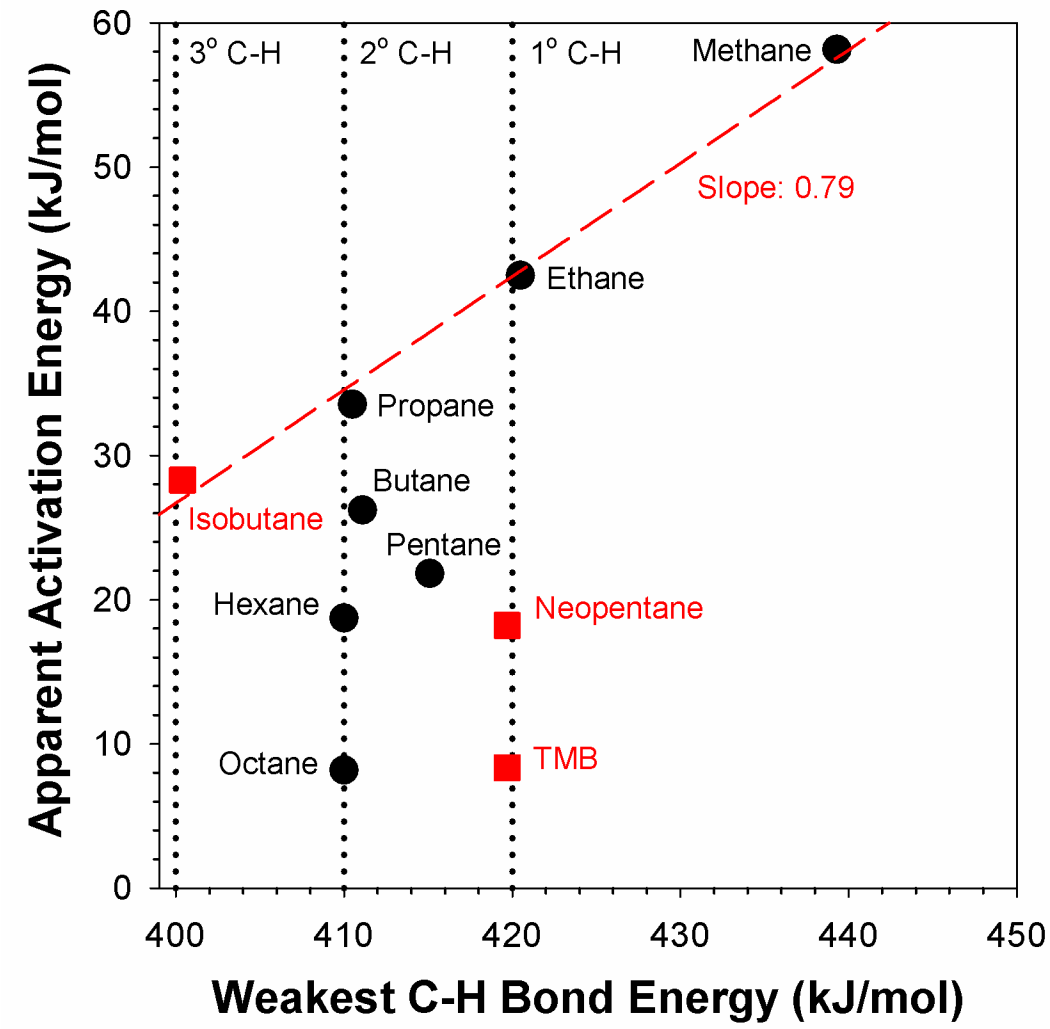

Figure 7.1: Apparent activation energy of dissociative chemisorption by initial C-H bond cleavage versus weakest C-H bond dissociation energy for alkanes on Pt(111). The slope among methane, ethane, n-propane, and isobutane is 0.79 with a 0.99 correlation coefficient. This correlation falls apart with larger alkanes.

more exothermic. The desorption energy is a good approximation of van der Waals interactions of an alkane with the Pt(111). As mentioned in Section 1.7 and Section 4, Campbell reported that the desorption energy of n-alkanes increases linearly with carbon-chain length. When activation energy decreases and desorption energy increases with respect to alkane size, it is reasonable to predict an Evans-Polanyi correlation between E_a and E_D, which has the form of,

$$\Delta_r H = \Delta_r H^0 - E_D \qquad \text{Equation 7.2}$$

$$E_a = -\gamma E_D + (\gamma \Delta_r H^0 + \beta) \qquad \text{Equation 7.3}$$

where $\Delta_r H^0$ is the heat of reaction in the absence of van der Waals interactions, which is simply the sum of the heats of all covalent bonds broken minus the sum of the heats of all covalent bonds formed.

7.2 Van der Waals Stabilization of Dissociative Chemisorption

Desorption energy values for linear alkanes were obtained from Campbell,[2] and are reported along with the Arrhenius and PMTT derived rate constants in Table 7.1 below. The desorption energies of isobutane, neopentane, and TMB are discussed in detail in Section 4 of this study and are shown in Table 7.1 as well. Figure 7.2 below shows the Evans-Polanyi plot between the apparent activation energy of dissociative chemisorption by initial C-H bond cleavage, calculated using Arrhenius fits of alkane DSC, and desorption energy for alkanes. An error-weighted linear least squares fit of the Arrhenius-derived E_a data to Equation 7.3 yielded $\gamma = 0.50 \pm 0.04$ and $E_{a,0} = 55.4 \pm 3.5$ kJ/mol, which is shown as the dashed line in Figure 7.2 below. A second error-weighted linear least squares fit of the PMTT-derived E_a data to Equation 7.3 yielded $\gamma = 0.51 \pm 0.06$ and $E_{a,0} = 55.6 \pm 3.8$ kJ/mol, which differ negligibly in comparison to the Arrhenius-derived values. All of the alkanes in this study, with exception to methane and

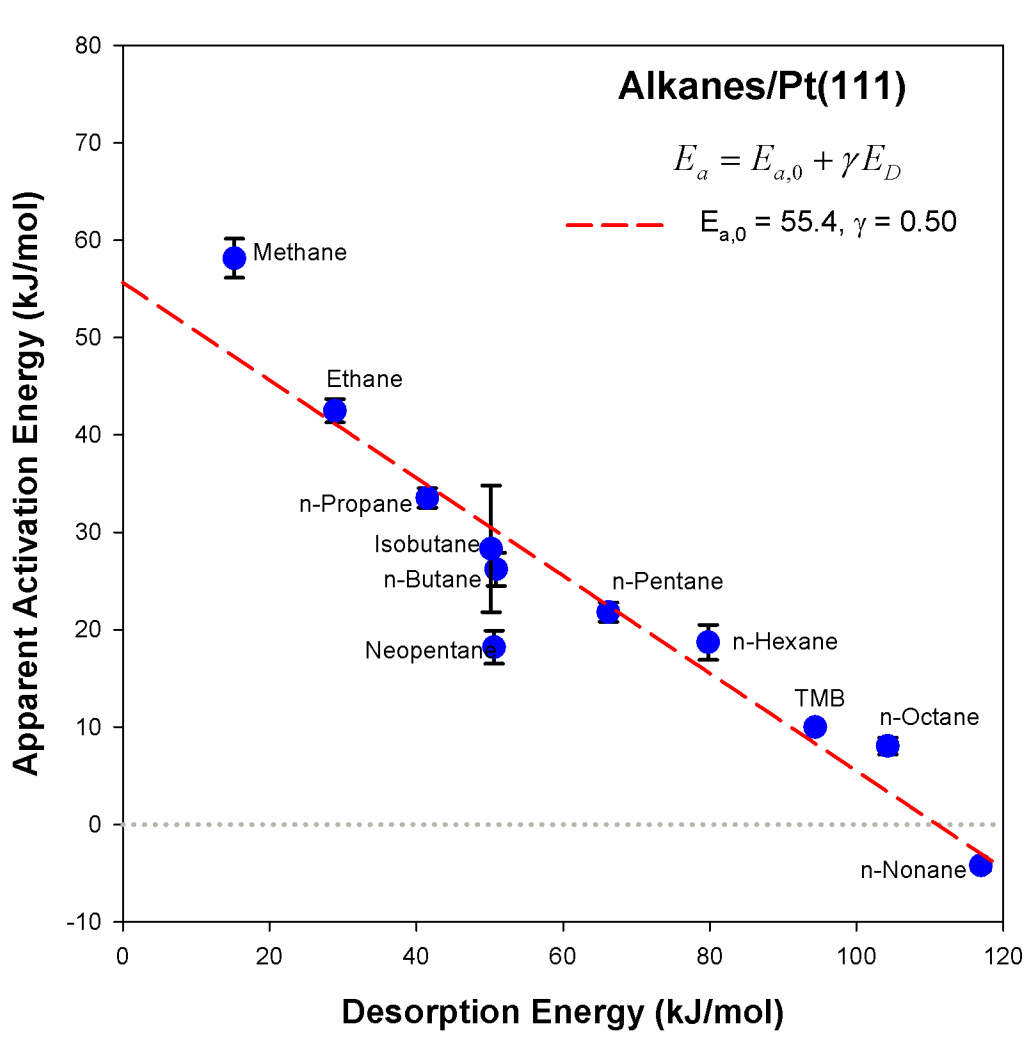

Figure 7.2: An Evans-Polanyi plot of the apparent activation energy for dissociative chemisorption versus the desorption energy for C_1-C_9 alkanes (blue dots), which correlate with $\gamma = 0.50 \pm 0.04$ and $E_{a,0} = 55.4 \pm 3.5$ kJ/mol, by the Arrhenius fit (dashed red line); error bars are the standard deviation in E_a, as calculated from Arrhenius fit, for each molecule.

Table 7.1: Activation energies for dissociative chemisorption of linear and branched alkanes; (†) data was gathered by Tait *et al*.[5] (‡) values were extrapolated using Tait's model; (*) value was found using E_a(400K)

		Desorption		PMTT			Arrhenius	
Alkane	**N_c**	**log(ν_d)**	**E_d**	**log(ν_r)**	**E_r-E_d**	**E_a(700K)**	**E_a**	**S_0**
Methane	1	12.1†	15.2†	12.3	58.1	58.1	58.1	1.7
Ethane	2	13.6†	28.9†	13.3	42.5	42.5	42.5	0.53
Propane	3	14.8†	41.5†	14.7	33.5	33.4	33.5	0.81
Butane	4	14.7†	50.9†	14.4	26.2	26.1	26.2	0.49
Isobutane	4	14.6	50.2	16.3	28.3	28.3	28.3	0.25
Pentane	5	16.2‡	66.2‡	16.1	21.9	21.6	21.8	0.68
Neopentane	5	14.8	50.6	14.4	18.3	18.1	18.2	0.28
Hexane	6	17.2†	79.8†	15.3	19.2	18.4	18.7	1.1
Octane	8	19.0‡	104‡	19.1	9.5	7.64	8.14	0.79
TMB	8	20.7	94.4	18.1	8.4	10.0	10.0	0.02
Nonane	9	20.0‡	117‡	18.9	-17.6	-6.24	-4.21	0.30

neopentane, fell in close proximity to these fits of the Evans-Polanyi plot. Methane and neopentane, as outliers, have features in common with each other that none of the other alkanes in this study share. Both molecules have the highest symmetry number ($\sigma = 12$) of alkanes in this study, with ethane and TMB ($\sigma = 6$) being the closest to them, and have numerous degenerate vibrational modes which contribute to their relatively poor gas-surface energy exchange. In the case where gas-surface energy exchange plays a significant role in stabilizing the transition state, perhaps by changing how late the transition state is (a larger γ), there should be a different Evans-Polanyi correlation among the alkanes which did not fully thermalize to the surface temperature (methane, ethane, n-propane, isobutane, and n-butane) when compared with the correlation among alkanes which did (n-pentane and larger alkanes). Direct dissociative chemisorption will be the term used to describe dissociative chemisorption which occurs with minimal or partial gas-surface energy exchange, whereas indirect dissociative chemisorption will be the term to describe dissociative chemisorption where the molecule thermalizes to the surface temperature, falling into the physisorption potential energy well prior to reaction.

An error-weighted linear least squares fit of the Arrhenius-derived E_a data for alkanes which undergo direct dissociative chemisorption yielded $\gamma = 0.95 \pm 0.12$ and $E_{a,0} = 71.4 \pm 4.6$ kJ/mol, which is shown as the dashed blue line in Figure 7.3 below. A second error-weighted linear least squares fit of the PMTT-derived E_a data for alkanes which undergo direct dissociative chemisorption yielded $\gamma = 0.95 \pm 0.11$ and $E_{a,0} = 71.3 \pm 4.4$ kJ/mol, which differ negligibly in comparison to the Arrhenius-derived values. The Evans-Polanyi correlation among direct alkanes is significantly different from the correlation among all alkanes. This indicates that the transition state of dissociative chemisorption for alkanes which have poor gas-surface energy exchange is late, with respect to motion towards the surface, when compared to the transition

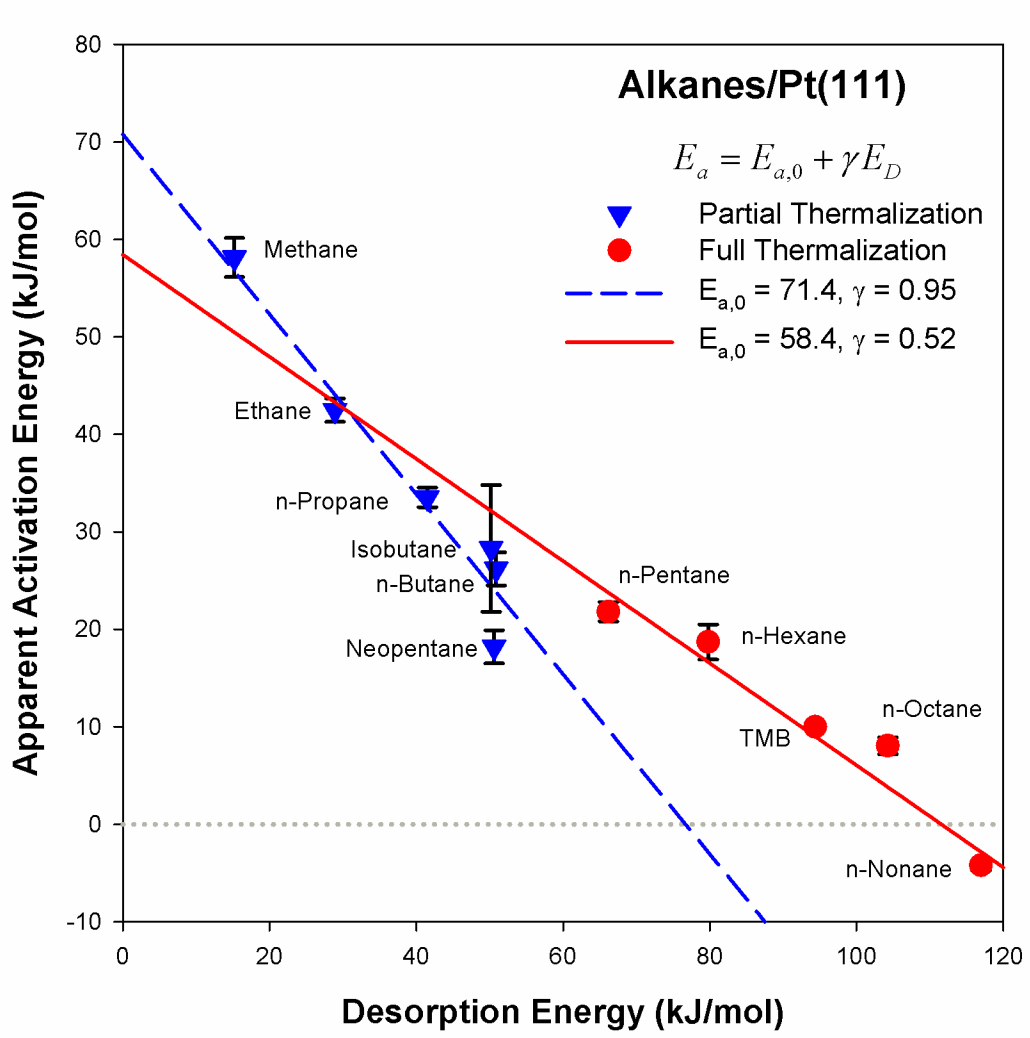

Figure 7.3: An Evans-Polanyi plot of the apparent activation energy for dissociative chemisorption versus the desorption energy for C_1-C_9 alkanes; neopentane, butane, and smaller alkanes (blue triangles) which do not fully thermalize to the surface temperature prior to reacting correlate with $\gamma = 0.95 \pm 0.12$ and $E_{a,0} = 71.4 \pm 4.6$ kJ/mol, by the Arrhenius fit (dashed blue line); larger alkanes which thermalize to the surface temperature (red dots) correlate with $\gamma = 0.52 \pm 0.09$ and $E_{a,0} = 58.4 \pm 9.5$ kJ/mol, by the Arrhenius fit (solid red line). The error bars are the standard deviation in E_a, as calculated from Arrhenius fit, for each molecule.

state of alkanes which thermalize to the surface temperature. An error-weighted linear least squares fit of the Arrhenius-derived E_a data for alkanes which undergo indirect dissociative chemisorption yielded $\gamma = 0.52 \pm 0.09$ and $E_{a,0} = 58.4 \pm 9.5$ kJ/mol, which is shown as the solid red line in Figure 7.3. A second error-weighted linear least squares fit of the PMTT-derived E_a data for alkanes which undergo indirect dissociative chemisorption yielded $\gamma = 0.46 \pm 0.09$ and $E_{a,0} = 53.1 \pm 8.1$ kJ/mol, which differ negligibly in comparison to the Arrhenius-derived values. These fits are similar to the Evans-Polanyi correlation among all alkanes and indicate that alkanes which exchange energy well with the surface have a relatively early, with respect to motion towards the surface, transition state for dissociative chemisorption.

7.3 Thermodynamic Correlation

It may be merely coincidence that the alkanes which undergo direct chemisorption and the alkanes which undergo indirect chemisorption have separate Evans-Polanyi correlations. Equation 7.3 above makes the assumption that $(\gamma\Delta_r H^0 + \beta)$ is constant. However, $\Delta_r H^0$ is not constant among all alkanes, in the same manner as C-H bond dissociation energies are not the same for all C-H bonds. Section 6 discusses the thermodynamics of alkane dissociative chemisorption. Table 6.4 shows $\Delta_r H_{C-H}$ and E_a of dissociative chemisorption by initial C-H bond cleavage for alkanes on Pt(111). An Evans-Polanyi plot of the apparent activation energies versus the exothermicity ($-\Delta_r H$) is shown in Figure 7.4 below.

A linear least squares fit of the apparent activation energies and heats of reaction (Table 7.2) for dissociative chemisorption of alkanes to Equation 7.1 yielded $\gamma = 0.46 \pm 0.04$ and $E_{a,0} = 56 \pm 23$ kJ/mol, which is shown as the dashed black line in Figure 7.4 below. This fit takes into account the different C-H bond types of the alkanes, including methyl, primary, secondary, and

Table 7.2: Heats of reaction ($\Delta_r H_{C-H}$) and activation energies for dissociative chemisorption by weakest C-H bond cleavage ($E_{a,C-H}$) are reported. The heats of reaction, $\Delta_r H_{C-H}$, have error of ± 20 which is systematic, because the source of error is identical for all reported heats. The bold numbers were calculated from experimental data; all other values are extrapolations from these values.

Alkane	ΔrH_{C-H}	$E_{a,C-H}$
Methane	**-9 ± 20**	58.1
Ethane	-33 ± 20	42.5
Propane	-52 ± 20	33.4
Butane	-61 ± 20	26.1
Isobutane	**-67 ± 20**	28.3
Pentane	-74 ± 20	21.6
Neopentane	-56 ± 20	18.1
Hexane	-90 ± 20	18.4
Octane	-115 ± 20	9.3
TMB	-99 ± 20	7.8

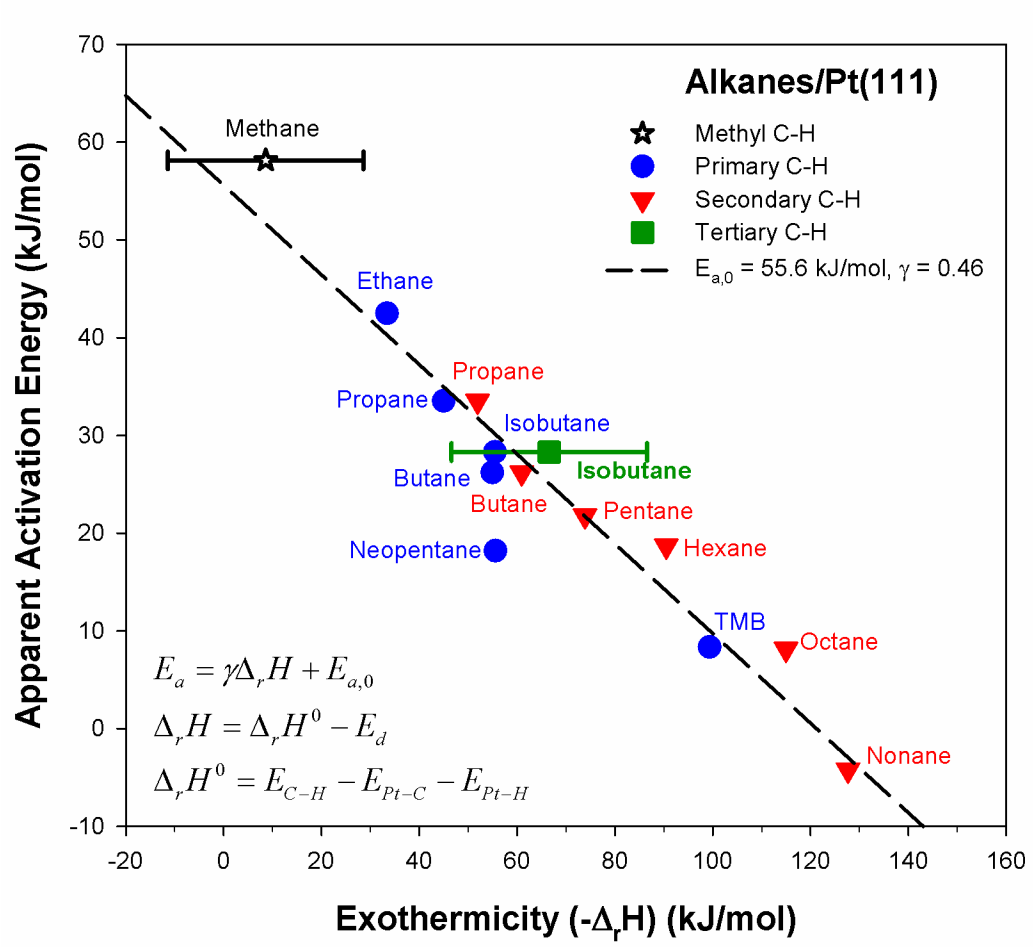

Figure 7.4: Evans-Polanyi plot of apparent activation energy for alkane dissociative chemisorption by initial C-H bond cleavage versus the exothermicity calculated from the weakest C-H bond. Points are separated into groups by the weakest C-H bond, including methyl (black open star), primary (blue dots), secondary (red triangles), and tertiary (green open square) C-H bonds. The error bars are associated with the Pt-alkyl bond energies experimentally measured by Campbell, which were used to derive the Pt-alkyl bond energies for the rest of the alkanes. The error shown for methane and isobutane have the same source and do not vary independently from each other.

tertiary C-H bonds where applicable. When compared to the Evans-Polanyi correlation between E_a and E_D, this fit does not differ significantly by either slope or $E_{a,0}$. Additionally, methane does not deviate significantly from the line. It should be noted, as described in Section 6.6, that the ± 20 error bars in Figure 7.4 come from the same measurement and have covariance. This indicates that the slope of $\gamma = 0.46 \pm 0.04$ and the relative position of alkanes along the $-\Delta_r H$ axis are not affected by this error. However, the intercept $E_{a,0} = 56 \pm 23$ does vary with the error, as all of the values of $-\Delta_r H$ for alkanes would change in unison depending where the true value among ± 20 lies. Neopentane still deviates from this line, having an E_a lower than expected for an alkane with $\Delta_r H = -58$ kJ/mol, for reasons which are not entirely clear from present evidence. There has been speculation that the distance of the hydrogen atoms in neopentane align well with the distance between three-fold hollow sites on Pt(111),[3] which may reduce some unmeasured strain that the other alkanes experience when undergoing dissociative chemisorption. The ~10 kJ/mol difference in activation energy between n-butane and neopentane is approximately equal to the ~13 kJ/mol torsional strain of eclipsed hydrogen atoms. It is plausible that neopentane has a low activation energy due to less overall torsional strain than other alkanes; however, there is not enough evidence in this study to resolve that question.

Additional least squares fits of the E_a and $-\Delta_r H$ data to Equation 7.1 were performed for direct and indirect dissociative chemisorption and yielded $\gamma = 0.61 \pm 0.10$ and $E_{a,0} = 62 \pm 25$ kJ/mol for the direct alkanes and $\gamma = 0.46 \pm 0.09$ and $E_{a,0} = 58 \pm 29$ kJ/mol for the indirect alkanes. These fits still indicate that direct dissociative chemisorption has a later transition state than indirect dissociative chemisorption. However, when considering the standard deviation of the fit, the $\gamma = 0.61 \pm 0.10$ among direct alkanes does not differ much from the $\gamma = 0.46 \pm 0.09$

Table 7.3: The constants for the Evans-Polanyi correlations between apparent activation energy, calculated from Arrhenius and PMTT model fits, and desorption energy and between apparent activation energy and exothermicity ($-\Delta_r H$), for all alkanes reported in the study, direct alkanes which do not fully thermalize to the surface temperature (methane, ethane, n-propane, n-butane, isobutane, and neopentane), and indirect alkanes which fully thermalize to the surface temperature (n-pentane and larger alkanes). The error bars are the standard deviation in E_a, as calculated from Arrhenius fit, for each molecule.

Model	$E_{a,0}$	γ	Direct $E_{a,0}$	Direct γ	Indirect $E_{a,0}$	Indirect γ
Arrhenius	55.3 ± 3.5	0.50 ± 0.04	71.4 ± 4.6	0.95 ± 0.12	58.4 ± 9.5	0.52 ± 0.09
PMTT	55.6 ± 3.8	0.51 ± 0.06	71.3 ± 4.4	0.95 ± 0.11	53.1 ± 8.1	0.46 ± 0.09
$\Delta_r H$	56 ± 23	0.46 ± 0.04	62 ± 25	0.61 ± 0.10	58 ± 29	0.46 ± 0.09

from the fit to indirect alkanes as well as $\gamma = 0.46 \pm 0.04$ from the fit to all alkanes. In the case where neopentane does experience less torsional strain than all other alkanes and is an outlier in Figure 7.4, the $\gamma = 0.61 \pm 0.10$ value would decrease to $\gamma = 0.55 \pm 0.05$, which indicates that gas-surface energy exchange may not significantly affect the transition state, or at least to the degree indicated by the Evans-Polanyi correlation between apparent activation energy and desorption energy. Rather, these fits indicate that the variation in Pt-C bond energies, reported in more detail in Section 6.6, and desorption energies with alkane size plays a significant role in stabilizing the transition state and products, which in turn lowers the apparent activation energy. Table 7.3 shows the Evans-Polanyi constants for the correlations between the Arrhenius-derived E_a versus E_D, the PMTT-derived E_a versus E_D, and the Arrhenius-derived E_a vs $-\Delta_r H$.

References

1. Haynes, W. M.; Lide, D. R.; Bruno, T. J., *Crc Handbook of Chemistry and Physics : A Ready-Reference Book of Chemical and Physical Data*, 2015.
2. Tait, S. L.; Dohnalek, Z.; Campbell, C. T.; Kay, B. D., N-Alkanes on Pt(111) and on C(0001)/Pt(111): Chain Length Dependence of Kinetic Desorption Parameters. *J. Chem. Phys.* **2006**, *125*, 234308.
3. Kao, C. L.; Madix, R. J., The Adsorption Dynamics of Molecular Methane, Propane, and Neopentane on Pd(111): Theory and Experiment. *J. Phys. Chem. B* **2002**, *106*, 8248-8257.

Section 8 – Graphene Growth by 2,2,3,3-Tetramethylbutane Chemical Vapor Deposition

Section **Page**

8.1 Identification of Graphene by AES

Methane, the least reactive alkane,[1-2] is known to form graphene on Pt(111) at temperatures of 800 K and above.[3-5] Consequently, larger, more reactive alkanes should also form graphene at these temperatures. AES spectra (Figure 8.1) analysis of TMB dosed onto heated Pt(111) at different surface temperatures support this prediction. It is not trivial to identify the hybridization of carbon deposited on a Pt(111) surface by Auger electron spectroscopy, because the low energy (< 270 eV) fingerprints below the 275 eV C KLL Auger peak are obscured by the Pt Auger peaks at 241 and 256 eV. Therefore the sp^2 and sp^3 characteristics for carbon on Pt can only be supported by analysis of the peak shape near 275 eV. A study by Hanagata demonstrated that graphene shifts the C KLL peak in AES to lower energies with respect to highly oriented pyrolytic graphite (HOPG),[6] which does not have a peak shift relative to diamond or amorphous carbon.[7] AES spectra of the C KLL peak measured for TMB dosed at 700 K and higher surface temperatures shifted to lower energies relative to the C KLL peaks of TMB dosed onto a 600 K or lower surface. The shift in the C KLL peak towards lower energies for TMB dosed onto Pt(111) at 700 K and higher, the surface temperature range at which graphene formation is known to occur for alkanes and alkenes, is indicative of graphene. Steffen reported that a secondary peak around 279 eV on the 275 eV C KLL peak was indicative of high sp^3 hybridization for amorphous carbon.[8] This 279 eV secondary peak was observed in AES spectra (Figure 8.2 Arrow) for TMB dosed at surface temperatures less than 600 K, mostly vanished but was still perceivable in the T_s = 600 K spectra, and was not observed in any amount in spectra from TMB dosed at surface temperatures of 700 K or greater. The high temperature red-shift of the C KLL AES peak supports TMB forming graphene at temperatures of 700 K and higher, which only differs from the case of methane in that TMB begins forming graphene at

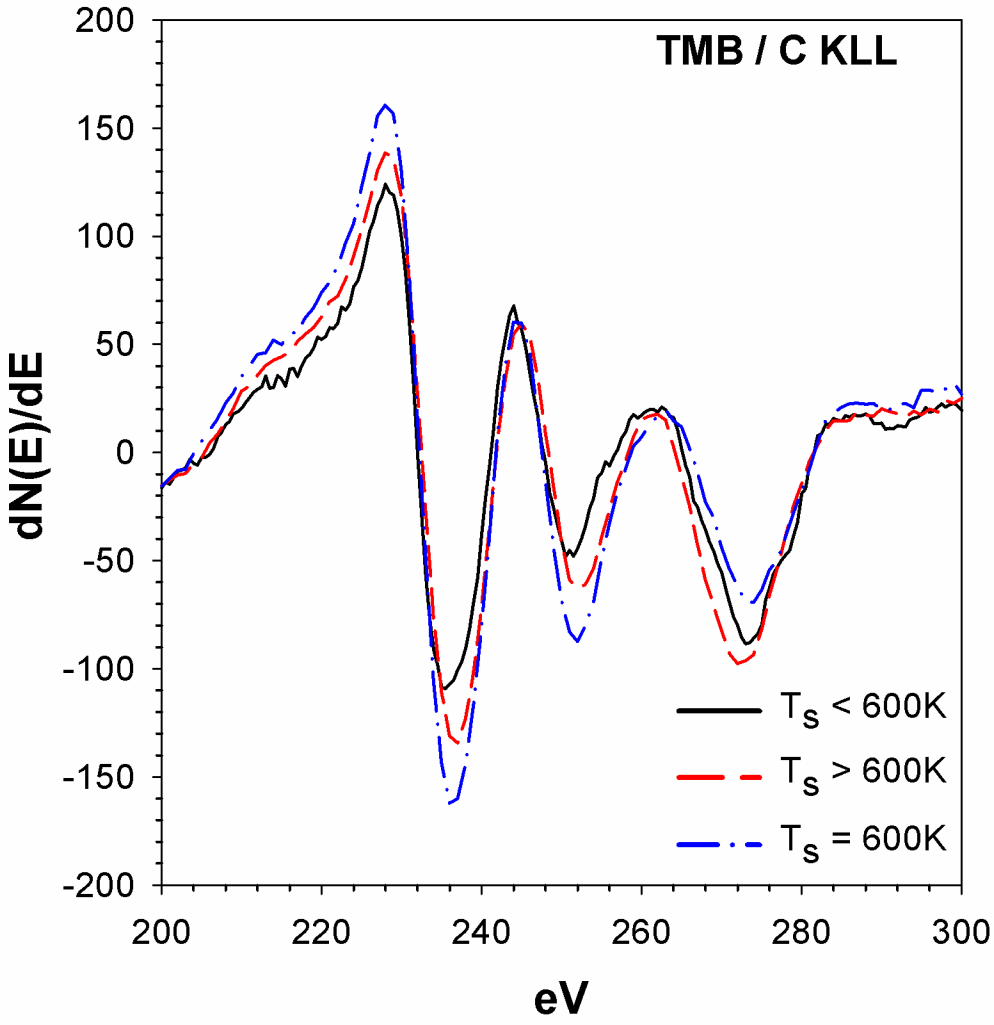

Figure 8.1: First differential, dN(E)/dE, AES spectra near the 275 eV C KLL auger peak for TMB dosed onto Pt(111) at different surface temperatures and near equal total carbon coverages; spectra obtained from TMB dosed onto surface temperatures of 300 to 500 K (Black Line) and of 700 to 1000 K (Red Dashed Line) were averaged together; data obtained from T_s = 600 K are shown independently (Blue Dot-Dashed Line); the arrow points to a peak at 279 eV which is indicative of high sp^3 hybridization[8]

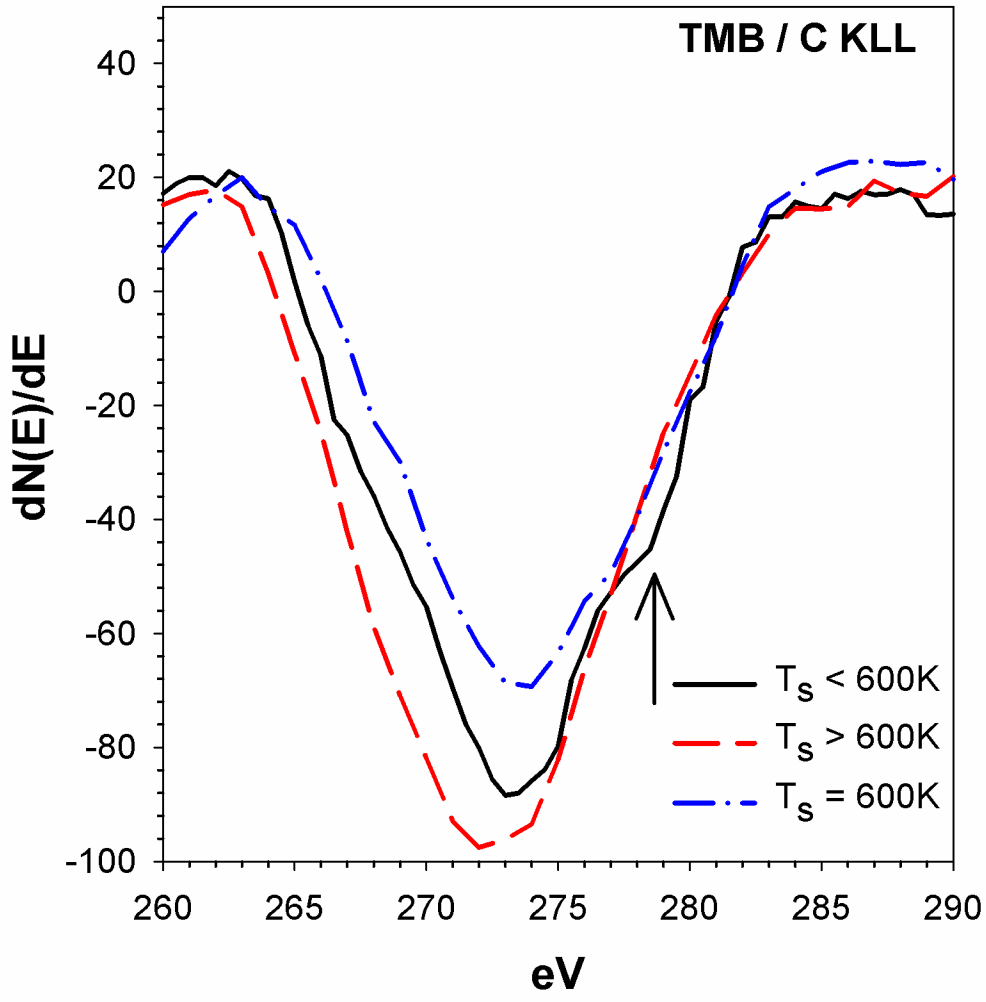

Figure 8.2: First differential, dN(E)/dE, AES spectra near the 275 eV C KLL auger peak for TMB dosed onto Pt(111) at different surface temperatures and near equal total carbon coverages; spectra obtained from TMB dosed onto surface temperatures of 300 to 500 K (Black Line) and of 700 to 1000 K (Red Dashed Line) were averaged together; data obtained from T_s = 600 K are shown independently (Blue Dot-Dashed Line); the arrow points to a peak at 279 eV which is indicative of high sp^3 hybridization[8]

surface temperatures below 800 K. The C KLL lineshape also matches with the expectation that TMB forms mostly sp^3 bonds with the Pt(111) surface at colder (< 600 K) surface temperatures.

6.2 Saturation Carbon Coverage

The rate and mechanism of TMB carbon deposition onto Pt(111) increases significantly with an increase in temperature, as shown by Figure 8.3. The dissociative sticking coefficients, energetics, and reaction mechanisms for the initial dissociative chemisorption of TMB will be discussed in more detail elsewhere, and a brief description follows. At surface temperatures lower than 560 K, TMB undergoes dissociative chemisorption by initial C-H bond cleavage, similar to observations for other alkanes. At 560 K and higher temperatures, dissociative chemisorption by initial C-C bond scission of the weak central bond between two quaternary carbons becomes the favored reaction pathway and rapidly increases the absolute dissociative sticking coefficient. A plot of experimental coverage versus exposure at different surface temperatures shown by Figure 8.3 matches with these temperature dependent reaction mechanisms. Least squares fits of the experimental coverage versus exposure data to Equation 3.33 were calculated for each surface temperature and are included as solid lines in Figure 8.3. At surface temperatures of 300 to 500 K, TMB had a saturation coverage of 0.858 ML with respect to platinum and required three binding sites. At 600 K the number of required binding sites decreased to two and the saturation coverage increased to 1.10 ML. Surface temperatures of 700 to 1000 K had saturation carbon coverages of 1.35 ML, and the number of binding sites decreased from two to one at 900 and 1000 K. While the coverage data at 600 K appears to be an outlier due to having a saturation coverage between 500 and 700 K, this is because a TMB molecule can undergo C-C bond dissociative chemisorption, unlike lower temperatures, but

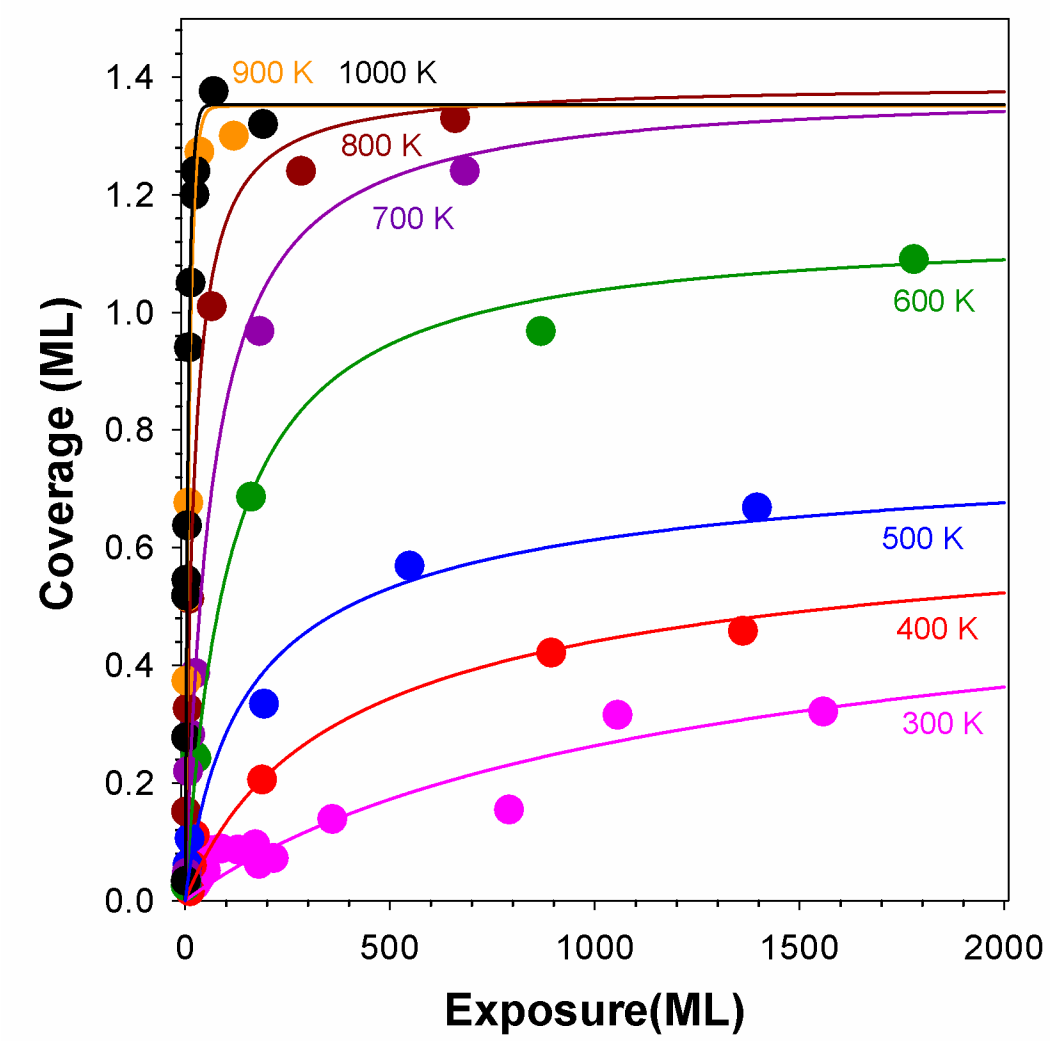

Figure 8.3: Carbon coverage vs TMB exposure plot for TMB dissociative chemisorption onto Pt(111) at surface temperatures ranging from 300 to 1000 K; experimental data (solid dots) are shown with least-squares fits to Equation 3.31 (lines), where n = 1 for 900 and 1000 K, n = 2 for 600 to 800 K, n = 3 for 300 to 500 K

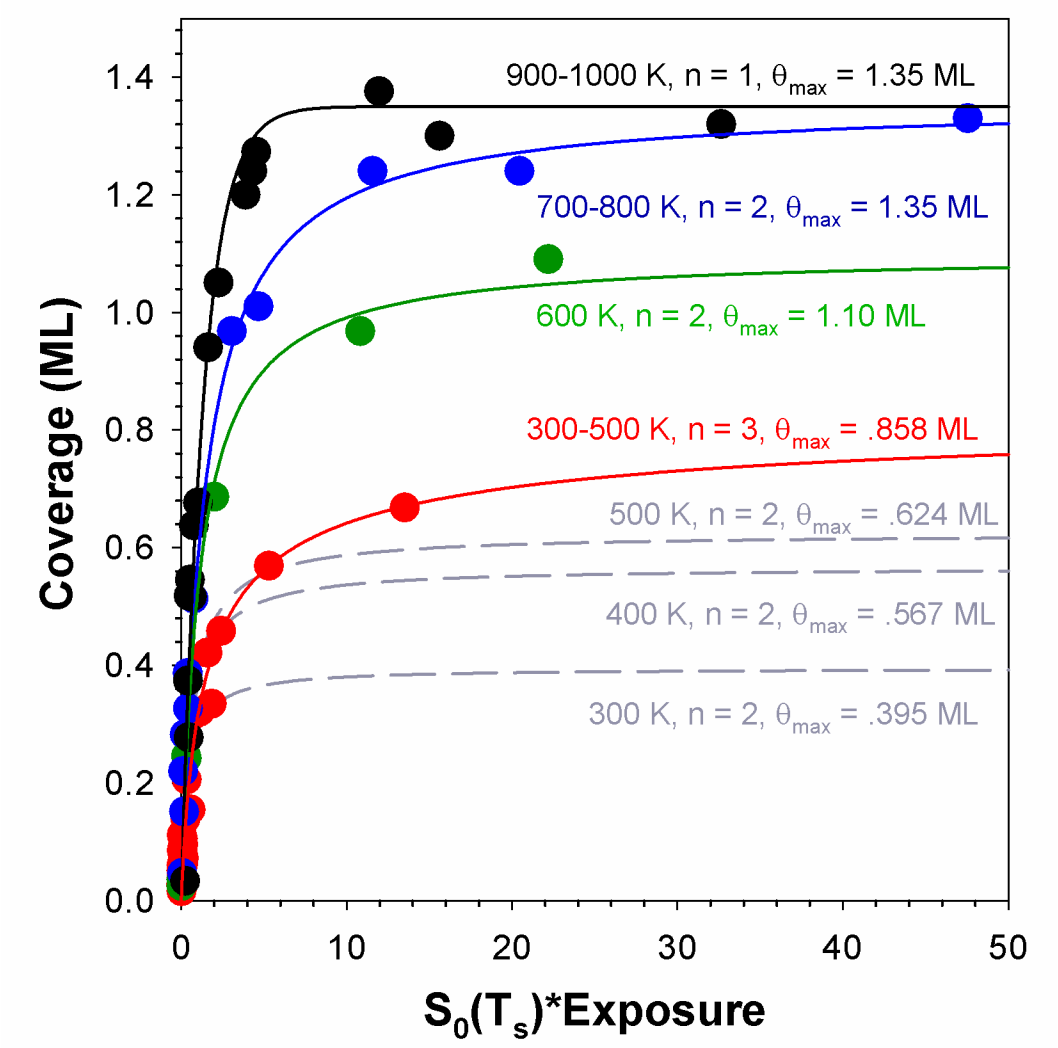

Figure 8.4: Carbon coverage vs TMB $S_0(T)$*Exposure plot with saturation coverages at each temperature; n = 2 fits are included for 300 to 500 K (Gray Dashed Lines)

cannot form a measurable amount of graphene, unlike higher temperatures, on Pt(111) at 600 K. Additional least-squares fits for the 300 to 500 K data with n = 2 are shown in Figure 8.3 in deference to a previous study by Figuéras which indicated that TMB required two binding sites when undergoing dissociative chemisorption prior to hydrogenation on large Ru (>3nm) nanoparticle surfaces at 500 K.[9] However, it is important to note that when n = 2, surface temperatures of 300, 400, and 500 K all diverge to separate saturation coverages, whereas when n = 3 , all three temperatures converge on 0.858 ML. The data shown in Figure 8.4 indicate that at low temperatures three binding sites are required for C-H bond dissociative chemisorption and two binding sites are required for C-C bond dissociation. At surface temperatures of 900 and 1000 K, TMB molecules rapidly decompose and form graphene, which reduces the apparent number of binding sites to one. The apparent shift from n = 2 to n = 1 from 800 to 900 K indicates that graphene forms quickly at surface temperatures greater than 900 K, because the chemisorbed fragments of each TMB molecule, which requires two adjacent binding sites for dissociative chemisorption by initial C-C bond cleavage, rapidly migrate to a graphene nucleation site of relatively high areal density. The fast surface diffusion of carbon at $T_s \geq 900K$ increases the number of n > 1 adjacent binding sites on Pt(111) at high graphene coverages, relative to lower surface temperatures where the surface diffusion of C fragments is slow relative to the impinging flux and desorption lifetime. Rapid surface diffusion of carbon at high surface temperatures increases the probability an impinging molecule encounters an area of Pt(111) with adjacent binding sites, which can shift the apparent number of binding sites to n = 1 at high temperatures, until the graphene coverage approaches the saturation limit. The saturation limit can then be predicted to decrease in proportion to the number of binding sites required for initial

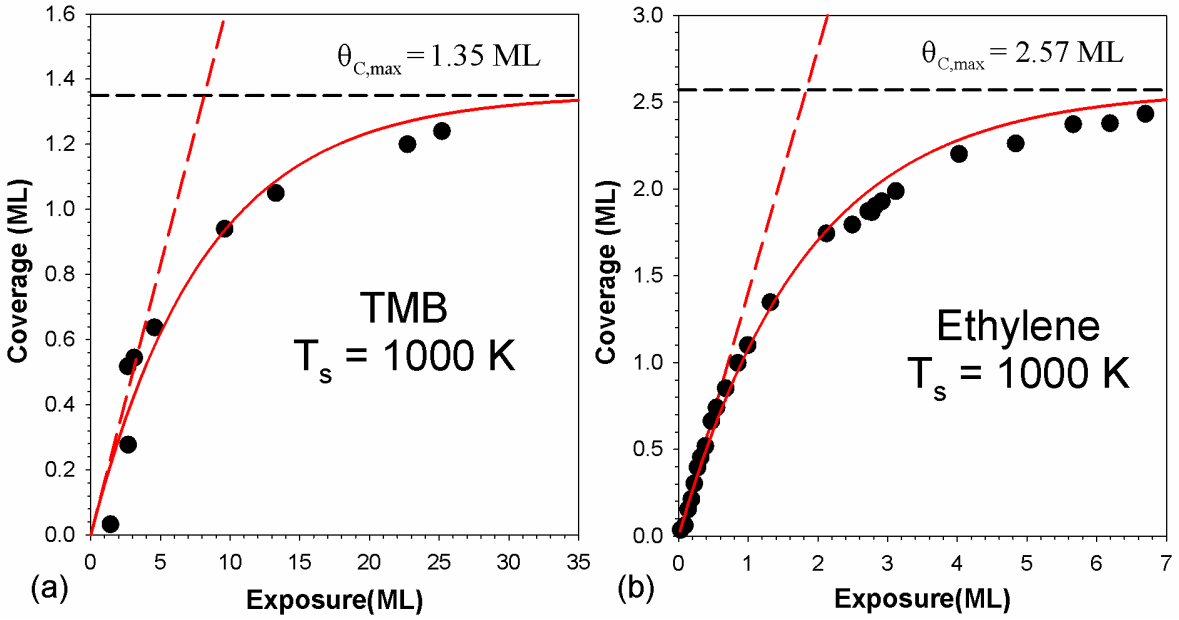

Figure 8.5: Carbon coverage versus exposure at surface temperatures of 1000 K for (a) TMB and (b) ethylene[10], which have saturation coverages of 1.35 and 2.57 ML respectively

dissociative chemisorption, as the probability of finding adjacent binding sites between two nearby graphene island decreases and approaches zero.

A previous study on the growth of graphene by ethylene CVD on Pt(111) showed that the expected saturation coverage limit for graphene carbon is 2.57 ML with respect to platinum.[10] The saturation coverage for TMB given the same reaction conditions was found to be nearly half that value at 1.35 ML. Disregarding the formation of graphene, alkanes are expected to fully decompose at 1000 K on Pt(111). A saturation carbon coverage of 1.35 ML with respect to platinum either indicates that some graphene formed or a large portion of carbon diffused into the platinum surface. However, the latter will not occur at these temperatures.[11] The 2.57 ML saturation coverage of ethylene on Pt(111) at 1000 K is negligibly different from the theoretical 2.55 ML monolayer coverage of graphene, as determined by the ratio of atomic areal densities of free standing graphene and platinum. This indicates that TMB forms graphene but has some limitation which prevents a full 2.57 ML saturated coverage. There are a few possibilities for the inefficiency in graphene growth by TMB chemical vapor deposition: a strong coverage dependence on the dissociative sticking coefficient due to poor molecular diffusion across graphene islands, several graphene nucleation sites formed by a small number of chemisorbed molecules, and inefficient packing of chemisorbed fragments and graphene islands, which are close enough to limit access to the Pt(111) surface in the space between but not close enough to form a combined structure.

3.5.3 Intrinsic vs Extrinsic Adsorption

As shown by Equation 3.33, the dissociative sticking coefficient for a particular reaction mechanism is dependent on temperature, carbon coverage, and the requisite binding sites. In

order for a reaction to occur on the Pt(111) surface, the molecule must form a reaction complex with an ensemble of *n* surface atoms. If these surface atoms are blocked from an impinging molecule by a monolayer island of other chemisorbed molecules, the impinging molecule must physisorb to the chemisorbed monolayer and diffuse across the surface to find an appropriate Pt(111) ensemble. Two molecules which require the same ensemble of surface binding sites may still have different dissociative sticking coefficients at the same carbon coverage and temperature, because the rate of desorption from the chemisorbed monolayer can significantly impact the probability that a diffusing molecule locates a Pt(111) ensemble before desorption. Evans reported that the relative rates of input and desorption of molecules onto and from the epitaxial (extrinsic) layer and the crystalline substrate (intrinsic), impact the coverage dependent dissociative sticking coefficient according to,[12]

$$S_{pre}(T,\theta) = S_{dir}(T,\theta)\frac{\left[1+R\left(S_{dir}(T,\theta)^{-1}-1\right)\right]}{\left[1+K\left(S_{dir}(T,\theta)^{-1}-1\right)\right]} \qquad \text{Equation 8.1}$$

where $S_{pre}(T, \theta)$ is the DSC considering an extrinsic precursor state, where a molecule which physisorbs onto the epitaxial layer has a possibility to diffuse to a binding site and react, $S_{dir}(T, \theta)$ is the DSC in the absence of an extrinsic precursor state, given by $S_0(T)\cdot(1-\theta/\theta_{max})$, R is the ratio of extrinsic to intrinsic input (i.e. physisorption sticking probability), and K is the ratio of extrinsic to intrinsic desorption rates. The ratio of extrinsic to intrinsic input is proportional to the DSC, so that if the molecular physisorption probability is greater on the epitaxial layer than on Pt(111), the dissociative sticking coefficient decreases less significantly, and perhaps even increases, with increasing carbon coverage than if the probabilities are less or equal. Conversely, the ratio of extrinsic to intrinsic desorption is inversely proportional to the DSC, so that if the desorption rate is greater from the chemisorbed monolayer than from Pt(111), the dissociative

sticking coefficient decreases more significantly than if the rates are less or equal. Assuming the ratio of extrinsic to intrinsic input is R = 1, such that the physisorption probabilities differ negligibly, the coverage dependent dissociative sticking coefficient, adjusted for the precursor state where the molecule can diffuse across the epitaxial layer, becomes,

$$S(T,\theta)=\left(1+K\left(\frac{1}{S_0(T)\cdot\left(1-\theta/\theta_{\max}\right)}-1\right)\right)^{-1} \qquad \text{Equation 8.2}$$

Equation 8.2 is a good approximation for the coverage dependent dissociative sticking coefficients for TMB and ethylene, where graphene and Pt(111) are the extrinsic and intrinsic materials, respectively, and the physisorption probabilities are assumed to be approximately 1 for both surfaces.

Although desorption rates of TMB from epitaxial graphene have not been measured, Campbell reported that both the desorption energy and pre-exponentials for desorption scale with the number of carbons in an alkane on both Pt(111) and C(0001)/Pt(111).[13] Using desorption rates for TMB on Pt(111) measured by this lab, reported elsewhere, and extrapolating from Campbell's C(0001)/Pt(111) data, a K ratio at 1000 K of 17.2 was calculated for TMB, with an estimated C(0001)/Pt(111) desorption energy of 68.1 kJ/mol. A fit of the TMB/Pt(111) 1000 K coverage versus exposure data to Equation 8.2, using constraints of K = 17.2 and $\theta_{C,max}$ = 1.35 ML, yielded an initial, zero-coverage DSC, S_0, of 0.217 at 1000 K. This fit S_0 = 0.217 at 1000 K from Equation 8.2 is 30.7% larger than the S_0 = 0.166 at 1000 K calculated from the fits to Equation 3.33 and shown in Figures 8.3 and 8.5. It should be noted that when constraints such as these are assigned when fitting data to Equation 8.2, the fit to the data is extremely poor. When TMB experimental coverage versus exposure data at 1000 K are fit to Equation 8.2, with $0 > S_0 > 1$, K > 0, and $\theta_{C,max} > 0$ as the only constraints, the fit yielded S_0 = 0.372 ± 0.080, K = 1.98 ±

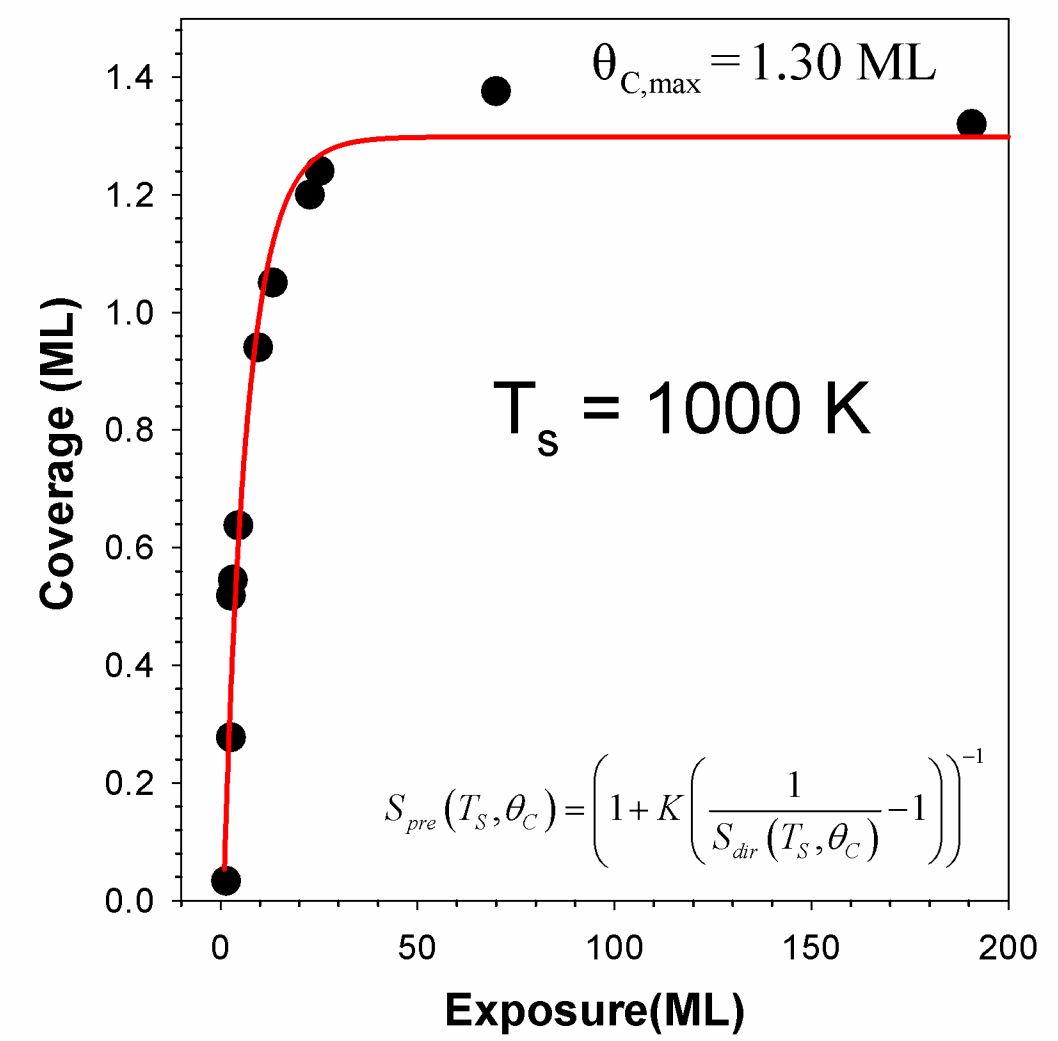

Figure 8.6: A coverage versus exposure plot showing the fit of TMB data at 1000 K to Equation 8.2; the fit yielded $S_0 = 0.372 \pm 0.080$, $K = 1.98 \pm 0.39$, and $\theta_{C,max} = 1.30 \pm 0.06$ ML

0.39, and $\theta_{C,max}$ = 1.30 ± 0.06 ML and is shown in Figure 8.6. These same data, when fit to Equation 3.33, yield an S_0 = 0.166, which is half the value yielded from Equation 8.2. However, when K > 1 and when S_0 < 1, S_0 in Equation 8.2 will be larger than the S_0 in Equation 3.33 when fit to the same experimental coverage versus exposure data, which can be observed in Figures 8.7 and 8.8 below. This is because $S(\theta = 0) = S_0$ is only true when K = 1 or S_0 = 1. When K > 1 and S_0 < 1, $S(\theta = 0) < S_0$, as shown in Figure 8.8 and 8.9. Figure 8.9 shows how the DSC varies as a function of K, at different coverage percentages and when S_0 = 0.372, according to the fit to Equation 8.2. The difference between the K ratio as calculated using measured and extrapolated desorption rate constants for TMB on Pt(111) and on C(0001), respectively, and as from the fit to Equation 8.2 may be because the extrapolated desorption rate constants for TMB on C(0001) are inaccurate.

Assuming that the desorption pre-exponential factors do not vary between the substrate and the epitaxial layer, the desorption energy for TMB on C(0001), according to K = 1.98 ± 0.39, should range from 87.2 to 90.5 kJ/mol with an average of 88.7 kJ/mol. This would indicate that the desorption energy of TMB does not significantly vary between substrates, which is contrary to the evidence shown by Campbell.[13] If the desorption energy of TMB extrapolated from Campbell's data (68.4 kJ/mol) is reasonable, that indicates that the desorption pre-exponential factor of TMB on Pt(111) is 4.25 x 10^{19} s^{-1}, which is an order of magnitude larger than the desorption pre-exponential factor on C(0001). In the case where the desorption transition states of TMB from Pt(111) and C(0001) are identical, which is reasonable, a smaller pre-exponential factor for desorption from C(0001) predicts that TMB has more entropy when physisorbed to graphene than on Pt(111). This may be reasonable, considering the relatively small lattice constant and exceedingly flat surface of graphene, which is referred to as a two-dimensional

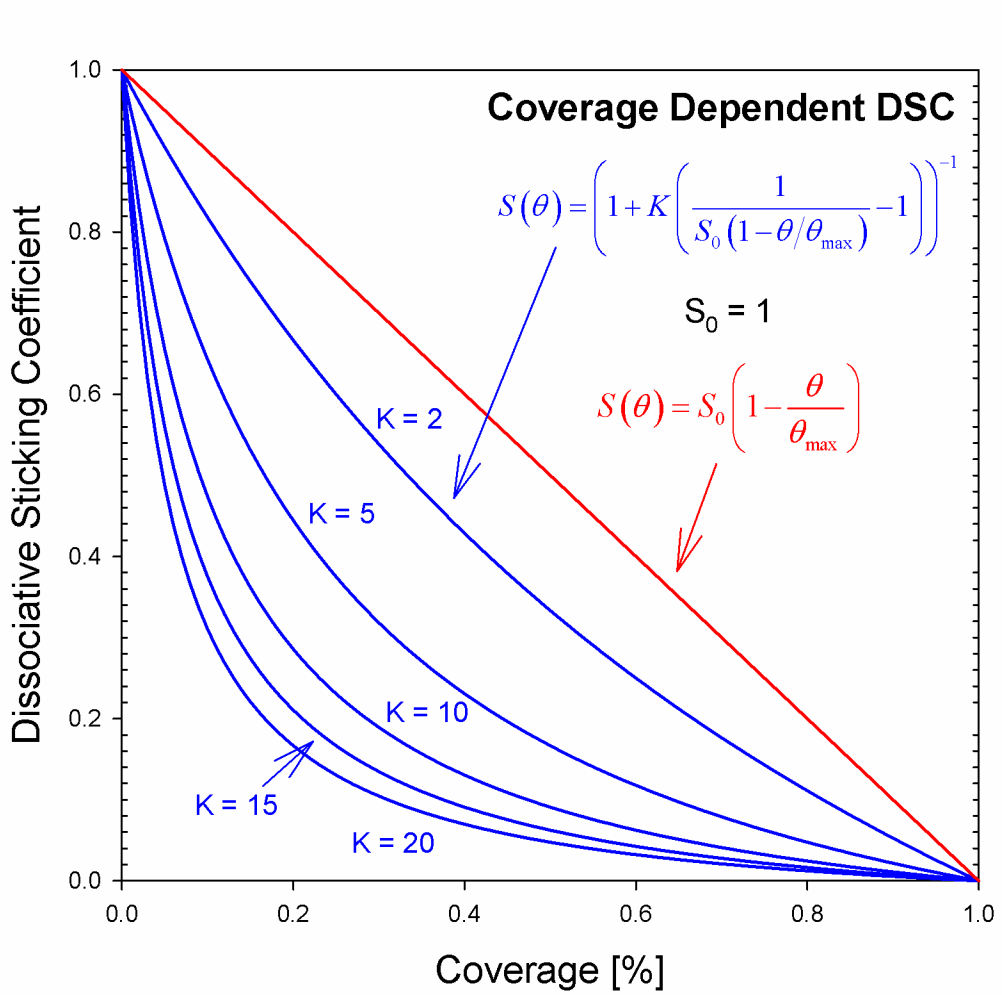

Figure 8.7: The dissociative sticking coefficient versus the surface coverage percentage using Equation 3.33 and Equation 8.2, with K = 2, 5, 10, 15, and 20, when $S_0 = 1$. When $S_0 = 1$, the DSC decreases more sharply with coverage when K is large, and when $\theta = 0$, $S_0 = 1$

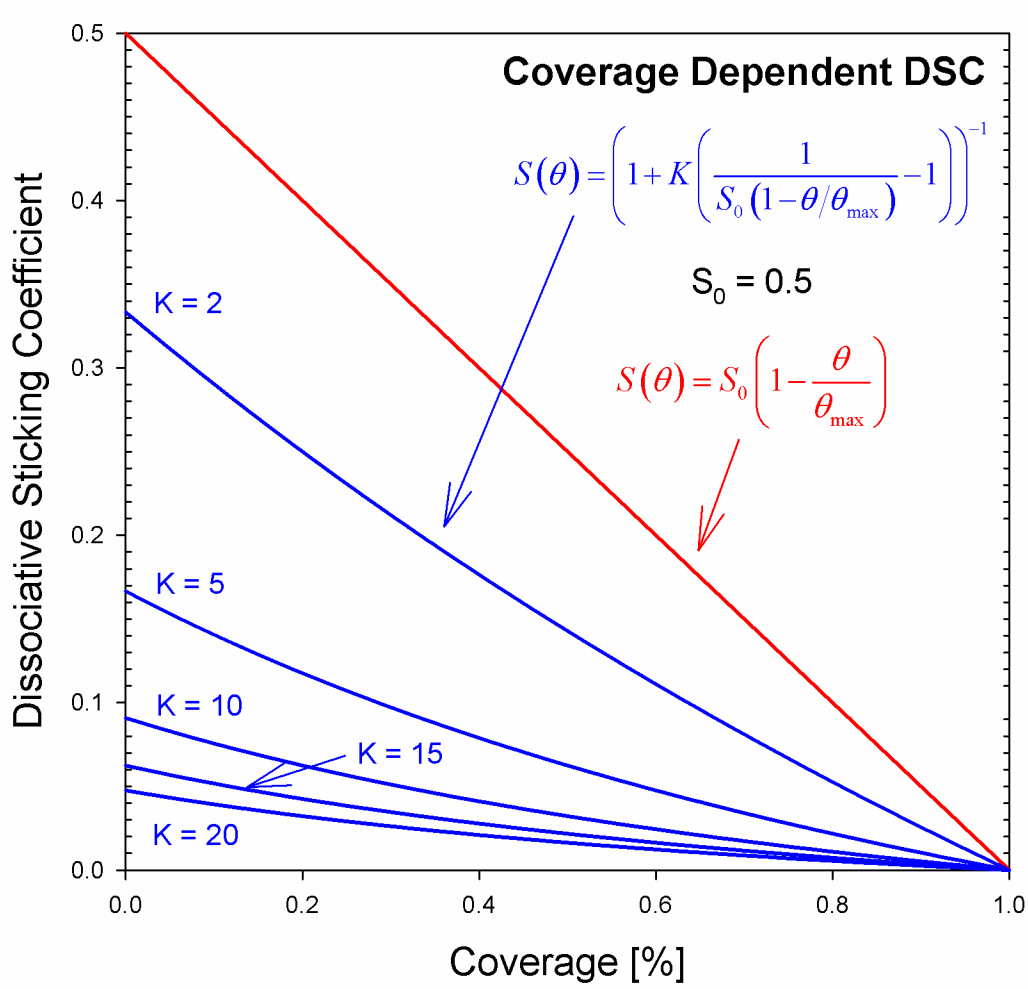

Figure 8.8: The dissociative sticking coefficient versus the surface coverage percentage using Equation 3.33 and Equation 8.2, with K = 2, 5, 10, 15, and 20, when $S_0 = 1$. When $S_0 = 0.5$, the DSC decreases more sharply with coverage when K is large, and when $\theta = 0$, $S_0 = 1$

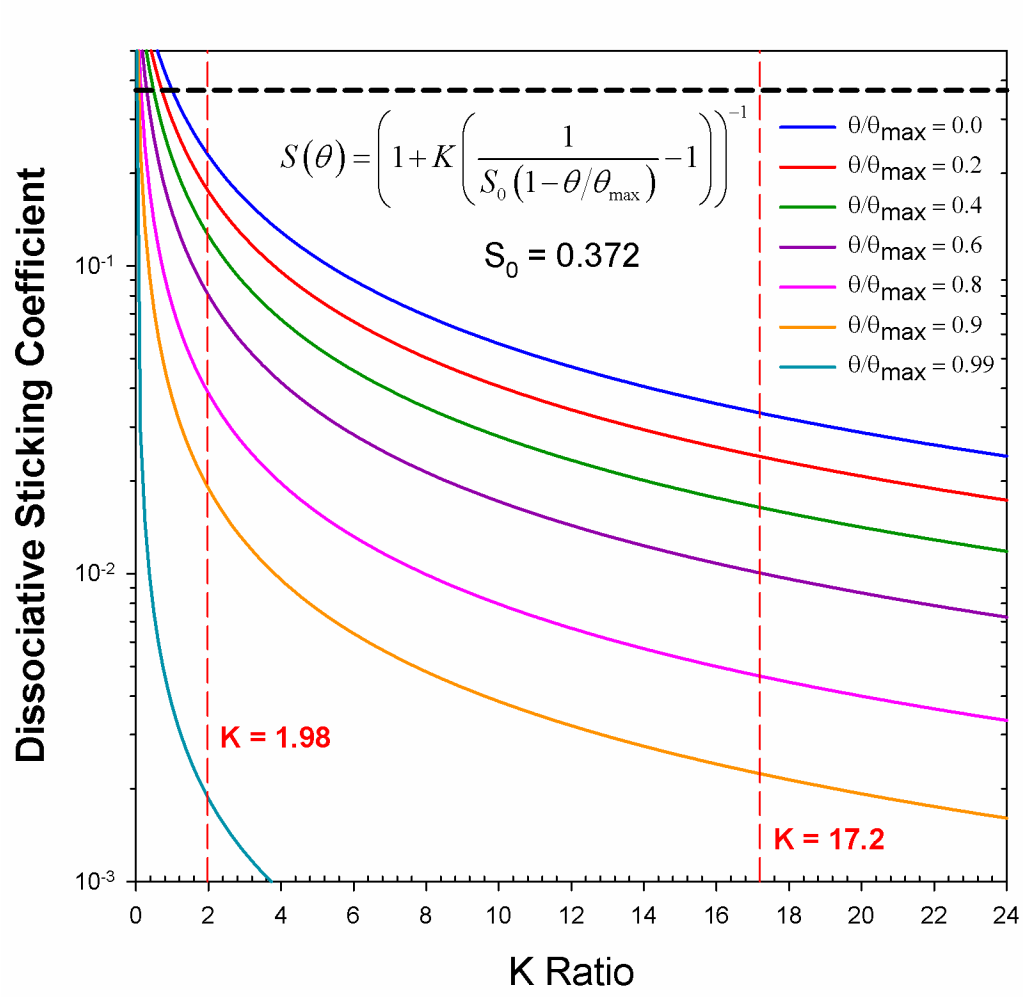

Figure 8.9: The apparent dissociative sticking coefficient as a function of K ratio (extrinsic to intrinsic desorption rates) at different coverage percentages with an initial sticking coefficient of S_0 = 0.372 (dashed black line) derived from the fit shown in Figure 8.6. The vertical dashed, red lines are the K ratio from the fit shown in Figure 8.6 (K = 1.98) and the value (K = 17.2) calculated using measured (i.e. TMB/Pt(111)) and extrapolated (i.e. TMB/C(0001)) rate constants

material. For a molecule the size of TMB, in addition to having a weaker physisorption energy, graphene may appear flatter than Pt(111), which would reduce frustrated translational and rotational degrees of freedom while physisorbed.

While Campbell's data showed that desorption energy scaled more significantly with respect to alkane size on Pt(111) than on C(0001),[13] as shown by Figure 8.6, there were no significant differences between the experimentally measured desorption pre-exponential factors on Pt(111) and C(0001). It should be noted that the pre-exponential factor for TMB on C(0001) of 4.25×10^{19} s^{-1}, calculated from K = 1.98 and E_D/C(0001) = 68.4 kJ/mol, is within the range of uncertainty of the desorption pre-exponential, $\ln(\nu_d) = 47.6 \pm 1.7$,calculated from the inversion analysis of TMB/Pt(111) TPD spectra discussed in Section 4. If the uncertainty in Campbell's measured desorption pre-exponential factors for other alkanes is similar to that as the uncertainty in the desorption pre-exponential factor for TMB, a ratio in the realm of $\nu_{d,C(0001)}/\nu_{d,Pt(111)} = 0.1$ would not be clearly identifiable in the range of uncertainty. Assuming that the desorption pre-exponential factors are identical for Pt(111) and C(0001) and scale with increasing alkane size, the K ratio of a molecule depends on the difference in desorption energies between the two substrates. Figure 8.10 shows that the desorption energies increase with respect to alkane size faster on Pt(111) and C(0001), and Figure 8.11 shows how the K ratio scales with alkane size, increasing with each additional carbon. The principal reason for the correlation between the K ratio and alkane size is how the desorption energy increases more rapidly with respect to carbon chain length on Pt(111) when compared to C(0001)/Pt(111). While the atomic areal density of graphene is greater than that of Pt(111), the electron areal density of graphene is approximately a third of platinum. Because van der Waals interactions scale with the number of electrons, it is expected for the surface with the larger areal density of electrons to also impose the larger

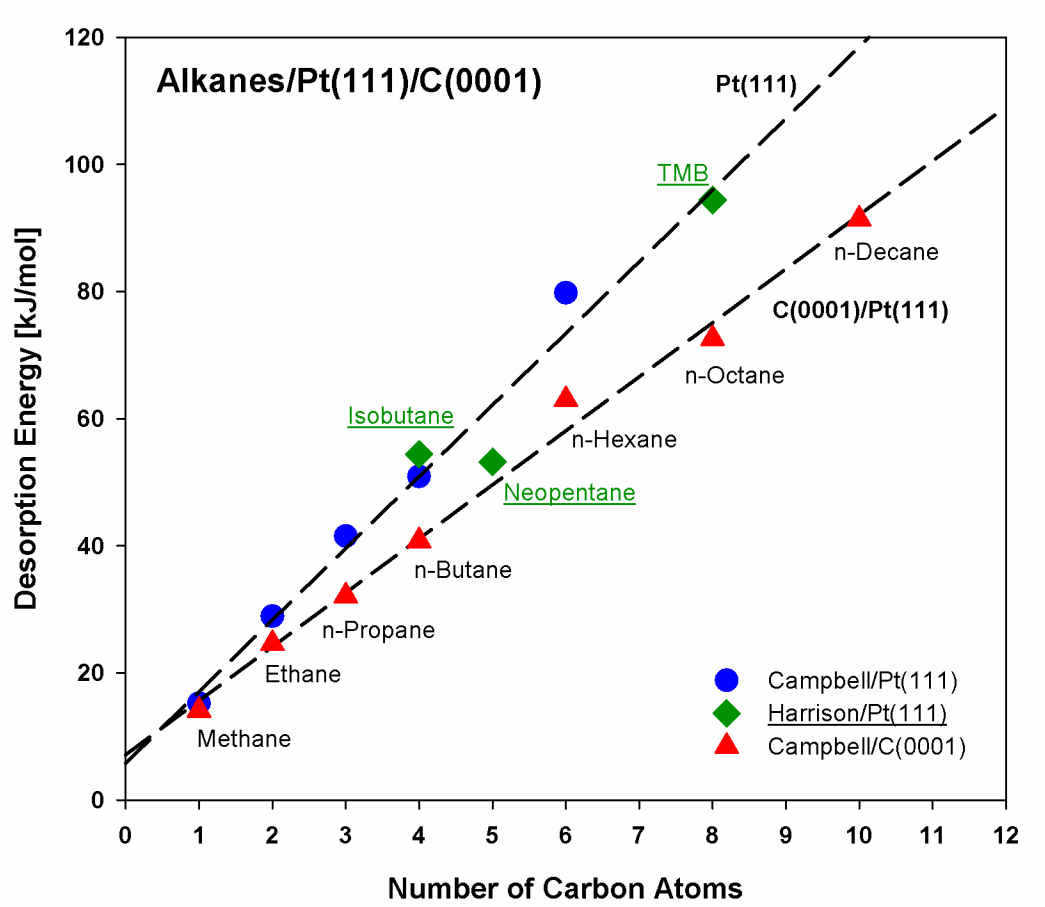

Figure 8.10: Desorption energy for n-alkanes on Pt(111) and epitaxial C(0001)/Pt(111) and branched alkanes on Pt(111) versus the number of carbon atoms in the alkane. The slopes with respect to Pt(111) and C(0001)/Pt(111) were calculated to be 11.3 and 8.50 kJ/mol, respectively.

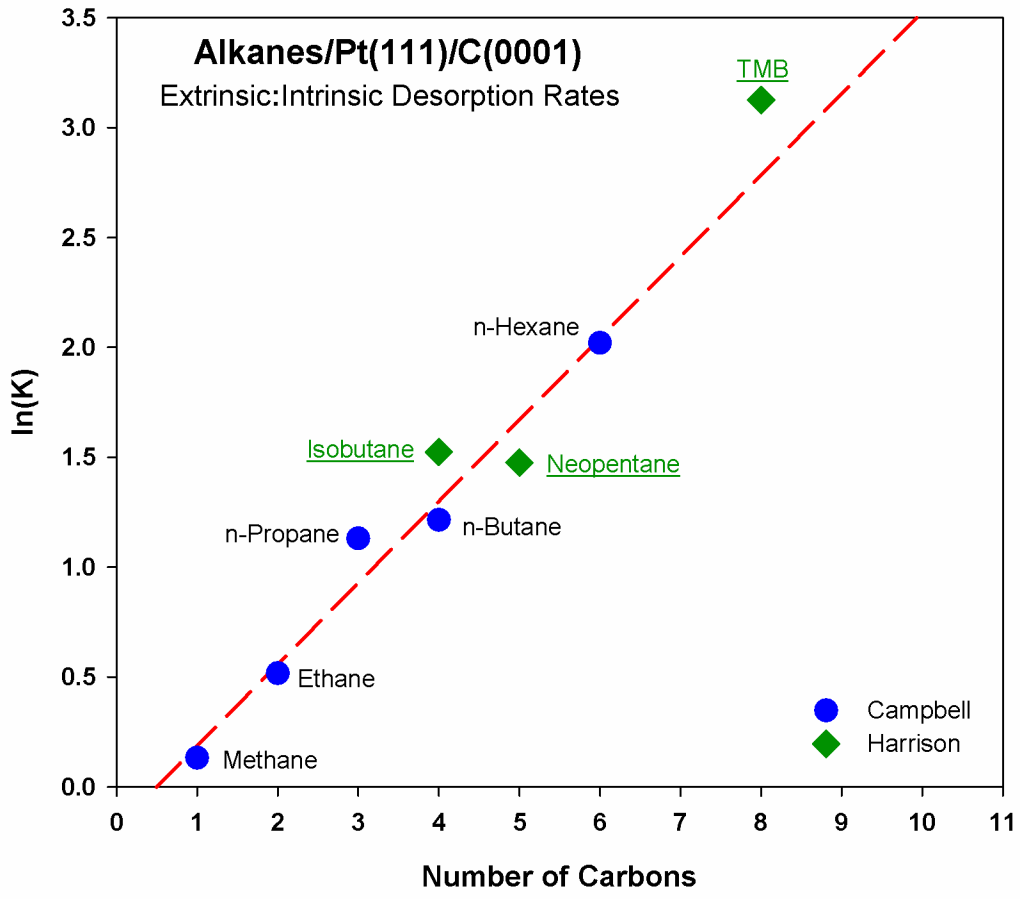

Figure 8.11: The natural log of the ratio between extrinsic, C(0001), and intrinsic, Pt(111), desorption rates, ln(K), at a temperature of 1000 K versus the number of carbons in alkanes. Desorption rate data for n-alkanes (blue dots) on Pt(111) and C(0001) were obtained from Campbell.[13] The desorption rates for isobutane, neopentane, and TMB (green diamonds) on Pt(111) were measured by this lab and are reported elsewhere. The branched alkane desorption rates on C(0001) were extrapolated from Campbell's data.

desorption energy onto a molecule, especially larger and more polarizable molecules. As a consequence, the slope of desorption energy versus the number of carbons plot for alkanes on C(0001)/Pt(111) is 0.75 of the slope on Pt(111).

It should be noted that Campbell's desorption energy correlations only apply to alkanes and are not characteristic of unsaturated hydrocarbons like ethylene. However, a report by Raaen showed that there are no discernable differences in the ethylene desorption from Pt(111) and C(0001)/Pt(111),[14] which indicates that ethylene has a K ratio of one despite having a desorption energy of 102 kJ/mol, which is greater than that of TMB on Pt(111).[10] This means that graphene islands more significantly decrease the DSC of TMB per unit coverage than in the case of ethylene. TMB desorbs from graphene either twice (K = 1.98) or K = 17.2 times faster than from Pt(111). Whereas ethylene has identical, or very similar, physisorption lifetimes on both Pt(111) and C(0001). The diffusion of molecules on the surface are hops between adjacent adsorption sites (atop, two-fold bridge, three-fold bridge) in random directions (random walk). The average number of hops a diffusing molecule can make before desorbing is proportional to the desorption energy of the molecule and the surface temperature. The average distance a randomly walking molecule travels on the surface before desorbing is the radius of diffusion. The radius of diffusion circles has the approximate expression of

$$r \simeq \sqrt{\frac{1}{\pi}} e^{\frac{E_d}{3RT_s}}$$

Equation 8.3

where E_d is the desorption energy and r is in lattice units, the distance between adjacent binding sites, which is the lattice constant (graphene[15] 1.42 Å, platinum[16] 3.912 Å).[17]. Assuming that the extrapolated desorption energy for TMB/C(0001) of 68.4 kJ/mol is accurate, TMB only has a diffusion radius of 12.5 Å on C(0001) at T_s = 1000 K, which is 7.71 times smaller than the 96.4 Å radius on Pt(111). Ethylene has a diffusion radius at T_s = 1000 K of 47.5 and 131 Å on

C(0001)/Pt(111) and Pt(111), respectively, the former of which is 3.8 times larger than TMB on C(0001). This indicates that ethylene can diffuse across larger graphene islands and find a binding site on Pt(111) without significantly decreasing the DSC when compared to TMB at T_s = 1000 K. As the surface concentration of graphene increases such that island radii become significantly larger than 12.5 Å, the probability that a TMB molecule which physisorbs to C(0001) finds a Pt(111) reactive ensemble (n = 2) rapidly approaches zero.

3.5.4 Surface Packing Density

Despite the large K ratio for TMB, given a sufficient amount of time and exposure, such that the low probability of a molecule diffusing on graphene and finding a Pt(111) binding site at high carbon coverage becomes irrelevant, it would be predicted that the saturation carbon coverage should approach the 2.57 ML with respect to platinum observed with ethylene. However, data in Figures 8.4 and 8.5 do not show evidence of this at any graphene forming temperature. This indicates that a constant portion of Pt(111) remains inaccessible to TMB and prevents a uniform monolayer of graphene from forming. There are two aspects of TMB which should be considered: the number of carbons and the area of the molecule with respect to the platinum surface. The eight carbons of TMB permits a single TMB molecule to form a graphene nucleation site, which means that absorbed atomic carbon does not need to build up in close proximity from multiple dissociative chemisorption reactions prior to graphene formation. TMB can therefore form many small graphene islands which need not be in close proximity to each other. Secondly, the smallest surface area which TMB can present to Pt(111) is 20 $Å^2$ (4.5 x 4.5 $Å^2$), which spans 3 platinum atoms, given the 1 x 10^{15} cm^{-2} areal density of Pt(111). This is in contrast to the largest surface area of 3.2 $Å^2$ which ethylene can present to Pt(111) that

encompasses 0.48 platinum atoms. These data indicate that as long as a binding site is available to ethylene, it can react with a probability equal to its initial DSC. However, TMB not only requires an available reaction site but enough space to approach the surface. As two graphene islands grow in size and approach 4.5 Å from each other, they start blocking impinging and diffusing molecules from the Pt(111) between the islands. When the space between graphene islands becomes less that the width of a TMB molecule, the portion of Pt(111) with no graphene over it still functions as if there were an epitaxial layer over it with respect to the molecule. With the combination of regions of inaccessible platinum atoms between graphene islands and the ability to self-nucleate graphene islands upon total decomposition on Pt(111), large alkanes such as TMB will only form inefficient, low surface packing density graphene monolayers. In the case of TMB, 47.5% of the Pt(111) surface remains inaccessible to molecules at the saturation graphene coverage.

References

1. Navin, J. K.; Donald, S. B.; Harrison, I., Angle-Resolved Thermal Dissociative Sticking of Light Alkanes on Pt(111): Transitioning from Dynamical to Statistical Behavior. *J. Phys. Chem. C* **2014**, *118*, 22003-22011.
2. Cushing, G. W.; Navin, J. K.; Donald, S. B.; Valadez, L.; Johanek, V.; Harrison, I., C-H Bond Activation of Light Alkanes on Pt(111): Dissociative Sticking Coefficients, Evans-Polanyi Relation, and Gas-Surface Energy Transfer. *J. Phys. Chem. C* **2010**, *114*, 17222-17232.
3. Kim, J.; Seo, J.; Jung, H. K.; Kim, S. H.; Lee, H. W., The Effect of Various Parameters for Few-Layered Graphene Synthesis Using Methane and Acetylene. *Journal of Ceramic Processing Research* **2012**, *13*, S42-S46.
4. Kim, H.; Kim, E.; Lee, W. J.; Jung, J., Effects of Hydrogen in the Cooling Step of Chemical Vapor Deposition of Graphene. *Electronic Materials Letters* **2013**, *9*, 417-420.
5. De Arco, L. G.; Zhang, Y.; Kumar, A.; Zhou, C. W., Synthesis, Transfer, and Devices of Single- and Few-Layer Graphene by Chemical Vapor Deposition. *Ieee Transactions on Nanotechnology* **2009**, *8*, 135-138.
6. Xu, M.; Fujita, D.; Gao, J.; Hanagata, N., Auger Electron Spectroscopy: A Rational Method for Determining Thickness of Graphene Films. *ACS Nano* **2010**, *4*, 2937-2945.
7. Fuchs, A.; Scherer, J.; Jung, K.; Ehrhardt, H., Determination of Sp2/Sp3 Carbon Bonding Ratio in a-C:H Including Irradiation Damage by Factor Analysis of Auger Electron Spectra. *Thin Solid Films* **1993**, *232*, 51-55.
8. Steffen, H. J., Use of Valence Band Auger Electron Spectroscopy to Study Thin Film Growth: Oxide and Diamond-Like Carbon Films. *Thin Solid Films* **1994**, *253*, 269-276.
9. Coq, B.; Crabb, E.; Figuéras, F., Catalytic and Structural Properties of Ruthenium Bimetallic Catalysts: Kinetics of 2,2,3,3-Tetramethylbutane Hydrogenolysis. *J. Mol. Catal. A: Chem.* **1995**, *96*, 35-48.
10. Cushing, G. W.; Johanek, V.; Navin, J. K.; Harrison, I., Graphene Growth on Pt(111) by Ethylene Chemical Vapor Deposition at Surface Temperatures near 1000 K. *J. Phys. Chem. C* **2015**, *119*, 4759-4768.
11. Stiegel, G. J.; Ramezan, M., Hydrogen from Coal Gasification: An Economical Pathway to a Sustainable Energy Future. *International Journal of Coal Geology* **2006**, *65*, 173-190.
12. Evans, J. W.; Thiel, P. A.; Bartelt, M. C., Morphological Evolution During Epitaxial Thin Film Growth: Formation of 2d Islands and 3d Mounds. *Surf. Sci. Rep.* **2006**, *61*, 1-128.
13. Tait, S. L.; Dohnalek, Z.; Campbell, C. T.; Kay, B. D., N-Alkanes on Pt(111) and on C(0001)/Pt(111): Chain Length Dependence of Kinetic Desorption Parameters. *J. Chem. Phys.* **2006**, *125*, 234308.
14. Vermang, B.; Juel, M.; Raaen, S., Temperature Programed Desorption of C2h4 from Pure and Graphite-Covered Pt(111). *J. Vac. Sci. Technol. A* **2007**, *25*, 1512-1518.
15. Gray, D.; McCaughan, A.; Mookerji, B., Crystal Structure of Graphite, Graphene and Silicon.
16. Davey, W. P., Precision Measurements of the Lattice Constants of Twelve Common Metals. *Phys. Rev.* **1925**, *25*, 753-761.
17. Bowker, M., The Role of Precursor States in Adsorption, Surface Reactions and Catalysis. *Journal of Physics-Condensed Matter* **2010**, *22*, 263002.

9.1 Conclusion

Van der Waals interactions, which are approximated by the desorption energy, were found to stabilize the products and transition state of alkane dissociative chemisorption by initial C-H bond cleavage on Pt(111), making the reaction more exothermic. The slope of the Evans-Polanyi correlation between the activation energy and heats of reaction for dissociative chemisorption of alkanes, $dE_a/d\Delta_r H = 0.46$, indicates that both bond energy and van der Waals interactions play a significant role in lowering the activation energy. This is a critical discovery, because many DFT calculations of surface reactions disregard van der Waals interactions. Previous studies of dissociative chemisorption on transition metal surfaces have mainly involved methane, ethane, and propane, which can give the false impression that activation energy scales only by the weakest bond dissociation energy. However, van der Waals interactions play the most significant role in stabilizing the dissociative chemisorption reaction, leading to dissociative chemisorption becoming an unactivated process by n-nonane, despite the weakest C-H bond varying negligibly between n-nonane and n-propane.

Before this study discovered that van der Waals interactions are the main stabilizing force for dissociative chemisorption, the only two Pt(111) single crystal surface calorimetry experiments reported thermodynamic bond energies for Pt-[methyl] and Pt-[t-butyl] Pt-C bonds of 194 and 216 kJ/mol, respectively, which do not follow expected trends among methyl, primary, secondary, and tertiary carbon bonds. However, after considering the role of van der Waals and defining the thermodynamic bond energy as $D^0\left(Pt-C\right)=D^{0-}\left(Pt-C\right)+E_D$, where $D^{0-}\left(Pt-C\right)$ is the covalent bond energy with the van der Waals component removed, it was possible to extract Pt-C covalent bond energies of Pt-[methyl] 180 kJ/mol and Pt-[t-butyl] 164 kJ/mol which differ by the same percentage (~10%) between methyl and tertiary carbons as C-H

bonds (e.g. [methyl]-H 440 kJ/mol, [t-butyl]-H 400 kJ/mol). It was then possible to predict the covalent bond energies, $D^{0-}\left(Pt-C\right)$, thermodynamic bond energies, $D^{0}\left(Pt-C\right)$, and heats of reaction of dissociative chemisorption by initial C-H and C-C bond cleavage for alkanes which have not been studied in extremely difficult single crystal calorimetry experiments, using the measured desorption energies of the alkanes and the two measured Pt-C bond energies. These predictions can provide guidelines for future calorimetry experiments or be used as estimates for thermodynamic calculations in the absence of calorimetry data. Additionally, the Evans-Polanyi correlation between activation energy and heat of reaction $dE_a/d\Delta_r H = 0.46$ allows for the estimation of activation energies from the predicted heats of reaction. In the case of other dissociative chemisorption reaction pathways (i.e. by initial C-C bond cleavage) the methods reported in this study give a framework for predicting heats of reaction and estimating a range of activation energies depending on the Evans-Polanyi slope, $0 < dE_a/d\Delta_r H < 1$, where a slope closer to 1 predicts a late transition state which resembles the products. An example of this was provided for dissociative chemisorption by initial C-C bond cleavage, where the activation energies were predicted for alkanes, which have not been observed to dissociate by C-C bond scission, by using the 40.0 kJ/mol $E_{a,C\text{-}C}$ of 2,2,3,3-tetramethylbutane (TMB), estimated heats of reaction, and assuming slopes of $dE_a/d\Delta_r H = 0.46$ and $dE_a/d\Delta_r H = 1$. The activation energies of dissociative chemisorption by initial C-C bond cleavage on Pt(111) of all studied alkanes were much larger (e.g. TMB E_a = 40 kJ/mol, n-octane E_a = 56 kJ/mol, and ethane E_a = 87 kJ/mol for $dE_a/d\Delta_r H = 0.46$, TMB E_a = 40 kJ/mol, n-octane E_a = 77 kJ/mol, ethane E_a = 139 kJ/mol for $dE_a/d\Delta_r H = 1$) than that of TMB, which supports the observation that C-C bond dissociation does not occur for other alkanes on Pt(111) at temperatures less than or equal to 1000 K.

Appendix

Section **Page**

Appendix

A.1 Liquid Nitrogen Transfer Tube Maintenance

The liquid nitrogen transfer tube allows for small amounts of liquid nitrogen to be siphoned out of a 70 L tank and into the Oxford cryostat system cold finger for the purposes of cooling crystals in the chamber. The transfer arm makes use of two capillary tubes in the center of a vacuum sleeve. The primary step in maintaining the function of the transfer arm is maintaining the vacuum in this sleeve, which limits the transfer of heat to liquid nitrogen in the capillaries. If the vacuum increases to too high of a pressure and/or a significant leak exists in the sleeve, the liquid nitrogen will heat up too much before it reaches the cryostat, and severely limit cooling.

When the pressure in the transfer arm has risen too high for efficient cooling, the vacuum sleeve needs to be pumped down. Transfer arms vary in size, but all typically have two valves. The valve closest to vacuum sleeve, the thickest part of the transfer arm, and the one which has a KF connector is the valve which separates the vacuum sleeve from the atmosphere. This valve should **never** be opened when there is an atmosphere of pressure on the outside of the valve. In order to lower the pressure inside the sleeve, attach a flexible KF tube to the valve outlet and a mechanical pump. Make **certain** before starting the mechanical pump that the KF tube is attached to the intake of the pump and not the exhaust, otherwise an overpressure will form and oil will erupt out of the pump on shut-off. When the KF tube is properly attached to the transfer arm and pump intake, hold a Kim-wipe or paper towel lightly over the exhaust of the pump, and start the pump. **Do not open the transfer arm valve**. A gust of air should move the wipe as the pump starts, indicating that air is moving into the intake. If there is no gust of air, immediately

shut off the pump, as either the pump has failed, or the KF tube was attached to the exhaust side of the pump. There will be an loud sound from the pump initially as it starts pumping out air from the KF tube, but it will quiet down after a few moments. When the pump noticeably quietens or the gust of air dampens from the exhaust that indicates that the KF transfer arm has been thoroughly pumped. At this point, the valve to the vacuum sleeve on the transfer arm may be opened. If there is an extensive amount of air in the vacuum sleeve, the mechanical pump may begin to make noise as air moves through the pump. If there is no leak in the vacuum sleeve, the noise of the pump will once more quiet down within a minute. With the valve on the transfer arm open, pump on the vacuum sleeve for at least 15 to 20 minutes. This will allow volatile molecules to desorb from surfaces within the sleeve and minimize the pressure inside. If it seems like there was a significant amount of air in the transfer arm, either due to not having pumped out the sleeve for a long time or due to a leak, pump on the vacuum sleeve for at least 30 minutes. Once the transfer arm has been pumped on for a sufficiently long enough time, close the valve to the vacuum sleeve, and then turn off the mechanical pump, in that exact order. A vacuum should still be in the KF tube when you remove it from the transfer arm and mechanical pump.

After pumping on the vacuum sleeve of the transfer arm, liquid nitrogen cooling should function more efficiently. If it does not, then that indicates that there may be other problems. Among these problems include: (a) inefficient pumping from the transfer arm siphon pump, (b) a clog in the transfer arm capillary tubes, (c) an old or broken o-ring where the transfer arm is inserted into the cryostat on the manipulator, (d) a significant leak in the vacuum sleeve which prevents any vacuum from being maintained. The first (a) and last (d) cases require either repair or replacement from the company or reseller. The o-ring on the cryostat allows a sufficient enough vacuum to form in the tube and cryostat for liquid nitrogen to flow. If it is broken, this

vacuum seal can fail and allow air and water vapor into the cryostat, which can result in inefficient cooling or a clog. Replacement o-rings should be made from Viton, which is a rubber which can withstand the high temperatures common during UHV bakeouts. The case of a clog can be resolved with the following technique.

A.2 Removing Clogs from a Liquid Nitrogen Transfer Arm

Occasionally water vapor will get into the liquid nitrogen transfer arm capillary tubes and form ice as liquid nitrogen is siphoned through. This ice can limit or completely block the flow of nitrogen, preventing cooling entirely. Identifying a clog is not simple and should be considered as a possibility when both the vacuum sleeve and the siphoning pump have been confirmed as functioning normally. Never siphon air though the transfer pump after siphoning liquid nitrogen. Not only does this not function as a clog test, this will result in water crystals forming on the surface of the capillary tube and will certainly cause a clog even if one wasn't present before. Siphoning air through a room temperature transfer arm will not identify a clog, because most clogs are the result of ice inside the tube.

When a clog is suspected in the transfer arm, water vapor must be forced out of the transfer arm. Arrange the transfer arm so that every part of it is easily accessible. Begin pumping on the vacuum sleeve as described in Section A.1 above. While the vacuum sleeve is pumping, use a heat gun to warm the metal all over the transfer arm. Make sure the liquid nitrogen flow valve on the transfer arm is open. While heating the transfer arm, avoid heating the vacuum sleeve or the area near the valves too much (beyond what is acceptable for touching with fingers). Typically the metal part which is inserted into the liquid nitrogen tank is fully metal and can be heated up safely relative to the sections which have rubber and plastic. However, avoid

overheating the metal sections as well. This heating process is to aid in the removal of water vapor from surfaces. In order to avoid trap-to-trap distillation, where the water vapor moves from the hottest surface to the coldest surface, it is ideal for the area near the valves to be warmer than the capillary inlets and outlets on both ends of the transfer arm. Because the transfer arm cannot be heated too significantly, carefully heat the transfer arm, moving the heat gun from the center of the arm outwards down both lengths of the arm, for approximately one hour. While the transfer arm is still warm, close the liquid nitrogen flow valve on the transfer arm. Stop pumping on the vacuum sleeve, as described in Section A.1 above. If the clog remains, repeat the previous procedure, but keep the liquid nitrogen flow valve closed.

B. Chamber TMP Cable Schematics

The following pages have schematics shown how pumps are connected to the power system. Figure B1 demonstrates the arrangement of the main chamber turbomolecular pump and the roughing pump. In summary, the turbomolecular pump and roughing pump are arranged to operate at the same time. If the turbomolecular pump fails, the roughing pump turns off. However, both are on the emergency power system and will continue to operate in the event of a power failure. An uninterruptible power supply (UPS) allows the turbomolecular pump to continue functioning during the delay between main power failing and emergency power activating.

Ion pumps and filament systems are connected to a switch which closes when main power fails, so that they turn off in the event of a main power failure and do no come back on unless manually reset. This prevents them from attempting to activate as the main power returns in the event that the chamber vented due to a failure in emergency power.

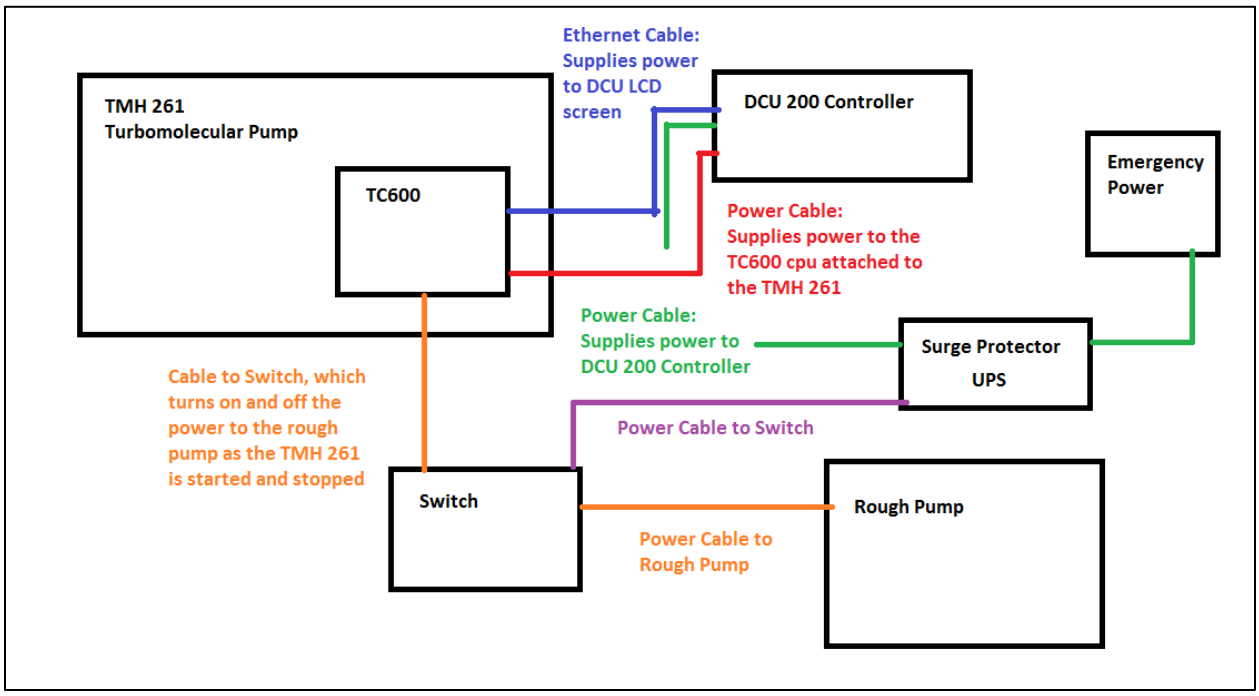

Figure B1: A power connection schematic for the main chamber turbomolecular pump system

C. Resistive Heating of a Single Crystal

C.1 Overview

The Pt(111) single crystal used in this study was resistively heated by two 75% W and 25% Re rods. A XFR 12-100 DC power supply from Xantrex and 906S Eurotherm temperature controller were used to control the heating of the crystal. Electrical power $P = IV$ is the important value in resistive heating, and both voltage and current are important. The Xantrex power supply and Eurotherm controller can be set so that the resistive heating is controlled by only modulating voltage $P = V^2/R$ or current $P = I^2R$. In other words, when set to control the circuit by voltage, the current dial on the Xantrex controller is disabled and will not increase the current or voltage by any degree when turned. However, the voltage dial will increase both the voltage and current when turned clockwise. Note that in the case of the XFR 12-100 DC power supply, if the power supply is turned on with the active dial turned, the power supply will immediately send power down the line and start heating the crystal. Always make sure both the current and voltage dials are off before turning on the power supply to avoid accidental and rapid heating. If the power supply is set to control the circuit by current, the voltage dial will become disabled instead. The precise arrangement of wires in order to change the control between current and voltage is described in the power supply and Eurotherm manuals.

In the case of our system, current control was found to be the most stable method for heating our Pt(111) single crystal. This is because the overall resistance from feedthrough to feedthrough was less than 1 ohm, and a slight increase in voltage lead to a more significant increase in current, power, and heating. In the case where the rate of heating wanted to be more sensitively controlled, to prevent the breaking of spot welds at high rates of heating due to different rates of thermal expansion, current was chosen. Because $\Delta I < \Delta V$ for the resistance

present in our circuit, current control allowed our heating to be manipulated with more precision than we were able to obtain with voltage control. Current control also alleviated potential problems associated with CPU gain scheduling by the Eurotherm temperature controller, requiring less strict PID parameters, because CPU modulating through different currents resulted in less significant changes in crystal temperature than when it modulated through different voltages, due to $\Delta I < \Delta V$.

Resistive heating of a single crystal using current control can be performed using four main methods in conjunction with a Eurotherm controller. This section will describe these methods in order of the most safe (in terms of reducing $dI/dt \propto dT/dt$) to least safe.

C.2 Manual Heating Control via Eurotherm (Current Control)

The first temperature controlling method can be considered manual control. This is achieved by setting the current and voltage dials to the off position on the Xantrex controller prior to turning on the device. The Eurotherm controller should also be set to manual, which can be done by pressing the button with the "hand" symbol until "MAN" appears on the screen. Pressing this button will cycle the controller between "MAN" and "SCH", where the latter stands for "Gain Scheduling" and represents CPU control of the Xantrex. The number in the bottom right of the screen indicates the amount of current in amps that the Eurotherm is requesting from the Xantrex power supply. It should be set to 0 before turning on the power supply; if it is not, decrease it to 0 prior to turning on the power supply. With all of the above mentioned preparations, it is safe to turn on the power supply. The Xantrex should report a minimum current of ~0.5 amps, and the crystal should not be heating. If the Xantrex reports a current larger than 1, check the current dial and make sure it is in the off position; if it is, but the current is still

greater than 1 amp, this represents a problem which is beyond the scope of this discussion. With the power supply on, the dial in the off position, the Xantrex reporting a current less than 1, and the Eurotherm set to request 0 amps, it is safe to increase the current dial. If the Eurotherm is set to "MAN" and 0 amps, the Xantrex should not report an increase in current. However, with the current dial increased past the off position, the amount of current put through the tungsten rods on the crystal mount can now be controlled by the Eurotherm. For the safest control, increase the current to the rods by 0.1, or a single button press, at a time. Do not hold down the "up arrow" button on the Eurotherm, because it will rapidly increase the current to values which will lead to undesired and potentially damaging ΔT. However, with patience, this method will result in the most precise control in the heating rate of the crystal.

C.3 Manual Heating Control via Xantrex (Current Dial)

While controlling the current directly and slowly using the manual function of the Eurotherm will result in the least chance of damage to the crystal and spot welds, it is impractical for a number of experiments, or when spot welds have already been properly annealed and have been previously shown to be robust. The method described in this section is a manual method of controlling the heating which can allow for larger ΔI values with less risk when compared to holding down the Eurotherm button, as warned against in the previous section.

As described in the previous section, prior to turning on the power supply, make sure the current and voltage dials are turned to the off position. The Eurotherm can be set to "SCH", where the lower right number is the crystal temperature in Kelvin, or to "MAN", where the lower right number is the amperage requested from the Xantrex device. If set to "SCH", the CPU will request the amount of current it predicts it will need to react the target temperature. Prior to

turning on the Xantrex controller, if the scheduled temperature is larger than the room temperature crystal temperature, the requested current will be the largest value it is permitted to request (HO1 in the gain scheduling settings). This heating technique permits the Eurotherm to request and value, and it is recommended to use "SCH" and set the Eurotherm to the desired temperature, rather than "MAN" and setting the upper limit of the current. However, whichever mode chose, the current requested by the Eurotherm must be greater than 0. **Note**, it is **exceedingly** important to **make sure the current dial is in the off position** prior to turning on the power supply.

When the power supply has been turned on and the Eurotherm has been set to "SCH" and a specific temperature, the current dial can be slowly increased. The Xantrex power supply should show the current increasing. Continue to increase the current dial until the crystal reaches the target surface temperature. Avoid turning the dial too fast to prevent too significant ΔT. It should be noted that if the light above the current dial turns on and is red, that means that the amount of current that the Eurotherm is requesting for is greater than what the dial is permitting.

C.4 Manual Heating Control via Eurotherm (Temperature Control)

This method is similar to Section C.2 above. The current and voltage dials should be in the off position before turning on the power supply. The Eurotherm should be set to "SCH" and just below room temperature. With these preparations, the power supply can be turned on. The current dial can be increased. If the Eurotherm is properly set, the current should not increase regardless of how far the dial is turned. Set the current dial at a constant position (not in the off position). Then slowly increase the temperature on the Eurotherm controller until the desired temperature is reached. This method may seem like it should be safer (less ΔT) than the

previous methods, which is true provided that the PID parameters are tight and don't allow for a lot of variance in current. However, because the CPU will determine the current needed to reach the set temperature, every increase in the temperature requires the CPU to recalculated. Depending on the rate of cooling, the Eurotherm may significantly overestimate and subsequently overcorrect the requested current from the power supply, leading to sharp $dI/dt \propto dT/dt$, leading to rapid and localized heating of the crystal which can lead to damage of spot welds. This can be prevented by setting low HO1 values (although keep in mind that this will prevent heating beyond temperatures which require that amount of coverage) or only turning on the current dial a short distance from the off position. It should be noted that if the light above the current dial turns on and is red, that means that the amount of current that the Eurotherm is requesting for is greater than what the dial is permitting.

C.5 CPU Heating Control via Eurotherm

Certain experiments require the Eurotherm to take complete control of the heating of the crystal (e.g. programs which heat the crystal at a linear ramp rate or the like). In general, it is better to heat the crystal using one of the previous methods when a heating program is not being used. However, the computer must control the heating of the crystal, the following is the method for doing so.

Following the method described in Section C.2, make sure the current and voltage dials are in the off position prior to turning on the power supply. Set the Eurotherm to the desired program or temperature using "SCH", then return to "MAN" mode and set the requested current to 0 amps. At this point the power supply can be turned on. With the power supply showing the minimum current (~0.5 amps), slowly increase the current dial. The current should not increase

as the dial is turned. Once the dial is set at a value other than the off position, press the button on the Eurotherm to switch the controller to "SCH" mode. This will immediately set the power supply to a current for reaching the target temperature. The computer will control the amount of current required to reach the set temperature. A plot of temperature vs time should show significant oscillation in dT/dt near t_0 and as the temperature reaches the target temperature, which can be minimized by appropriate PID settings (although these will vary depending on the temperature range and the rate of cooling). It should be noted that if the light above the current dial turns on and is red, that means that the amount of current that the Eurotherm is requesting for is greater than what the dial is permitting.

When a Eurotherm program is used, as in the case of a TPD program for linear heating ramp rates, it is best to set the target temperature by "SCH" to the minimum value of 63 K, which is impossible to reach with liquid nitrogen cooling. This will prevent the Eurotherm from requesting a current until the program is enabled. Additionally, when the program is terminated, the gain scheduling will return to 63 K and will not request any more current until the program is activated again.

C.6 Voltage Control

In the case where voltage control is desired over current control, the above mentioned techniques all work. Replace the terms "current" and "voltage" in the sections above. In the case of our system, voltage control resulted in significant overestimation and overcorrection by the Eurotherm, which was hard to curtail using PID parameters. However, the methods of heating described above are not exclusive to current control.